

THE UNIVERSITY OF MANITOBA

“PREDICTION OF DEVELOPING TURBULENT
PIPE FLOW BY A MODIFIED K- ϵ - γ MODEL”

BY

YOU QIN WANG

A THESIS
SUBMITTED TO THE FACULTY OF
GRADUATE STUDIES IN PARTIAL FULFILMENT
OF THE REQUIREMENTS FOR THE DEGREE OF
DOCTOR OF PHILOSOPHY IN THE DEPARTMENT
OF MECHANICAL AND INDUSTRIAL ENGINEERING

WINNIPEG, MANITOBA

APRIL, 1999



National Library
of Canada

Acquisitions and
Bibliographic Services

395 Wellington Street
Ottawa ON K1A 0N4
Canada

Bibliothèque nationale
du Canada

Acquisitions et
services bibliographiques

395, rue Wellington
Ottawa ON K1A 0N4
Canada

Your file Votre référence

Our file Notre référence

The author has granted a non-exclusive licence allowing the National Library of Canada to reproduce, loan, distribute or sell copies of this thesis in microform, paper or electronic formats.

The author retains ownership of the copyright in this thesis. Neither the thesis nor substantial extracts from it may be printed or otherwise reproduced without the author's permission.

L'auteur a accordé une licence non exclusive permettant à la Bibliothèque nationale du Canada de reproduire, prêter, distribuer ou vendre des copies de cette thèse sous la forme de microfiche/film, de reproduction sur papier ou sur format électronique.

L'auteur conserve la propriété du droit d'auteur qui protège cette thèse. Ni la thèse ni des extraits substantiels de celle-ci ne doivent être imprimés ou autrement reproduits sans son autorisation.

0-612-41631-3

**THE UNIVERSITY OF MANITOBA
FACULTY OF GRADUATE STUDIES

COPYRIGHT PERMISSION PAGE**

**“PREDICTION OF DEVELOPING TURBULENT PIPE FLOW BY A MODIFIED K- ϵ - γ
MODEL”**

BY

YOU QIN WANG

**A Thesis/Practicum submitted to the Faculty of Graduate Studies of The University
of Manitoba in partial fulfillment of the requirements of the degree
of
DOCTOR OF PHILOSOPHY**

YOU QIN WANG ©1999

Permission has been granted to the Library of The University of Manitoba to lend or sell copies of this thesis/practicum, to the National Library of Canada to microfilm this thesis and to lend or sell copies of the film, and to Dissertations Abstracts International to publish an abstract of this thesis/practicum.

The author reserves other publication rights, and neither this thesis/practicum nor extensive extracts from it may be printed or otherwise reproduced without the author's written permission.

ABSTRACT

A modified k - ϵ - γ model that eliminates the need for wall functions for internal flow has been proposed by the author. Instead of employing conditional zone averaged moments, this intermittency model is based on the conventional Reynolds averaged moments. Therefore, it is a more economical intermittency model compared with those employing conditional zone averaged moments because it halves the number of partial differential equations which need to be solved. This k - ϵ - γ model is superior to those employing wall functions for wall bounded flows because the use of wall functions limits the model's applicability.

In order to validate the code and assess the model performance, simulation results obtained by three other turbulence models are also presented. They are the Van Driest mixing-length model, the standard k - ϵ model and Chien's k - ϵ model. Tests were performed for a smooth circular pipe with a length-to-diameter ratio of 83.8 at a variety of bulk Reynolds numbers from $Re=10,000$ to $Re=500,000$. All model equations were discretized using an approximate exponential differencing scheme and solved by the well-established finite volume method. The SIMPLEC algorithm and staggered grids were used for the test cases. Each discretized governing equation was solved iteratively by the Line Gauss-Seidel method until the solution converged. Convergence was declared if the average of the magnitude of mass residual throughout the computational domain was less than 10^{-13} .

Simulation results show that the predicted Reynolds shear stress in the inlet region obtained by the present k - ϵ - γ model is in the best agreement with the experimental data among the four models. Furthermore, it predicts the mean velocity field as well as if not

better than Chien's model according to the comparison with various experimental data. The satisfactory simulation results indicate that this $k-\varepsilon-\gamma$ model is capable of predicting internal flows. For the first time, the intermittent factor was taken into account in the prediction of developing turbulent pipe flow, and for the first time the distributions of the intermittency factor are presented in detail for the pipe flow.

ACKNOWLEDGEMENT

First of all, I would like to express my sincere gratitude to my advisor, Dr. R. W. Derksen, for his valuable guidance and helpful discussions. I am also very grateful to the members of my advisory committee, Dr. R. S. Azad, Dr. J. Doering, and Dr. S. Kocabiyik for their time and efforts in reviewing my thesis, and for their thoughtful comments on it.

My particular appreciation is extended to my husband, Mingchuan. Without his support, it is impossible for me to be able to complete this thesis.

Finally, I would like to acknowledge the Duff Roblin Graduate Fellowship provided by the University of Manitoba, and the financial assistance provided by the NSERC through a grant to Dr. R. W. Derksen.

TABLE OF CONTENTS

ABSTRACT	I
ACKNOWLEDGEMENT	III
TABLE OF CONTENTS	IV
LIST OF FIGURES	VI
LIST OF TABLES	XVI
NOMENCLATURE	XVII
1 INTRODUCTION	1
1.1 Background and Objective	1
1.2 Layout of the Thesis	2
1.3 General Assumptions and Mean-Flow Equations	3
1.4 Turbulence and Turbulence Models	6
1.5 Literature Review On Pipe Flow	16
2 NUMERICAL PROCESS	17
2.1 Finite Volume Method and Discretization Equations	17
2.2 The Successive Over-Relaxation Solver	27
2.3 Staggered Grid	28
2.4 SIMPLEC Algorithm	29
3. VAN DRIEST'S MIXING-LENGTH MODEL	34
3.1 Model Equation	34
3.2 The Numerical Consideration	35
3.3 Results	40

4. THE STANDARD K- ϵ MODEL	54
4.1 Model Equations.....	54
4.2 Wall Functions: Expressions for k and ϵ Near Wall	55
4.3 Results	58
5. CHIEN'S K- ϵ MODEL	84
5.1 Model Equations.....	84
5.2 Numerical Considerations	85
5.3 Results	86
5.4 Model Assessment.....	88
6. MODIFIED K- ϵ - γ MODEL	105
6.1 Model Equations.....	105
6.2 Numerical Considerations	106
6.3 Results	117
7 COMPARISON OF THE FOUR MODELS	149
7.1 Predictions of Mean Velocity.....	149
7.2 Predictions for Turbulent Quantities	153
7.3 Model Performance Assessment	156
7.4 Physical Process in Developing Turbulent Pipe Flow	159
8. CONCLUSIONS AND RECOMMENDATIONS	174
REFERENCES	177
APPENDIX: LIST OF FREQUENTLY USED ABBREVIATIONS	185

LIST OF FIGURES

Figure 2.1	A control volume in cylindrical coordinates	19
Figure 2.2	Control volume for the two-dimensional situation	20
Figure 2.3	Distance associated with the interface e.	26
Figure 2.4	Control volumes for a staggered grid	29
Figure 3.1	Simulation results obtained using two grid systems for $Re = 50,000$ (the solid smooth lines represent the simulation results obtained using finer grids and the open circles represent the simulation results obtained using course grids).....	42
Figure 3.2	Confirmation of the convergence of the iteration for $Re = 50,000$ (the solid smooth lines represent the simulation results with 300 iterations and the open circles represent the simulation results with 600 iterations)	42
Figure 3.3	Confirmation of the convergence of the iteration for $Re = 500,000$ (the solid smooth lines represent the simulation results with 500 iterations and the open circles represent the simulation results with 1000 iterations)	43
Figure 3.4	Optimum "time step" tests for finer grids for $Re = 50,000$	44
Figure 3.5	Optimum "time step" tests for coarse grids for $Re = 50,000$	44
Figure 3.6	Optimum "time step" tests for finer grids for $Re = 500,000$	45
Figure 3.7	Optimum overrelaxation factor tests for finer grids for $Re = 50,000$	45
Figure 3.8	Contour plot for the non-dimensional axial velocity for $Re = 50,000$	46
Figure 3.9	Contour plot for the non-dimensional radial velocity for $Re = 50,000$	46
Figure 3.10	Contour plot for the non-dimensional axial velocity for $Re=50,000$	47
Figure 3.11	Axial velocity vs r/R at six downstream locations for $Re = 50,000$	47
Figure 3.12	Radial velocity vs r/R at six downstream locations for $Re=50,000$	48
Figure 3.13	Development of axial velocity for $Re = 50,000$	48
Figure 3.14	Contour plot for the non-dimensional axial velocity for $Re = 500,000$	49
Figure 3.15	Contour plot for the non-dimensional radial velocity for $Re = 500,000$	49
Figure 3.16	Contour plot for the non-dimensional axial velocity for $Re = 500,000$	50

Figure 3.17 Axial velocity vs r/R at six downstream locations for $Re = 500,000$	50
Figure 3.18 Radial velocity vs r/R at six downstream locations for $Re = 500,000$	51
Figure 3.19 Development of axial velocity for $Re = 500,000$	51
Figure 3.20 Contour plot for Reynolds shear stress for $Re=50,000$	52
Figure 3.21 Contour plot for Reynolds shear stress for $Re=500,000$	52
Figure 3.22 Reynolds shear stress vs r/R for $Re=50,000$	53
Figure 3.23 Reynolds shear stress vs r/R for $Re=500,000$	53
Figure 4.1 Y^+ vs x/D for $Re=50,000$ using three different locations to apply the wall functions.....	61
Figure 4.2 Y^+ vs r/R for $Re=50,000$ using three different locations to apply the wall functions.....	61
Figure 4.3 Results at $x/D=3.2$ for $Re=50,000$ using three different locations to apply the wall functions.....	62
Figure 4.4 Results at $x/D=19.6$ for $Re=50,000$ using three different locations to apply the wall functions.....	63
Figure 4.5 Results at $x/D=83.1$ for $Re=50,000$ using three different locations to apply the wall functions.....	64
Figure 4.6 Y^+ vs x/D for $Re=150,000$ using three different locations to apply the wall functions.....	65
Figure 4.7 Y^+ vs r/R for $Re=150,000$ using three different locations to apply the wall functions.....	65
Figure 4.8 Results at $x/D=3.2$ for $Re=150,000$ using three different locations to apply the wall functions.....	66
Figure 4.9 Results at $x/D=19.6$ for $Re=150,000$ using three different locations to apply the wall functions.....	67
Figure 4.10 Results at $x/D=83.1$ for $Re=150,000$ using three different locations to apply the wall functions.....	68
Figure 4.11 Convergence of the iterations.....	69
Figure 4.12 Contour plot for the non-dimensional axial velocity for $Re = 50,000$	70
Figure 4.13 Contour plot for the non-dimensional radial velocity for $Re = 50,000$	70
Figure 4.14 Contour plot for non-dimensional axial velocity for $Re=50,000$	71

Figure 4.15 Axial velocity vs r/R at six downstream locations for $Re=50,000$	71
Figure 4.16 Radial velocity vs r/R at six downstream locations for $Re=50,000$	72
Figure 4.17 Development of Axial velocity for $Re=50,000$	72
Figure 4.18 Contour plot for non-dimensional Turbulent Kinetic Energy for $Re = 50,000$	73
Figure 4.19 Contour plot for Reynolds shear stress for $Re = 50,000$	73
Figure 4.20 Contour plot for non-dimensional turbulent kinetic energy for $Re = 50,000$	74
Figure 4.21 Turbulent kinetic energy vs r/R at six downstream locations for $Re=50,000$	74
Figure 4.22 Development of turbulent kinetic energy for $Re=50,000$	75
Figure 4.23 Reynolds shear stress vs r/R at six downstream locations for $Re=50,000$	75
Figure 4.24 Development of Reynolds shear stress for $Re=50,000$	76
Figure 4.25 Turbulent dissipation rate vs r/R at six downstream locations for $Re=50,000$	76
Figure 4.26 Contour plot for the non-dimensional axial velocity for $Re = 150,000$	77
Figure 4.27 Contour plot for the non-dimensional radial velocity for $Re = 150,000$	77
Figure 4.28 Contour plot for non-dimensional axial velocity for $Re=150,000$	78
Figure 4.29 Axial velocity vs r/R at six downstream locations for $Re=150,000$	78
Figure 4.30 Radial velocity vs r/R at six downstream locations for $Re=150,000$	79
Figure 4.31 Development of axial velocity for $Re=150,000$	79
Figure 4.32 Contour plot for non-dimensional Turbulent Kinetic Energy for $Re = 150,000$	80
Figure 4.33 Contour plot for Reynolds shear stress for $Re = 150,000$	80
Figure 4.34 Contour plot for non-dimensional turbulent kinetic energy for $Re = 150,000$	81
Figure 4.35 Turbulent kinetic energy vs r/R at six downstream locations for $Re=150,000$	81
Figure 4.36 Development of turbulent kinetic energy for $Re=150,000$	82
Figure 4.37 Reynolds shear stress vs r/R at six downstream locations for $Re=150,000$..	82

Figure 4.38	Development of Reynolds shear stress for $Re=150,000$	83
Figure 4.39	Turbulent dissipation rate vs r/R at six downstream locations for $Re=150,000$	83
Figure 5.1	Contour plot for the non-dimensional axial velocity for $Re = 50,000$	90
Figure 5.2	Contour plot for the non-dimensional radial velocity for $Re = 50,000$	90
Figure 5.3	Contour plot for non-dimensional axial velocity for $Re=50,000$	91
Figure 5.4	Axial velocity vs r/R at six downstream locations for $Re=50,000$	91
Figure 5.5	Development of axial velocity for $Re=50,000$	92
Figure 5.6	Radial velocity vs r/R at six downstream locations for $Re=50,000$	92
Figure 5.7	Contour plot for non-dimensional Turbulent Kinetic Energy for $Re = 50,000$	93
Figure 5.8	Contour plot for Reynolds shear stress for $Re = 50,000$	93
Figure 5.9	Contour plot for non-dimensional turbulent kinetic energy for $Re=50,000$..	94
Figure 5.10	Turbulent kinetic energy vs r/R at six downstream locations for $Re=50,000$	94
Figure 5.11	Development of turbulent kinetic energy for $Re=50,000$	95
Figure 5.12	Reynolds shear stress vs r/R at six downstream locations for $Re=50,000$..	95
Figure 5.13	Development of Reynolds shear stress for $Re=50,000$	96
Figure 5.14	Turbulent dissipation rate vs r/R at six downstream locations for $Re=50,000$	96
Figure 5.15	Contour plot for the non-dimensional axial velocity for $Re = 10,000$	97
Figure 5.16	Contour plot for the non-dimensional radial velocity for $Re = 10,000$	97
Figure 5.17	Contour plot for non-dimensional axial velocity for $Re=10,000$	98
Figure 5.18	Axial velocity vs r/R at six downstream locations for $Re=10,000$	98
Figure 5.19	Development of axial velocity for $Re=10,000$	99
Figure 5.20	Radial velocity vs r/R at six downstream locations for $Re=10,000$	99
Figure 5.21	Contour plot for non-dimensional Turbulent Kinetic Energy for $Re = 10,000$	100
Figure 5.22	Contour plot for Reynolds shear stress for $Re = 10,000$	100
Figure 5.23	Contour plot for non-dimensional turbulent kinetic energy for $Re=10,000$	101

Figure 5.24	Turbulent kinetic energy vs r/R at six downstream locations for $Re=10,000$	101
Figure 5.25	Development of turbulent kinetic energy for $Re=10,000$	102
Figure 5.26	Reynolds shear stress vs r/R at six downstream locations for $Re=10,000$	102
Figure 5.27	Development of Reynolds shear stress for $Re=10,000$	103
Figure 5.28	Turbulent dissipation rate vs r/R at six downstream locations for $Re=10,000$	103
Figure 5.29	Convergence of mass residual.....	104
Figure 6.1	Model constant test 1 (the solid lines represent the simulation results obtained for $\sigma_k = 1.0$, and the open circles represent the simulation results obtained for $\sigma_k = 1.4$)	121
Figure 6.2	Turbulent kinetic energy distribution for model constant test 1 (the lines represent the simulation results obtained for $\sigma_k = 1.0$, and the open circles represent the simulation results obtained for $\sigma_k = 1.4$)	121
Figure 6.3	Model constant test 2 (the solid lines represent the simulation results obtained for $C_c = 0.0115$, and the open circles represent the simulation results obtained for $C_c = 0.013$)	122
Figure 6.4	Turbulent kinetic energy distribution for model constant test 2 (the lines represent the simulation results obtained for $C_c = 0.0115$, and the open circles represent the simulation results obtained for $C_c = 0.013$)	122
Figure 6.5	Model constant test 3 (the solid lines represent the simulation results obtained for $m = 3$, and the open circles represent the simulation results obtained for $m = 2.5$).....	123
Figure 6.6	Turbulent kinetic energy distribution for model constant test 3 (the lines represent the simulation results obtained for $m = 3$, and the open circles represent the simulation results obtained for $m = 2.5$).....	123

Figure 6.7	Model constant test 4 (the solid lines represent the simulation results obtained for $m = 3$, and the open circles represent the simulation results obtained for $m = 3.5$).....	124
Figure 6.8	Turbulent kinetic energy distribution for model constant test 4 (the lines represent the simulation results obtained for $m = 3$, and the open circles represent the simulation results obtained for $m = 3.5$).....	124
Figure 6.9	Model constant test 5 (the solid lines represent the simulation results obtained for $C_{\mu g} = 0.10$, and the open circles represent the simulation results obtained for $C_{\mu g} = 0.15$)	125
Figure 6.10	Turbulent kinetic energy distribution for model constant test 5 (the lines represent the simulation results obtained for $C_{\mu g} = 0.10$, and the open circles represent the simulation results obtained for $C_{\mu g} = 0.15$).....	125
Figure 6.11	Model constant test 6 (the solid lines represent the simulation results obtained for $C_{g3} = 0.16$, and the open circles represent the simulation results obtained for $C_{g3} = 0.20$).....	126
Figure 6.12	Turbulent kinetic energy distribution for model constant test 6 (the lines represent the simulation results obtained for $C_{g3} = 0.16$, and the open circles represent the simulation results obtained for $C_{g3} = 0.20$).....	126
Figure 6.13	Model constant test 7 (the solid lines represent the simulation results obtained for $C_{\epsilon 4} = 0.1$, and the open circles represent the simulation results obtained for $C_{\epsilon 4} = 0.2$).....	127
Figure 6.14	Turbulent kinetic energy distribution for model constant test 7 (the lines represent the simulation results obtained for $C_{\epsilon 4} = 0.1$, and the open circles represent the simulation results obtained for $C_{\epsilon 4} = 0.2$).....	127
Figure 6.15	Contour plot for axial mean velocity.....	128
Figure 6.16	Contour plot for intermittency factor γ	128

Figure 6.17	Simulation results obtained using two grid systems for $Re=200,000$ (the solid smooth lines represent the simulation results obtained using course grids and the open circles represent the simulation results obtained using finer grids).....	129
Figure 6.18	Confirmation of the convergence of the iteration for $Re=50,000$ (the solid smooth lines represent the simulation results with 1200 iterations and the open circles represent the simulation results with 600 iterations).....	129
Figure 6.19	Confirmation of the convergence of the iteration for $Re=200,000$ (the solid smooth lines represent the simulation results with 600 iterations and the open circles represent the simulation results with 1200 iterations).....	130
Figure 6.20	Convergence of mass residual.....	130
Figure 6.21	Contour plot for the non-dimensional axial velocity for $Re = 50,000$	131
Figure 6.22	Contour plot for the non-dimensional radial velocity for $Re = 50,000$	131
Figure 6.23	Contour plot for non-dimensional axial velocity for $Re=50,000$	132
Figure 6.24	Axial velocity vs r/R at six downstream locations for $Re=50,000$	132
Figure 6.25	Development of axial velocity for $Re=50,000$	133
Figure 6.26	Radial velocity vs r/R at six downstream locations for $Re=50,000$	133
Figure 6.27	Contour plot for non-dimensional Turbulent Kinetic Energy for $Re = 50,000$	134
Figure 6.28	Contour plot for Reynolds shear stress for $Re = 50,000$	134
Figure 6.29	Contour plot for non-dimensional turbulent kinetic energy for $Re=50,000$	135
Figure 6.30	Turbulent kinetic energy vs r/R at six downstream locations for $Re=50,000$	135
Figure 6.31	Development of turbulent kinetic energy for $Re=50,000$	136
Figure 6.32	Reynolds shear stress vs r/R at six downstream locations for $Re=50,000$	136
Figure 6.33	Development of Reynolds shear stress for $Re=50,000$	137

Figure 6.34 Turbulent dissipation rate vs r/R at six downstream locations for $Re=50,000$	137
Figure 6.35 Contour plot for intermittency factor for $Re = 50,000$	138
Figure 6.36 Contour plot for pressure for $Re = 50,000$	138
Figure 6.37 Intermittency factor vs r/R at eight different downstream positions for $Re=50,000$	139
Figure 6.38 Contour plot for the non-dimensional axial velocity for $Re = 200,000$	140
Figure 6.39 Contour plot for the non-dimensional radial velocity for $Re = 200,000$	140
Figure 6.40 Contour plot for non-dimensional axial velocity for $Re=200,000$	141
Figure 6.41 Axial velocity vs r/R at six downstream locations for $Re=200,000$	141
Figure 6.42 Development of axial velocity for $Re=200,000$	142
Figure 6.43 Radial velocity vs r/R at six downstream locations for $Re=200,000$	142
Figure 6.44 Contour plot for non-dimensional Turbulent Kinetic Energy for $Re = 200,000$	143
Figure 6.45 Contour plot for Reynolds shear stress for $Re = 200,000$	143
Figure 6.46 Contour plot for non-dimensional turbulent kinetic energy for $Re=200,000$	144
Figure 6.47 Turbulent kinetic energy vs r/R at six downstream locations for $Re=200,000$	144
Figure 6.48 Development of turbulent kinetic energy for $Re=200,000$	145
Figure 6.49 Reynolds shear stress vs r/R at six downstream locations for $Re=200,000$	145
Figure 6.50 Development of Reynolds shear stress for $Re=200,000$	146
Figure 6.51 Turbulent dissipation rate vs r/R at six downstream locations for $Re=200,000$	146
Figure 6.52 Contour plot for intermittency factor for $Re = 200,000$	147
Figure 6.53 Contour plot for pressure for $Re = 200,000$	147
Figure 6.54 Intermittency factor vs r/R at eight different downstream positions for $Re=200,000$	148
Figure 7.1 Variation of axial velocity with distance downstream of pipe inlet for $Re=50,000$ by four models	161

Figure 7.2	Variation of axial velocity with distance downstream of the pipe inlet for $Re=300,000$ by four models.....	161
Figure 7.3	Axial velocity vs r/R for $Re=50,000$, compared with the data of Deissler. See Figure 7.4 for line style legend.	162
Figure 7.4	Axial velocity vs r/R at $x/D=80.5$ for $Re=50,000$	162
Figure 7.5	Axial velocity vs r/R at $x/D=10, 20, 30$ for $Re=300,000$, compared with the data of Richman and Azad. See Figure 7.4 for line style legend.	163
Figure 7.6	Axial velocity vs r/R at $x/D=40,60, 70$ for $Re=300,000$, compared with the data of Richman and Azad. See Figure 7.4 for line style legend.	163
Figure 7.7	Variation of axial velocity with distance downstream of pipe inlet for $Re=50,000$, compared with the data of Reichert and Azad.	164
Figure 7.8	Variation of axial velocity with distance downstream of pipe inlet for $Re=50,000$, compared with the data of Richman and Azad.	164
Figure 7.9	Variation of axial velocity with distance downstream of pipe inlet by zero equation model for $Re=300,000$	165
Figure 7.10	Variation of axial velocity with distance downstream of pipe inlet by standard $k-\epsilon$ model for $Re=300,000$	165
Figure 7.11	Variation of axial velocity with distance downstream of pipe inlet by Chien's model for $Re=300,000$	166
Figure 7.12	Variation of axial velocity with distance downstream of pipe inlet by $k-\epsilon-\gamma$ model for $Re=300,000$	166
Figure 7.13	Mean velocity distribution at $x/D=83.8$ for $Re=50,000$ from the different models.	167
Figure 7.14	Mean velocity distribution at $x/D=83.8$ for $Re=300,000$ from the different models.	167
Figure 7.15	u^+ vs y^+ at $x/D=83.8$ for $Re=50,000$	168
Figure 7.16	u^+ vs y^+ at $x/D=83.8$ for $Re=300,000$	168
Figure 7.17	Turbulent kinetic energy vs r/R for $Re=50,000$	169

Figure 7.18	Turbulent kinetic energy vs r/R for $Re=300,000$.	169
Figure 7.19	Reynolds shear stress vs r/R for $Re=50,000$.	170
Figure 7.20	Reynolds shear stress vs r/R for $Re=300,000$.	170
Figure 7.21	Skin friction distributions.	171
Figure 7.22	Variation of skin friction along the longitudinal distance of the pipe, compare with the data of Reichert and Azad for $Re=54,800$ (o), $Re=75,000$ (x), and $Re=133,000$ (*).	171
Figure 7.23	Convergence of mass residue for $Re=300,000$.	172
Figure 7.24	Radial velocity vs. r/R at ten downstream locations for $Re=50,000$.	172
Figure 7.25	Contour plot for intermittent factor for $Re=50,000$.	173

LIST OF TABLES

Table 4.1	The values of the model constant in the standard k- ϵ model.....	55
Table 5.1	Skin-friction coefficients comparing with experimental data	89
Table 6.1	Mean flow properties obtained from numerical simulations and experiments by Eggels etc.	113
Table 6.2	Analysis of discretization errors	116
Table 6.3	The standard deviation for axial mean velocity.....	117
Table 7.1	Centerline “overshoot” peak position and peak value.....	150
Table 7.2	Skin friction coefficients for fully developed pipe flow.....	156
Table 7.3	Grid selection and CPU time	157

NOMENCLATURE

a	Coefficient in the discretization equation
A	Coefficient Matrix; constant; also area of the interface in a control volume
A_-, A_+	Constants
B	Constant
b	Constant term in the discretization equation
c	Species concentration
C	Constant
C_f, C_f^*	Skin-friction coefficient
$C_i, C_{\delta i}$	$i=1, 2, 3, 4$ model constants
C_{g_i}	$i=1,2,3$ model constants
$C_{uv}, C_{\mu g}$	Model constants
C_μ	Model constant
d, D	Diameter of the pipe
D	Diffusivity
e	Convergence error
f_e	Length ratio
f_2, f_μ, f	Dump function
F_x'''	Body force in the x direction
F_r'''	Body force in the r direction
h	Mesh length
H	Higher order term in Taylor series in discretization error equation
i	Inertia
I	Intermittent indicator function
k	Turbulent kinetic energy
k	Ratio of grid sizes ($\Delta y_- / \Delta y_+$ or $\Delta y_j / \Delta y_{j+1}$)
l_m	Mixing length
l, L	Length scale

N, M	Grid numbers
M_p	Mass in the control volume
m	Model constant of k - ϵ - γ model
\dot{m}	Mass flow rate
p	Pressure; exponent in discretization error equation
p'	Pressure correction
p^*	Guessed pressure
P	Fluid mechanical property
Pe	Peclet number
P_k	Stress production of k
Pr	Prandtl number
\mathbf{Q}	Vector
Q_p	Constant part of the linearized source term
r	Radial co-ordinate
R	Radius of the pipe
R_p	Coefficient of ϕ_p in the linearized source expression
Re	Reynolds number
s_{ij}	Mean strain rate
S_g	Source term in γ equation
S_ϕ	Source term of quantity ϕ
S_ϕ^c	Constant part of the linearized source term
S_ϕ^p	Coefficient of ϕ_p in the linearized source expression
t	Time
T	Temperature
U, V	Mean velocity components in x, r direction
U_b	Bulk velocity
U_e	Boundary-layer edge velocity
u, v	Fluctuating velocity components in x, r direction
u_*, u_τ	Friction velocity
U^*	Velocity based on the guessed pressure p^*

U^+	Non-dimensional velocity
U_i	Velocity in tensor notation
V^*, W^*	Similar to U^*
x	Axial co-ordinate
x_i, x_j	Co-ordinates in tensor notation
x_p	Peak overshoot position
y	Distance from the wall
y^+	Non-dimensional distance from the wall
w	Overrelaxation factor

Greek

α	Weighting factor, a variable value in discretization error equation
β	Weighting factor
χ	Vortex stretching invariant term
δ, δ^*	Displacement thickness
δ_{ij}	Kronecker delta
δr	r-direction distance between two adjacent grid points
δx or δz	Similar to δr .
ε	Turbulence dissipation rate
ε_h^h	Discretization error on grid h
ϕ	Fluctuating scalar quantity, generalized variable
γ	Intermittency factor
κ	Von Karman 's universal constant
λ	Molecular diffusivity
μ	Dynamic viscosity
μ_t	Eddy viscosity
ν	Kinematic molecular viscosity ($=\mu/\rho$)
ν_t	Eddy viscosity

θ	Cylinder coordinate in angular direction
ρ	Fluid density, residual
$\sigma_k, \sigma_\epsilon, \sigma_g$	Model constants
τ_o, τ_w	Wall shear stress
τ_{ij}	Reynolds stress tensor
ω	Dissipation per unit turbulent kinetic energy
ω	Overrelaxation factor
Φ	Mean scalar quantity
Γ	Turbulent diffusivity of heat or mass
Γ_ϕ	Effective diffusion coefficient
Δt	Time step
Δr	r-direction width of the control volume
Δx or Δz	Similar to Δr

Subscripts

c	Values on the centerline
i,j	Index
E, N, P, S, W	Grid notation
e	Control volume face between P and E.
n, w, s	Control volume face, similar to e.
r, θ , x or z	Cylindrical coordinates

Superscripts

c	Coefficients in the algebraic equation of mass conservation
o	Old value (at time t) of the variable
u	Coefficients in the algebraic equation for U
v	Coefficients in the algebraic equation for U
*	Previous-iteration value of a variable; also velocities based on a guessed pressure

Special symbols

\overline{uv}	Reynolds stress
$\overline{u_i u_j}$	Reynolds stress in tensor notation

$\overline{u_i \phi}$	Turbulent mass/heat fluxes
$\overline{u^2}$	Normal stress in x direction
$\overline{v^2}$	Normal stress in r direction
(Vol)	Volume

1 INTRODUCTION

1.1 Background and Objective

In the past ten years the computer industry has developed so fast so that it has changed most people's life. As CFD (Computational Fluid Dynamics) development depends heavily on computational facilities, a great step in progress has been made in recent years. The development of inexpensive, large memory, and high-speed computers is central to this advancement. With these accomplishments, it is now possible to explore some real world flow problems using CFD.

CFD is at the same stage that finite element analyses was probably at 5-10 years ago. Because it is a relatively young, commercial software is far from perfect. Most commercial codes have been successfully at solving flows similar to those they have been calibrated for. However, there is still some doubt about their ability to simulate complex flows due to questions regarding the flow modelling. It is impossible to predict which flows can be accurately simulated without extensive testing. Additionally, commercial packages don't predict quantities we may be interested in, such as intermittency. In fact, providing the prediction of the intermittency for the developing turbulent pipe flow for the first time is one of this thesis contributions.

Turbulence modeling, grid generation and algorithm development are three key elements in CFD. Comparing with the other two key elements, the development of turbulence modeling has been relatively slow. Some algebraic or two-equation models that are still widely used today are 20 years old. In order to develop more sophisticated turbulence models, serious efforts to include the intermittency in the turbulence model have been made by many

researchers. Among them, Cho and Chung's (1992) $k-\epsilon-\gamma$ model successfully resolved the anomaly of various turbulent free shear stress flows, e.g., the plane-wake/plane-jet. The plane-wake/plane-jet anomaly indicates the contradictory behavior of predicted results obtained for plane far wake when the eddy viscosity $k-\epsilon$ model is used. If the model constants are adjusted to obtain the correct spreading rate of the plane jet, the spreading rate of the plane wake is under-predicted by as much as 30% below the experimental values. Since Cho and Chung proposed their $k-\epsilon-\gamma$ model in 1992, their model has been successfully used for predicting some external shear flows (Kim and Chung, 1995, Ahn and Sung, 1995). But so far, no predictions have been made by this model for internal flow. Furthermore, Cho and Chung's $k-\epsilon-\gamma$ model is based on the standard $k-\epsilon$ model, and if it is used for wall bounded flow, wall functions are required. The major drawback in using wall functions is that they are not universal and a priori knowledge of the flow is necessary. The objective of my thesis work is to propose a modified $k-\epsilon-\gamma$ model for internal flow, which eliminates the need for wall functions. In fact, successfully proposing such a model is this thesis most important contribution.

1.2 Layout of the Thesis

In this Chapter, some general assumptions are presented in the next section. This is followed by a brief literature review on both the development of turbulence models and experimental investigation on pipe flow. In Chapter 2, the numerical process used in the present simulations is explained in detail. Chapter 3-6 contains equations for the four turbulence models and the result obtained by these models. It begins with the zero equation model in Chapter 3. Then two $k-\epsilon$ models are presented in Chapter 4 and 5. The modified

k- ϵ - γ model is presented in Chapter 7 with discussions on some important numerical considerations, such as error analysis. Model performance assessment for four models is presented in Chapter 7. Conclusions of the present numerical investigation and recommendations for future work are given in the last Chapter.

1.3 General Assumptions and Mean-Flow Equations

Tests were performed for a smooth circular pipe with a length-to-diameter ratio of 83.8. It has been assumed that the pipe flow is a two dimensional, viscous, turbulent, incompressible and Newtonian flow. A brief description on some related concepts is given below.

Inviscid and viscous flows: Flows in which the effects of viscosity are negligible are termed inviscid flows. When the effects of viscosity within flows are not negligible, the flows are called viscous flows.

Laminar and turbulent flows: Viscous flow regimes are classified as laminar or turbulent on the basis of flow structure. Flow structure in the laminar region is characterized by smooth motion in laminae, or layers. Flow structure in the turbulent region is characterized by random motions of fluid particles in addition to the mean motion.

Internal and external flows: Flows completely bounded by solid surfaces are called internal flows. Flows over bodies immersed in an unbounded fluid are termed external flows.

Compressible and incompressible flows: Flows in which variations in density are negligible are termed incompressible flows. When density variations within flows are not negligible, the flows are called compressible flows.

Newtonian and non-Newtonian fluids: Fluids in which shear stress is directly proportional to deformation rate are Newtonian fluids. Fluids in which shear stress is not directly proportional to deformation rate are non-Newtonian fluids.

The origin of those equations which govern the distribution of the mean-flow quantities are the conservation laws for mass, momentum, thermal energy and species concentration. For incompressible flows, these laws can be expressed in tensor notation as:

Mass conservation (continuity equation):

$$\frac{\partial U_i}{\partial x_i} = 0 \quad (1.1)$$

Momentum conservation (Navier-Stokes equations):

$$\frac{\partial U_i}{\partial t} + U_j \frac{\partial U_i}{\partial x_j} = -\frac{1}{\rho} \frac{\partial P}{\partial x_i} + \nu \frac{\partial^2 U_i}{\partial x_j \partial x_j} \quad (1.2)$$

Thermal energy/species concentration conservation:

$$\frac{\partial \Phi}{\partial t} + U_j \frac{\partial \Phi}{\partial x_j} = \lambda \frac{\partial^2 \Phi}{\partial x_i \partial x_i} + S_\Phi, \quad (1.3)$$

where U_i is the instantaneous velocity component in the direction x_i , P is the instantaneous static pressure, and Φ is a scalar quantity which may stand for either temperature T or species concentration c . S_Φ is a volumetric source term expressing, for example, heat generation due to chemical or biological reactions. ν and λ are the molecular viscosity and diffusivity of Φ respectively. Eq.(1.1) to Eq. (1.3) form a closed set. The most direct approach is to solve these exact equations without averaging or approximation. This approach is called direct numerical simulation (DNS). In spite of all the recent advances in computer technology, direct numerical simulation is possible only at low Reynolds numbers or simple geometry

because the storage capacity and speed of present-day computer is still not sufficient to allow a solution with sufficient grid points. As such the statistical approach has been used, where the quantities are averaged over a time scale that is long compared with that of the turbulent motion. The resulting equations describe the distribution of mean velocity, pressure, temperature and species concentration in the flow. Unfortunately, the process of averaging has created a new problem: the equations no longer constitute a closed system since they contain unknown terms representing the transport of mean momentum, heat and mass by the turbulent motion. The system can be closed only with the aid of empirical information. The approximated relationship between the turbulent transport quantities and the mean flow field is what turbulence modeling about. Let's have a look in this statistical approach.

First of all, the instantaneous values of the velocity U_i , the pressure P and the scalar quantity Φ are separated into mean and fluctuating quantities as:

$$U_i = \overline{U}_i + u_i, P = \overline{P} + p, \Phi = \overline{\Phi} + \phi, \quad (1.4)$$

where the mean quantities are defined as:

$$\overline{U}_i = \frac{1}{t_2 - t_1} \int_{t_1}^{t_2} U_i dt, \quad \overline{P} = \frac{1}{t_2 - t_1} \int_{t_1}^{t_2} P dt, \quad \overline{\Phi} = \frac{1}{t_2 - t_1} \int_{t_1}^{t_2} \Phi dt. \quad (1.5)$$

The averaging time $t_2 - t_1$ is long compared with the time scale of the turbulent motion. Introducing (1.4) into (1.1) to (1.3) and subsequent averaging in the way indicated by Eq. (1.5) yields the following equations (for brevity, the overbars indicating averaged values have been dropped from U_i , P and Φ):

Continuity equation:

$$\frac{\partial U_i}{\partial x_i} = 0 \quad (1.6)$$

Momentum equations:

$$\frac{\partial U_i}{\partial t} + U_j \frac{\partial U_i}{\partial x_j} = -\frac{1}{\rho} \frac{\partial P}{\partial x_i} + \frac{\partial}{\partial x_j} \left(\nu \frac{\partial U_i}{\partial x_j} - \overline{u_i u_j} \right) \quad (1.7)$$

Temperature/concentration equation:

$$\frac{\partial \Phi}{\partial t} + U_j \frac{\partial \Phi}{\partial x_j} = \frac{\partial}{\partial x_i} \left(\lambda \frac{\partial \Phi}{\partial x_i} - \overline{u_i \Phi} \right) + S_\Phi . \quad (1.8)$$

There are the equations governing the mean-flow quantities U_i , P and Φ . The equations are still exact since no assumptions have been introduced in deriving them; but they no longer form a closed set. Due to the nonlinearity of Eqs. (1.2) and (1.3), the averaging process has introduced unknown correlations between the fluctuating velocities, $\overline{u_i u_j}$, and between velocity and scalar fluctuations $\overline{u_i \Phi}$. Physically, this correlation, multiplied by the density ρ , represent the transport of momentum and heat or mass due to the fluctuating motion. In most flow regions, the turbulent stresses ($-\rho \overline{u_i u_j}$) and fluxes ($-\rho \overline{u_i \Phi}$) are much larger than their laminar counterparts ($\mu \frac{\partial U_i}{\partial x_j}$) and ($\rho \lambda \frac{\partial \Phi}{\partial x_i}$), and therefore the latter are often negligible.

Equations (1.6) to (1.8) can be solved for the mean values of velocity, pressure and temperature or concentration only when the turbulence correlation $\overline{u_i u_j}$, and $\overline{u_i \Phi}$ can be determined in some way. The determination of this correlation is the main problem in turbulence modeling.

1.4 Turbulence and Turbulence Models

It is very difficult to give a precise definition of turbulence. As Tennekes and Lumley (1972) mentioned in their book: "All one can do is list some of the characteristics of turbulent flows." The most important features of turbulence are irregularity, diffusivity, rotational and

three dimensional nature, and dissipation.

Irregularity: Turbulent flows are highly unsteady. A plot of the fluctuating velocity as a function of time would always appear random.

Diffusivity: The high diffusivity of turbulence causes rapid mixing and increased rates of momentum, heat, and mass transfer.

Rotational and three-dimensional nature: Turbulent flows always exhibit high levels of fluctuating vorticity and a three-dimensional nature. The time-averaged velocity may be a function of only two coordinates, but the instantaneous field appears essentially random. In fact, vortex stretching as one of the principal mechanisms by which the intensity of the turbulence is increased is absent in two-dimensional flow.

Dissipation: Turbulent flows are always dissipative. The large eddies interact with the mean flow, thereby extracting kinetic energy from the mean motion and feeding it into the large-scale turbulent motion. Due to the vortex stretching, the energy is passed on to smaller and smaller eddies until viscous forces become active and dissipate the energy. This process is called energy cascade. Turbulence needs a continuous supply of energy to make up for these viscous losses. If no energy is supplied, turbulence decays rapidly.

Because of all these turbulence features, turbulent motions contribute significantly to the transport of momentum, heat and mass in most flows of practical interest and therefore have a determining influence on the distributions of velocity, temperature and species concentration over the flow field.

Before discussing in development of turbulence modeling, it is useful to give a description on two basic concepts that strongly related with the development of turbulence modeling: eddy-viscosity and eddy-diffusivity. The eddy-viscosity concept (Rodi, 1984)

assumes that, in analogy to the viscous stresses in laminar flows, the turbulent stresses are proportional to the mean-velocity gradients. For general flow situations, this concept may be expressed as

$$\overline{-u_i u_j} = \nu_t \left(\frac{\partial U_i}{\partial x_j} + \frac{\partial U_j}{\partial x_i} \right) - \frac{2}{3} k \delta_{ij}, \quad (1.9)$$

where $\delta_{ij} = 1$ for $i = j$ and $\delta_{ij} = 0$ for $i \neq j$. The quantity ν_t is the turbulent or eddy viscosity which is proportional to a velocity scale V and a length scale L ($\nu_t \propto VL$). In contrast to the molecular viscosity ν , ν_t is not a fluid property but strongly depends on the state of turbulence. It may vary significantly from one point in the flow to another and also from flow to flow. The eddy-diffusivity concept (Rodi, 1984) assumes that, in analogy to the turbulent momentum transport, the turbulent heat or mass transport is related to the gradient of the transported quantity by:

$$\overline{-u_i \phi} = \Gamma \frac{\partial \Phi}{\partial x_i}, \quad (1.10)$$

where Γ is the turbulent diffusivity of heat or mass. Like the eddy viscosity, Γ is not a fluid property but depends on the state of the turbulence. It is closely related to ν_t , as $\Gamma = \nu_t / \sigma_t$, where σ_t is called the turbulent Prandtl number (for heat transport) or Schmidt number (for mass transport) respectively.

Among the many approaches for studying turbulent flows, there are three important numerical approaches: Direct Numerical Simulation (DNS), Large Eddy Simulation (LES), and the Reynolds Averaged Navier-Stokes equations (RANS). DNS refers a complete time-dependent solution of the Navier-Stokes and continuity equations. It is an established numerical technique to study the details of turbulent flows. Databases generated by DNS

offer the opportunity to extract information from the flow field, which maybe cannot be obtained from experiments. The availability of this detailed flow information has certainly improved our understanding of turbulence structure and physical processes that can be of value in developing turbulence control methods or prediction methods. However, even as computers become more and more powerful, DNS is still possible only at low Reynolds number.

LES, is a method in which the large eddies are computed and the smallest eddies are modeled. As we know, turbulent flows contain a wide range of length and time scales. The large scale motions generally play a dominant role in energy transfer, that is why a simulation which treats the large eddies more exactly than the small ones may make sense. In a LES, much larger timesteps can be taken than are possible in a DNS, therefor for a given computing cost, it is possible to achieve much higher Reynolds numbers with LES than with DNS. Both DNS and LES are outside the scope of this thesis. For further details about DNS and LES, see Leonard (1995) and Ferziger (1995), respectively.

Comparing with the RANS models, both DNS and LES are very expensive. That is why RANS is the most popular approach. Among RANS models, it has become customary to classify models according to the number of transport equations used in the model. According to this classification, by the early 1950's four main categories of RANS models had evolved, and with the coming of the age of computers since the 1960's, further development of all classes of turbulence models has occurred.

Algebraic (Zero-Equation) Models: The first well-known turbulence model dates back to 1925 when Prandtl (1925) introduced the mixing-length hypothesis and a straight forward

prescription for computing the eddy viscosity in terms of the mixing length. The Prandtl mixing-length hypothesis could be expressed as:

$$\nu_t = l_m^2 \left| \frac{\partial U}{\partial y} \right|. \quad (1.11)$$

The mixing length, l_m , is crudely similar to the mean free path between molecules, in that it is taken as some effective interaction distance, except that it is between eddies rather than molecules. The mixing-length model has been, and still is applied with great success for relatively simple flows, because l_m can be specified by simple empirical formulae in many situations. Another zero-equation model was also proposed by Prandtl (1942) and is called the free-shear-layer model. In this model he assumed the eddy viscosity ν_t to be constant over any cross section of the layer, the length scale L of the turbulence to be proportional to the layer width δ , and the velocity scale V to be proportional to the maximum velocity difference $|U_{\max} - U_{\min}|$ across the layer. According to $\nu_t \propto VL$, it yields the following eddy-viscosity formula

$$\nu_t = C\delta |U_{\max} - U_{\min}|, \quad (1.12)$$

where C is an empirical constant. δ is defined as the distance between points where the velocity differs from the free stream velocity by 1% of the maximum velocity difference across the layer. This model is applicable only to free shear layers.

One-Equation Models: In order to improve the ability to predict properties of turbulent flows, Prandtl (1945) postulated a model in which the eddy viscosity depends upon the kinetic energy of the turbulent fluctuations. He proposed a modeled differential equation to approximate the exact equation for k . Thus was born the concept of the so-called one-equation model of turbulence. The first one-equation model appears as follows:

$$\rho \frac{\partial k}{\partial t} + \rho U_j \frac{\partial k}{\partial x_j} = \tau_{ij} \frac{U_i}{\partial x_j} - C_d \rho \frac{k^{3/2}}{l} + \frac{\partial}{\partial x_j} \left[\left(\mu + \frac{\mu_t}{\sigma_k} \right) \frac{\partial k}{\partial x_j} \right], \quad (1.13)$$

where τ_{ij} , the Reynolds stress tensor, is given by

$$\tau_{ij} = 2\mu_t S_{ij} - \frac{2}{3} \rho k \delta_{ij}. \quad (1.14)$$

The mean strain rate S_{ij} is defined by

$$S_{ij} = \frac{1}{2} \left(\frac{\partial U_i}{\partial x_j} + \frac{\partial U_j}{\partial x_i} \right) \quad (1.15)$$

The eddy viscosity is given by

$$\mu_t = \rho k^{1/2} l. \quad (1.16)$$

Before the model can be used in applications, the length scale, l , and the closure coefficients σ_k and C_d must be specified. Emmons (1954) applied this model to several flows with some degree of success using $\sigma_k = 1$ and C_d ranging between 0.07 and 0.09. The length scale distributions were similar to those used for the mixing-length model.

One-equation models account for convective and diffusive transport of the turbulent velocity scale and are therefore superior to the mixing-length hypothesis when this transport is important.

Two-Equation Models: Two-equation models have served as the foundation for much of the turbulence model research during the past three decades. They are, in fact, the simplest complete turbulence models. A model is complete if it can be used to predict properties of a given turbulent flow with no prior knowledge of the turbulence structure. By far, the most popular two-equation models are the k - ϵ models, where ϵ is the dissipation rate. The earliest development efforts based on this model were those of Harlow and Nakayama (1968), and

Jones and Launder (1972). Later Jones and Launder's model became so well known that it is often referred to as the standard k- ϵ model. The equations of the standard k- ϵ model are given by

Eddy viscosity:

$$\nu_t = C_\mu k^2 / \epsilon \quad (1.17)$$

Turbulent kinetic energy:

$$\rho u \frac{\partial k}{\partial x} + \rho v \frac{\partial k}{\partial y} = \left[\left(\mu + \frac{\mu_t}{\sigma_k} \right) \frac{\partial k}{\partial y} \right] + \mu_t \left(\frac{\partial u}{\partial y} \right)^2 - \rho \epsilon - 2\mu \left(\frac{\partial k^{1/2}}{\partial y} \right)^2 \quad (1.18)$$

Dissipation rate:

$$\rho u \frac{\partial \epsilon}{\partial x} + \rho v \frac{\partial \epsilon}{\partial y} = \frac{\partial}{\partial y} \left[\left(\mu + \frac{\mu_t}{\sigma_\epsilon} \right) \frac{\partial \epsilon}{\partial y} \right] + c_1 \frac{\epsilon}{k} \mu_t \left(\frac{\partial u}{\partial y} \right)^2 - \frac{c_2 \rho \epsilon}{k} + 2.0 \frac{\mu \mu_t}{\rho} \left(\frac{\partial^2 u}{\partial y^2} \right)^2 \quad (1.19)$$

Closure coefficients are given by $C_{1\epsilon} = 1.45$, $C_{2\epsilon} = 2.0$, $C_\mu = 0.09$, $\sigma_k = 1.0$, and $\sigma_\epsilon = 1.3$.

To improve the ability to predict properties of turbulent flows, many modified k- ϵ models have been proposed during the past two decades. The works done by Hoffman (1975), Lam and Bremhorst (1981), Chien (1982), Nagano and Tagawa (1990), and Yang and Shih (1993) are only some examples. Among them only Chien's modified k- ϵ model will be discussed in detail later in Chapter 4. The second most popular two-equation model is the k- ω model that was first proposed by Kolmogorov (1942). Here ω is the dissipation per unit turbulence kinetic energy ($\omega \sim \epsilon/k$). With no prior knowledge of Kolmogorov's work, Saffman (1970) formulated another k- ω model that would prove superior to the Kolmogorov model.

Second-Order Closure (Stress/Flux-Equation) Models: The models reviewed so far assume that the local state of turbulence can be characterized by velocity and length scales and that the individual Reynolds stresses can be related to these scales by an eddy-viscosity

formula. In order to obtain more physically realistic models of the Reynolds stresses and to account properly for their transport, models were developed which employ transport equations for the individual stresses $\overline{u_i u_j}$. Analogous transport equations were introduced for the turbulent heat/mass fluxes $\overline{u_i \phi}$, and models based on these equations are often referred to as second-order-closure models. The most important contributions toward the development of this class of model were made by Donaldson and Rosenbaum (1968), Daly and Harlow (1970), Launder, Reece and Rodi (1975), and more recent contributions were made by Lumley (1978), Speziale (1985), Reynolds (1987). Second-order-closure models have great potential and are the only promising models in flow situations where the transport of stresses and fluxes is essential and cannot be approximated well by relating it to the transport of k . However, because these models are complex and computationally expensive, they have not reached the same state of practical application as two-equation models have.

An intermittency model could be used in any of the four types of models if the intermittency factor is included in the calculation of the Reynolds stress. It may helpful give a definition of the intermittency factor now before we go further in discussing of the development of the intermittency model. Let $I(x,t)$ be the indicator function defined as

$$I(x,t) = \begin{cases} 1 & \text{if } (x,t) \text{ is in the turbulent zone} \\ 0 & \text{if } (x,t) \text{ is in the nonturbulent zone} \end{cases} \quad (1.20)$$

Let $P(x,t)$ be any fluid mechanical property and its unconditioned average be \overline{P} , then its conditioned average is defined by

$$\overline{P}_1 = \frac{\overline{IP}}{\overline{I}} = \frac{\overline{IP}}{\gamma}, \quad \text{and} \quad \overline{P}_0 = \frac{\overline{(1-I)P}}{1-\overline{I}} = \frac{\overline{(1-I)P}}{1-\gamma} \quad (1.21)$$

where the subscripts 1 and 0 refer to the turbulent and non-turbulent zone respectively, and

the intermittency factor, γ , is defined as

$$\gamma = \bar{I}. \quad (1.22)$$

The existence of a sharp interface between turbulent and non turbulent fluid for a variety of shear flows was found several decades ago. The experimental treatment of intermittently turbulent flows was initiated by Corrsin and Kistler (1954). Later, closure models were suggested by Libby (1975,1976), and further important developments were contributed by Dopazo (1977), Dopaza and O'Brien (1979), Byggstoyl and Kollmann (1981,1986a, 1986b), Janicka and Kollmann (1985), and Kollmann (1985). Efforts to reflect the effect of intermittency in developing computational intermittency models have also been made by Chevray and Tutu (1977), Patel and Scheuerer (1981), Cebeci etc. (1986), and Haworth and Pope (1987), and they suggested a new eddy viscosity relation, which was modified with an intermittency factor γ . As it has been mentioned before, Cho and Chung (1992) proposed a new type of intermittency model. In contrast to the Byggstoyl and Kollmann intermittency model which employs conditional zone averaged moments, this k- ϵ - γ model is based on the conventional Reynolds averaged moments. It is a more economical model compared with Byggstoyl and Kollmann's as it halves the number of partial differential equations that need to be solved. The literature has shown that Cho and Chung's k- ϵ - γ model has been successfully used to predict a two-dimensional momentumless wake (Ahn and Sung, 1995), and to predict the turbulent flow field around an aerofoil (Kim and Chung, 1995). Recently, based on Cho and Chung's k- ϵ - γ model, Dewan, Arakeri and Srinivasan (1997) proposed a k- ϵ - \overline{I}^2 - γ model to predict the axisymmetric plume. The details of Cho and Chung's k- ϵ - γ model are as follows.

Eddy viscosity:

$$\nu_t = C_\mu \left\{ 1 + C_{\mu g} \frac{k^3}{\varepsilon^2} \gamma^{-m} (1-\gamma) \frac{\partial \gamma}{\partial x_k} \frac{\partial \gamma}{\partial x_k} \right\} \frac{k^2}{\varepsilon} \quad (1.23)$$

Turbulent kinetic energy:

$$\frac{Dk}{Dt} = \frac{\partial}{\partial x_i} \left(\frac{\nu_t}{\sigma_k} \frac{\partial k}{\partial x_i} \right) + P_k - \varepsilon \quad (1.24)$$

where P_k represents the production of k due to the shear strain and the normal strain given by (in cylindrical coordinates)

$$P_k = \nu_t \left(\frac{\partial U}{\partial r} + \frac{\partial V}{\partial x} \right)^2 - \left(\overline{u^2} - \overline{v^2} \right) \frac{\partial U}{\partial x} \quad (1.25)$$

Dissipation rate:

$$\frac{D\varepsilon}{Dt} = \frac{\partial}{\partial x_i} \left(\frac{\nu_t}{\sigma_\varepsilon} \frac{\partial \varepsilon}{\partial x_i} \right) + \frac{\varepsilon^2}{k} \left[C_{\varepsilon 1} \frac{P_k}{\varepsilon} - C_{\varepsilon 2} + C_{\varepsilon 4} \Gamma \right] \quad (1.26)$$

where

$$\Gamma = \frac{k^{2.5}}{\varepsilon^2} (\nabla|U|) \cdot (\nabla\gamma) \quad (1.27)$$

Here, the vortex stretching invariant term χ , used in the ε equation of Cho and Chung is dropped in Eq. (1.26). In two-dimensional flow χ vanishes, and for axisymmetric flow is proportional to $\omega^2 V/r$. Here ω is the mean flow vorticity. The radial velocity is insignificant in a pipe except in a small region near the wall at the entrance. This region is also nearly two-dimensional. Hence χ can be neglected for this flow.

Intermittency factor:

$$\frac{D\gamma}{Dt} = \frac{\partial}{\partial x_j} \left((1-\gamma) \frac{\nu_t}{\sigma_g} \frac{\partial \gamma}{\partial x_j} \right) + S_g \quad (1.28)$$

where

$$S_g = C_{g1}\gamma(1-\gamma)\frac{P_k}{k} + C_{g2}\frac{k^2}{\varepsilon}\frac{\partial\gamma}{\partial x_j}\frac{\partial\gamma}{\partial x_j} - C_{g3}\gamma(1-\gamma)\frac{\varepsilon}{k}\Gamma \quad (1.29)$$

Closure coefficients:

$$C_\mu = 0.09, C_{\mu g} = 0.10, m = 3.0, C_{uv} = 0.33, \sigma_k = 1.0, \sigma_\varepsilon = 1.0, \\ \sigma_g = 1.0, C_{\varepsilon 1} = 1.44, C_{\varepsilon 2} = 1.92, C_{\varepsilon 4} = 0.1, C_{g1} = 1.6, C_{g2} = 0.15, \\ C_{g3} = 0.16.$$

1.5 Literature Review On Pipe Flow

A survey of the literature on turbulent developing pipe flow reveals that numerous research work has been done including both the experimental studies and the numerical studies. Some well-known experimental work has been done by Nikuradse (1932), Deissler (1950,1955), Laufer (1954), Cockrell and Markland (1962), Barbin and Jones (1963), Cockrell (1964,1967), Sale (1967), Patel and Head (1969), Miller (1971), Weir, Priest and Sharan (1974), Priest (1975), Reichert and Azad (1976), Pozzorini (1976), Reichert (1977), Laws, Lim and Livesey (1979), Klein (1981), den Toonder and Nieuwstadt (1997), and Zagarola and Smits (1998). Some important numerical studies include work done by Uspuras, Vilemas, and Poskas (1989), Martinuzzi (1985), and Martinuzzi and Pollard (1989). Richman and Azad (1973) and Eggels etc. (1994) have made both numerical and experimental investigation on the turbulent pipe flow. No predictions for developing turbulent pipe flow that take the intermittency character into account, although it is known that the inlet region of a smooth pipe is a highly intermittent region. Furthermore, it is believed that the understanding of the intermittency character in developing pipe flow is important for modeling more complicated internal flows.

2 NUMERICAL PROCESS

A modified $k\text{-}\varepsilon\text{-}\gamma$ model, which eliminates the need for wall functions for internal flow, has been proposed by the author. The model equations and simulation results are presented in Chapter 7. Tests were performed for a smooth circular pipe with a length-to-diameter ratio of 83.8, bulk Reynolds number from 10,000 to 500,000. In order to validate the code and assess the model performance, simulation results obtained by three other models are also included. They are Van Driest's mixing length model, Standard $k\text{-}\varepsilon$ model, and Chien's $k\text{-}\varepsilon$ model. All model equations were discretized using Raithby and Torrance's (1974) approximate exponential differencing scheme and solved by the well-established finite volume method. The SIMPLEC algorithm and staggered grids were used for the test cases. Each discretized governing equation was solved iteratively by the line Gauss-Seidel method until the solution was converged. Convergence was declared if the average of the magnitude of mass residual throughout the computational domain was less than 10^{-13} .

In this Chapter, the discretization equations, which have been used in the present numerical investigation, are discussed in detail in the first section. That is followed by the sections with a brief discussion on the solver and grids. Then the procedure of the SIMPLEC algorithm is summarized in the last section.

2.1 *Finite Volume Method and Discretization Equations*

After selecting the mathematical model, one has to choose a suitable discretization method, i.e. a method of approximating the differential equations by a system of algebraic equations for the variables at some set of discrete locations in space and time. There are three important discretization approaches: the finite difference method (FDM), the finite volume

method (FVM), and the finite element method (FEM). The FDM is the oldest method for numerical solution of PDE's (partial differential equations). It is also the easiest method to use for simple geometry. On structured grids, the FDM is very simple and effective. It is especially easy to obtain higher-order schemes on regular grids. The disadvantage of the FDM is that the conservation is not enforced unless special care is taken. Also, the restriction to simple geometry is a significant disadvantage in complex flows. The FVM can accommodate any type of grid, so it is suitable for complex geometry. Because all terms that need be approximated have physical meaning, the FVM is perhaps the simplest to understand and to program. The disadvantage of FVM compared to FDM is that it is not easy to obtain higher-order schemes for 3D flow. The FEM is similar to the FVM in many ways. An important advantage of FEM is the ability to deal with arbitrary geometry. FEM is relatively easy to analyze mathematically and can be shown to have optimality properties for certain types of equations. The principal drawback, which is shared by any method that uses unstructured grids, is that the matrices of the linearized equations are not as well structured as those for regular grids making it more difficult to find efficient solution methods. Each type of method yields the same solution if the grid is very fine. However, some methods are more suitable to some classes of problems than others. The FVM is the most popular for CFD (Computational Fluid Dynamics) therefore it was used in the present numerical simulations. A detailed description of the FVM will be given below. For more information about the FDM and the FEM, see the books by Anderson, Tannehill and Pletcher (1984) and by Ninomiya and Onishi (1991).

Discretization Equation: The FVM uses the integral form of the conservation equation as the starting point:

$$\int_S \rho \phi v \cdot n dS = \int_S \Gamma \text{grad} \phi \cdot n dS + \int_{\Omega} q_{\phi} d\Omega \quad (2.1)$$

The solution domain is subdivided into a finite number of small control volumes (CVs) by a grid which, in contrast to the finite difference method, defines the control volume boundaries, not the computational nodes. A typical control volume in cylindrical coordinates is shown below (Figure 2.1).

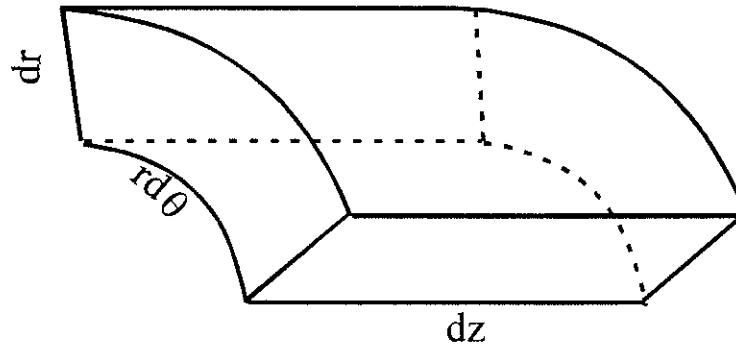


Figure 2.1 A control volume in cylindrical coordinates

The governing equation is given by:

$$\begin{aligned} \frac{\partial}{\partial t}(\rho \phi) + \frac{\partial}{\partial r}(\rho u_r \phi) + \frac{\partial}{r \partial \theta}(\rho u_{\theta} \phi) + \frac{\partial}{\partial z}(\rho u_z \phi) = \\ \frac{\partial}{\partial r}(\Gamma \frac{\partial \phi}{\partial r}) + \frac{\partial}{r \partial \theta}(\Gamma \frac{\partial \phi}{r \partial \theta}) + \frac{\partial}{\partial z}(\Gamma \frac{\partial \phi}{\partial z}) + S \end{aligned} \quad (2.2)$$

and the equation of conservation of mass is given by:

$$\frac{\partial}{\partial t}(\rho) + \frac{\partial}{\partial r}(\rho u_r) + \frac{\partial}{r \partial \theta}(\rho u_{\theta}) + \frac{\partial}{\partial z}(\rho u_z) = 0. \quad (2.3)$$

For axisymmetric problems, we assume u_{θ} is zero. Thus a three-dimensional problem reduces to a two-dimensional problem. A portion of a two-dimensional grid is shown in Figure 2.2.

Therefore we have the equation of the conservation of mass:

$$\frac{\partial}{\partial t}(\rho) + \frac{\partial}{\partial r}(\rho u_r) + \frac{\partial}{\partial z}(\rho u_z) = 0 \quad , \quad (2.4)$$

and the equation for transport of ϕ becomes

$$\frac{\partial}{\partial t}(\rho \phi) + \frac{\partial}{\partial r}(\rho u_r \phi) + \frac{\partial}{\partial z}(\rho u_z \phi) = \frac{\partial}{\partial r}(\Gamma \frac{\partial \phi}{\partial r}) + \frac{\partial}{\partial z}(\Gamma \frac{\partial \phi}{\partial z}) + S. \quad (2.5)$$

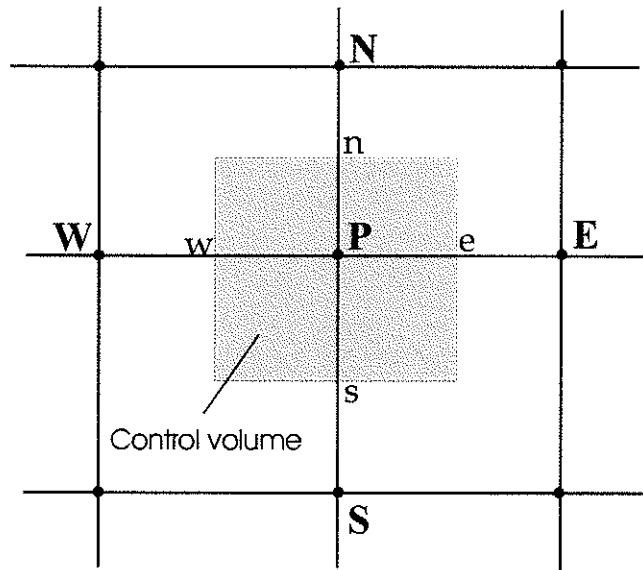


Figure 2.2 Control volume for the two-dimensional situation

To obtain the discretization equation we must consider changes in time and space. We now integrate Equation (2.4) over a typical control volume and over a time step Δt term by term:

$$\int_t^{t+\Delta t} \int_V \frac{\partial}{\partial t}(\rho) dV dt + \int_t^{t+\Delta t} \int_V \frac{\partial}{\partial r}(\rho u_r) dV dt + \int_t^{t+\Delta t} \int_V \frac{\partial}{\partial z}(\rho u_z) dV dt = 0. \quad (2.6)$$

Where Term I becomes

$$\int_t^{t+\Delta t} \int_V \frac{\partial}{\partial t} (\rho) dV dt = (\rho_p - \rho_p^o)(Vol)_p = (M_p - M_p^o), \quad (2.7)$$

Term II becomes

$$\int_t^{t+\Delta t} \int_V \frac{\partial}{\partial r} (\rho u_r) dV dt = \int_t^{t+\Delta t} \int_A \int_s^n \frac{\partial}{\partial r} (\rho u_r) dr dA dt = \int_t^{t+\Delta t} \{(\rho A u_r)_n - (\rho A u_r)_s\} dt = (\dot{m}_n - \dot{m}_s) \Delta t, \quad (2.8)$$

and Term III becomes

$$\int_t^{t+\Delta t} \int_V \frac{\partial}{\partial z} (\rho u_z) dV dt = \int_t^{t+\Delta t} \int_A \int_w^e \frac{\partial}{\partial z} (\rho u_z) dz dA dt = \int_t^{t+\Delta t} \{(\rho A u_z)_e - (\rho A u_z)_w\} dt = (\dot{m}_e - \dot{m}_w) \Delta t. \quad (2.9)$$

M_p in Eq. (2.7) is mass over the typical control volume, and \dot{m}_n , \dot{m}_s in Eq. (2.8) is the mass flux through the 'n' face and the 's' face respectively. Analogous to \dot{m}_n and \dot{m}_s , \dot{m}_e and \dot{m}_w in Eq. (2.9) is the mass flux through the 'e' face and the 'w' face. Next substitute Equations (2.7) to (2.9) into Equation (2.6) and divide by Δt to obtain

$$\frac{(M_p - M_p^o)}{\Delta t} = (\dot{m}_w - \dot{m}_e + \dot{m}_s - \dot{m}_n), \quad (2.10)$$

where the left side is the rate of storage of mass in the c.v. and the right side is the net inflow of mass. Thus we integrate Equation (2.5) over the control volume which yields:

$$\begin{aligned} & \int_t^{t+\Delta t} \int_V \frac{\partial}{\partial t} (\rho \phi) dV dt + \int_t^{t+\Delta t} \int_V \frac{\partial}{\partial r} (\rho u_r \phi) dV dt + \int_t^{t+\Delta t} \int_V \frac{\partial}{\partial z} (\rho u_z \phi) dV dt \\ & = \int_t^{t+\Delta t} \int_V \frac{\partial}{\partial r} (\Gamma \frac{\partial \phi}{\partial r}) dV dt + \int_t^{t+\Delta t} \int_V \frac{\partial}{\partial z} (\Gamma \frac{\partial \phi}{\partial z}) dV dt + \int_t^{t+\Delta t} \int_V S dV dt \end{aligned} \quad (2.11)$$

Now we have Term I:

$$\int_t^{t+\Delta t} \int_V \frac{\partial}{\partial t} (\rho \phi) dV dt = \{(\rho \phi)_p - (\rho \phi)_p^o\} (Vol)_p = (M_p \phi_p - M_p^o \phi_p^o). \quad (2.12)$$

Term II:

$$\int_t^{t+\Delta t} \int_V \frac{\partial}{\partial \mathbf{r}} (\rho \mathbf{u}_r \phi) dV dt = \int_t^{t+\Delta t} \int_A \int_s^n \frac{\partial}{\partial \mathbf{r}} (\rho \mathbf{u}_r \phi) dr dA dt = \int_t^{t+\Delta t} \{(\rho A u_r \phi)_n - (\rho A u_r \phi)_s\} dt = (\dot{m}_n \phi_n - \dot{m}_s \phi_s) \Delta t. \quad (2.13)$$

If we choose $\phi_n = \left(\frac{1}{2} + \alpha_n\right) \phi_P + \left(\frac{1}{2} - \alpha_n\right) \phi_N,$ (2.14)

and $\phi_s = \left(\frac{1}{2} + \alpha_s\right) \phi_S + \left(\frac{1}{2} - \alpha_s\right) \phi_P.$ (2.15)

The formula for calculating α is given by Eq. (2.39). We can substitute Equations (2.14) and (2.15) into Equation (2.13) to yield

$$\begin{aligned} \text{Term II} &= \{ \dot{m}_n [\left(\frac{1}{2} + \alpha_n\right) \phi_P + \left(\frac{1}{2} - \alpha_n\right) \phi_N] - \dot{m}_s [\left(\frac{1}{2} + \alpha_s\right) \phi_S + \left(\frac{1}{2} - \alpha_s\right) \phi_P] \} \Delta t \\ &= \{ \dot{m}_n \left(\frac{1}{2} - \alpha_n\right) \phi_N - \dot{m}_s \left(\frac{1}{2} + \alpha_s\right) \phi_S + [\dot{m}_n \left(\frac{1}{2} + \alpha_n\right) - \dot{m}_s \left(\frac{1}{2} - \alpha_s\right)] \phi_P \} \Delta t \end{aligned} \quad (2.16)$$

Term III is calculated in a manner analogous to that used for Term II, and is given by

$$\text{Term III} = \{ \dot{m}_e \left(\frac{1}{2} - \alpha_e\right) \phi_E - \dot{m}_w \left(\frac{1}{2} + \alpha_w\right) \phi_W + [\dot{m}_e \left(\frac{1}{2} + \alpha_e\right) - \dot{m}_w \left(\frac{1}{2} - \alpha_w\right)] \phi_P \} \Delta t, \quad (2.17)$$

where the equations

$$\phi_e = \left(\frac{1}{2} + \alpha_e\right) \phi_P + \left(\frac{1}{2} - \alpha_e\right) \phi_E \quad (2.18)$$

and $\phi_w = \left(\frac{1}{2} + \alpha_w\right) \phi_W + \left(\frac{1}{2} - \alpha_w\right) \phi_P$ (2.19)

are used.

Term IV is given by

$$\int_t^{t+\Delta t} \int_V \frac{\partial}{\partial \mathbf{r}} \left(\Gamma \frac{\partial \phi}{\partial \mathbf{r}} \right) dV dt = \int_t^{t+\Delta t} \int_A \int_s^n \frac{\partial}{\partial \mathbf{r}} \left(\Gamma \frac{\partial \phi}{\partial \mathbf{r}} \right) dr dA dt = \int_t^{t+\Delta t} \left\{ \Gamma_n A_n \frac{\partial \phi}{\partial \mathbf{r}} \Big|_n - \Gamma_s A_s \frac{\partial \phi}{\partial \mathbf{r}} \Big|_s \right\} dt \quad (2.20)$$

Let
$$\left. \frac{\partial \phi}{\partial r} \right|_n = \beta_n \frac{(\phi_N - \phi_P)}{(\delta r)_n}, \quad (2.21)$$

and
$$\left. \frac{\partial \phi}{\partial r} \right|_s = \beta_s \frac{(\phi_P - \phi_S)}{(\delta r)_s}, \quad (2.22)$$

then

$$\begin{aligned} \text{Term IV} &= \int_t^{t+\Delta t} \left\{ \Gamma_n A_n \beta_n \frac{(\phi_N - \phi_P)}{(\delta r)_n} - \Gamma_s A_s \beta_s \frac{(\phi_P - \phi_S)}{(\delta r)_s} \right\} dt \\ &= \left\{ \frac{\Gamma_n A_n \beta_n}{(\delta r)_n} (\phi_N - \phi_P) - \frac{\Gamma_s A_s \beta_s}{(\delta r)_s} (\phi_P - \phi_S) \right\} \Delta t \\ &= \left\{ \frac{\Gamma_n A_n \beta_n}{(\delta r)_n} \phi_N + \frac{\Gamma_s A_s \beta_s}{(\delta r)_s} \phi_S - \left(\frac{\Gamma_n A_n \beta_n}{(\delta r)_n} + \frac{\Gamma_s A_s \beta_s}{(\delta r)_s} \right) \phi_P \right\} \Delta t \end{aligned} \quad (2.23)$$

where the formula for calculating β is also given by Eq. (2.39).

$$\begin{aligned} \text{Term V} &= \int_t^{t+\Delta t} \int_V \frac{\partial}{\partial z} \left(\Gamma \frac{\partial \phi}{\partial z} \right) dV dt = \int_t^{t+\Delta t} \int_{A_w}^e \frac{\partial}{\partial z} \left(\Gamma \frac{\partial \phi}{\partial z} \right) dz dA dt = \int_t^{t+\Delta t} \left\{ \Gamma_e A_e \left. \frac{\partial \phi}{\partial z} \right|_e - \Gamma_w A_w \left. \frac{\partial \phi}{\partial z} \right|_w \right\} dt \\ &= \int_t^{t+\Delta t} \left\{ \Gamma_e A_e \beta_e \frac{(\phi_E - \phi_P)}{(\delta z)_e} - \Gamma_w A_w \beta_w \frac{(\phi_P - \phi_W)}{(\delta z)_w} \right\} dt \\ &= \left\{ \frac{\Gamma_e A_e \beta_e}{(\delta z)_e} (\phi_E - \phi_P) - \frac{\Gamma_w A_w \beta_w}{(\delta z)_w} (\phi_P - \phi_W) \right\} \Delta t \\ &= \left\{ \frac{\Gamma_e A_e \beta_e}{(\delta z)_e} \phi_E + \frac{\Gamma_w A_w \beta_w}{(\delta z)_w} \phi_W - \left(\frac{\Gamma_e A_e \beta_e}{(\delta z)_e} + \frac{\Gamma_w A_w \beta_w}{(\delta z)_w} \right) \phi_P \right\} \Delta t, \end{aligned} \quad (2.24)$$

where

$$\left. \frac{\partial \phi}{\partial z} \right|_e = \beta_e \frac{(\phi_E - \phi_P)}{(\delta z)_e}, \quad (2.25)$$

and
$$\left. \frac{\partial \phi}{\partial z} \right|_w = \beta_w \frac{(\phi_P - \phi_W)}{(\delta z)_w}. \quad (2.26)$$

$$\begin{aligned} \text{Finally Term VI} &= \int_{t}^{t+\Delta t} \int_{\mathcal{V}} S d\mathcal{V} dt \approx (Vol)_p \int_t^{t+\Delta t} \{S_c + S_p \phi_p\} dt = \{S_c (Vol)_p + S_p (Vol)_p \phi_p\} \Delta t \\ &= \{Q_p + R_p \phi_p\} \Delta t \end{aligned} \quad (2.27)$$

Now, assembling all terms and dividing through by Δt one obtains

$$\begin{aligned} &\frac{(M_p \phi_p - M_p^o \phi_p^o)}{\Delta t} + \dot{m}_e \left(\frac{1}{2} - \alpha_e\right) \phi_E - \dot{m}_w \left(\frac{1}{2} + \alpha_w\right) \phi_W + \left[\dot{m}_e \left(\frac{1}{2} + \alpha_e\right) - \dot{m}_w \left(\frac{1}{2} - \alpha_w\right) \right] \phi_P \\ &\quad + \dot{m}_n \left(\frac{1}{2} - \alpha_n\right) \phi_N - \dot{m}_s \left(\frac{1}{2} + \alpha_s\right) \phi_S + \left[\dot{m}_n \left(\frac{1}{2} + \alpha_n\right) - \dot{m}_s \left(\frac{1}{2} - \alpha_s\right) \right] \phi_P \\ &= \left(\frac{\Gamma_e A_e \beta_e}{(\delta z)_e} \right) \phi_E + \left(\frac{\Gamma_w A_w \beta_w}{(\delta z)_w} \right) \phi_W - \left(\frac{\Gamma_e A_e \beta_e}{(\delta z)_e} + \frac{\Gamma_w A_w \beta_w}{(\delta z)_w} \right) \phi_P \\ &\quad + \left(\frac{\Gamma_n A_n \beta_n}{(\delta r)_n} \right) \phi_N + \left(\frac{\Gamma_s A_s \beta_s}{(\delta r)_s} \right) \phi_S - \left(\frac{\Gamma_n A_n \beta_n}{(\delta r)_n} + \frac{\Gamma_s A_s \beta_s}{(\delta r)_s} \right) \phi_P + Q_p + R_p \phi_p \end{aligned} \quad (2.28)$$

Gather terms to write in the form:

$$a_p \phi_p = \sum a_{NP} \phi_{NP} + b_p. \quad (2.29)$$

Where

$$\sum a_{NP} \phi_{NP} = a_E \phi_E + a_W \phi_W + a_N \phi_N + a_S \phi_S \quad (2.30)$$

$$\begin{aligned} a_E &= \beta_e D_e + \alpha_e \dot{m}_e - \frac{1}{2} \dot{m}_e \\ a_W &= \beta_w D_w + \alpha_w \dot{m}_w + \frac{1}{2} \dot{m}_w \\ a_N &= \beta_n D_n + \alpha_n \dot{m}_n - \frac{1}{2} \dot{m}_n \\ a_S &= \beta_s D_s + \alpha_s \dot{m}_s + \frac{1}{2} \dot{m}_s \end{aligned} \quad (2.31)$$

$$a_p = \left[\frac{M_p^o}{\Delta t} + a_p^* - R_p \right] \quad (2.32)$$

$$a_p^* = \sum a_{NP} = a_W + a_E + a_S + a_N \quad (2.33)$$

$$b_p = \frac{M_p^o}{\Delta t} \phi_p^o + Q_p \quad (2.34)$$

$$\begin{aligned} D_e &= \frac{\Gamma_e A_e}{(\delta z)_e} \\ D_w &= \frac{\Gamma_w A_w}{(\delta z)_w} \\ D_n &= \frac{\Gamma_n A_n}{(\delta r)_n} \\ D_s &= \frac{\Gamma_s A_s}{(\delta r)_s} \end{aligned} \quad (2.35)$$

The mass fluxes are given by

$$\begin{aligned} \dot{m}_w &= (\rho U_z A)_w \\ \dot{m}_e &= (\rho U_z A)_e \\ \dot{m}_s &= (\rho U_r A)_s \\ \dot{m}_n &= (\rho U_r A)_n \end{aligned} \quad (2.36)$$

The value of the diffusion coefficient, Γ , at a control volume face is calculated using the harmonic mean, which, for a non-uniform grid, is given for the east face in the following example:

$$\Gamma_e = \frac{\Gamma_P \Gamma_E}{(f_e \Gamma_P + (1 - f_e) \Gamma_E)} \quad (2.37)$$

where

$$f_e = \frac{(\delta z)_{e+}}{(\delta z)_e} = \frac{(\delta z)_{e+}}{((\delta z)_{e-} + (\delta z)_{e+})} \quad (2.38)$$

for the dimensions shown in Figure 2.3.

The r-direction interpolations are done analogously. To obtain the exponential differencing scheme (EDS) the following specifications for α and β should be used. For example, at the east face:

$$\alpha_e = \frac{1}{2} \frac{\left[\exp\left(\frac{1}{2}(Pe)_e\right) - 1 \right]}{\left[\exp((Pe)_e) - 1 \right]} \quad (2.39)$$

$$\beta_e = \frac{(Pe)_e \left[\exp\left(\frac{1}{2}(Pe)_e\right) \right]}{\left[\exp((Pe)_e) - 1 \right]}$$

where

$$(Pe)_e = \frac{(\rho AU_z)_e}{\left(\frac{(\Gamma A)_e}{(\delta z)_e} \right)} = \frac{\dot{m}_e}{D_e} \quad (2.40)$$

Similar expressions are used to calculate α_w and β_w .

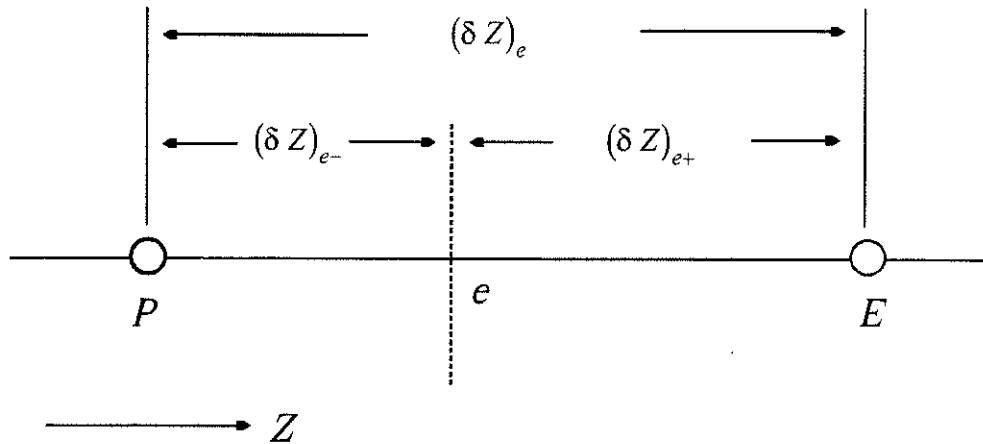


Figure 2.3 Distance associated with the interface e.

An accepted approximation is Raithby and Torrance's (1974) approximate exponential differencing scheme (AEDS). There are two advantages for using AEDS. The first, AEDS is much cheaper to compute than using EDS. The second, AEDS doesn't require check code for underflow or overflow of the exponent function (i.e. $\exp((Pe)_e)$ or $\exp((0.5(Pe)_e)$) because both α and β will always be positive. The AEDS expressions for α and β are:

$$\alpha_e = \frac{1}{2} \frac{(Pe)^2}{[5 + (Pe)^2]}$$

$$\beta_e = \frac{1 + 0.005(Pe)^2}{1 + 0.05(Pe)^2} \quad (2.41)$$

2.2 The Successive Over-Relaxation Solver

The successive over-relaxation (SOR) solver was used for solving the non-linear equations derived in Section 2.1. Actually SOR is an accelerated version of the Gauss-Seidel method, which we shall describe below. Eq. (2.29) can be rewritten as:

$$\phi_p = \frac{a_E \phi_E + a_W \phi_W + a_N \phi_N + a_S \phi_S + b_p}{a_p} \quad (2.42)$$

If each iteration is started at the lower left (southwest) corner of the domain, the Gauss-Seidel method can be written:

$$\phi_p^{n+1} = \frac{a_E \phi_E^n + a_W \phi_W^{n+1} + a_N \phi_N^n + a_S \phi_S^{n+1} + b_p}{a_p}, \quad (2.43)$$

and the SOR method can be written:

$$\phi_p^{n+1} = \omega \frac{a_E \phi_E^n + a_W \phi_W^{n+1} + a_N \phi_N^n + a_S \phi_S^{n+1} + b_p}{a_p} + (1 - \omega) \phi_p^n \quad (2.44)$$

where ω is the over-relaxation factor (which must be greater than 1 for acceleration), and n is the iteration counter.

The Gauss-Seidel method does not always converge. A sufficient condition for the convergence of the Gauss-Seidel method has been formulated by Scarborough (1958). The condition is:

$$\frac{\sum |a_{nb}|}{|a_p|} \begin{cases} \leq 1 & \text{for all equations} \\ < 1 & \text{for at least one equation} \end{cases} \quad (2.45)$$

When the condition is satisfied, the convergence of the Gauss-Seidel method is guaranteed. However, we may violate the criterion and still obtain the convergence solution.

A major disadvantage of the Gauss-Seidel point-by-point method is that its convergence is too slow. So instead of using the Gauss-Seidel point-by-point method, a line-by-line method was used in all test cases. The line-by-line scheme is a combination of the direct method, TDMA (Tridiagonal matrix algorithm), and the Gauss-Seidel method. More detail about this method can be found in Patankar's book (1980).

2.3 Staggered Grid

There are two types of FV grids: One has grid points placed at the centers of the CVs and the other has CV faces located midway between the grid points. The advantage of the first approach is that the grid point value represents the mean over the CV volume to higher accuracy than in the second approach, since the grid point is located at the center of the CV. The advantage of the second approach is that CDS (central difference scheme) approximations of derivatives at CV faces are more accurate since the face is midway between two grids. The first type of grid is used more often, and was also adopted in present computational simulations.

There is no need for all variables to share the same grid. A different arrangement may turn out to be advantageous. Typical staggered control volumes that were used in the test cases are shown in Figure 2.4. The control volumes for u_z and u_r are displaced with respect to the control volume for the continuity equation. Because of non-uniform grids, the velocity nodes are not at the centers of their control volumes (in the r direction). Cell faces 'e' and 'w' for u_z and 'n' and 's' for u_r lie midway between the nodes. For convenience, from now on we

will use U instead of U_z and V instead of U_r , and x instead of z as well.

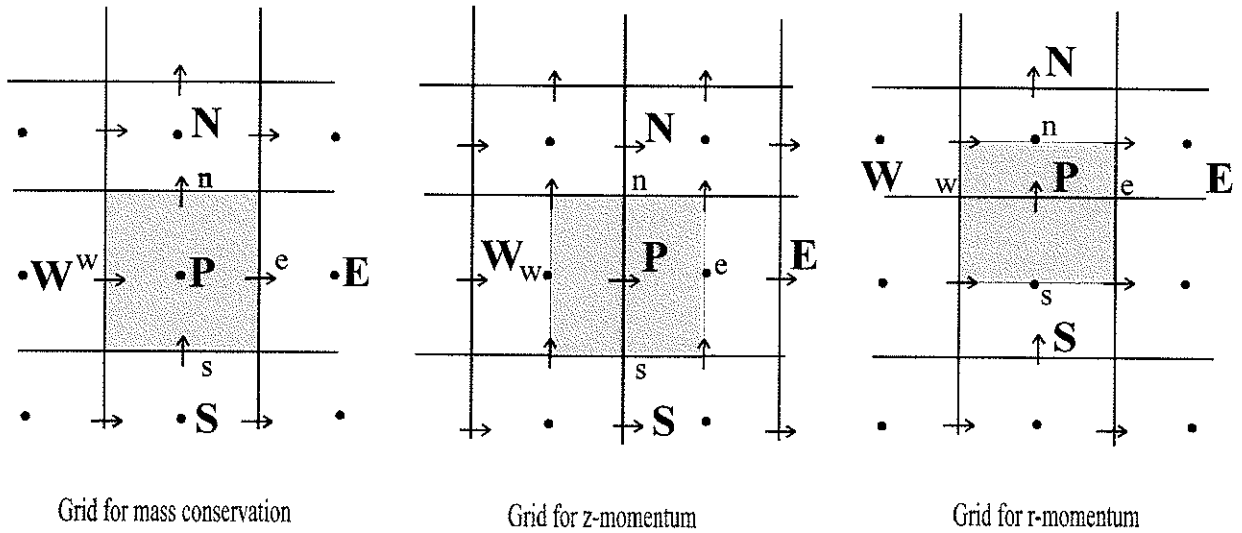


Figure 2.4 Control volumes for a staggered grid

2.4 SIMPLEC Algorithm

Integration of the mass conservation Equation (2.4) yields Equation (2.10). For incompressible flow, we have $M_p = M_p^o$. So Equation (2.10) turns into:

$$(\rho A)_e U_e - (\rho A)_w U_w + (\rho A)_n V_n - (\rho A)_s V_s = 0 \quad (2.46)$$

In terms of nodal velocities, we get (with a sign change)

$$(\rho A)_w U_w - (\rho A)_e U_e + (\rho A)_s V_s - (\rho A)_n V_n = 0 \quad (2.47)$$

or

$$a_w^c U_w + a_e^c U_e + a_s^c V_s + a_n^c V_n = 0. \quad (2.48)$$

Using the general equation for transport of ϕ (Equation 2.5) with U instead of ϕ , μ instead of Γ and $(-\partial P / \partial x + F_x^m)$ instead of S , we obtain the x-momentum equation (or z-momentum equation)

$$\frac{\partial}{\partial t}(\rho U) + \frac{\partial}{\partial x}(\rho U U) + \frac{\partial}{\partial r}(\rho V U) = \frac{\partial}{\partial x}\left(\mu \frac{\partial U}{\partial x}\right) + \frac{\partial}{\partial r}\left(\mu \frac{\partial U}{\partial r}\right) - \frac{\partial P}{\partial x} + F_x. \quad (2.49)$$

Analogously, we obtain the r-momentum equation:

$$\frac{\partial}{\partial t}(\rho V) + \frac{\partial}{\partial x}(\rho U V) + \frac{\partial}{\partial r}(\rho V V) = \frac{\partial}{\partial x}\left(\mu \frac{\partial V}{\partial x}\right) + \frac{\partial}{\partial r}\left(\mu \frac{\partial V}{\partial r}\right) - \frac{\partial P}{\partial r} + F_r. \quad (2.50)$$

Integration of $(-\partial P / \partial x)$, one of the source terms in Equation (2.49), we obtain

$$\begin{aligned} \frac{1}{\Delta t} \int_i^{i+\Delta t} \int_V \left(-\frac{\partial P}{\partial x}\right) dV dt &\approx \left(-\frac{\partial P}{\partial x}\right) \cdot (Vol)_P^u = -\frac{(P_e - P_w)}{(\delta x)_P^u} \cdot (Vol)_P^u \\ &= -\frac{(P_E - P_P)}{(\delta x)_P^u} \cdot (Vol)_P^u = C_P^u (P_P - P_E), \end{aligned} \quad (2.51)$$

where

$$C_P^u = \frac{(Vol)_P^u}{(\delta x)_P^u}. \quad (2.52)$$

So the complete algebraic equation for U_p is

$$a_P^u U_P = a_E^u U_E + a_W^u U_W + a_N^u U_N + a_S^u U_S + b_P^u + C_P^u (P_P - P_E), \quad (2.53)$$

where

$$a_P^u = \frac{M_P^o}{\Delta t} + \sum a_{NP}^u - R_P^u \quad (2.54)$$

and

$$b_P^u = \frac{M_P^o}{\Delta t} U_P^o + Q_P^u. \quad (2.55)$$

$\sum a_{NP}^u$ is given by Equation (2.33). Analogous to the U_p equation derivation, we obtain the complete algebraic equation for V_p :

$$a_P^v V_P = a_E^v V_E + a_W^v V_W + a_N^v V_N + a_S^v V_S + b_P^v + C_P^v (P_P - P_N), \quad (2.56)$$

where

$$a_p^v = \frac{M_p^o}{\Delta t} + \sum a_{NP}^v - R_p^v, \quad (2.57)$$

$$b_p^v = \frac{M_p^o}{\Delta t} V_p^o + Q_p^v, \quad (2.58)$$

and

$$C_p^v = \frac{(Vol)_p^v}{(\delta y)_p^v}. \quad (2.59)$$

Now we obtain the algebraic equation set which includes Equation (2.48), Equation (2.53) and Equation (2.56). How do we solve these equations for U, V and P? One possibility would be to solve all three equations at once using a direct solution. But we must repeat the solution of these equations because they are non-linear and coupled. There is another approach called the segregated approach for solving these equations. The equations are linearized to remove inter-equation coupling, and each equation is solved separately in sequence. Actually, the SIMPLE (Semi-Implicit Method for Pressure-Linked Equations) algorithm, a well-known and often used method for solving the flow equations (U, V, and P), belongs to the segregated approach. SIMPLEC (SIMPLE-Consistent) is an improved formulation proposed by Van Doormal and Raithby (1984). The procedure of SIMPLEC is summarized as below.

1. Guess the pressure field P^* .
2. Solve the momentum equations to obtain U^* , V^* , and W^* :

$$\begin{aligned} a_e U_e^* &= \sum a_{nb} U_{nb}^* + b + (P_p^* - P_E^*) A_e, \\ a_n V_n^* &= \sum a_{nb} V_{nb}^* + b + (P_p^* - P_N^*) A_n, \\ a_t W_t^* &= \sum a_{nb} W_{nb}^* + b + (P_p^* - P_T^*) A_t. \end{aligned} \quad (2.60)$$

3. Solve the P' equation:

$$a_p P_p' = \sum a_{nb} P_{nb}' + b. \quad (2.61)$$

4. Calculate P by adding P' to P*:

$$P = P^* + P' \quad (2.62)$$

5. Calculate U, V, W from their starred values using the velocity-correction formulas:

$$\begin{aligned} U_e &= U_e^* + d_e(P'_P - P'_E) \\ V_n &= V_n^* + d_n(P'_P - P'_N) \\ W_t &= w_t^* + d_t(P'_P - P'_T) \end{aligned} \quad (2.63)$$

6. Solve the discretization equation for other ϕ 's (turbulence quantities such as k, ϵ and γ).
7. Treat the corrected pressure P as a new guessed pressure P*, return to step 2, and repeat the whole procedure until a converged solution is obtained.

Here the basic idea is to defined a guessed field U*, V* and P* and correction U', V' and P'. Then we get U, V and P by:

$$\begin{aligned} U &= U^* + U' \\ V &= V^* + V' \\ P &= P^* + P' \end{aligned} \quad (2.64)$$

First let us derive the formula to calculate d_e and d_n ($d_t = 0$ for 2D flow) in Equations (2.63).

Let us start with the guessed pressure field to calculate the guessed velocity field using the U and V equations (Equation 2.53 and Equation 2.56).

$$a_p^u U_p^* = \sum a_{NP}^u U_{NP}^* + b_p^u + C_p^u (P_P^* - P_P^*) \quad (2.65)$$

Now, subtracting the U_p^* equation from the U_p equation, we obtain:

$$a_p^u U_p' = \sum a_{NP}^u U_{NP}' + C_p^u (P_P' - P_E') \quad (2.66)$$

Then subtracting $\sum a_{NP}^u U_{NP}'$ from both sides of the Equation (2.66), we obtain:

$$(a_P^u - \sum a_{NP}^u)U_P' = \sum a_{NP}^u (U_{NP}' - U_P') + C_P^u (P_P' - P_E') \quad (2.67)$$

If we assume that the P' gradient accelerates the center and neighbor nodes uniformly, we could drop $\sum a_{NP}^u (U_{NP}' - U_P')$ from Equation (2.67), so we obtain:

$$U_P' = \frac{C_P^u}{(a_P^u - \sum a_{NP}^u)} (P_P' - P_E') \quad (2.68)$$

and

$$U_P = U_P^* + \frac{C_P^u}{(a_P^u - \sum a_{NP}^u)} (P_P' - P_E'). \quad (2.69)$$

Comparison of Equation (2.69) with Equation (2.63), yields:

$$d_e^u = \frac{C_P^u}{(a_P^u - \sum a_{NP}^u)} \quad (2.70)$$

Analogous to the U_p equation derivation, we have

$$d_n^v = \frac{C_P^v}{(a_P^v - \sum a_{NP}^v)} \quad (2.71)$$

Now let us return to the continuity equation to derive the P' equation. Substitute the face velocities into Equation (2.48), gather terms and rearrange into the form

$$a_P^p P_P' = \sum a_{NP}^p P_{nb}' + b_P^p \quad (2.72)$$

where

$$\begin{aligned} a_E^p &= -a_E^c d_e^u = (\rho A)_e d_e^u \\ a_W^p &= a_W^c d_w^u = (\rho A)_w d_w^u \\ a_N^p &= -a_N^c d_n^u = (\rho A)_n d_n^u \\ a_S^p &= a_S^c d_s^u = (\rho A)_s d_s^u \\ a_P^p &= a_E^p + a_W^p + a_N^p + a_S^p = \sum a_{NP}^p \\ b_P^p &= a_E^c U_P^* + a_W^c U_W^* + a_N^c V_P^* + a_S^c V_S^* \end{aligned} \quad (2.73)$$

3. Van Driest's Mixing-Length Model

In this chapter, a zero-equation model, Van Driest's mixing-length model, is presented in Section 3.1. This is followed by the discussion on the numerical consideration: grids, boundary conditions, convergence of the solutions, and convergence of the iterations. Then, the simulation results for $Re=50,000$ and $Re=500,000$ are presented in Section 3.3.

3.1 Model Equation

Combining Van Driest's mixing-length model (1956) with Clauser's (1956) eddy viscosity model, we obtain a two-layer model. Here μ_t is given by separate expressions in each layer:

$$\mu_t = \rho \kappa^2 \left[1 - \exp\left(\frac{-yu_*}{26\nu}\right) \right]^2 y^2 \left| \frac{\partial U}{\partial y} \right| \quad \text{for } y \leq y_m \text{ (inner layer)} \quad (3.1)$$

$$\text{and} \quad \mu_t = 0.018 \rho U_e \delta^* \quad \text{for } y > y_m \text{ (outer layer)} \quad (3.2)$$

Where u_* , the friction velocity is given by

$$u_* = \sqrt{\frac{\tau_w}{\rho}}, \quad (3.3)$$

Von Karman's constant is $\kappa=0.41$, U_e is the boundary-layer edge velocity, and δ^* is the displacement thickness defined by

$$\delta^* = \int_0^\delta (1 - U/U_e) dy \quad (3.4)$$

3.2 The Numerical Consideration

Coordinate System and Grids: The control-volume discretization equation is derived based on cylindrical coordinates. However, u_θ is assumed to be zero therefore all the algebraic equations reduce to two-dimensional formulations. Two grid systems (120 x 99 grids and 61 x 51 grids) were selected for zero-equation model tests in order to check the convergence of the solution. It has been found that the solutions are grid-independent. An equal grid spacing in the axial direction and an unequal grid spacing in the radial were used for tests. The nonuniform grid was set up by defining k , a constant ratio between two adjacent increments ($k = \Delta y_- / \Delta y_+ = \Delta y_j / \Delta y_{j+1}$) and were selected to be 0.96 and 0.968 respectively for the two grids system. The values were determined by trial and error.

Boundary Conditions: First of all, the radial velocity was assumed zero at all boundaries. As for the axial velocity, at the pipe inlet, it was assigned the bulk value, U_b ; at the pipe axis, symmetry conditions were assumed; and at the wall, no-slip conditions were imposed. Finally, the pipe section was chosen to be sufficiently long so that fully developed conditions could be assumed at the outlet, i.e. $\partial U / \partial x = 0$. As to initial conditions, uniform profiles were assumed for U and V , i.e., $U=U_b$, $V=0$.

Convergence of the solutions: A numerical method is said to be convergent if the solution of the discretized equation tends to the exact solution of the differential equation as the grid spacing tends to zero. For non-linear problems which are strongly influenced by boundary conditions, the stability and convergence of a method are difficult to demonstrate. Therefore convergence is usually checked using numerical experiments, i.e. repeating the calculation on a series of successively refined grids. If the method is stable and if all approximations used in the discretization process are consistent, the solution will converge to a grid-independent

solution. The results of the grid-independence test for present model are presented in Figure 3.1 where the solid smooth lines represent the simulation results obtained using finer grids whereas the open circles represent the simulation results obtained using course grids. We find that the solutions obtained by two grid systems are almost identical. Therefore the solution proved grid-independent. Furthermore the numerical method proved convergent.

Convergence of the iterations: When using iterative solvers, it is important to know when to quit. The most common procedure is based on the difference between two successive iterates. The procedure is stopped when this difference, measured by some norm, is less than a pre-selected value. Calculating the convergence error is the most straightforward method for estimating the difference between two successive iterates. But unfortunately, in most case, this process involves a complicated complex eigenvalue calculation. Here we only derive the equation that determines the behavior of the convergence error. As to the calculation of the convergence error, a detailed derivation can be found in Ferziger and Peric's book (1996, Chapter 5). In Chapter two we have derived a system of linear algebraic equations by making a finite difference approximation at each grid node (see Eq. 2.29). The system can be written in matrix notation as follows:

$$A\phi = Q, \quad (3.5)$$

where A is the square, sparse coefficient matrix, ϕ is a vector containing the variable values at the grid nodes, and Q is the vector containing all the terms which do not contain unknown variable values. After n iterations we have an approximate solution ϕ^n which does not satisfy these equations exactly. Instead, there is a non-zero residual ρ^n :

$$A\phi^n = Q - \rho^n \quad (3.6)$$

By subtracting this equation from Eq. (3.5), we obtain

$$A(\phi - \phi^n) = \rho^n \quad (3.7)$$

Defining convergence error by:

$$\mathbf{e}^n = \phi - \phi^n, \quad (3.8)$$

we obtain a relation between the convergence error and the residual:

$$A\mathbf{e}^n = \rho^n \quad (3.9)$$

If we have $\lim_{n \rightarrow \infty} \rho^n = 0$, we could say the iterative method converges because we will have

$\lim_{n \rightarrow \infty} \mathbf{e}^n = 0$ too. As we have shown, reduction of the residual is accompanied by reduction of

the convergence error, so we can use the reduction of the residual as a stopping criterion. We

recall that Eq. (2.44), one equation which we want to solve, is derived from the mass

conservation law. Now if we use the reduction of the mass residual as a stopping criterion,

the mass conservation is guaranteed for each individual control volume and for the solution

domain as a whole. For the test cases, convergence was declared if the average magnitude of

the mass residual throughout the computation domain was less than 10^{-13} . The results of the

convergence of the iteration test for $Re = 50,000$ and $Re = 500,000$ are presented in Figure

3.2 and Figure 3.3 respectively. In Figure 3.2, the solid smooth lines represent the simulation

results after 300 iterations whereas the open circles represent the simulation results after 600

iterations. The average magnitude of the mass residual throughout the computation domain is

$0.16E-13$ and $0.34E-19$ respectively. It can be seen that the two solutions are almost identical.

Therefore the convergence of the iterations has been proved. In Figure 3.3, the solid smooth

lines represent the simulation results after 500 iterations whereas the open circles represent

the simulation results after 1000 iterations. The average magnitude of the mass residual

throughout the computation domain is $0.12E-10$ and $0.28E-14$ respectively. We find the two

solutions are almost identical again. This confirms that choosing the average magnitude of

the mass residual throughout the computation domain less than 10^{-13} as the indicator of the convergence of the iteration is conservative enough to insure the accuracy of the solution.

The Overrelaxation and Underrelaxation Factor: In the iterative solution of the algebraic equations or in the overall iterative scheme employed for handling non-linearity, it is often desirable to speed up or to slow down the changes, from iteration to iteration, in the values of the dependent variable. This process is called overrelaxation or underrelaxation, depending on whether the variable changes are accelerated or slowed down. There are many ways of introducing overrelaxation or underrelaxation. One practice, the derivation of a SOR formulation, has been described in Section 2.3. Another technique of overrelaxation or underrelaxation will be described here. Replacing the discretization equation (2.29) with

$$(a_p + i)\phi_p = \sum a_{NP}\phi_{NP} + b_p + i\phi_p^* , \quad (3.10)$$

where ϕ_p^* is the value of ϕ_p from the previous iteration and i is the so-called inertia. For positive values of i , Eq. (3.10) has the effect of underrelaxation, while negative values of i produce overrelaxation. From Eq. (3.10), we can deduce that i should be comparable to a_p , and the greater the magnitude of i the stronger will be the effect of the relaxation.

In the present simulations, the solution of a steady-state problem is obtained through the use of the discretization equations for a corresponding unsteady situation. Thus, the "time steps" become the same as iterations, and the "old" value ϕ_p^o simply represents the previous-iteration value ϕ_p^* . In this sense, the term $(M_p^o / \Delta t)\phi_p^o$ in Eq. (2.34) acts in the same way as the term $i\phi_p^*$ in Eq. (3.10). The inertia i is analogous to the coefficient $M_p^o / \Delta t$ in the unsteady formulation. The practice of solving a steady-state problem via the unsteady formulation can now be recognized as simply a particular kind of underrelaxation procedure.

The smaller the time step chosen, the stronger is the resulting underrelaxation. Underrelaxation is a very useful device for nonlinear problem. It is often employed to avoid divergence in the iterative solution of strongly nonlinear equations. The underrelaxation factor is always problem-dependent. The optimum "time steps" for the test cases was obtained by trial and error. The numerical experimental results for flow with bulk Reynolds number of 50,000 for two grid systems are presented in Figure 3.4 and Figure 3.5 respectively. For a "time step" less than the optimum, the convergence is oscillatory. When the optimum "time step" is exceeded, the convergence is monotonic and the rate of convergence increases as the "time step" decreases. The results of optimum "time step" test for $Re=500,000$ are presented in Figure 3.6. Comparing Figure 3.4 with Figure 3.6, it could be seen that when simulating flow with high Reynolds number, the rate of convergence is slower, and therefore more iterations are needed to reach the same order of average magnitude of the mass residual for a flow with a lower Reynolds number.

Recall that in Eq. (2.44), there is an overrelaxation factor ω . Similar to the "time step", the optimum overrelaxation factor was also obtained by trial and error because there are no general rules for choosing the best value of ω in the present test cases. The optimum value depends upon a number of factors, such as the nature of the problem, the number of grid points, the grid spacing, and the iterative procedure used. However, we have found that the behavior of the method is similar to all the cases. When values of ω less than the optimum, the convergence is monotonic and the rate of convergence increases as ω increase. When the optimum ω is exceeded, the convergence is oscillatory. This knowledge was used to search for the optimum ω values. The numerical experimental results are presented in Figure 3.7. For flow with bulk Reynolds number of 50,000, 120 x 99 grids, the optimum ω is 1.4.

3.3 Results

Simulation results using Van Driest mixing-length model for bulk Reynolds numbers of 50,000 and 500,000 are presented below. Comparison with experimental data and with simulation results obtained by other models as well as the physical process in the pipe flow will be given in Chapter 7.

Simulation Results for Flow with Bulk Reynolds Number of 50,000: Figure 3.8 and Figure 3.9 are contour plots with color interpolation for the non-dimensional axial mean velocity U/U_e and radial mean velocity V/U_e respectively. Here the mean velocity information is very nicely represented by color. It can be seen that at about $x/D = 40$, the flow reaches its full-developed state. The contour plot for the non-dimensional axial velocity U/U_e without color interpolation is plotted in Figure 3.10. The non-dimensional axial velocity profiles at six downstream locations are plotted in Figure 3.11. We can see that the non-dimensional axial velocity profiles at $x/D = 60.9$ and $x/D = 80.5$ are almost identical. The non-dimensional radial velocity profiles at six downstream locations are plotted in Figure 3.12. The development of the axial velocity in the downstream direction at various locations is shown in Figure 3.13.

Simulation Results for Flow with Bulk Reynolds Number of 500,000: Figure 3.14 and Figure 3.15 are contour plots with color interpolation for the non-dimensional axial mean velocity U/U_e and radial mean velocity V/U_e respectively. The contour plot for the non-dimensional axial velocity U/U_e without color interpolation is plotted in Figure 3.16. The non-dimensional axial velocity profiles at six downstream locations are plotted in Figure 3.17. We can see that the non-dimensional axial velocity profiles at $x/D = 60.9$ and $x/D = 80.5$ are also almost identical. However, in Figure 3.15 we can see the flow hasn't reach its

fully developed stage at $x/D = 40$. It implies that the flow probably reached its full-developed state within $40 < x/D < 60$. It is consistent with the previously observation (White, 1986) that for higher Reynolds number flow, it takes longer to become fully developed. The non-dimensional radial velocity profiles at six downstream locations are plotted in Figure 3.18, and the development of the axial velocities in the downstream direction at various locations is shown in Figure 3.19. Finally the contour plots of the non-dimensional Reynolds shear stress, \overline{uv}/u_*^2 , for $Re=50,000$ and $Re=500,000$ are plotted in Figure 3.20 and Figure 3.21, respectively. The non-dimensional Reynolds shear stress distributions at six downstream locations for $Re=50,000$ and $Re=500,000$ are plotted in Figure 3.22 and Figure 3.23. Because separate expressions are given to μ_t for each layer (Eq. 3.1 for inner layer and Eq. 3.2 for outer layer), there is a jag in the profile of \overline{uv} at the interface between the inner and outer layer. No effort was made to correct for this jag in the Reynolds stress as it did not affect the calculation of the mean velocity field.

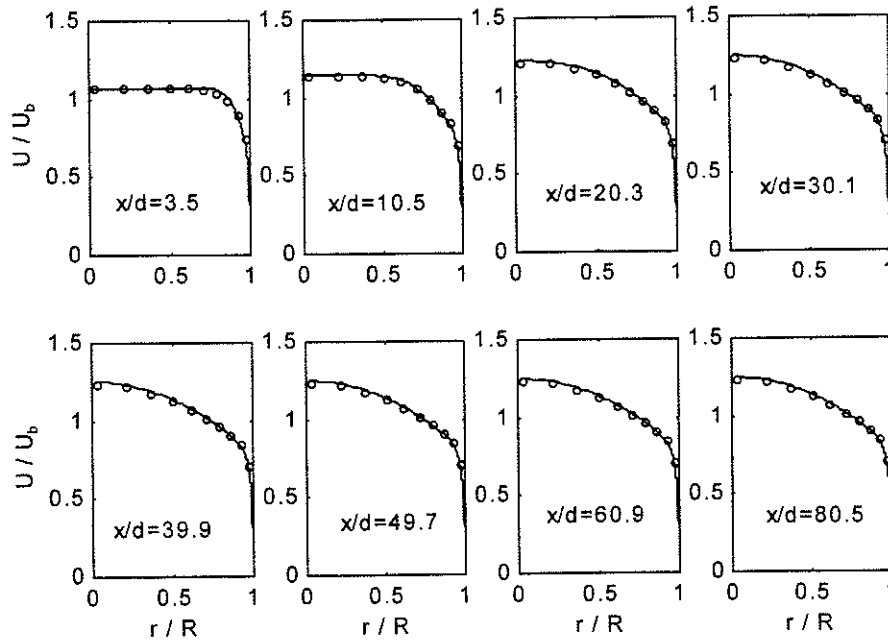


Figure 3.1 Simulation results obtained using two grid systems for $Re = 50,000$ (the solid smooth lines represent the simulation results obtained using finer grids and the open circles represent the simulation results obtained using coarse grids)

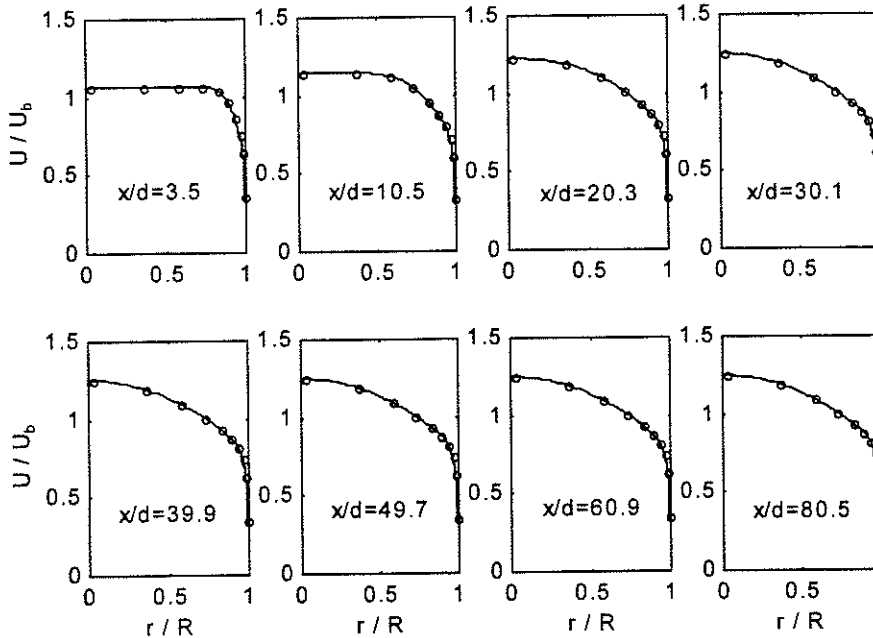


Figure 3.2 Confirmation of the convergence of the iteration for $Re = 50,000$ (the solid smooth lines represent the simulation results with 300 iterations and the open circles represent the simulation results with 600 iterations)

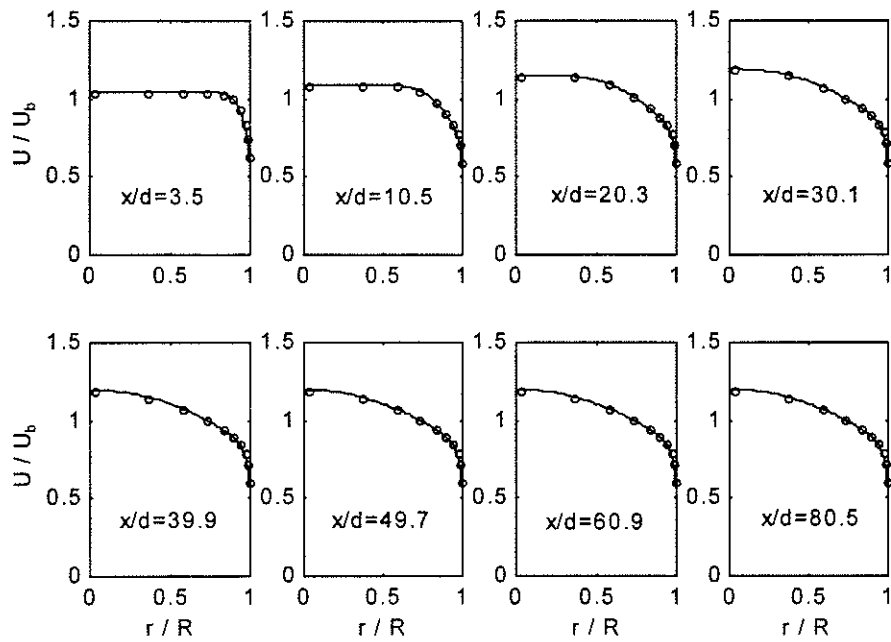


Figure 3.3 Confirmation of the convergence of the iteration for $Re = 500,000$ (the solid smooth lines represent the simulation results with 500 iterations and the open circles represent the simulation results with 1000 iterations)

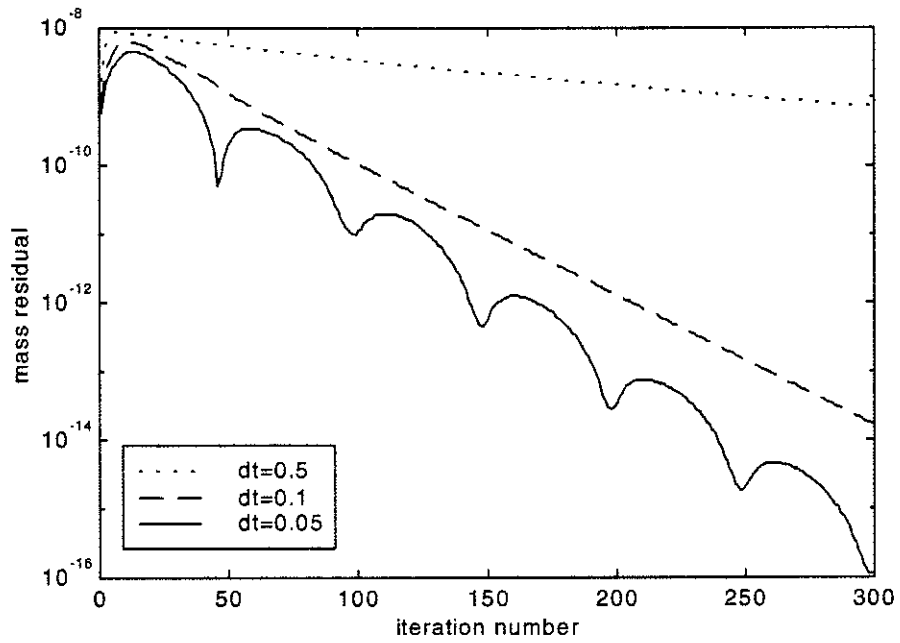


Figure 3.4 Optimum "time step" tests for finer grids for $Re = 50,000$

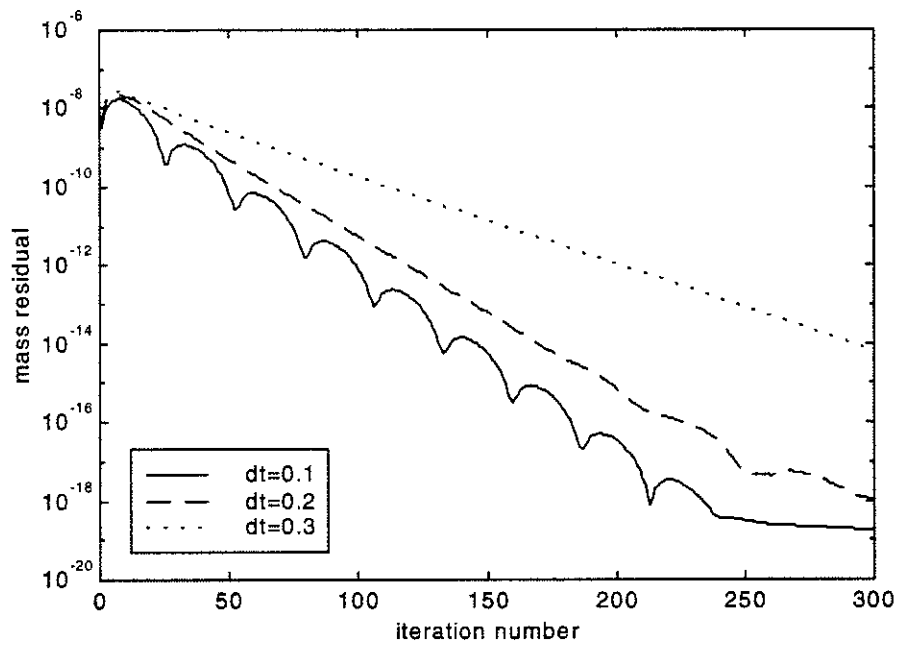


Figure 3.5 Optimum "time step" tests for coarse grids for $Re = 50,000$

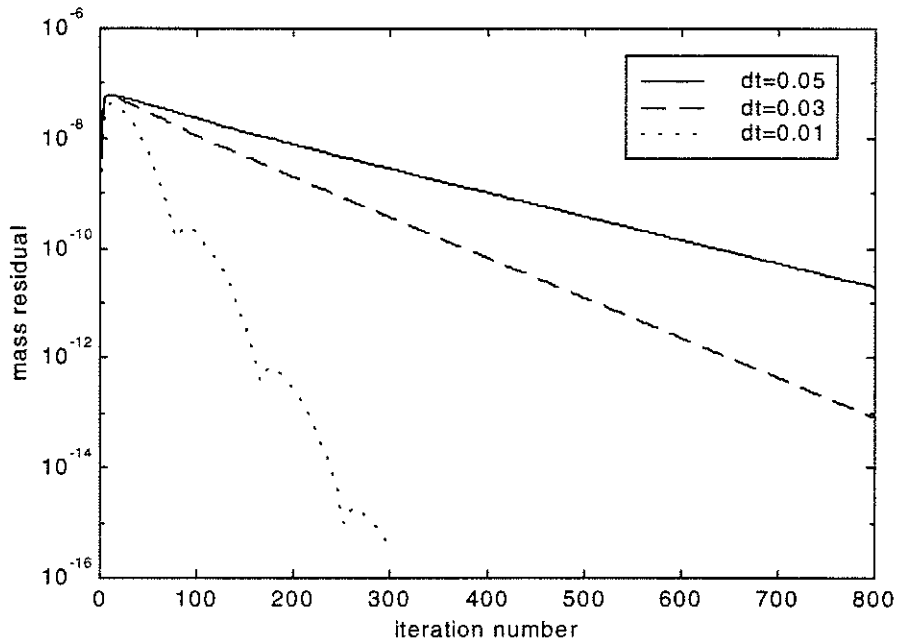


Figure 3.6 Optimum “time step” tests for finer grids for $Re = 500,000$

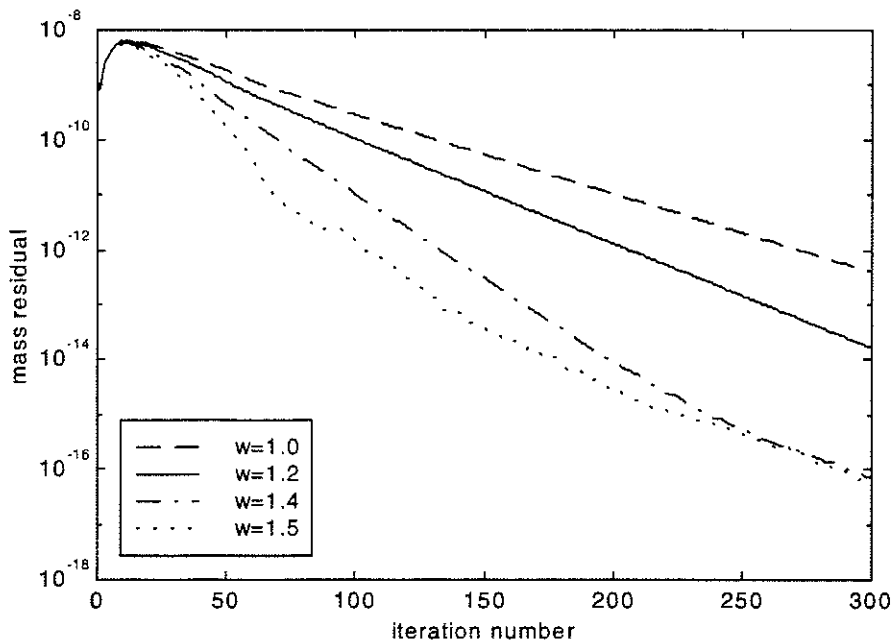


Figure 3.7 Optimum overrelaxation factor tests for finer grids for $Re = 50,000$

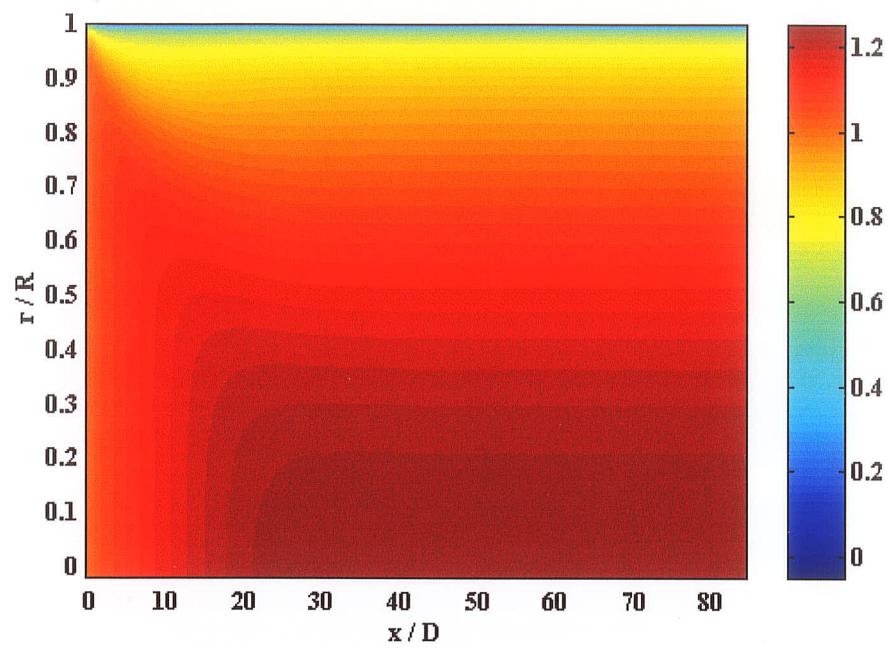


Figure 3.8 Contour plot for the non-dimensional axial velocity for $Re = 50,000$

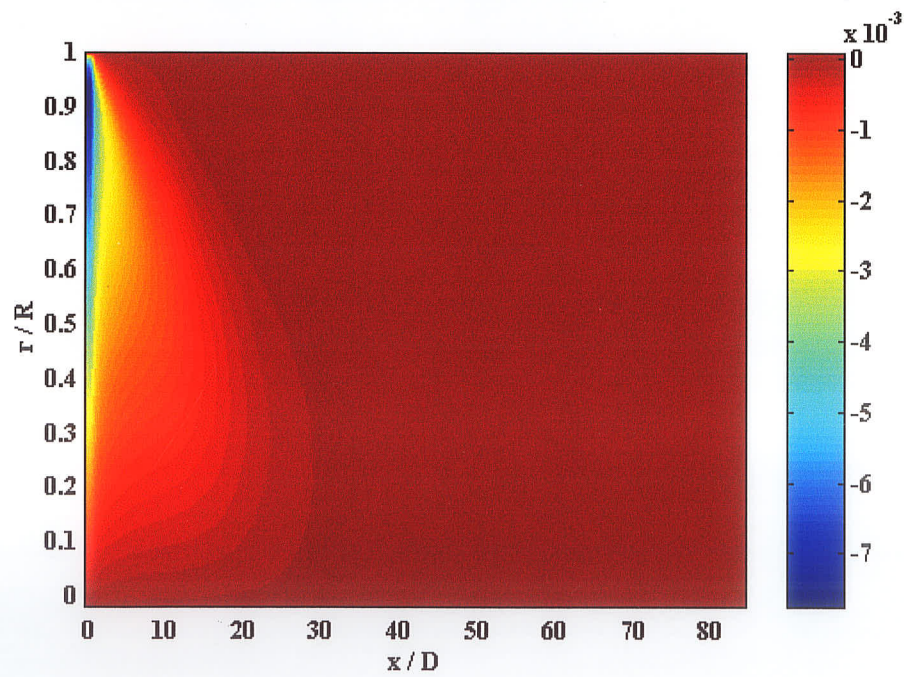


Figure 3.9 Contour plot for the non-dimensional radial velocity for $Re = 50,000$

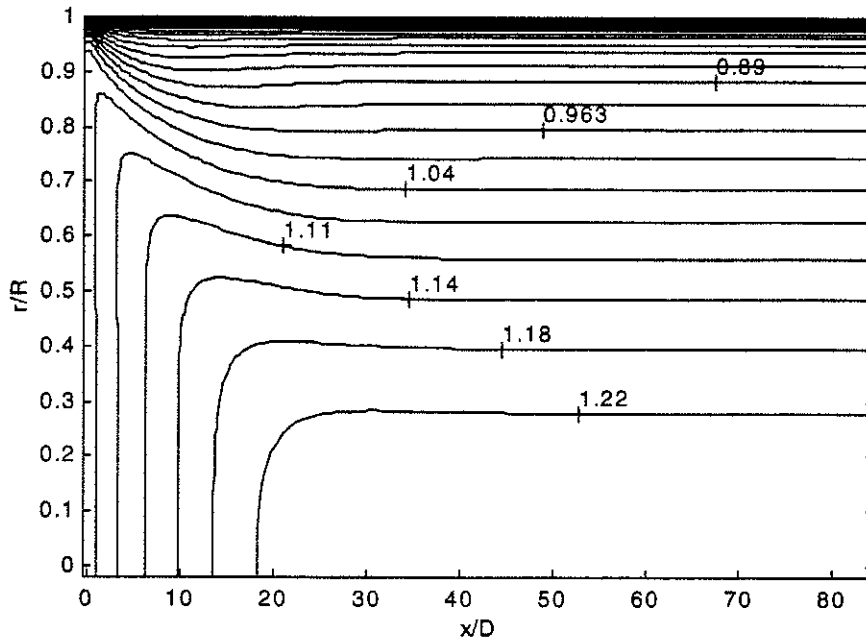


Figure 3.10 Contour plot for the non-dimensional axial velocity for $Re=50,000$

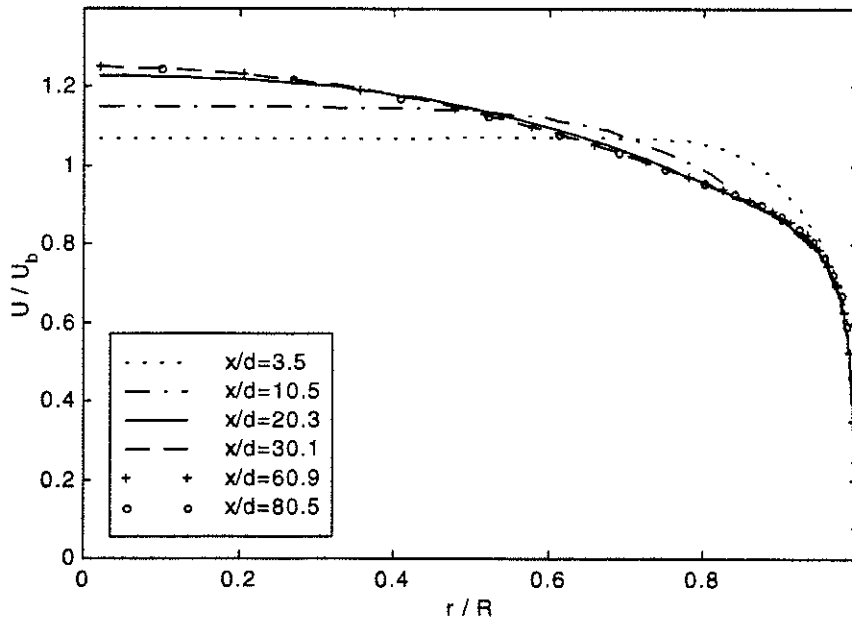


Figure 3.11 Axial velocity vs r/R at six downstream locations for $Re = 50,000$

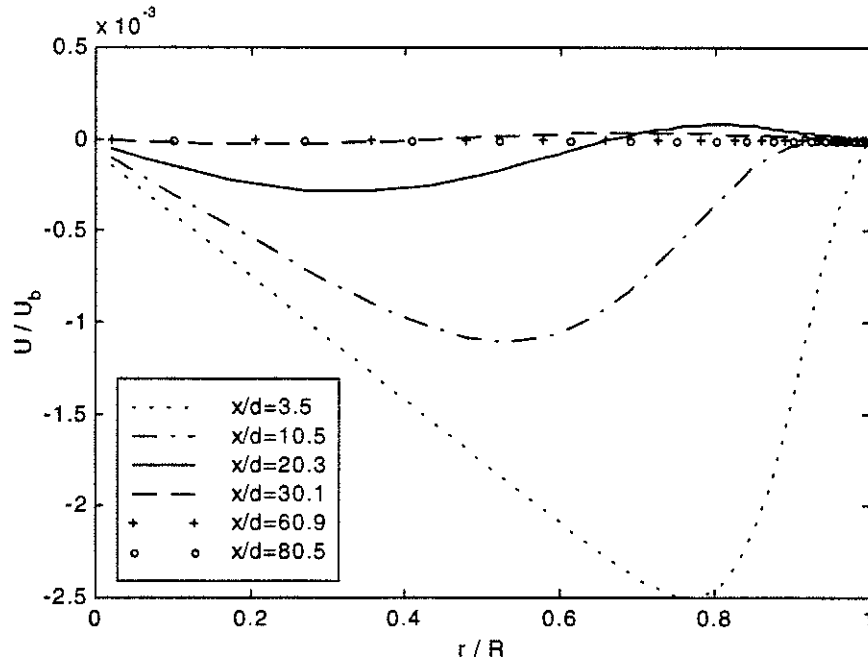


Figure 3.12 Radial velocity vs r/R at six downstream locations for $Re=50,000$

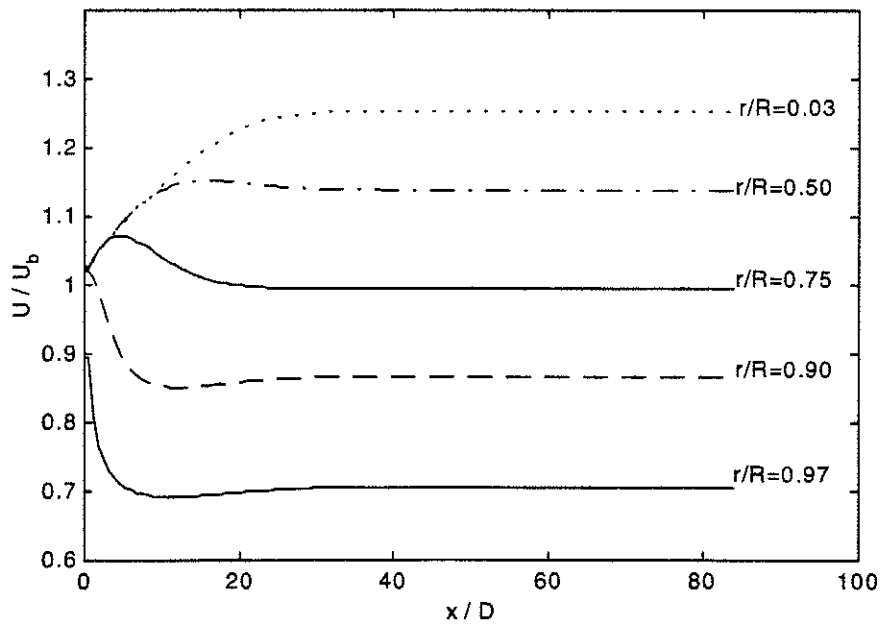


Figure 3.13 Development of axial velocity for $Re = 50,000$

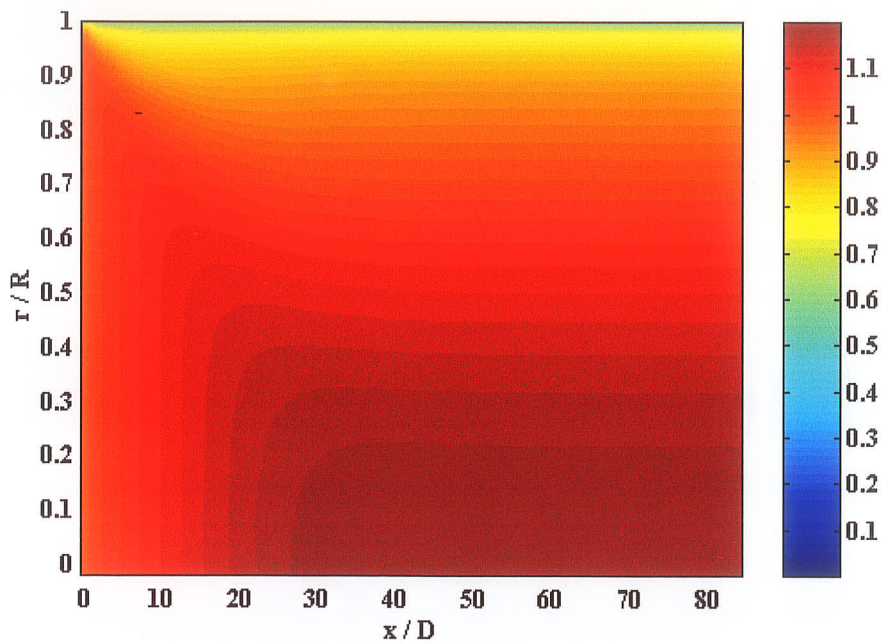


Figure 3.14 Contour plot for the non-dimensional axial velocity for $Re = 500,000$

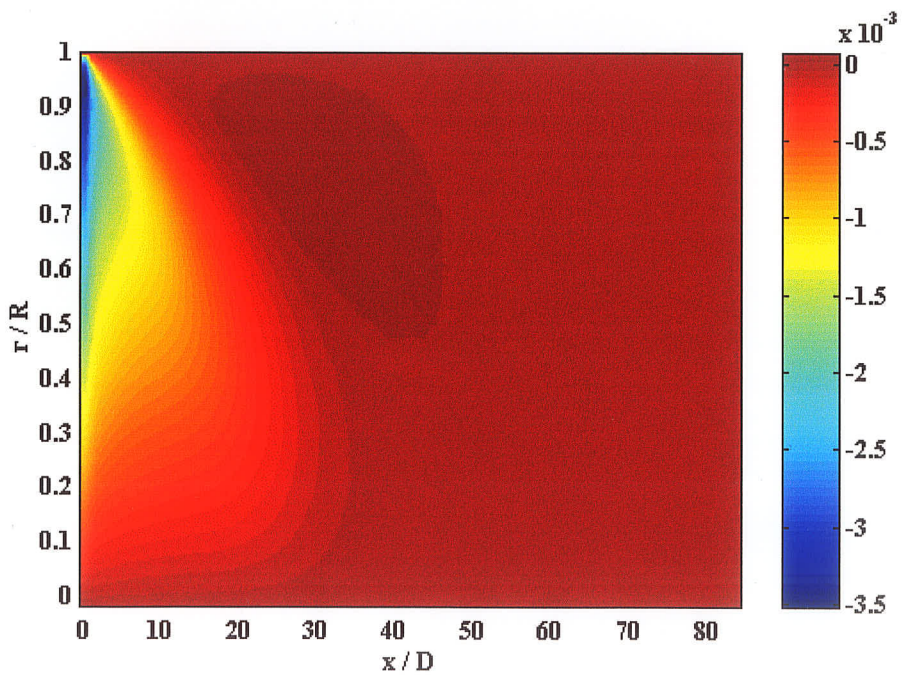


Figure 3.15 Contour plot for the non-dimensional radial velocity for $Re = 500,000$

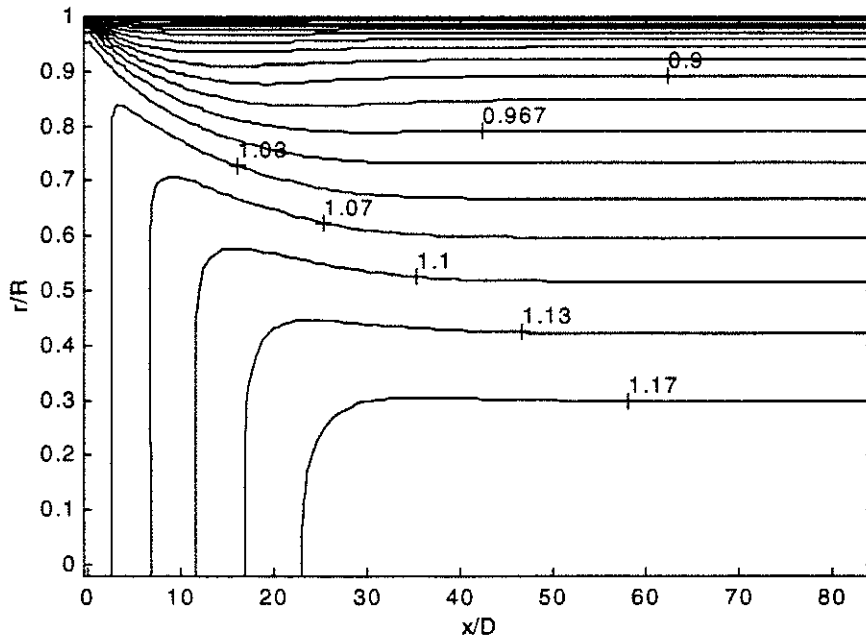


Figure 3.16 Contour plot for the non-dimensional axial velocity for $Re = 500,000$

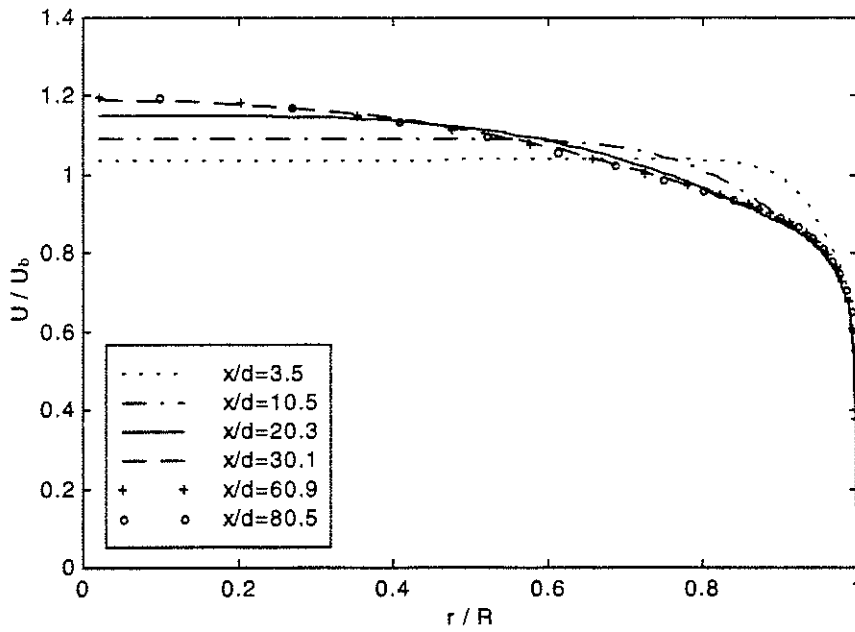


Figure 3.17 Axial velocity vs r/R at six downstream locations for $Re = 500,000$

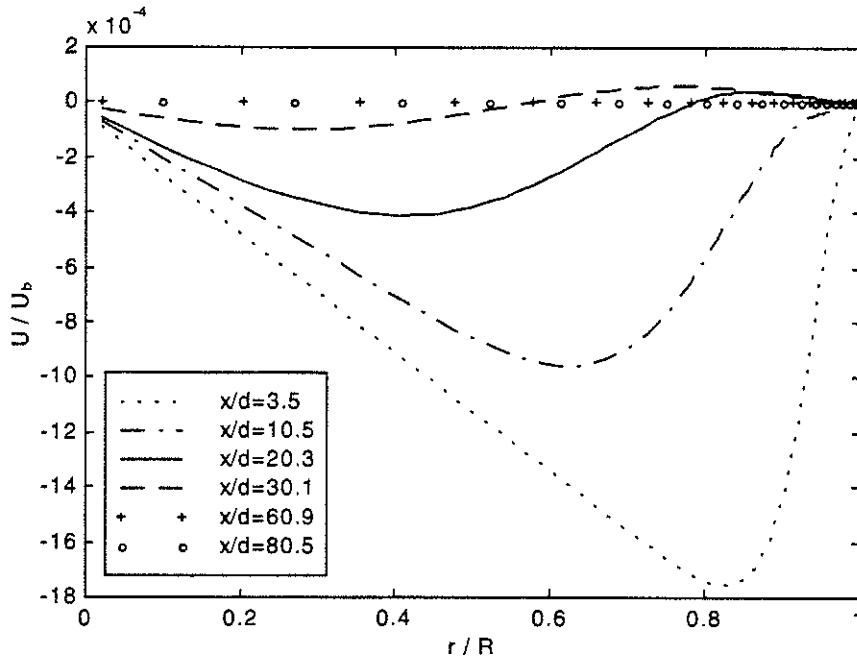


Figure 3.18 Radial velocity vs r/R at six downstream locations for $Re = 500,000$

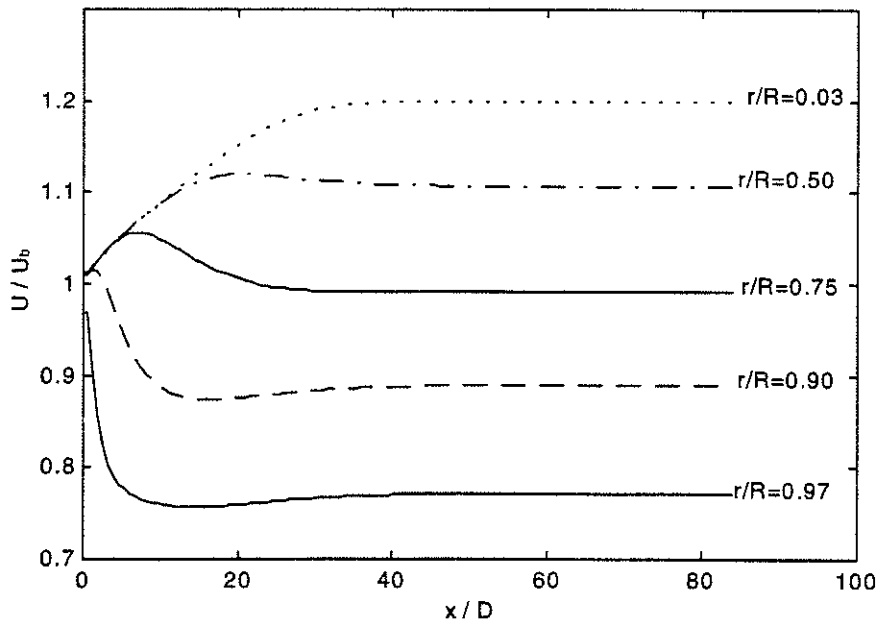


Figure 3.19 Development of axial velocity for $Re = 500,000$

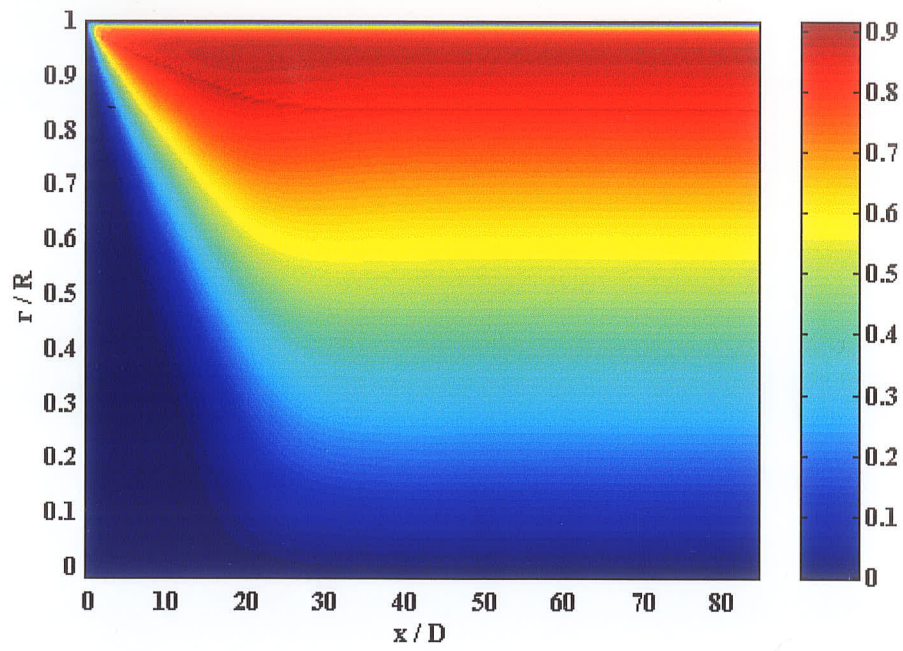


Figure 3.20 Contour plot for Reynolds shear stress for $Re=50,000$

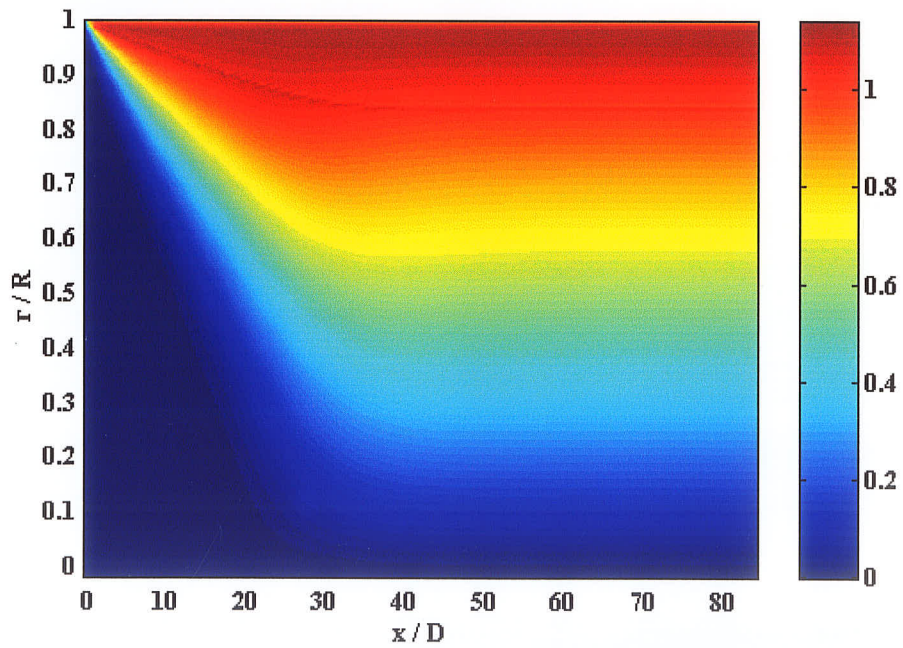


Figure 3.21 Contour plot for Reynolds shear stress for $Re=500,000$

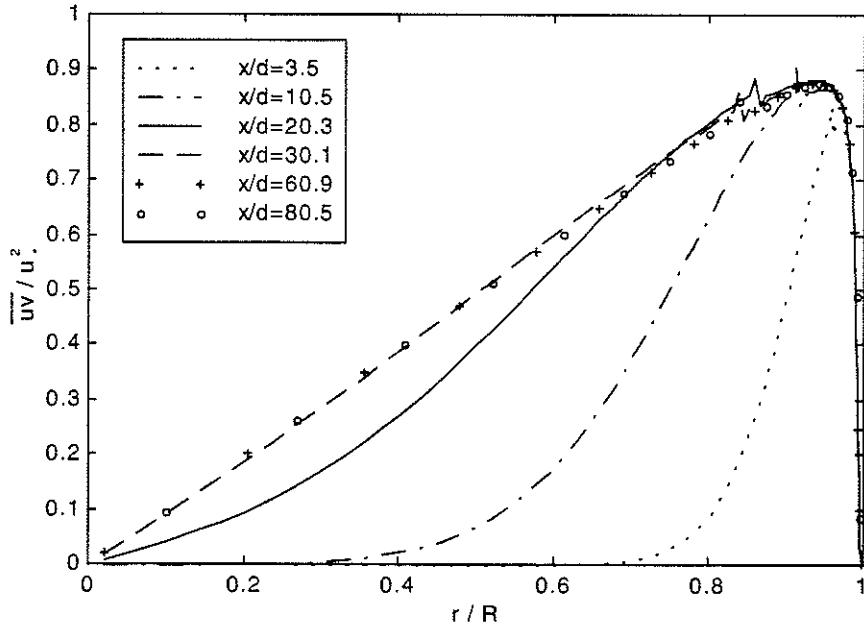


Figure 3.22 Reynolds shear stress vs r/R for $Re=50,000$

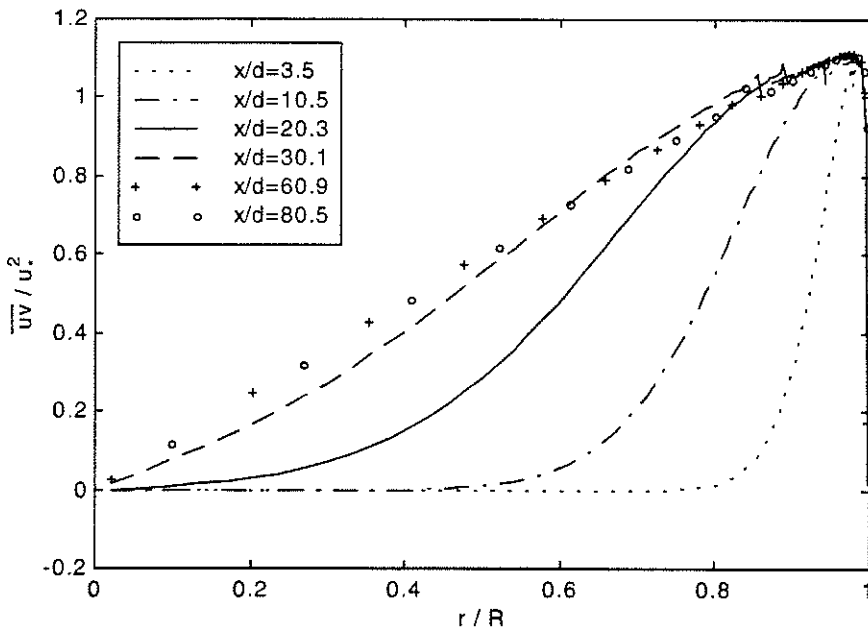


Figure 3.23 Reynolds shear stress vs r/R for $Re=500,000$

4. The Standard k-ε Model

In this chapter, the equations of the standard k-ε model are presented in section 4.1. This is followed by a brief discussion on wall functions. Then, the simulation results for Re=50,000 and Re=150,000 are presented in the section 4.3.

4.1 Model Equations

The equations for the standard k-ε model have been presented in chapter one (see Eq. 1.16 - Eq. 1.18). The model was original proposed by Jones and Launder (1972) and employs the five empirical constants given in Table 3.1. Later, Launder and Sharma (1974) reexamined the model closure coefficients, and now most researchers use the newer model presented in the 1974 paper. Launder and Sharma's (1974) model equations are given below.

The transport equation for turbulence kinetic energy k:

$$\frac{\partial k}{\partial t} + U_i \frac{\partial k}{\partial x_i} = \frac{\partial}{\partial x_i} \left(\frac{\nu_t}{\sigma_k} \frac{\partial k}{\partial x_i} \right) + \nu_t \left(\frac{\partial U_i}{\partial x_j} + \frac{\partial U_j}{\partial x_i} \right) \frac{\partial U_i}{\partial x_j} - \epsilon . \quad (4.1)$$

The transport equation for Turbulence dissipation rate ε:

$$\frac{\partial \epsilon}{\partial t} + U_i \frac{\partial \epsilon}{\partial x_i} = \frac{\partial}{\partial x_i} \left(\frac{\nu_t}{\sigma_\epsilon} \frac{\partial \epsilon}{\partial x_i} \right) + C_{1\epsilon} \frac{\epsilon}{k} \nu_t \left(\frac{\partial U_i}{\partial x_j} + \frac{\partial U_j}{\partial x_i} \right) \frac{\partial U_i}{\partial x_j} - C_{2\epsilon} \frac{\epsilon^2}{k} , \quad (4.2)$$

and turbulent viscosity μ_t :

$$\mu_t = C_\mu \rho k^2 / \epsilon . \quad (4.3)$$

The model constants are given in Table 4.1.

Table 4.1 The values of the model constant in the standard k-ε model

model \ model contests	C_μ	C_1	C_2	σ_k	σ_ε
Jones-Launder's model	0.09	1.55	2.0	1.0	1.3
Launder-Sharma's model	0.09	1.44	1.92	1.0	1.3

4.2 Wall Functions: Expressions for k and ε Near Wall

For solid walls with no slip at the boundary, it is not practical to carry the computation down through the very thin, viscous sublayer. Assuming local equilibrium at the top of the buffer layer ($\varepsilon = P = u_*^2 \partial U / \partial y$), the law of the wall gives

$$\frac{U}{u_*} = \frac{1}{\kappa} \ln \frac{yu_*}{\nu} + 5.0. \quad (4.4)$$

Therefore we have

$$\frac{\partial U}{\partial y} = \frac{u_*}{\kappa y} \quad (4.5)$$

and

$$\varepsilon = \frac{u_*^3}{\kappa y}. \quad (4.6)$$

Here $u_* = \sqrt{\tau_o / \rho}$ is the friction velocity, τ_o is the wall shear stress, $\kappa = 0.4$ is von Karman's constant, and $y = 12\nu / u_*$ is the effective viscous sublayer thickness. The main assumption for the turbulent kinetic wall function is the presence of an equilibrium layer where the generation and dissipation of k are in balance. Launder and Spalding (1974) deduced that

$$k = \frac{u_*^2}{\sqrt{C_\mu}} \quad (4.7)$$

by an analysis of experimental data and dimensional analysis. Eq. (4.6) and Eq. (4.7) were used as wall function formulations for the present simulations. We should note that Eq. (4.6) and Eq. (4.7) are approximate formulations. Actually, Hwang and Liou (1991) have given analytic expressions for both the k and ε distributions in the near-wall region. The derivation of these expressions is not going to be discussed here, but the interested reader can find it in Hwang and Liou's (1991) paper. Here we will only give the expressions for k and ε near the wall. From a simplified governing equation of k for the boundary or the fully developed turbulent pipe flows, Hwang and Liou deduced that

$$k^* = \begin{cases} 3 \left[\frac{(A_+ y^+)^h - 1}{(A_+ y^+)^h + 1} \right]^2 - 2 & \text{for } \frac{dk^*}{dy^+} > 0 \\ 3 \left[\frac{(A_- y^+)^{-h} - 1}{(A_- y^+)^{-h} + 1} \right]^2 - 2 & \text{for } \frac{dk^*}{dy^+} < 0 \end{cases} \quad (4.8)$$

where

$$k^* = C_\mu^{1/2} k / u_*^2, \quad (4.9)$$

$$y^+ = \rho u_* y / \mu, \quad (4.10)$$

and

$$h = (2\sigma_k)^{1/2} C_\mu^{1/4} / \kappa. \quad (4.11)$$

The constants A_+ and A_- can be determined by matching Eq. (4.8) with the solution for the viscous sublayer ($y^+ = 5.0$)

$$k^* = a_c C_\mu^{1/2} y^{+2}, \quad (4.12)$$

and with $k^*=0$ at the pipe axis or at the edge of the boundary layer, respectively. The constant a_c has a mean value of 0.045, recommended by Derksen and Azad (1981).

A combination of $\mu_t = \rho k y u_*$, $\varepsilon = C_\mu \rho k^2 / \mu_t$, and $\varepsilon^+ = \mu \varepsilon / \rho u_*^4$ leads to

$$\varepsilon^+ = \frac{k^{*2}}{\kappa y^+} \quad (4.13)$$

for the near-wall region. When $k^*=1$ (i.e. A_+ or A_- is zero), Eq. (4.9) reduced to Eq. (4.7) and Eq. (4.13) reduced to Eq.(4.6).

It is believed that the wall functions should be applied to a near-wall point whose y^+ value is in the range $30 < y^+ < 100$. The question is whether the same results will be obtained if the wall functions are applied to two different near-wall points, both points within the range specified above. A test about how sensitive the results are to the position where wall functions are applied has been done for both $Re=50,000$ and $Re=150,000$. First of all, the y^+ vs x/D at three near-wall points for $Re=50,000$ is plotted in Figure 4.1 and the y^+ vs r/R at six downstream locations is plotted in Figure 4.2. In the inlet region, the values of y^+ quickly drop, after $x/D=10$, they are almost constant. At $r/R=0.975$, $31.5 < y^+ < 45.7$, at $r/R=0.957$, $53.0 < y^+ < 76.0$, and at $r/R=0.946$, $75.9 < y^+ < 107.8$ (only one point $y^+ > 100.0$). Comparison of the results for mean velocity, turbulent kinetic energy, Reynolds shear stress, and turbulent dissipation rate at $x/D=3.2, 19.6$ and 83.1 are plotted from Figure 4.3 to Figure 4.5. It is obvious that no matter which of these points the wall functions are applied, the distributions of mean velocity are almost identical, so are the distributions of ε . However, the distributions of k and \overline{uv} are affected by the positions where the wall functions are applied. For $Re=150,000$, the y^+ vs x/D at three near-wall points is plotted in Figure 4.6 and the y^+ vs r/R at six downstream locations is plotted in Figure 4.7. At $r/R=0.992$, $27.3 < y^+ < 37.8$, at $r/R=0.978$, $74.7 < y^+ < 102.8$ (one point whose $y^+ > 100.0$), and at $r/R=0.957$, $145.1 < y^+ < 200.5$. Comparison of the results for mean velocity, turbulent kinetic energy, Reynolds shear

stress, and turbulent dissipation rate at $x/D=3.2, 19.6$ and 83.1 are plotted from Figure 4.8 to Figure 4.10. Now for $r/R=0.957$, all of the points had y^+ values larger than 100.0 , but the distributions of mean velocity are nearly same as those obtained by setting wall functions at points whose y^+ values are at the range of $30.0 < y^+ < 100.0$. Therefore we can say that the simulation results are sufficiently accurate for most situations if the wall functions are applied to a point which has y^+ value between 30 to 200.

In the region where the wall functions are applied, instead of using Eq. 4.3, the Van Driest mixing-length model equation (Eq. 3.1) was used for calculating the eddy viscosity μ_t . At the point where a different expression for μ_t is used, we can see there is a jag in the profile of \overline{uv} .

4.3 Results

Numerical Considerations: The 120×99 grid system, as discussed in Chapter 3, was used for the standard $k-\varepsilon$ model tests. Bulk Reynolds number of 50,000 and 150,000 were selected as test cases. The optimum “time step” was selected by trial and error. The convergence of the iterations is plotted in Figure 4.11, which indicates that higher the Reynolds number is, the faster the iteration converges.

Flow with Bulk Reynolds Number of 50,000: Figure 4.12 and Figure 4.13 are color contour plots with shading interpreter for the non-dimensional axial mean velocity U/U_e and radial mean velocity V/U_e respectively. The contour plot for the non-dimensional axial mean velocity U/U_e with 30 contour lines in black is plotted in Figure 4.14. The non-dimensional axial velocity profiles at six downstream locations are plotted in Figure 4.15, and the non-dimensional radial velocity profiles at six downstream locations are plotted in Figure 4.16.

The development of the axial velocities in the downstream direction at various locations is shown in Figure 4.17. It can be seen that the downstream position of the centerline overshoot peak, henceforth referred to as the centerline peak overshoot position (x/D) is about 21, and about at $x/D = 70$, the flow reaches its full-develop stage. The color contour plot with shading interpreter for non-dimensional turbulent kinetic energy, k/u_*^2 , and the non-dimensional Reynolds shear stress, \overline{uv}/u_*^2 , are plotted in Figure 4.18 and Figure 4.19 respectively. The contour plot for non-dimensional turbulent kinetic energy, k/u_*^2 , with 25 contour lines in black is plotted in Figure 4.20. In the entrance region, there is a triangular region where the turbulent kinetic energy value is very small. Actually the same region is also believed to be highly intermittent. Outside this triangle area, in the downstream direction there is a very narrow area where the derivative of turbulent kinetic energy is extremely high. At the centerline, this narrow region matches with the centerline peak overshoot position. Turbulent kinetic energy vs r/R at six downstream locations are presented in Figure 4.21, whereas the development of turbulent kinetic energy in downstream direction is presented in Figure 4.22. As for Reynolds shear stress, the contour plot indicates that an undershoot peak can be found at the velocity overshoot peak position. Furthermore, Reynolds shear stress vs r/R at six downstream locations are presented in Figure 4.23, and the development of Reynolds shear stress in the downstream direction is plotted in Figure 4.24. Finally, turbulent dissipation rates vs r/R at six downstream locations are presented in Figure 4.25.

Flow with Bulk Reynolds Number of 150,000: The results are presented analogously with the results for flow with bulk Reynolds number of 50,000. Figure 4.26 and Figure 4.27 are color contour plots with shading interpreter for the non-dimensional axial mean velocity U/U_e and radial mean velocity V/U_e respectively. The contour plot for the non-dimensional axial

mean velocity U/U_e with 30 contour lines in black is plotted in Figure 4.28. The non-dimensional axial velocity profiles at six downstream locations are plotted in Figure 4.29, and the non-dimensional radial velocity profiles at six downstream locations are plotted in Figure 4.30. The development of the axial velocities in the downstream direction at various locations is shown in Figure 4.31. It can be seen that the centerline peak overshoot position (x/D) is about 24, and about at $x/D = 70$, the flow reaches its full-develop stage. The color contour plot with shading interpreter for non-dimensional turbulent kinetic energy, k/u_*^2 , and the non-dimensional Reynolds shear stress, \overline{uv}/u_*^2 , are plotted in Figure 4.32 and Figure 4.33 respectively. The contour plot for non-dimensional turbulent kinetic energy, k/u_*^2 , with 25 contour lines in black is plotted in Figure 4.34. Turbulent kinetic energy vs r/R at six downstream locations are presented in Figure 4.35, whereas the development of turbulent kinetic energy in the downstream direction is presented in Figure 4.36. As for Reynolds shear stress, the contour plot indicates that an undershoot peak can be found at the velocity overshoot peak position again. Furthermore, Reynolds shear stress vs r/R at six downstream locations are presented in Figure 4.37, whereas the development of Reynolds shear stress in the downstream direction is plotted in Figure 4.38. Finally, turbulent dissipation rates vs r/R at six downstream locations are presented in Figure 4.39.

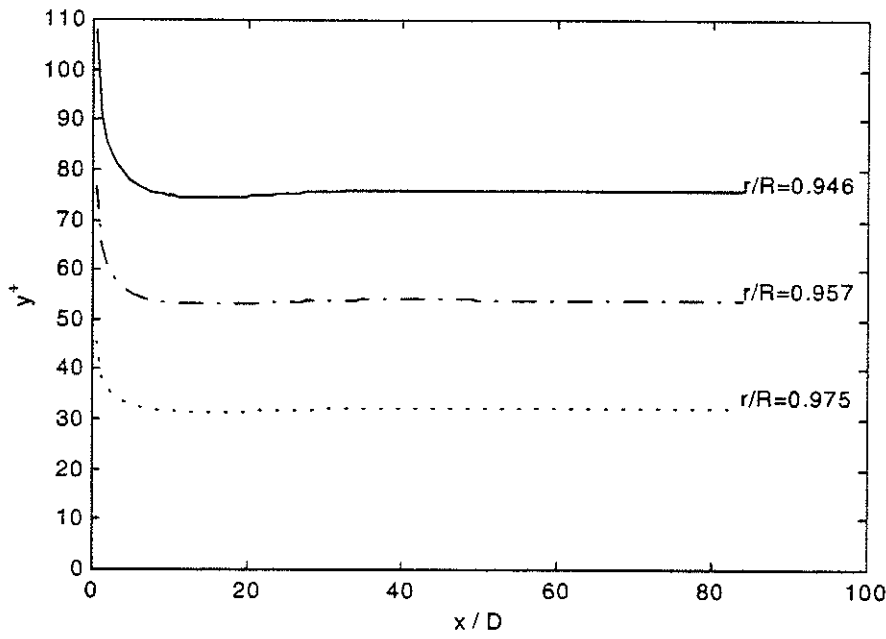


Figure 4.1 Y^+ vs x/D for $Re=50,000$ using three different locations to apply the wall functions.

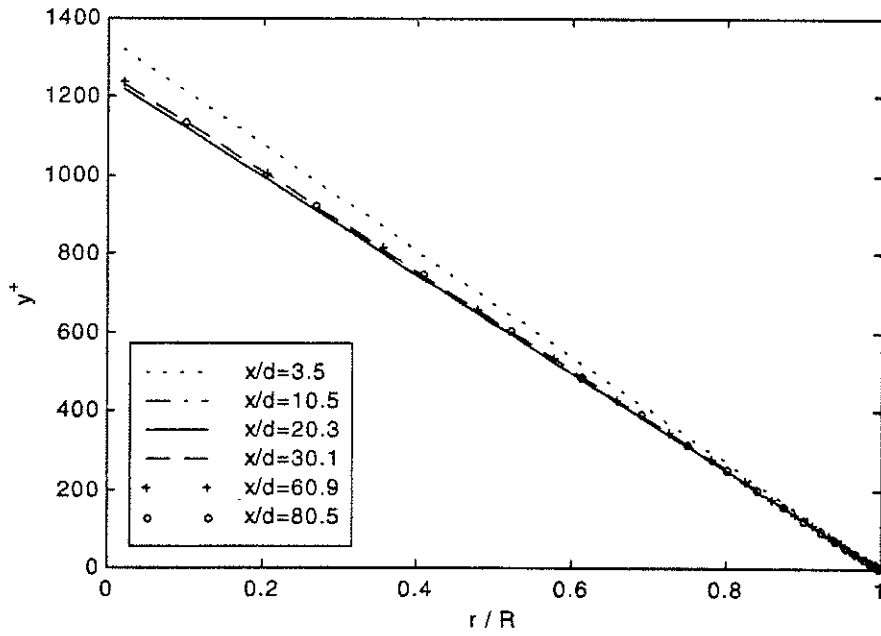


Figure 4.2 Y^+ vs r/R for $Re=50,000$ using three different locations to apply the wall functions

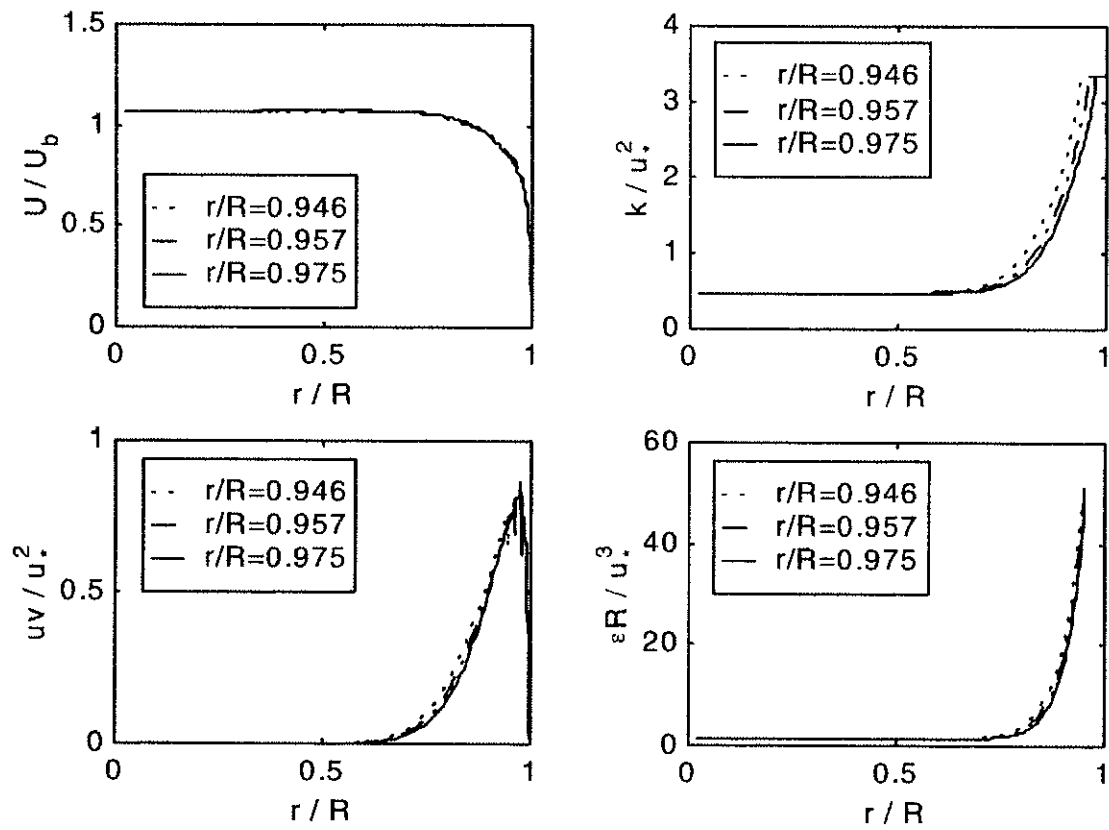


Figure 4.3 Results at $x/D=3.2$ for $Re=50,000$ using three different locations to apply the wall functions

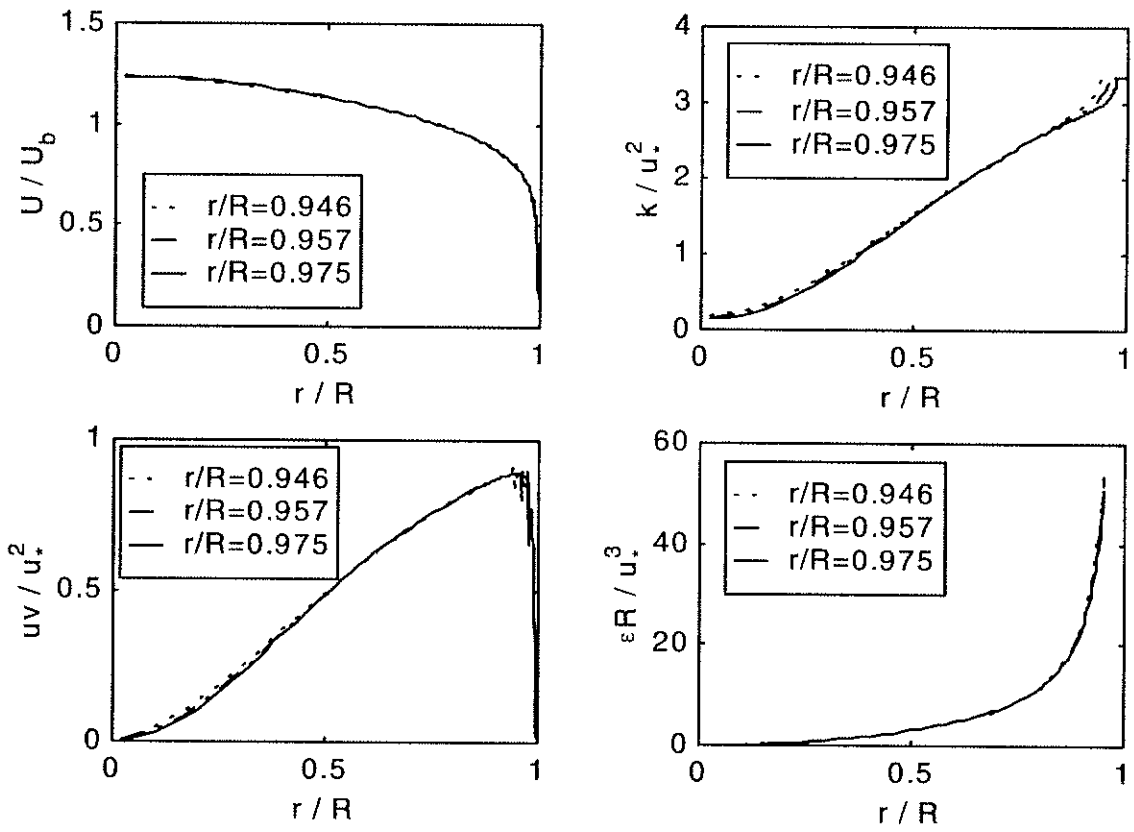


Figure 4.4 Results at $x/D=19.6$ for $Re=50,000$ using three different locations to apply the wall functions

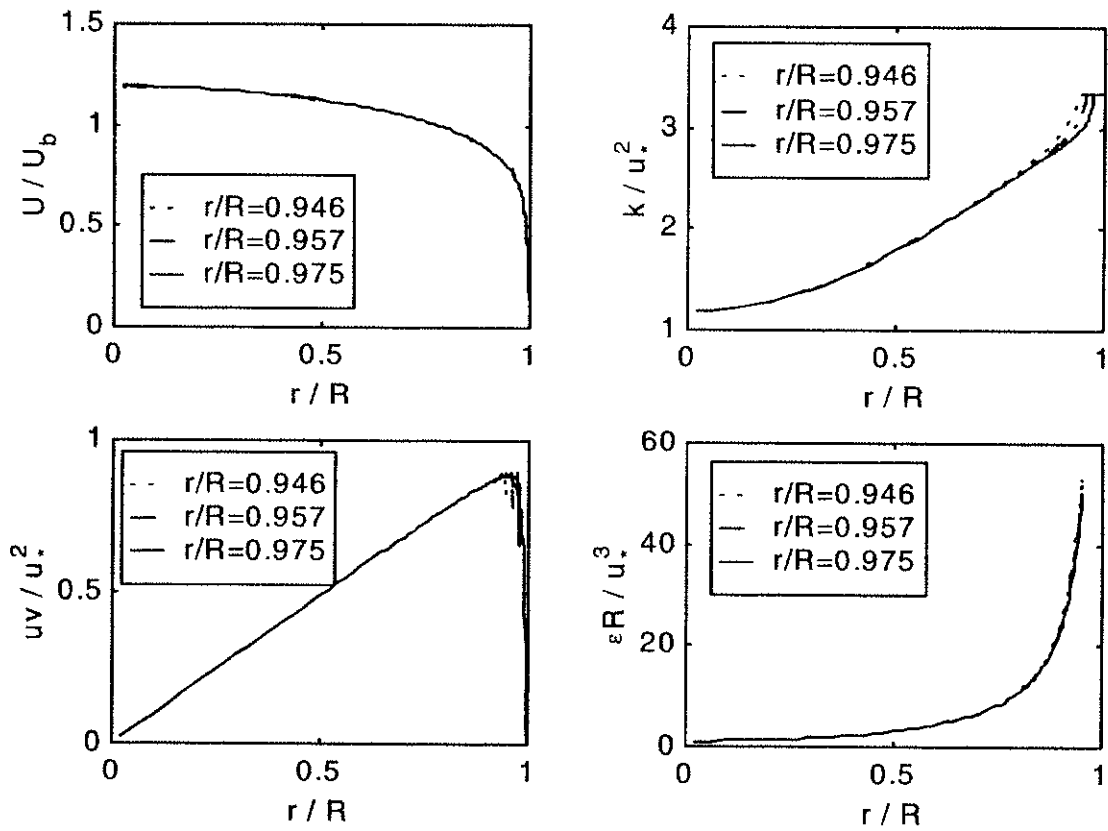


Figure 4.5 Results at $x/D=83.1$ for $Re=50,000$ using three different locations to apply the wall functions

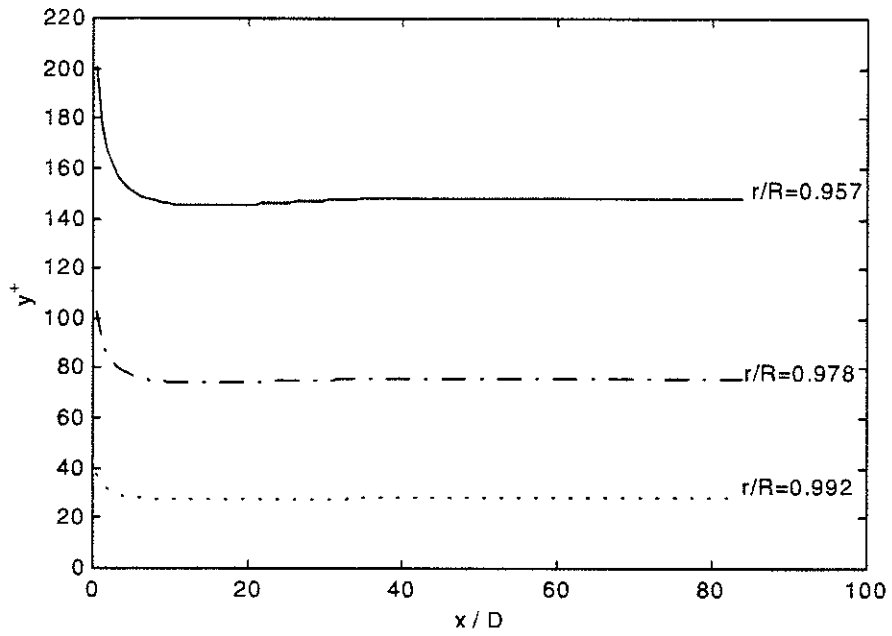


Figure 4.6 Y^+ vs x/D for $Re=150,000$ using three different locations to apply the wall functions

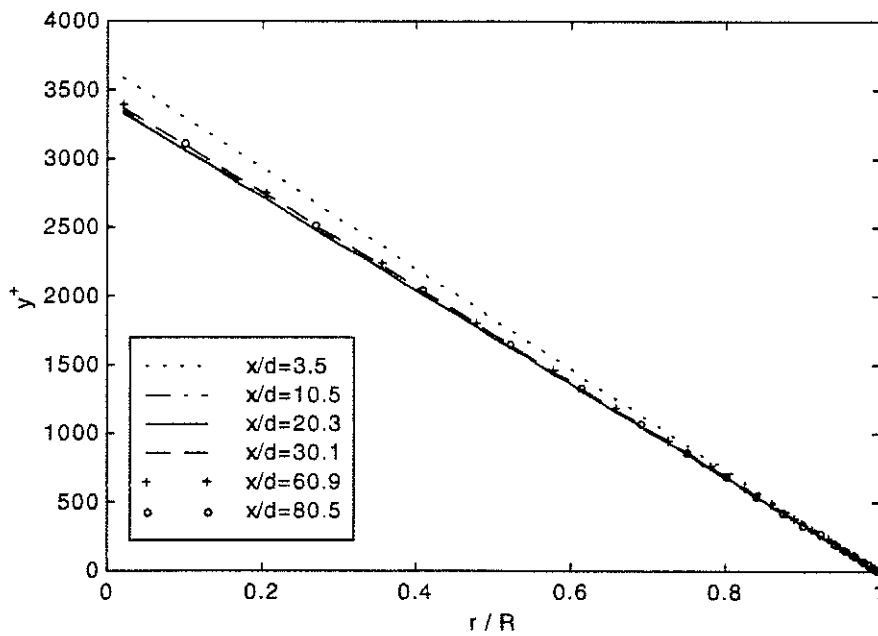


Figure 4.7 Y^+ vs r/R for $Re=150,000$ using three different locations to apply the wall functions

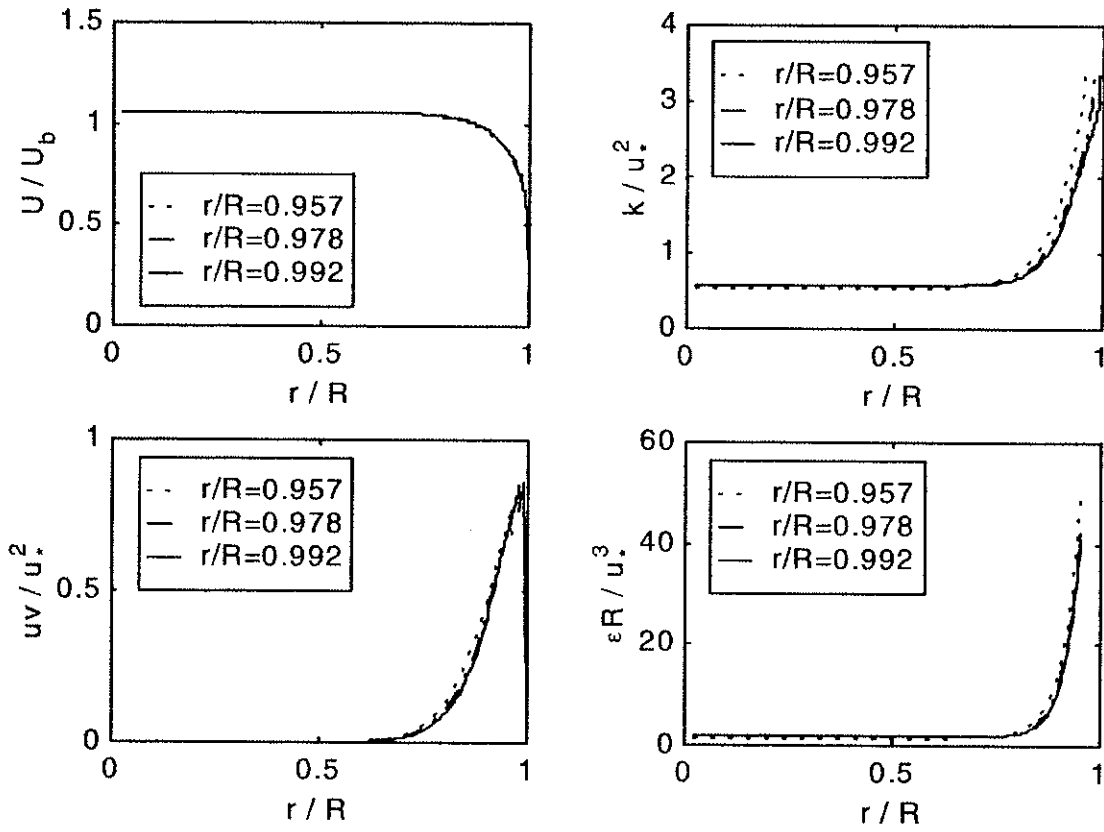


Figure 4.8 Results at $x/D=3.2$ for $Re=150,000$ using three different locations to apply the wall functions

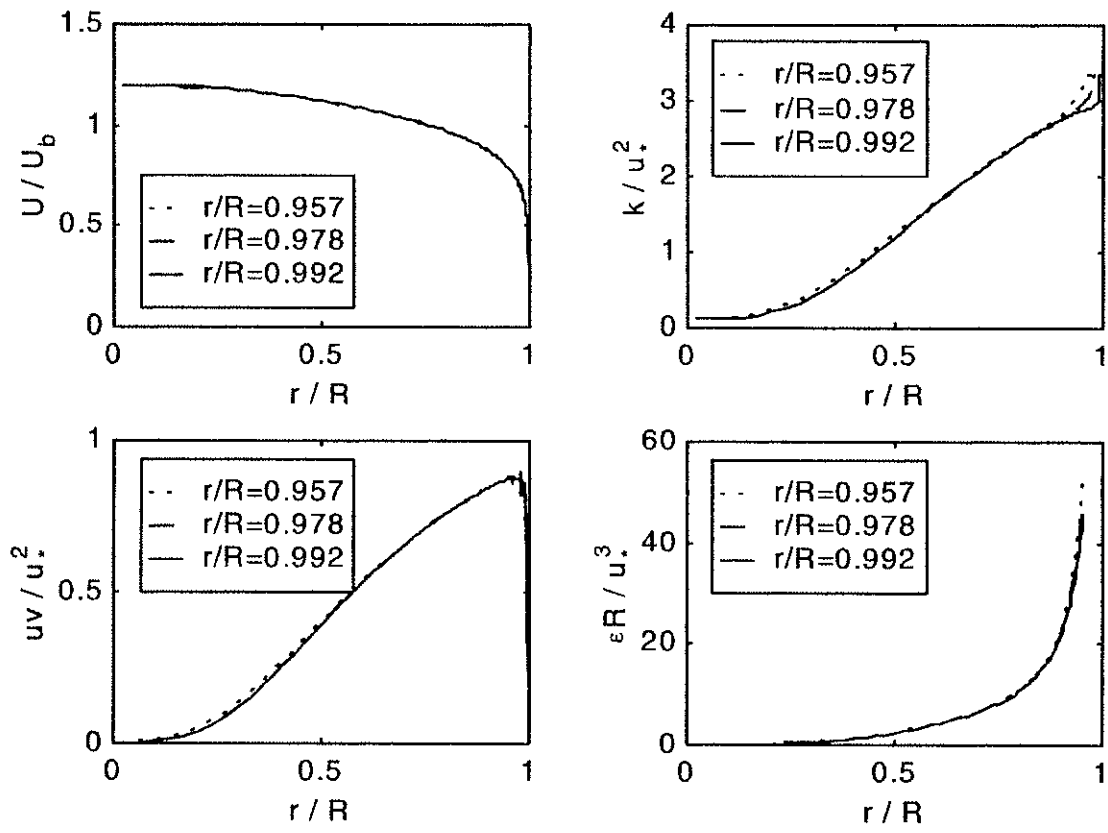


Figure 4.9 Results at $x/D=19.6$ for $Re=150,000$ using three different locations to apply the wall functions

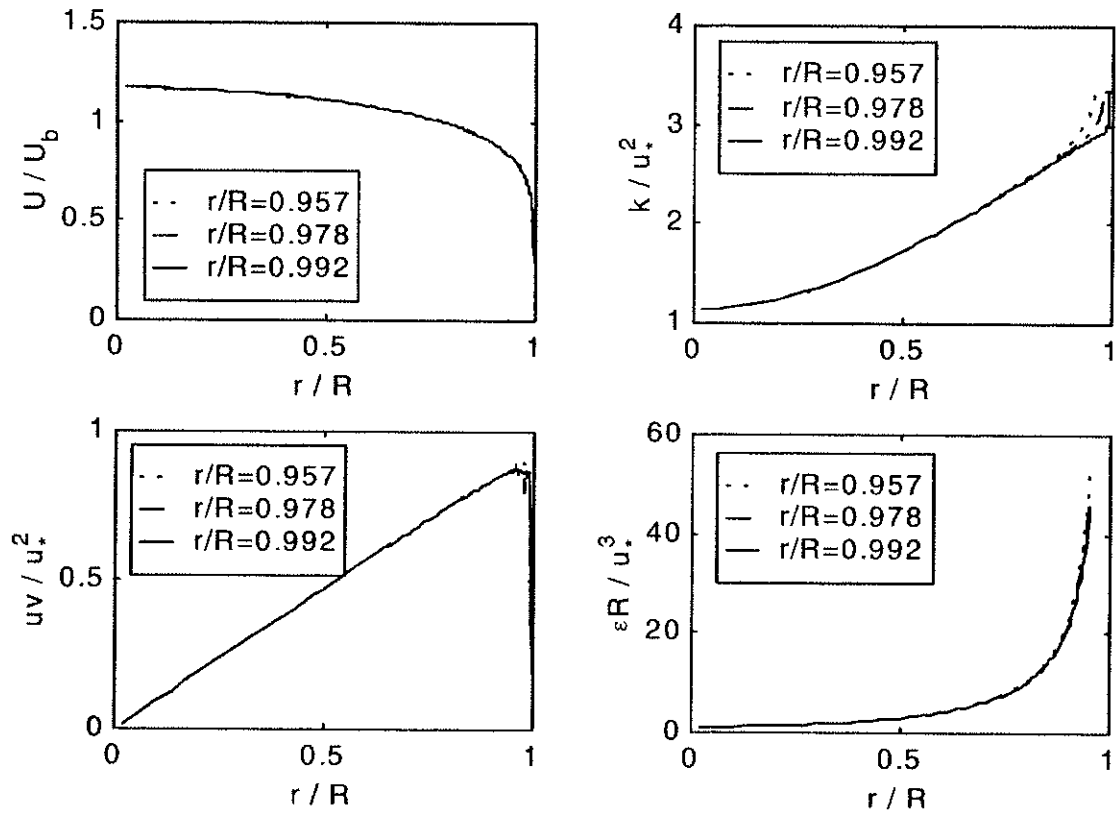


Figure 4.10 Results at $x/D=83.1$ for $Re=150,000$ using three different locations to apply the wall functions

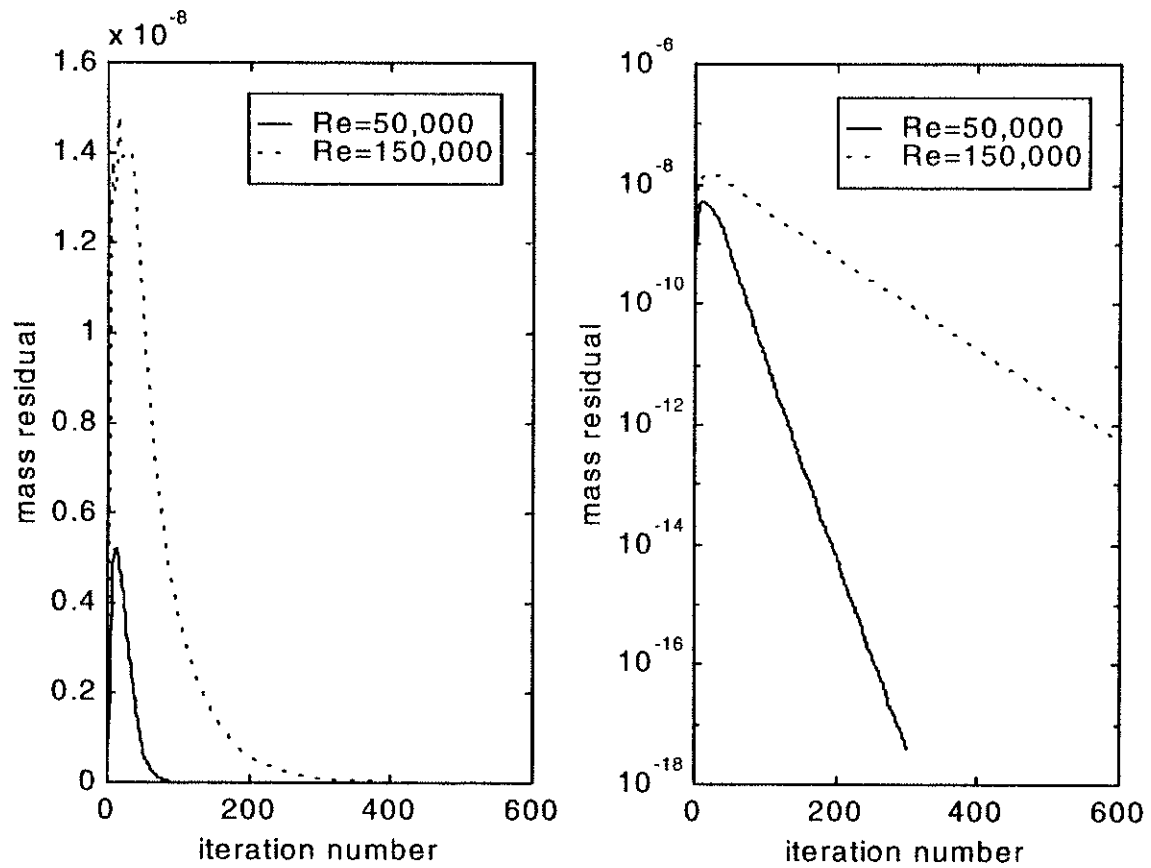


Figure 4.11 Convergence of the iterations

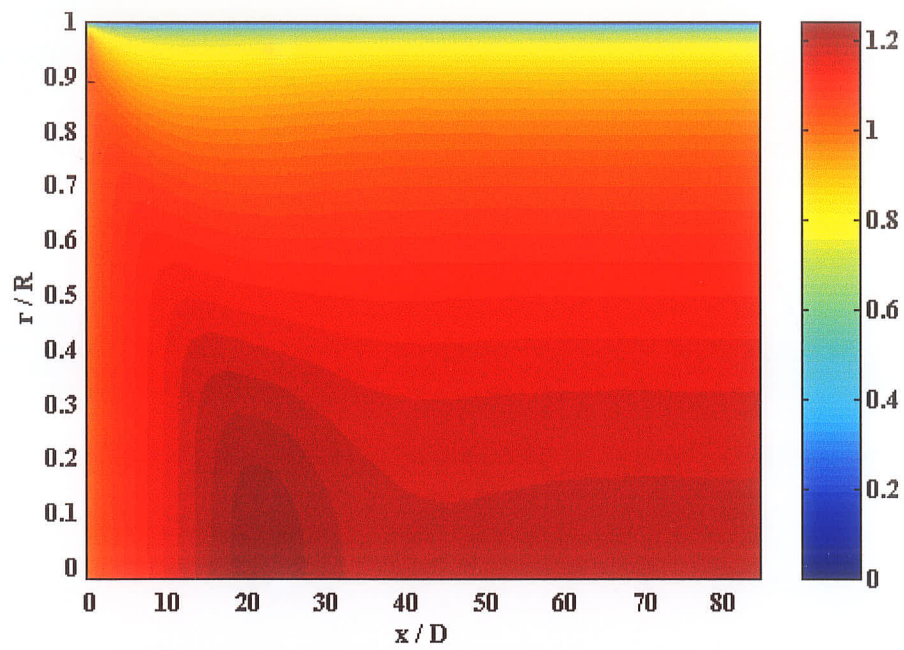


Figure 4.12 Contour plot for the non-dimensional axial velocity for $Re = 50,000$

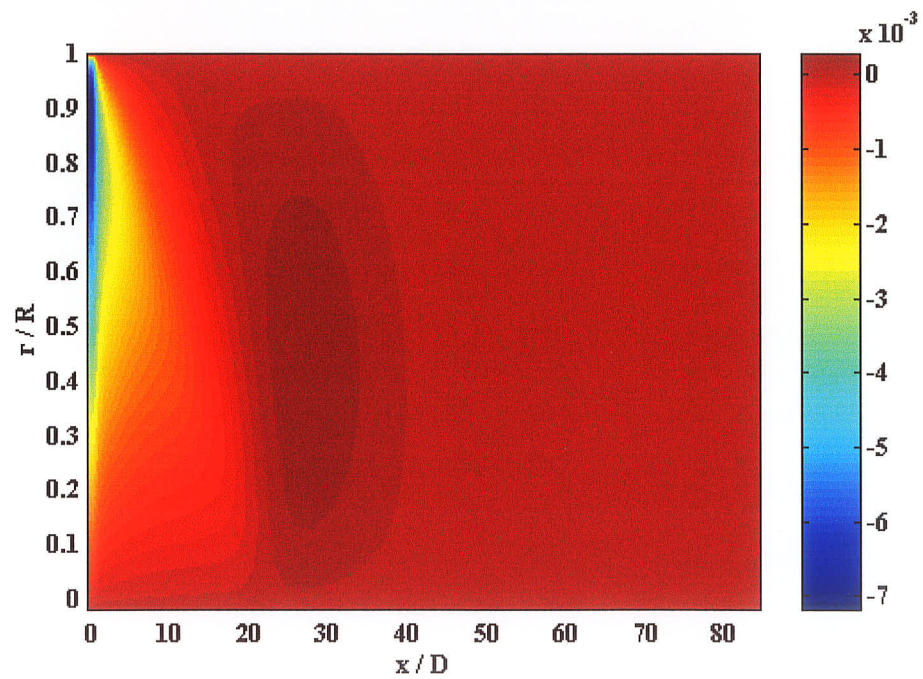


Figure 4.13 Contour plot for the non-dimensional radial velocity for $Re = 50,000$

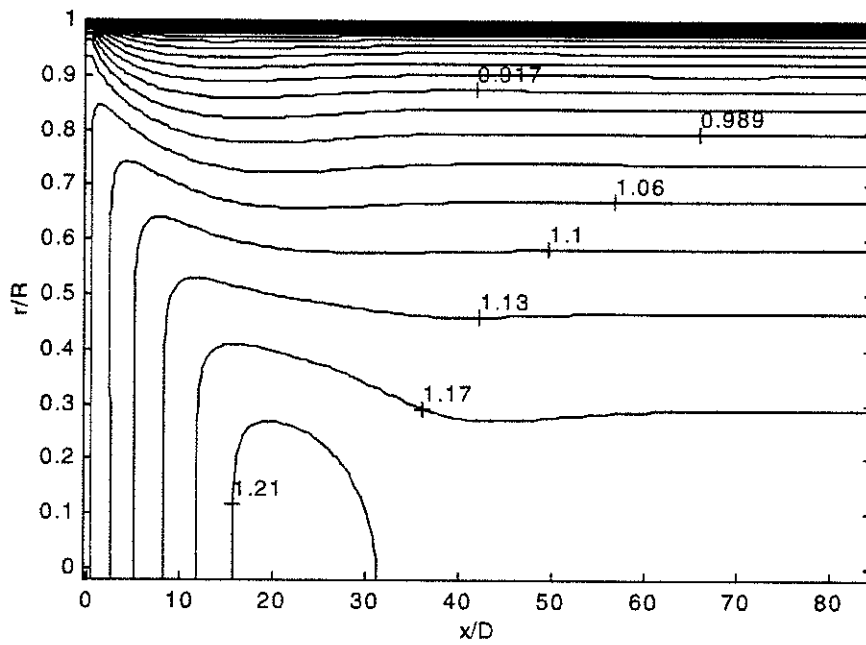


Figure 4.14 Contour plot for non-dimensional axial velocity for $Re=50,000$

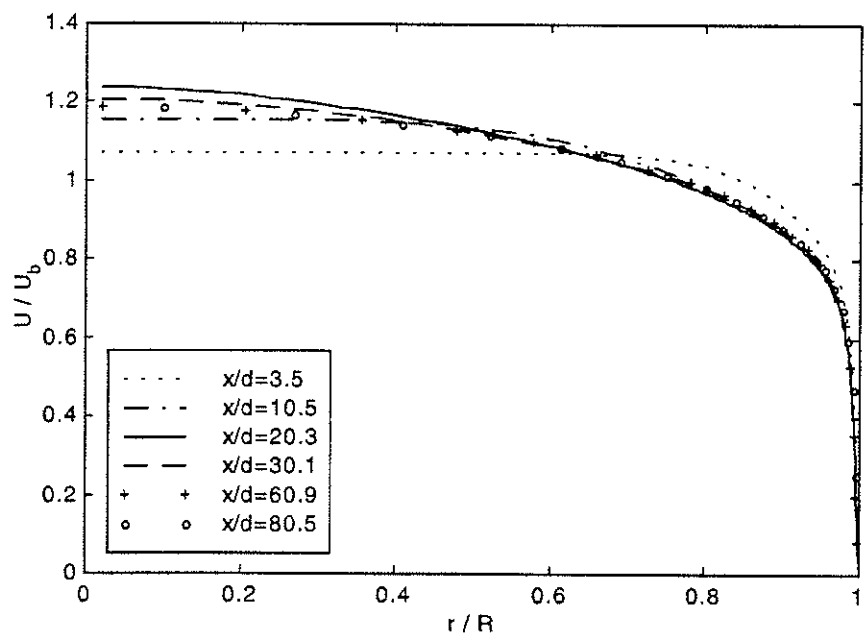


Figure 4.15 Axial velocity vs r/R at six downstream locations for $Re=50,000$

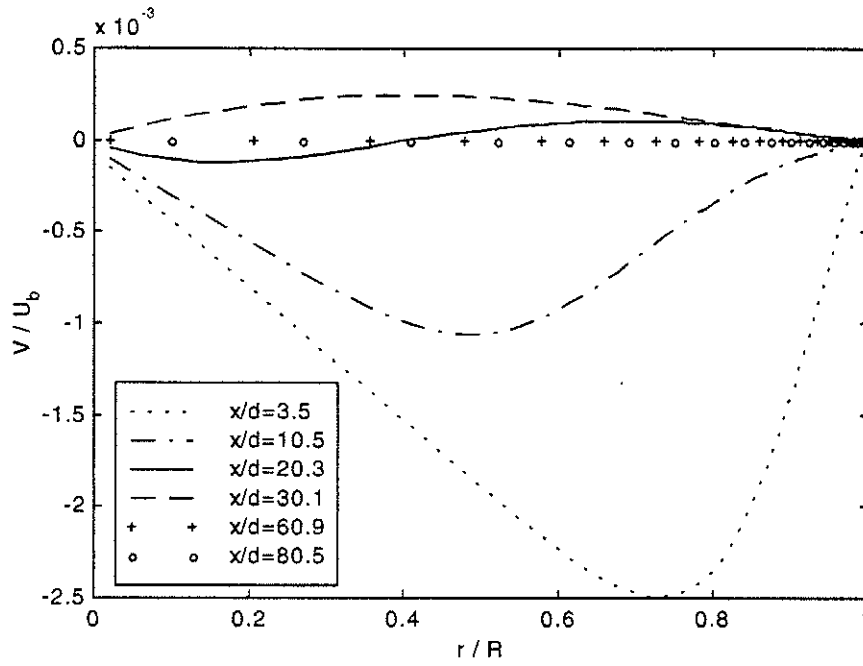


Figure 4.16 Radial velocity vs r/R at six downstream locations for $Re=50,000$

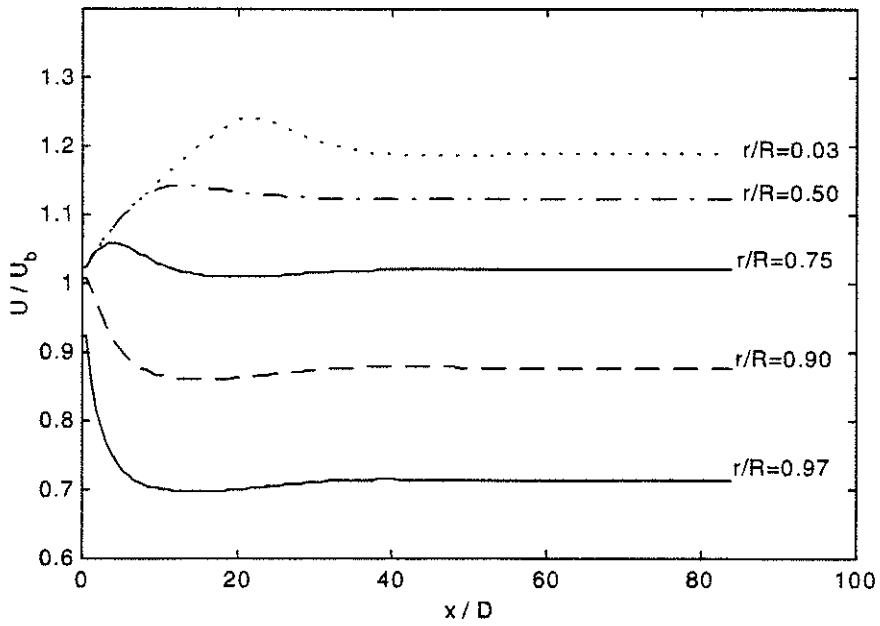


Figure 4.17 Development of Axial velocity for $Re=50,000$

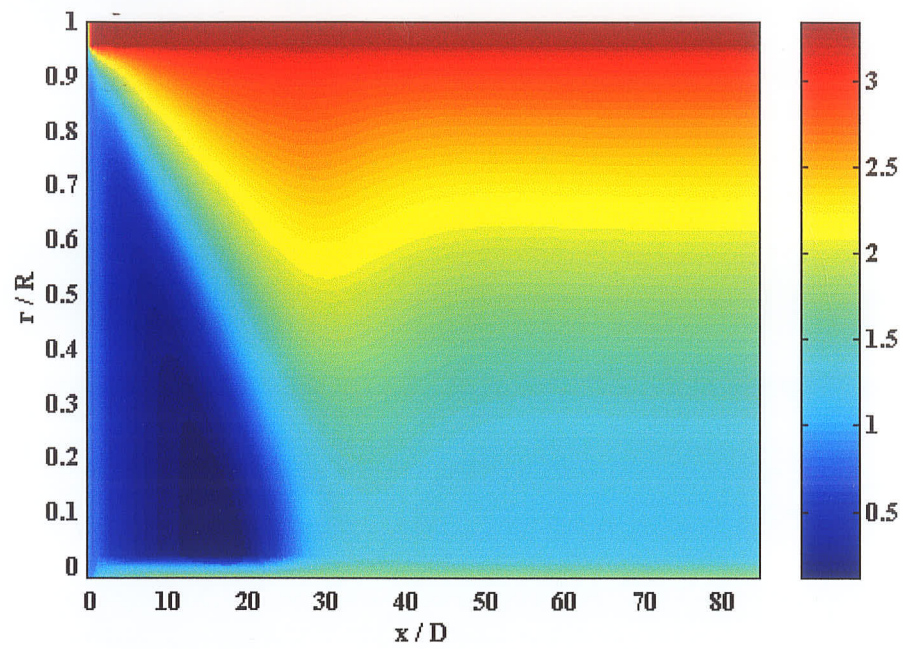


Figure 4.18 Contour plot for non-dimensional Turbulent Kinetic Energy for $Re = 50,000$

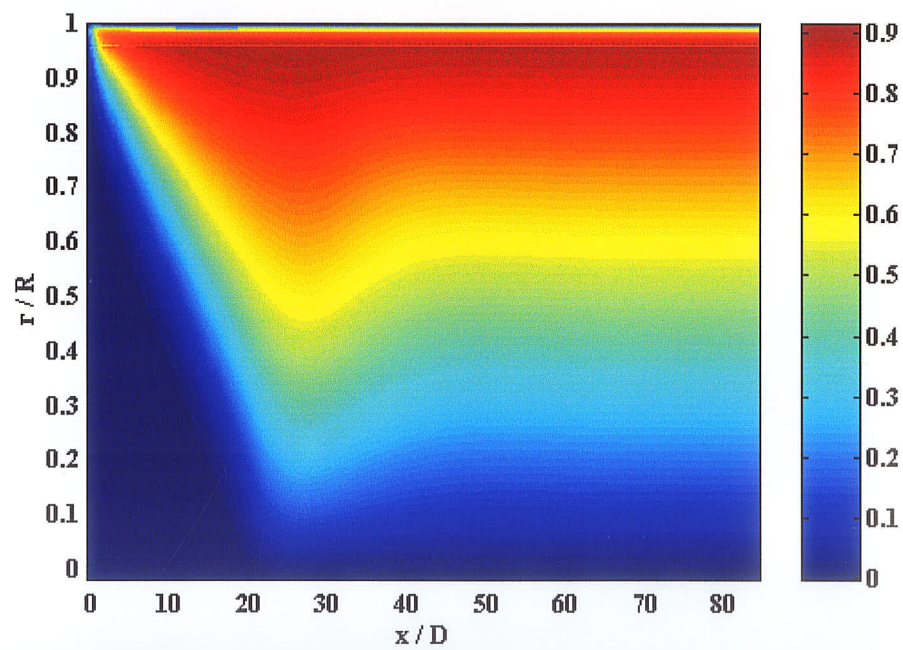


Figure 4.19 Contour plot for Reynolds shear stress for $Re = 50,000$

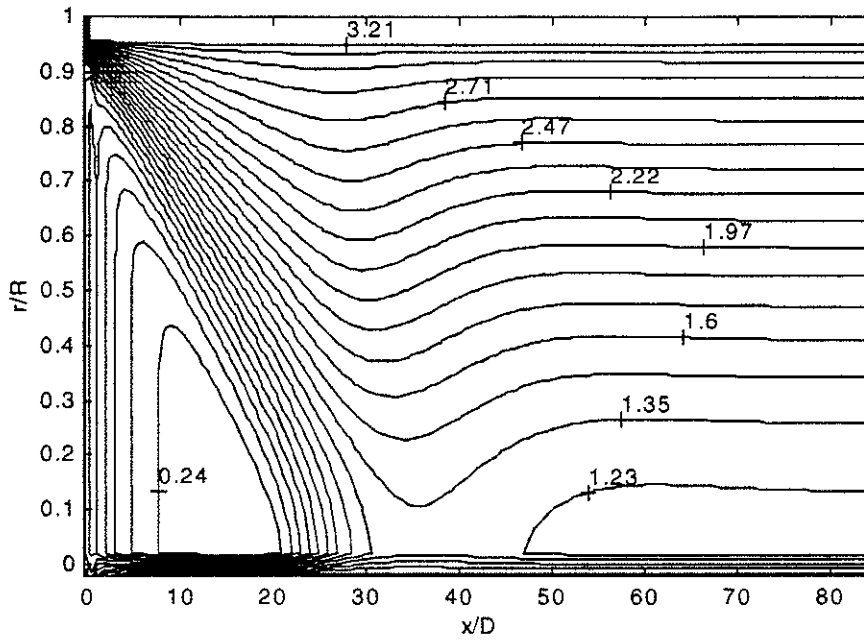


Figure 4.20 Contour plot for non-dimensional turbulent kinetic energy for $Re = 50,000$

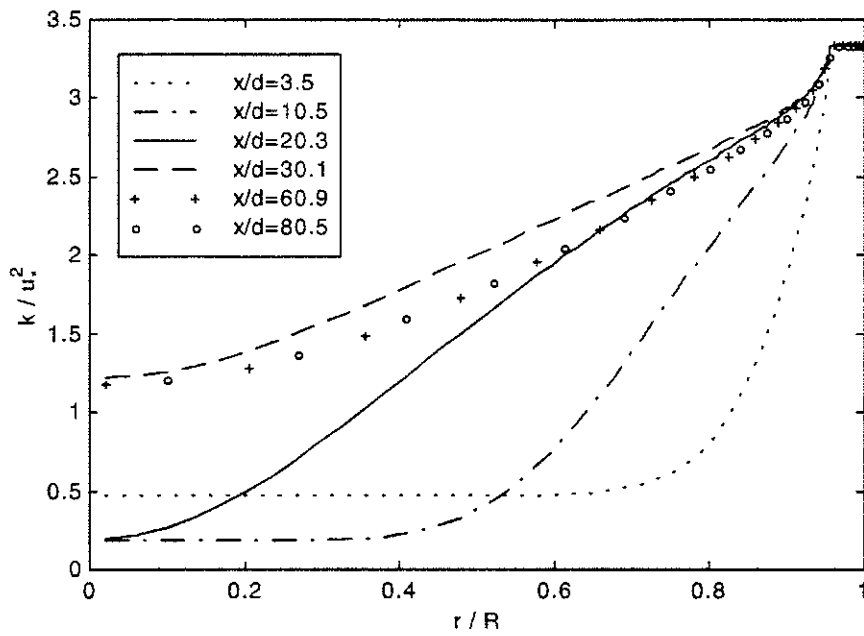


Figure 4.21 Turbulent kinetic energy vs r/R at six downstream locations for $Re=50,000$

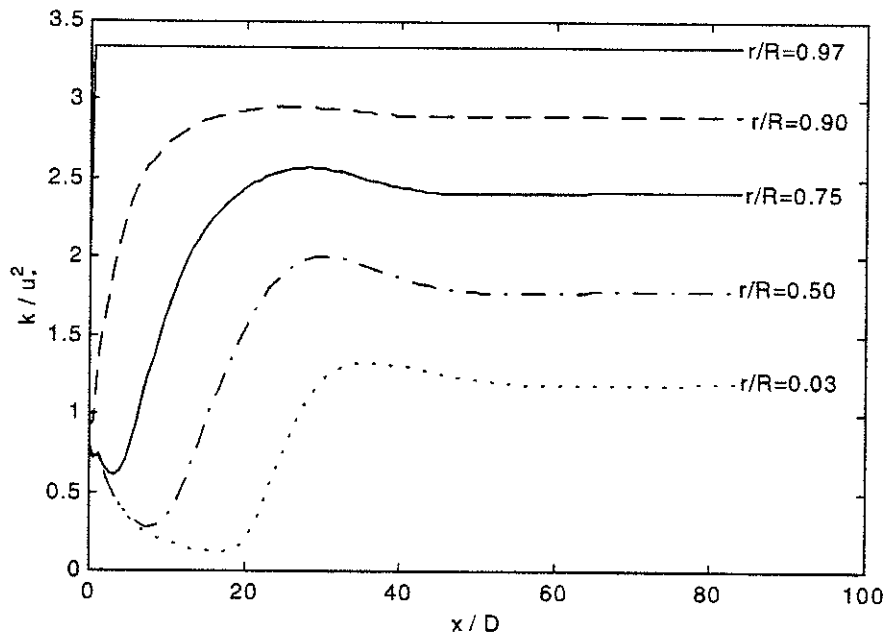


Figure 4.22 Development of turbulent kinetic energy for $Re=50,000$

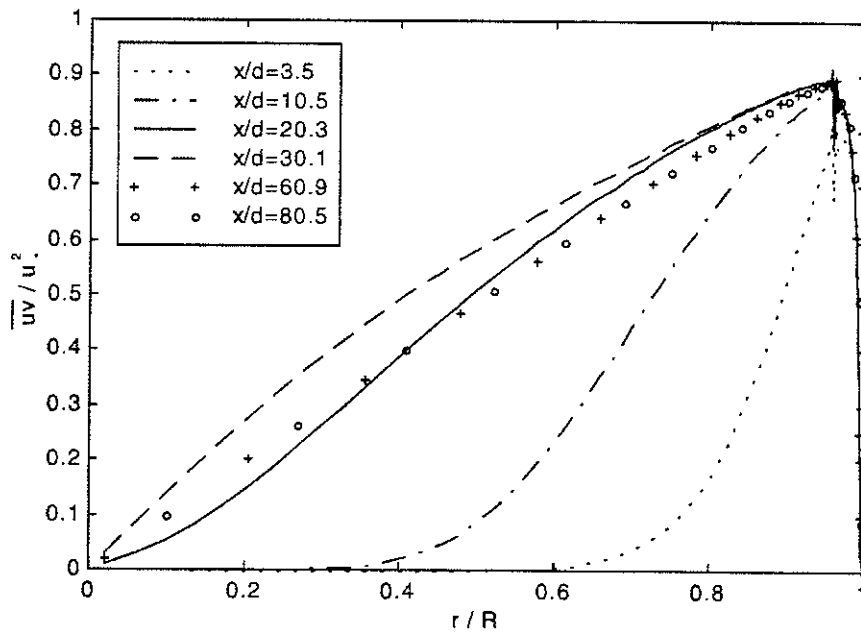


Figure 4.23 Reynolds shear stress vs r/R at six downstream locations for $Re=50,000$

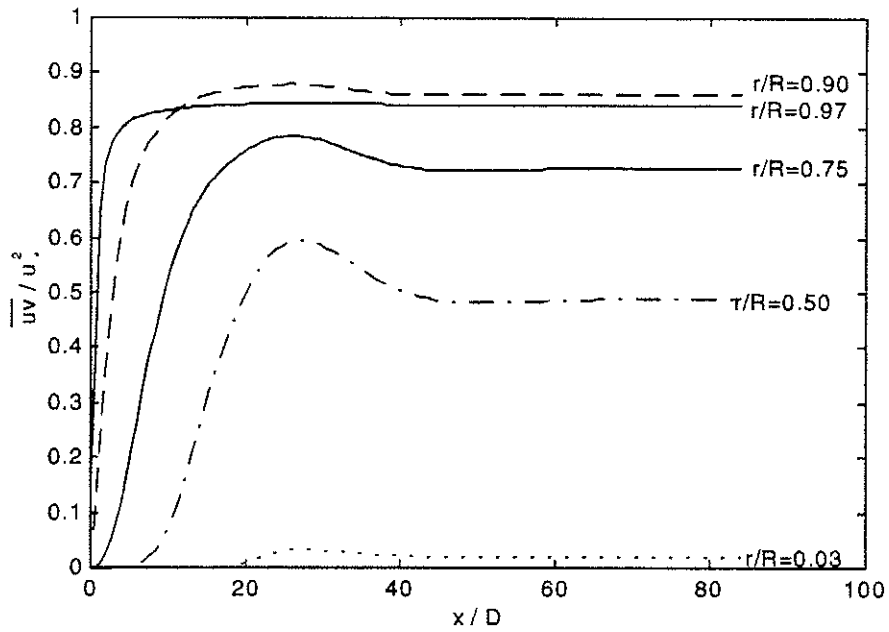


Figure 4.24 Development of Reynolds shear stress for $Re=50,000$

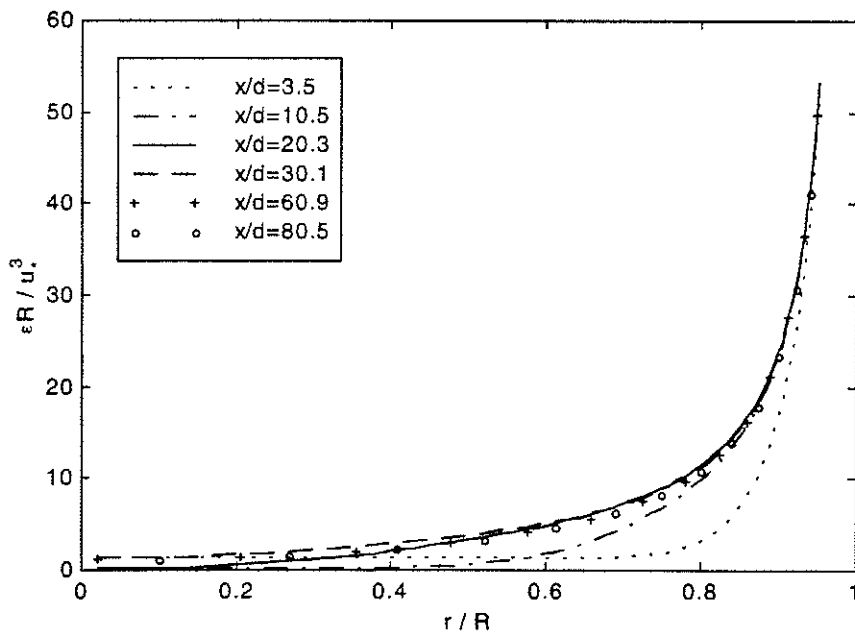


Figure 4.25 Turbulent dissipation rate vs r/R at six downstream locations for $Re=50,000$

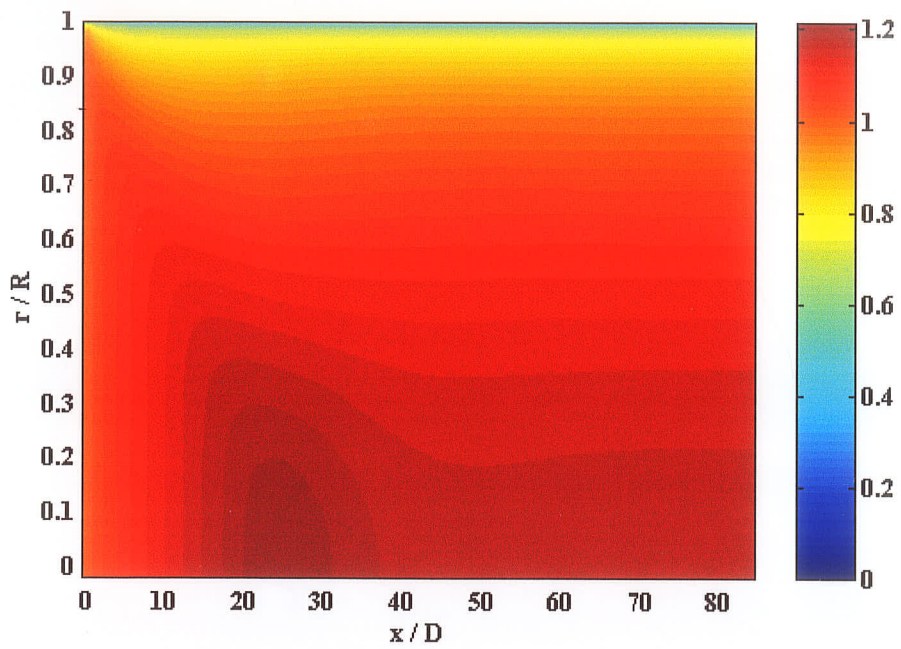


Figure 4.26 Contour plot for the non-dimensional axial velocity for $Re = 150,000$

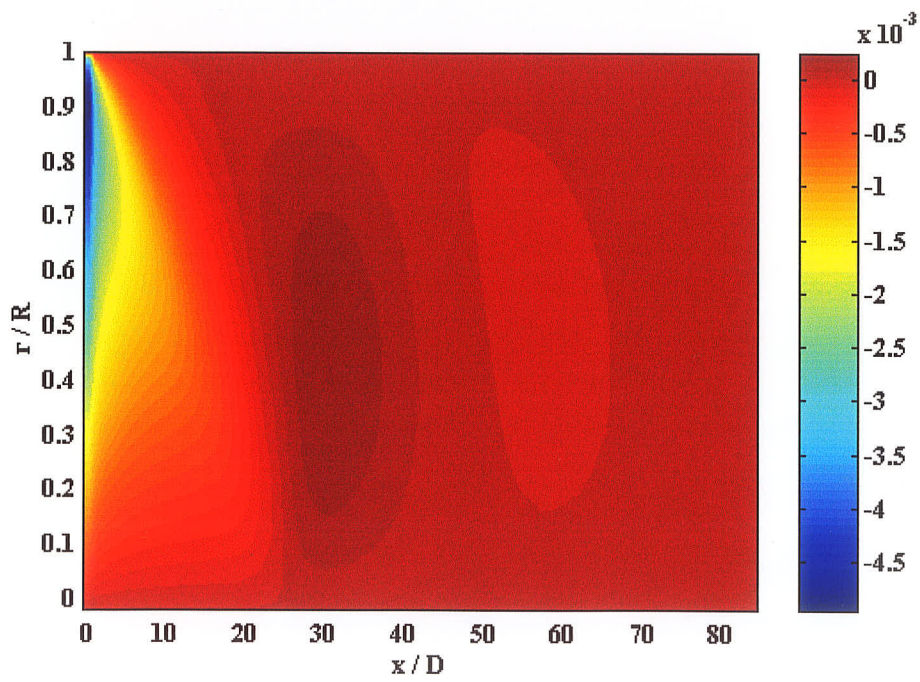


Figure 4.27 Contour plot for the non-dimensional radial velocity for $Re = 150,000$

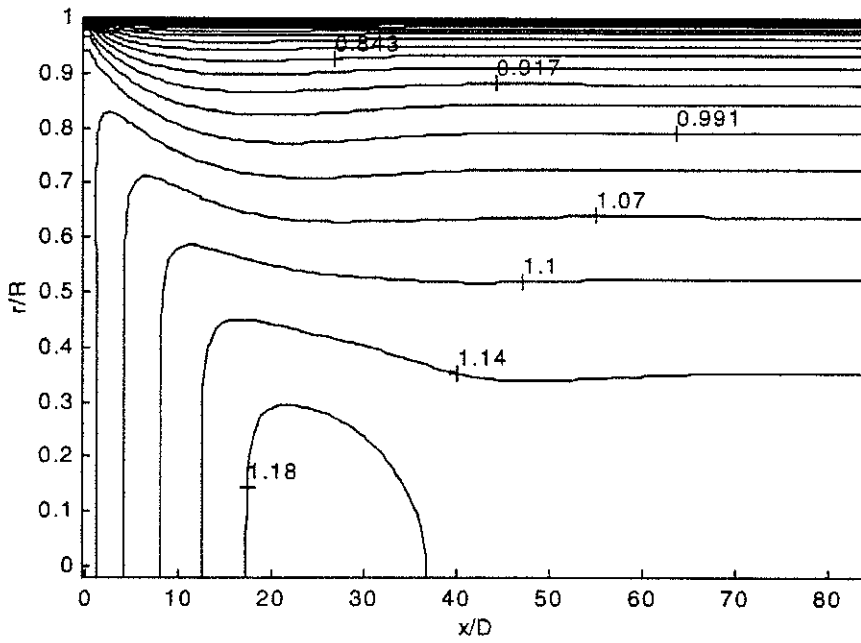


Figure 4.28 Contour plot for non-dimensional axial velocity for $Re=150,000$

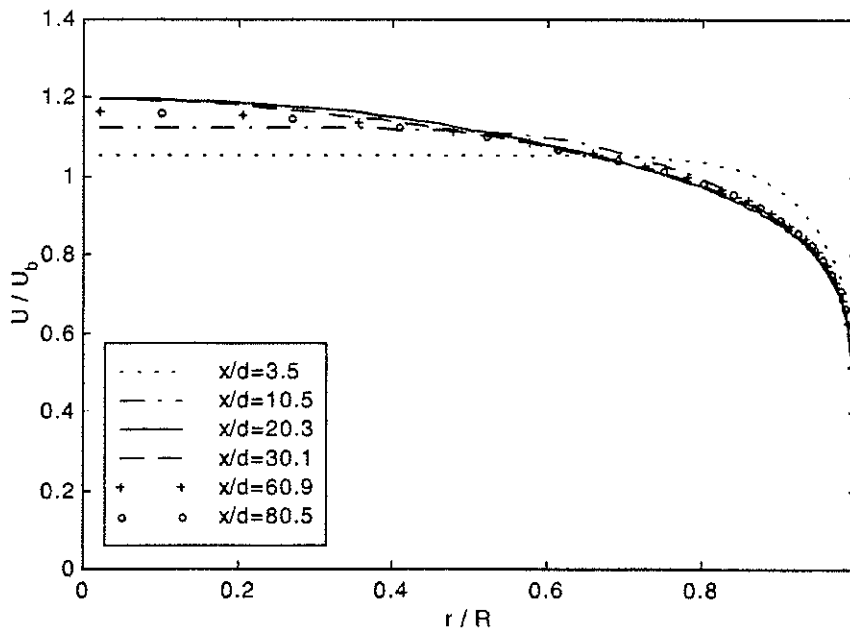


Figure 4.29 Axial velocity vs r/R at six downstream locations for $Re=150,000$

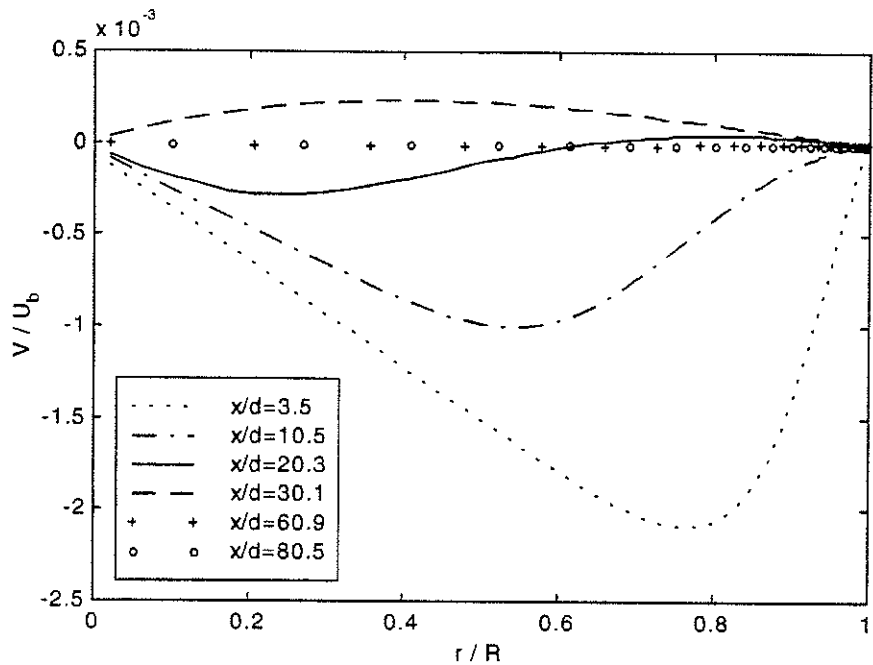


Figure 4.30 Radial velocity vs r/R at six downstream locations for $Re=150,000$

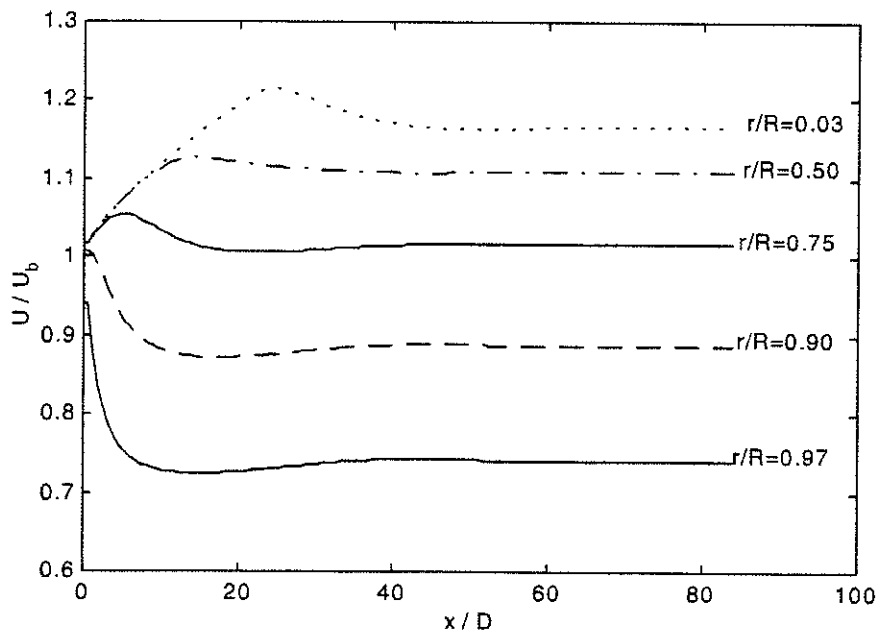


Figure 4.31 Development of axial velocity for $Re=150,000$

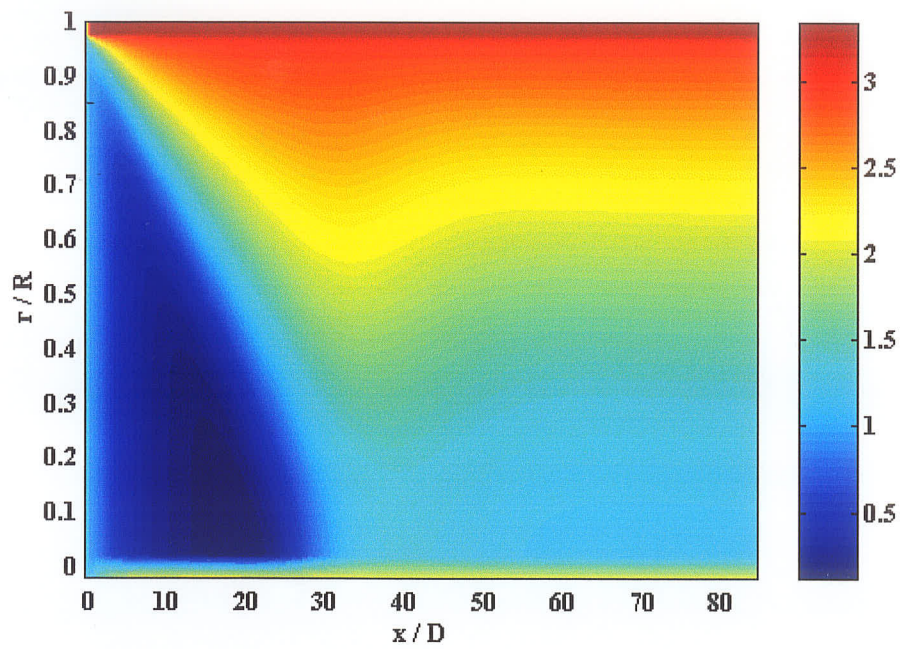


Figure 4.32 Contour plot for non-dimensional Turbulent Kinetic Energy for $Re = 150,000$

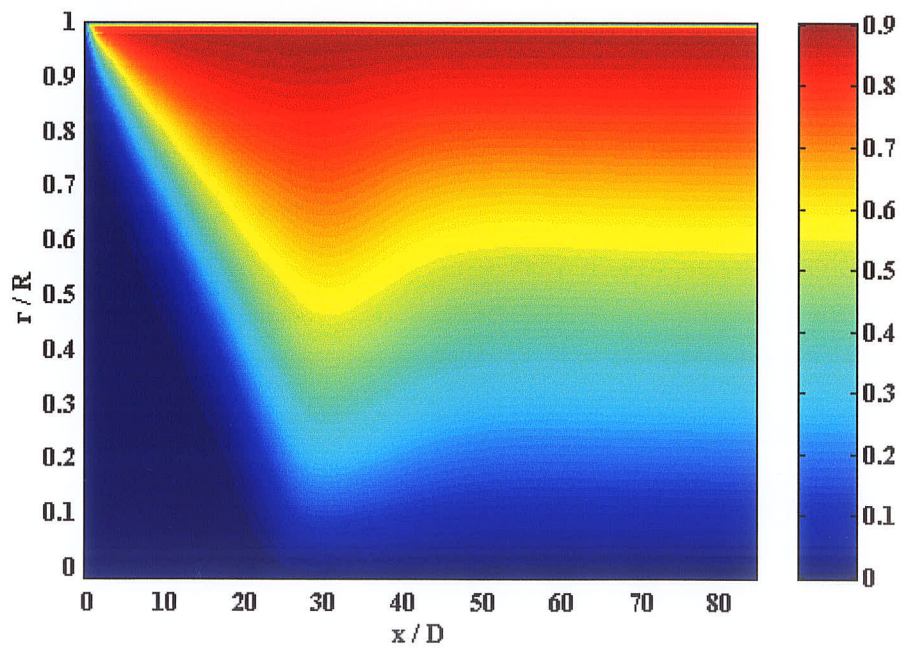


Figure 4.33 Contour plot for Reynolds shear stress for $Re = 150,000$

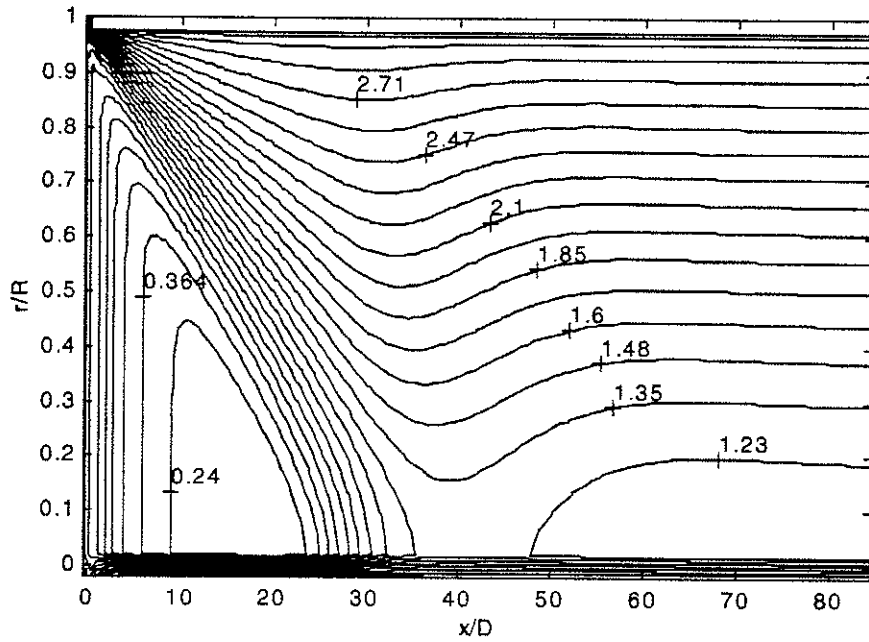


Figure 4.34 Contour plot for non-dimensional turbulent kinetic energy for $Re = 150,000$

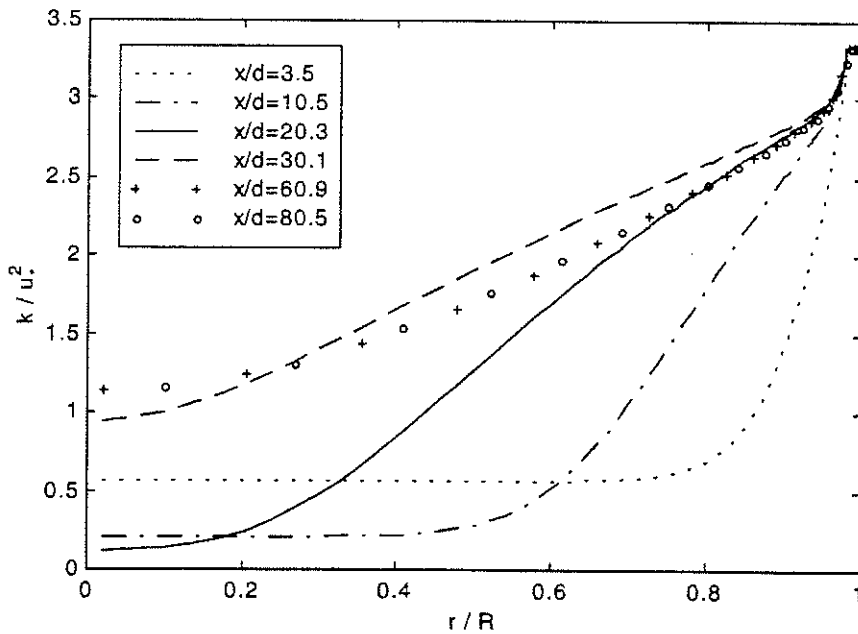


Figure 4.35 Turbulent kinetic energy vs r/R at six downstream locations for $Re=150,000$

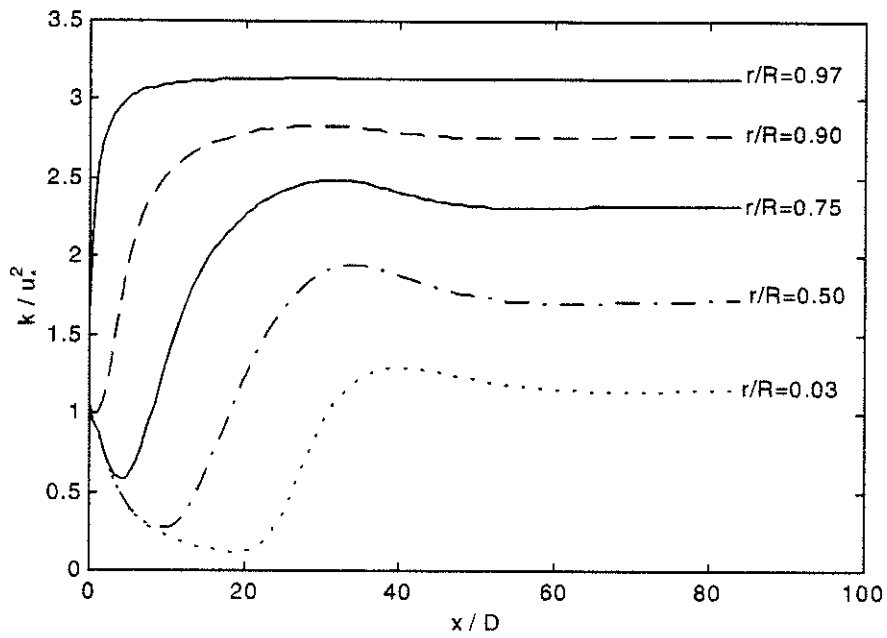


Figure 4.36 Development of turbulent kinetic energy for $Re=150,000$

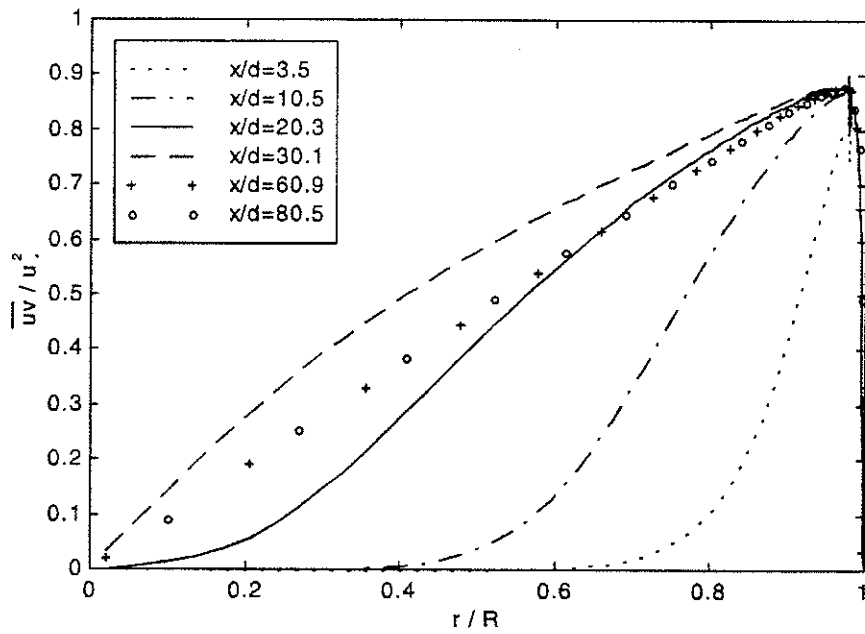


Figure 4.37 Reynolds shear stress vs r/R at six downstream locations for $Re=150,000$

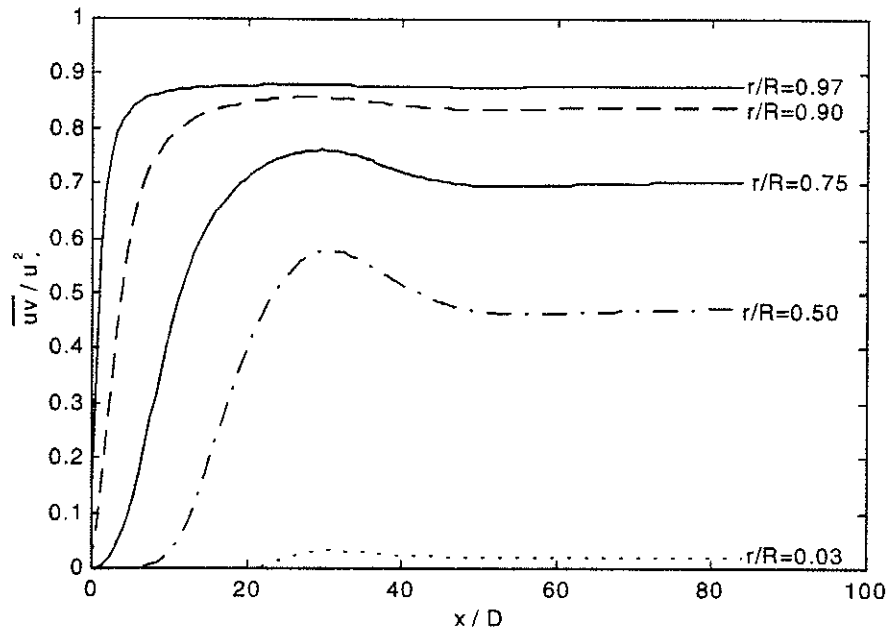


Figure 4.38 Development of Reynolds shear stress for $Re=150,000$

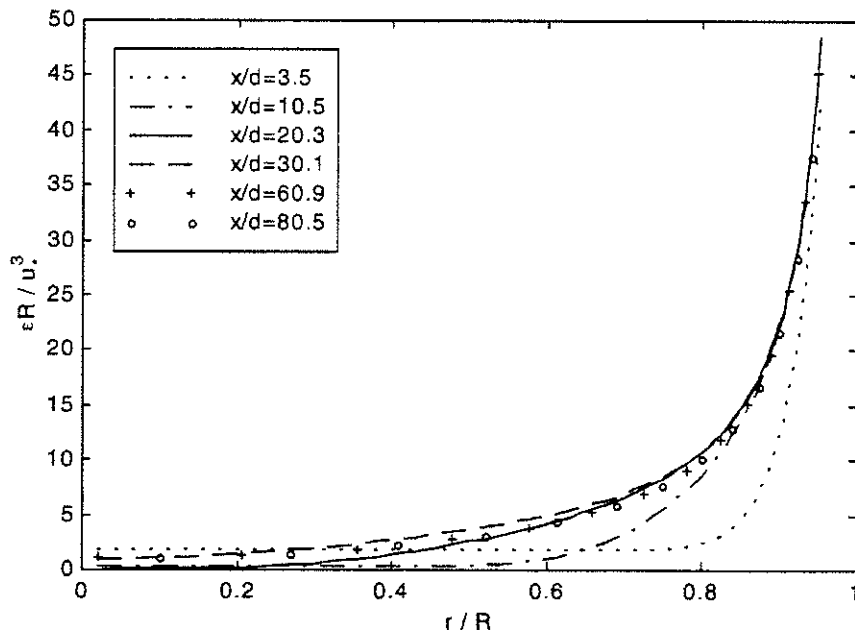


Figure 4.39 Turbulent dissipation rate vs r/R at six downstream locations for $Re=150,000$

5. Chien's k-ε Model

In this chapter, the equations of Chien's k-ε model are present in the Section 5.1. This is followed by the Section 5.2 on numerical considerations with a discussion on source-term linearization. Then, the simulation results for Re=50,000 and Re=10,000 are presented in the Section 5.3. Finally, a brief literature review on Chien's model assessment is given in Section 5.4.

5.1 Model Equations

Although the general approach is similar to that of Jones and Launder (1972), Chien's (1982) k-ε model is valid down to a solid wall. It eliminates the need for wall functions, which makes it more generally applicable compared with Jones and Launder's k-ε model.

The equations of Chien's k-ε model are given as follows.

Eddy viscosity:

$$\nu_t = C_\mu (k^2 / \varepsilon) [1 - \exp(-C_3 u_* y / \nu)] \quad (5.1)$$

where ν_t is the turbulent (or eddy) viscosity, u_* is the friction velocity, y is the distance from the wall, and C_μ , C_3 are the model constants.

Turbulent kinetic energy:

$$\frac{Dk}{Dt} = \frac{\partial}{\partial x_i} [(v + \nu_t) \frac{\partial k}{\partial x_i}] + \nu_t \left(\frac{\partial U_i}{\partial x_j} + \frac{\partial U_j}{\partial x_i} \right) \frac{\partial U_i}{\partial x_j} - \varepsilon - \frac{2\nu k}{y^2} \quad (5.2)$$

Dissipation rate:

$$\frac{D\varepsilon}{Dt} = \frac{\partial}{\partial x_i} \left[\left(v + \frac{\nu_t}{\sigma_\varepsilon} \right) \frac{\partial \varepsilon}{\partial x_j} \right] + C_1 \frac{\varepsilon}{k} \nu_t \left(\frac{\partial U_i}{\partial x_j} + \frac{\partial U_j}{\partial x_i} \right) \frac{\partial U_i}{\partial x_j} - \frac{\varepsilon}{k} \left[C_2 f \varepsilon + \frac{2\nu k}{y^2} e^{-C_4 u_* y / \nu} \right] \quad (5.3)$$

where

$$f = 1 - \frac{0.4}{1.8} e^{-(k^2 / 6\nu\varepsilon)^2} \quad (5.4)$$

The closure coefficients are: $C_1=1.35$, $C_2=1.8$, $C_3=0.0115$, $C_4=0.5$, $C_\mu=0.09$, and $\sigma=1.3$.

5.2 Numerical Considerations

Source-term linearization: The linearization method for the source term is very important for obtaining numerical convergence. The governing equations can generally be written in tensor notation as follows:

$$\frac{\partial}{\partial x_i}(\rho U_i \phi) = \frac{\partial}{\partial x_i} \left(\Gamma_\phi \frac{\partial \phi}{\partial x_i} \right) + S_\phi. \quad (5.5)$$

Here, ϕ denotes the dependent variable (U , V , k , ε etc.), and Γ_ϕ is the effective diffusion coefficient. S_ϕ represents the source term ($S_\phi = S_\phi^c + \phi_p S_\phi^p$). When S_ϕ is a nonlinear function of ϕ , we must linearize it, i.e., specify the value of S_ϕ^p and S_ϕ^c , which themselves depend on ϕ . The choice of the S_ϕ^p and S_ϕ^c is not unique, but the linearization of S_ϕ should be a good representation of the $S_\phi \sim \phi$ relationship. Further, the basic rule about non-positivity of S_ϕ^p must be obeyed to maintain the diagonal dominance of the matrix to be solved. For the present simulations, the choice of the coefficients of S_ϕ^p and S_ϕ^c for Eq. (5.2) is:

$$S_\phi^p = - \left(\frac{\varepsilon}{k} + \frac{2\nu}{y^2} \right), \quad (5.6)$$

$$S_\phi^c = \nu_t \left(\frac{\partial U_i}{\partial x_j} + \frac{\partial U_j}{\partial x_i} \right) \frac{\partial U_i}{\partial x_j}. \quad (5.7)$$

The choice for the coefficients of S_ϕ^p and S_ϕ^c for Eq. (5.3) is:

$$S_\phi^p = - \left[C_2 f \frac{\varepsilon}{k} + \frac{2\nu e^{-C_4 y^+}}{y^2} \right], \quad (5.8)$$

$$S_\phi^c = C_1 \frac{\varepsilon}{k} \nu_t \left(\frac{\partial U_i}{\partial x_j} + \frac{\partial U_j}{\partial x_i} \right) \frac{\partial U_i}{\partial x_j}. \quad (5.9)$$

Boundary conditions: At the pipe inlet, the axial velocity was assigned the bulk value, and the radial velocity was assumed zero. Empirical relationships were used to assign to k and ε ; that is, $k=0.005U_b^2$, and $\varepsilon = C_\mu^{3/4} k^{3/2} / 0.03R$. The pipe section was chosen to be sufficiently long so that fully developed conditions could be assumed to prevail at the outlet, i.e. $\partial\phi / \partial x = 0$, where ϕ can be any of U , V , k , and ε . At the pipe axis, symmetry conditions ($\partial\phi / \partial y = 0$) were assumed for all quantities except for V ($V=0$). At the wall, the value of U , V , k and ε were set to be zero. As to initial conditions, uniform profiles were assumed for all quantities, i.e., $U=U_b$, $V=0$, $k=0.005U_b^2$, $\varepsilon = C_\mu^{3/4} k^{3/2} / 0.03R$.

5.3 Results

Flow with Bulk Reynolds Number of 50,000: Figure 5.1 and Figure 5.2 are color contour plots with shading interpreter for the non-dimensional axial mean velocity U/U_e and the non-dimensional radial velocity V/U_e respectively. The contour plot for the non-dimensional axial mean velocity U/U_e with 30 contour lines in black is plotted in Figure 5.3. The non-dimensional axial velocity profiles at six downstream locations are plotted in Figure 5.4. We can see that the non-dimensional axial velocity profiles at $x/D = 60.9$ and $x/D = 80.5$ are almost identical. The development of the axial velocities in the downstream direction at various locations is shown in Figure 5.5. It can be seen that the centerline peak overshoot position (x/D) is about 24, and the overshoot rate is 1.24. The flow doesn't reach its full-develop stage until about $x/D = 65$. The non-dimensional radial velocity profiles at six downstream locations are plotted in Figure 5.6. The color contour plots with shading interpreter for non-dimensional turbulent kinetic energy, k/u_*^2 , and the non-dimensional Reynolds shear stress, \overline{uv}/u_*^2 , are plotted in Figure 5.7 and Figure 5.8 respectively. The

contour plot for the non-dimensional turbulent kinetic energy, k/u_*^2 , with 25 contour lines in black is plotted in Figure 5.9. Turbulent kinetic energy vs. r/R at six downstream locations are presented in Figure 5.10, whereas the development of turbulent kinetic energy in the downstream direction is presented in Figure 5.11. As for Reynolds shear stress, the contour plot indicates that an undershoot peak can be found at the velocity overshoot peak position. Furthermore, Reynolds shear stress vs. r/R at six downstream locations is presented in Figure 5.12, whereas the development of Reynolds shear stress in the downstream direction is plotted in Figure 5.13. It can be seen that after about $x/D = 10$, the maximum Reynolds stress value shifts $r/R = 0.97$ to $r/R = 0.90$. Finally, turbulent dissipation rates vs r/R at six downstream locations are presented in Figure 5.14.

Flow with Bulk Reynolds Number of 10,000: The simulation results are presented analogously with the simulation results for flow with bulk Reynolds number of 50,000. Figure 5.15 and Figure 5.16 are color contour plots with shading interpreter for the non-dimensional axial mean velocity U/U_e and radial velocity V/U_e respectively. The contour plot for the non-dimensional axial mean velocity U/U_e with 30 contour lines in black is plotted in Figure 5.17. The non-dimensional axial velocity profiles at six downstream locations are plotted in Figure 5.18. We can see that the non-dimensional axial velocity profiles at $x/D = 60.9$ and $x/D = 80.5$ are almost identical. The development of the axial velocities in the downstream direction at various locations is shown in Figure 5.19. It can be seen that the centerline peak overshoot position (x/D) is about 21, and the overshoot rate is 1.32. About at $x/D = 50$, the flow reaches its full-develop state. The non-dimensional radial velocity profiles at six downstream locations are plotted in Figure 5.20. The color contour plots with shading interpreter for non-dimensional turbulent kinetic energy, k/u_*^2 , and the non-dimensional

Reynolds shear stress, \overline{uv}/u_*^2 , are plotted in Figure 5.21 and Figure 5.22 respectively. The contour plot for non-dimensional turbulent kinetic energy, k/u_*^2 , with 25 contour lines in black is plotted in Figure 5.23. Turbulent kinetic energy vs. r/R at six downstream locations are presented in Figure 5.24, whereas the development of turbulent kinetic energy in the downstream direction is presented in Figure 5.25. As for Reynolds shear stress, the contour plot indicates that an undershoot peak can be found at the velocity overshoot peak position again. Furthermore, Reynolds shear stress vs. r/R at six downstream locations is presented in Figure 5.26, whereas the development of Reynolds shear stress in downstream direction is plotted in Figure 5.27. Turbulent dissipation rates vs. r/R at six downstream locations are presented in Figure 5.28. Finally the convergence of the iterations are plotted in Figure 5.29 for both Reynolds numbers, and the optimum “time steps” were selected by trial and error.

5.4 Model Assessment

Since 1982, Chien’s model has become a popular two-equation model. Comparing with Jones-Launder’s model (Jones and Launder, 1972), Chien’s model provides better prediction of the peak turbulent kinetic energy (Chien, 1982). Among seven k - ϵ models, namely those of Chien (1982), Dutoya and Michard (1981), Hassid and Poreh (1978), Hoffmann (1975), Lam and Bremhorst (1981), Launder and Sharma (1974), and Reynolds (1976), it has been found that the best fit to the law of the wall for predicting the flat plate flow is achieved by Chien’s model (Patel, Rodi, and Scheuerer, 1984). It also predicts C_f quite accurately. Table 6.2 lists the skin-friction coefficients obtained by these k - ϵ models for flat plate boundary layer compared with the experimental data of Wieghardt and Tillmann (1951), and they were presented in Patel, Rodi, and Scheuerer’s review paper (1984).

Table 5.1 Skin-friction coefficients comparing with experimental data

	C_f	$\Delta C_f, \%$	$C_f Re_\theta^{1/6}$
Experiment data	0.00243	-	0.012
Launder-Sharma	0.00224	-7.8	0.011
Hassid-Poreh	0.00299	23.0	0.015
Hoffman	0.00219	-9.9	0.011
Dutoya-Michard	0.00214	-11.9	0.010
Chien	0.00246	1.2	0.012
Lam-Bremhorst	0.00263	8.2	0.013

From the above discussion, it is quite obvious that Chien model has remarkable performance. Shih (1990) has compared the simulation results obtained by Chien model with the DNS data for fully developed turbulent channel flow. His results show that except in the center of the channel, Chien's model provides excellent predictions for the axial mean velocity. In the center of the channel, it over-predicts the mean velocity about 6.0%. Overall, the average of the modeling errors for axial mean velocity is estimated as 1.6% (the definition of the modeling error will be given in Chapter 6).

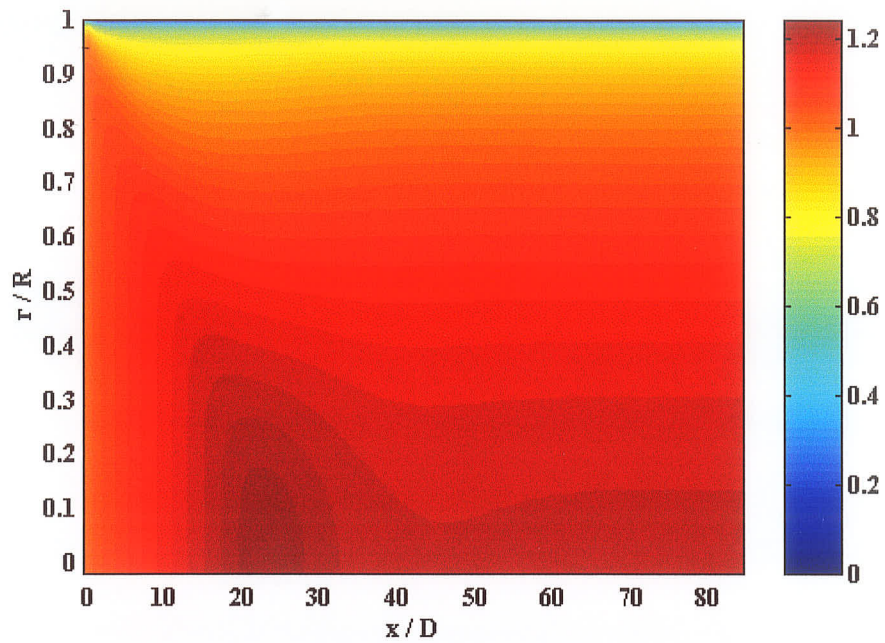


Figure 5.1 Contour plot for the non-dimensional axial velocity for $Re = 50,000$

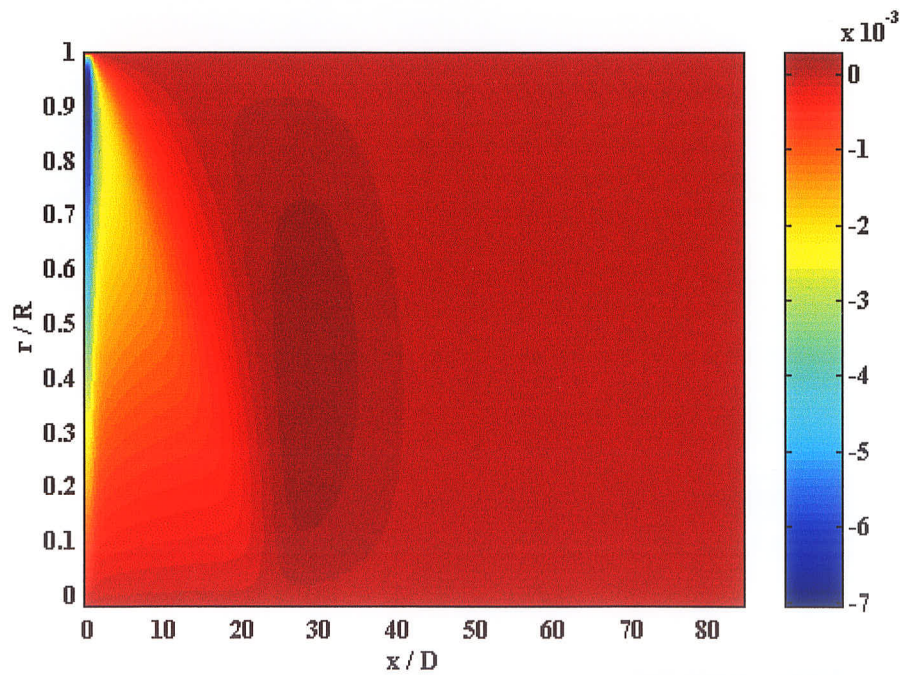


Figure 5.2 Contour plot for the non-dimensional radial velocity for $Re = 50,000$

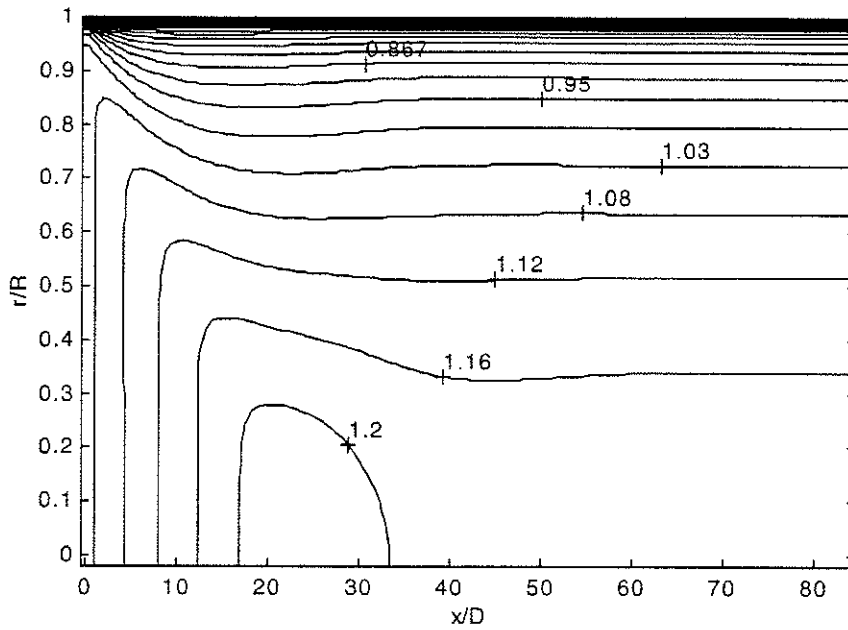


Figure 5.3 Contour plot for non-dimensional axial velocity for $Re=50,000$

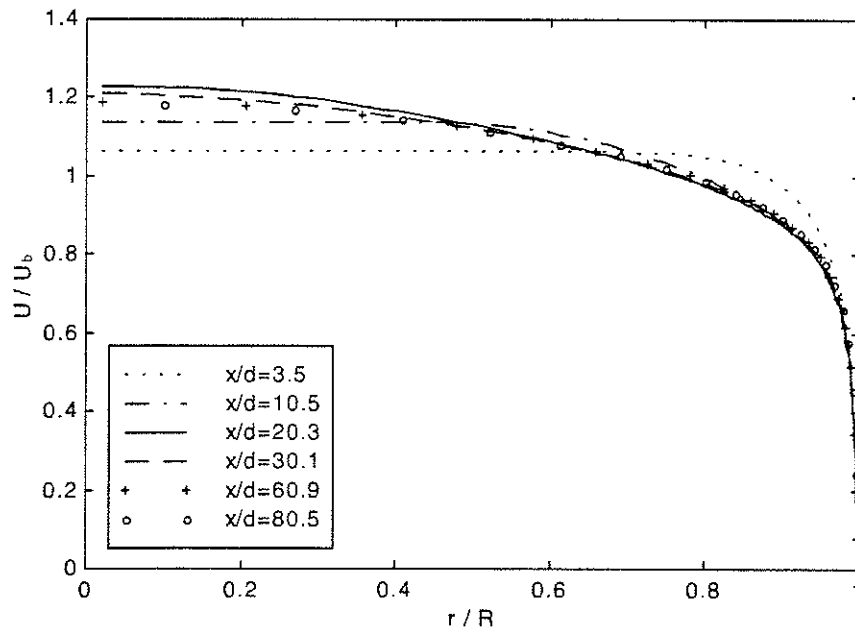


Figure 5.4 Axial velocity vs r/R at six downstream locations for $Re=50,000$

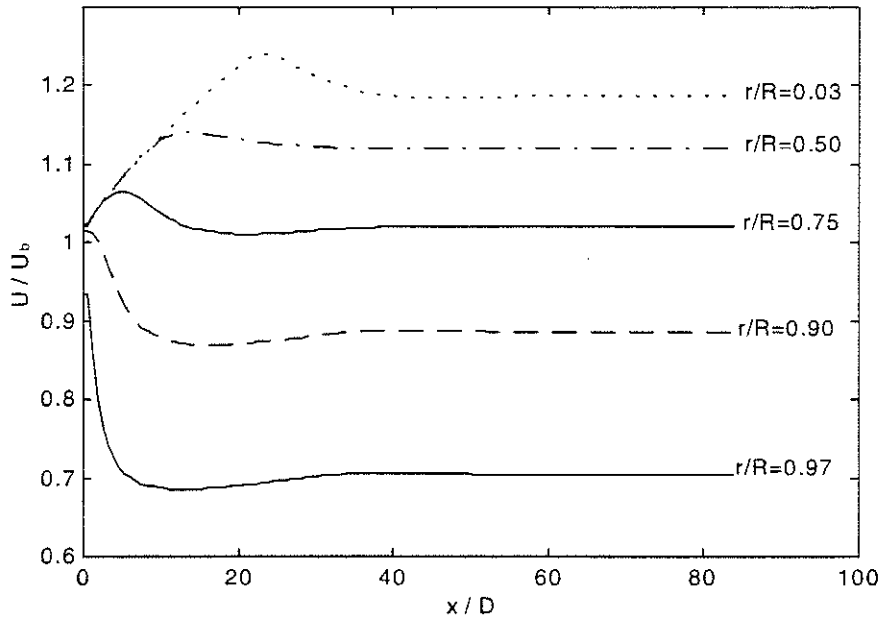


Figure 5.5 Development of axial velocity for $Re=50,000$

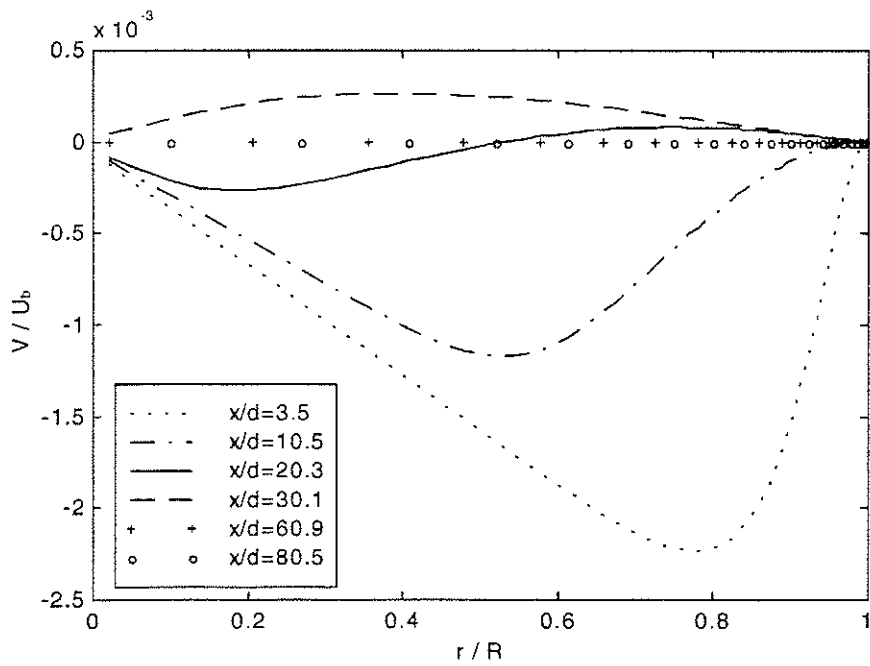


Figure 5.6 Radial velocity vs r/R at six downstream locations for $Re=50,000$

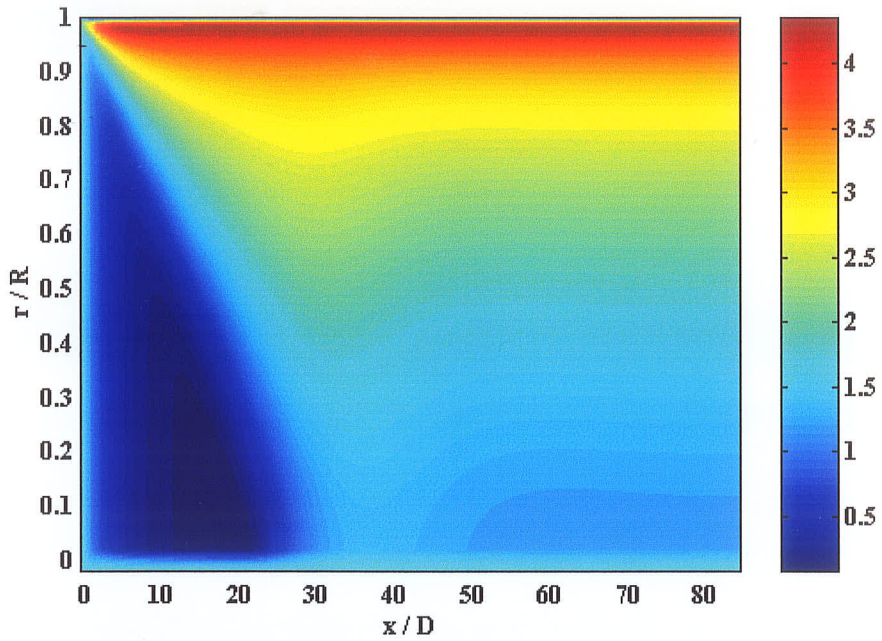


Figure 5.7 Contour plot for non-dimensional Turbulent Kinetic Energy for $Re = 50,000$

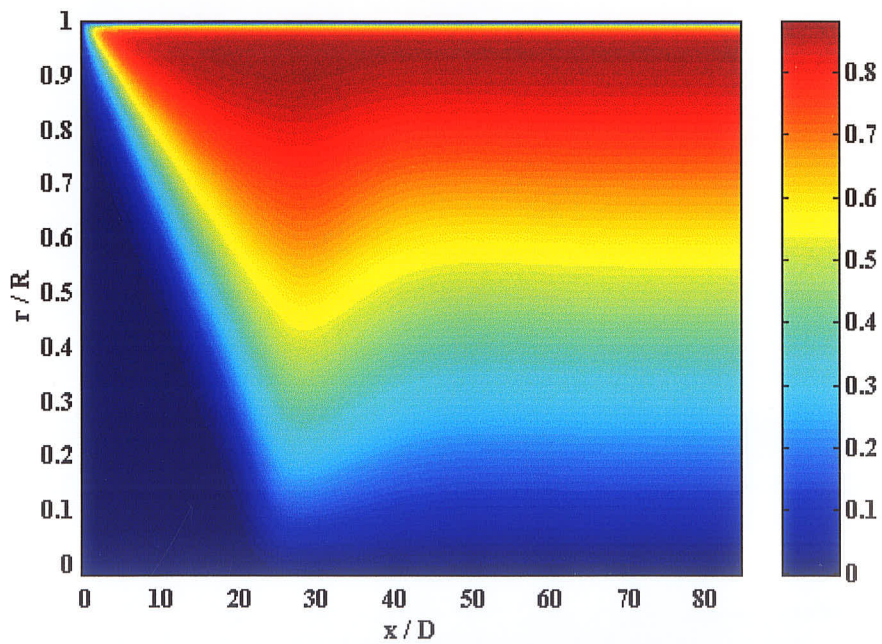


Figure 5.8 Contour plot for Reynolds shear stress for $Re = 50,000$

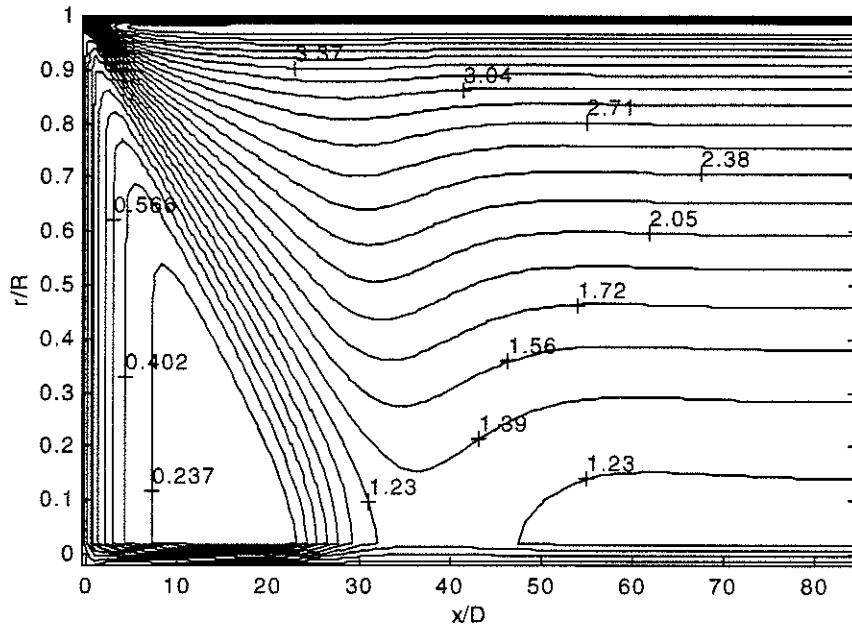


Figure 5.9 Contour plot for non-dimensional turbulent kinetic energy for $Re=50,000$

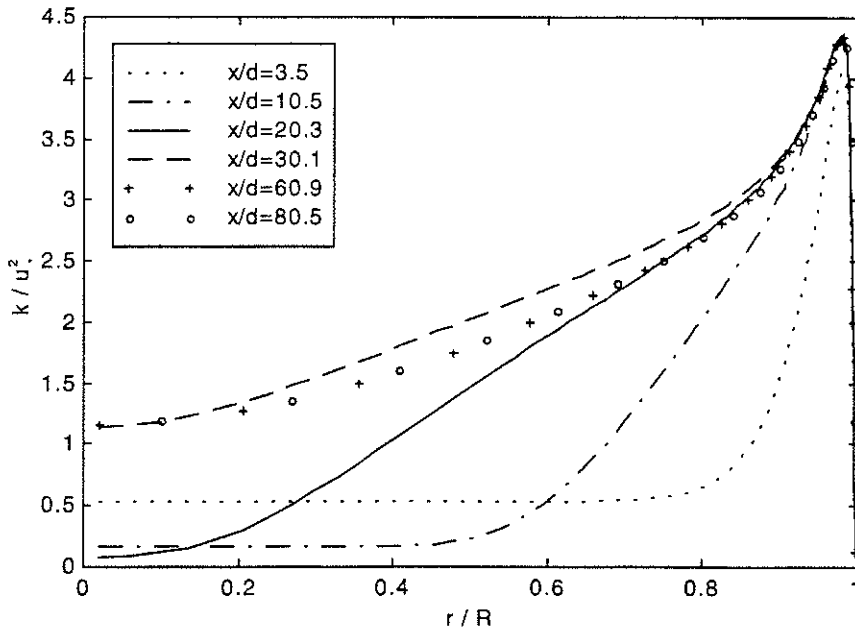


Figure 5.10 Turbulent kinetic energy vs r/R at six downstream locations for $Re=50,000$

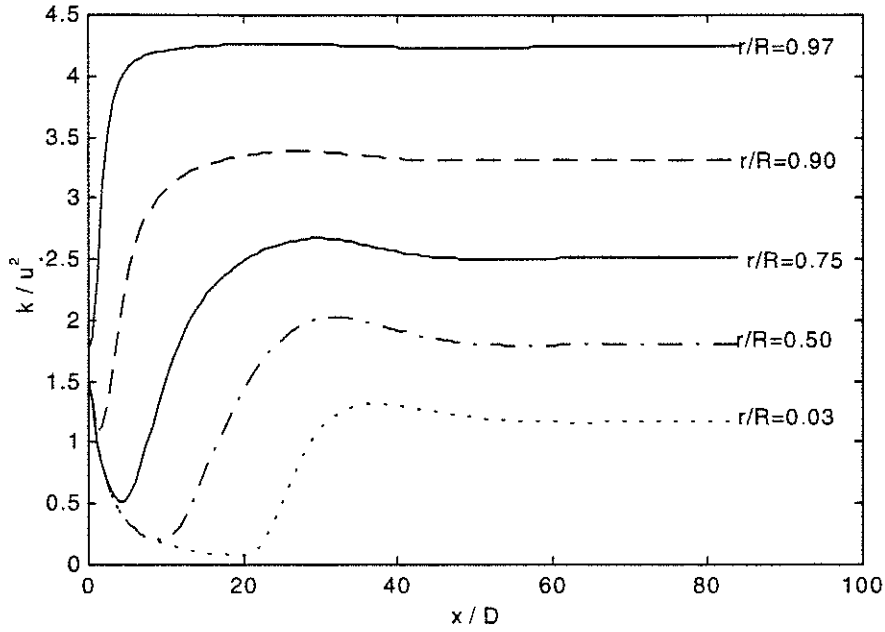


Figure 5.11 Development of turbulent kinetic energy for $Re=50,000$

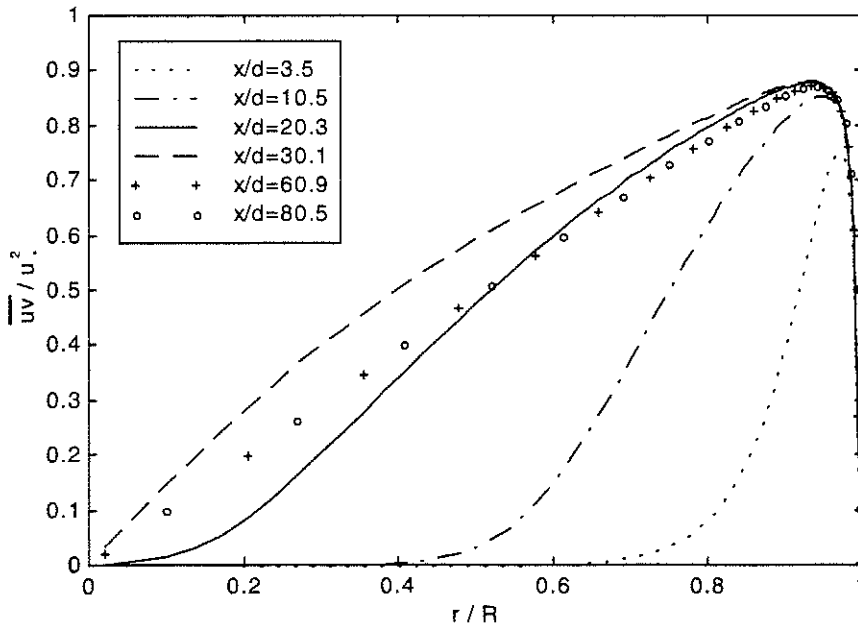


Figure 5.12 Reynolds shear stress vs r/R at six downstream locations for $Re=50,000$

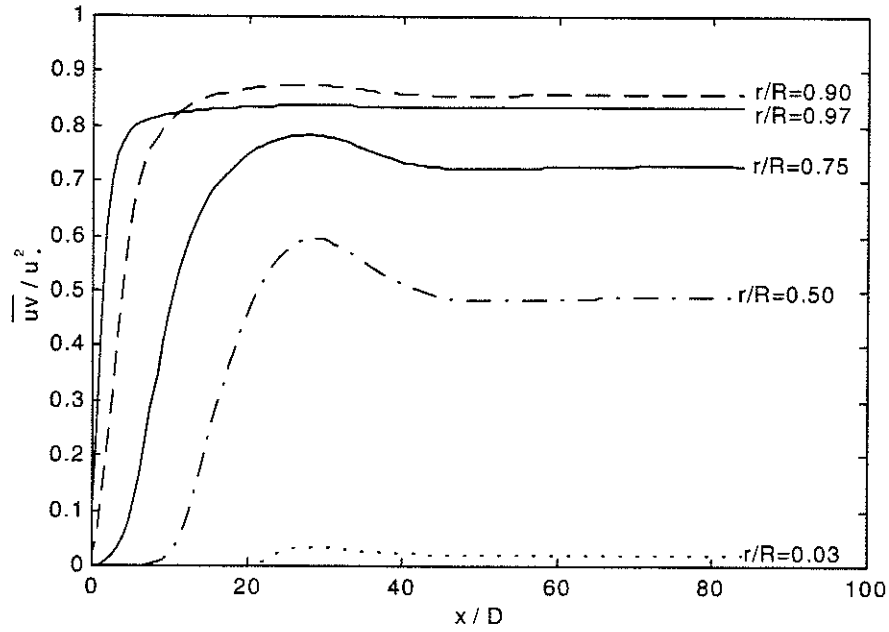


Figure 5.13 Development of Reynolds shear stress for $Re=50,000$

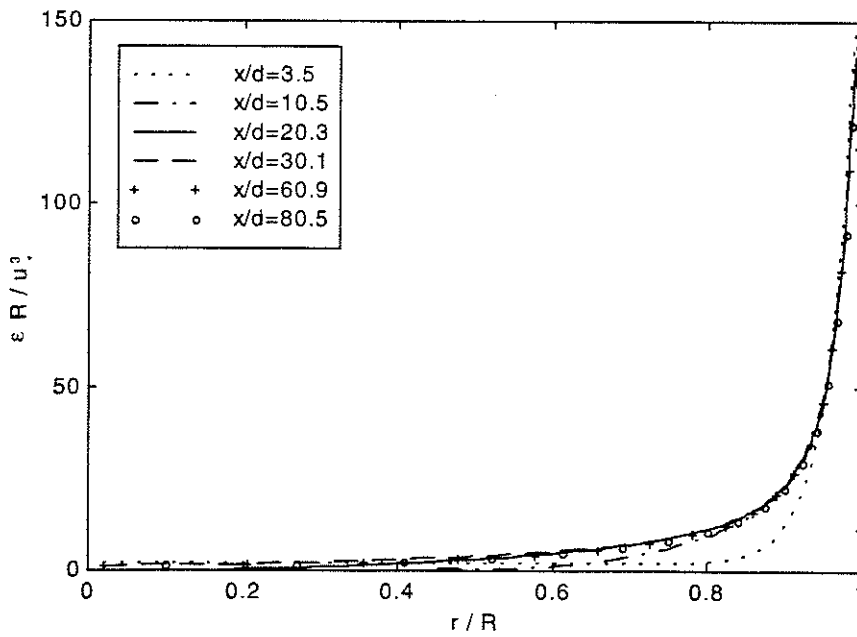


Figure 5.14 Turbulent dissipation rate vs r/R at six downstream locations for $Re=50,000$

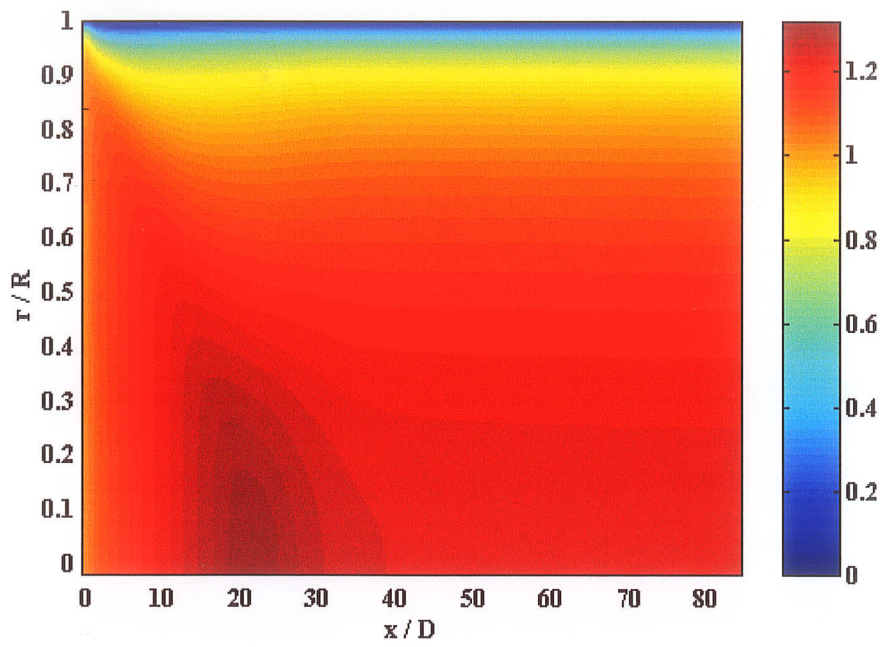


Figure 5.15 Contour plot for the non-dimensional axial velocity for $Re = 10,000$

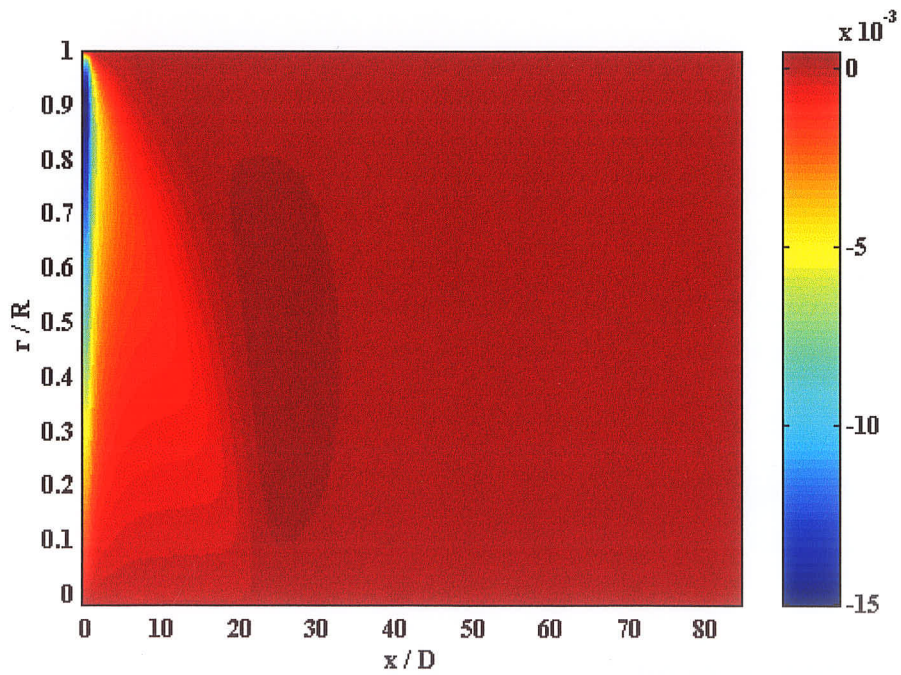


Figure 5.16 Contour plot for the non-dimensional radial velocity for $Re = 10,000$

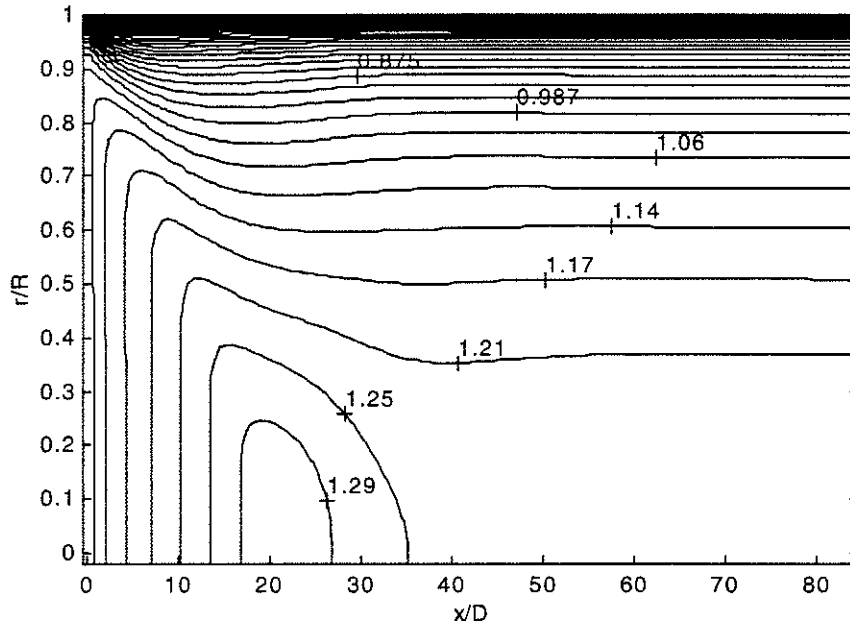


Figure 5.17 Contour plot for non-dimensional axial velocity for $Re=10,000$

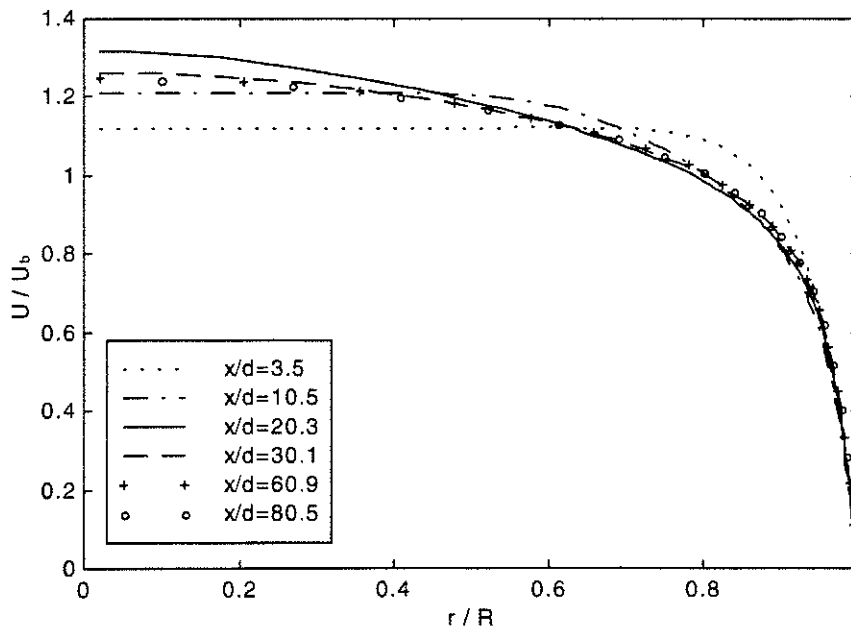


Figure 5.18 Axial velocity vs r/R at six downstream locations for $Re=10,000$

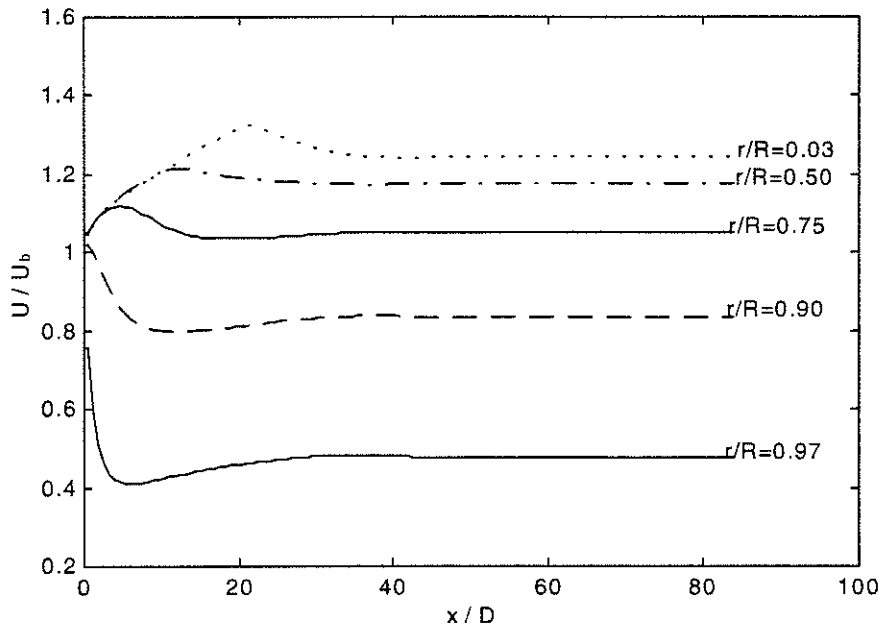


Figure 5.19 Development of axial velocity for $Re=10,000$

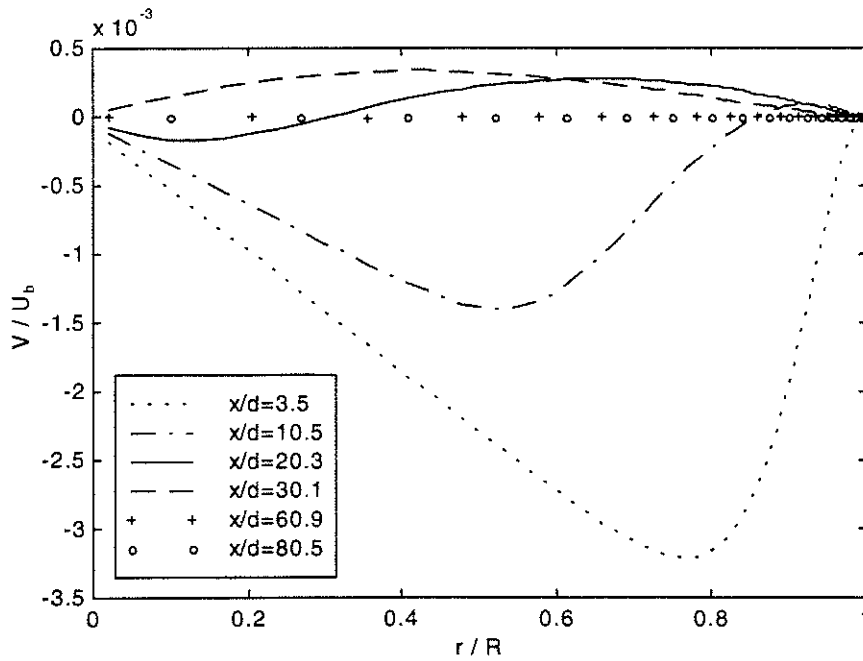


Figure 5.20 Radial velocity vs r/R at six downstream locations for $Re=10,000$

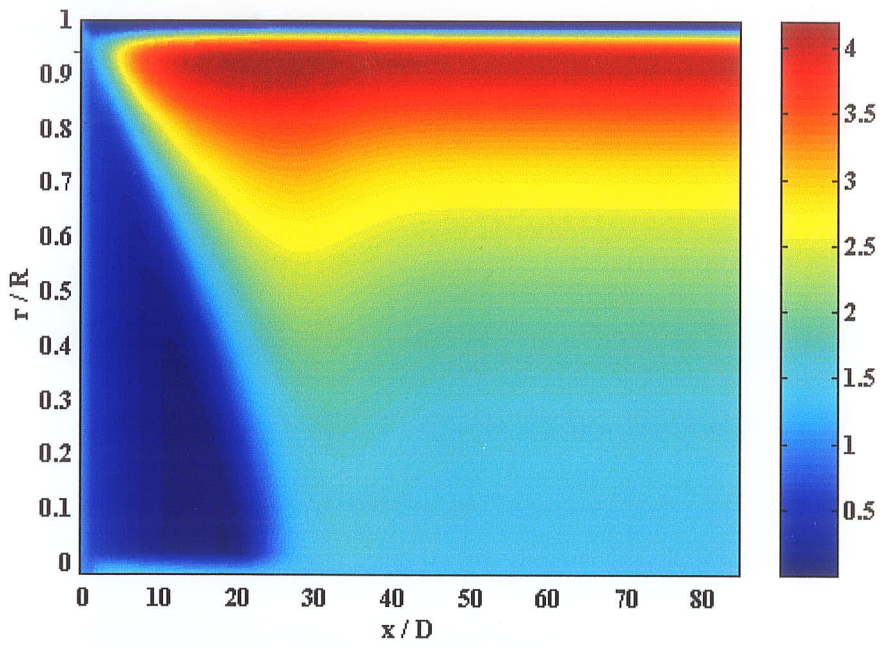


Figure 5.21 Contour plot for non-dimensional Turbulent Kinetic Energy for $Re = 10,000$

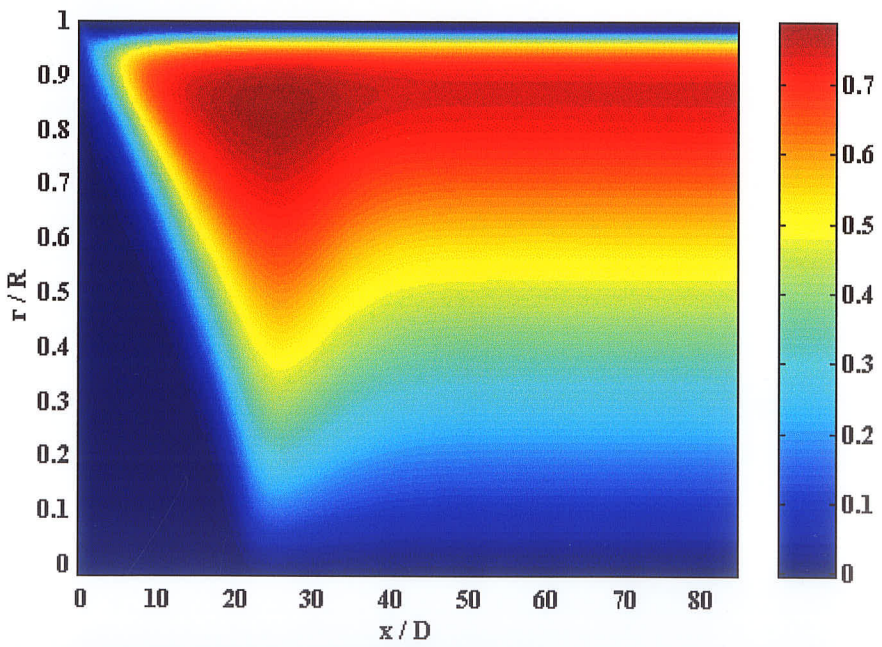


Figure 5.22 Contour plot for Reynolds shear stress for $Re = 10,000$

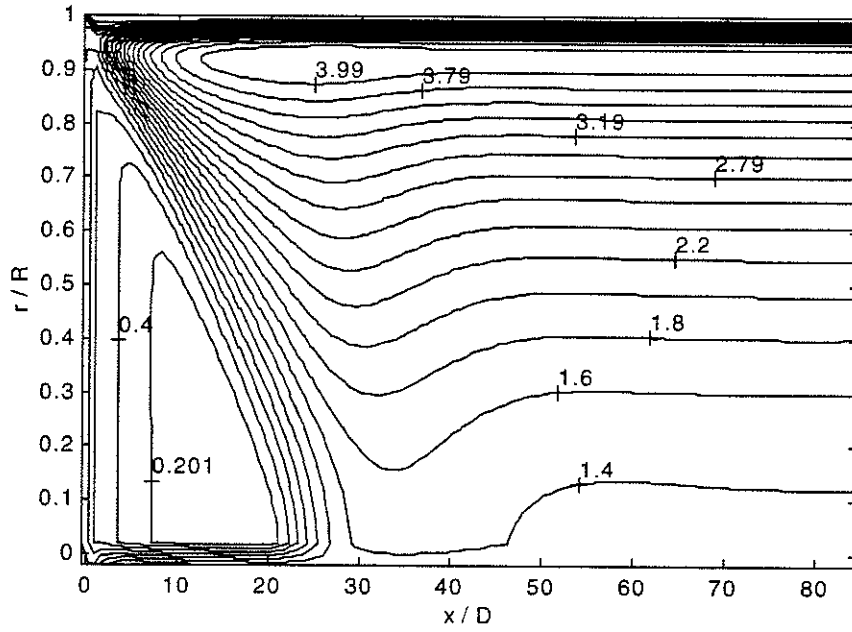


Figure 5.23 Contour plot for non-dimensional turbulent kinetic energy for $Re=10,000$

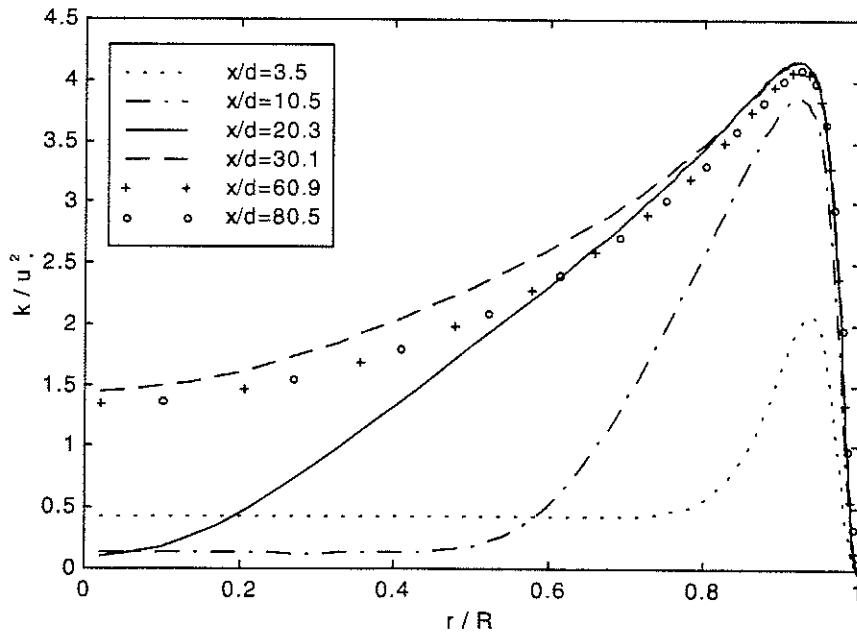


Figure 5.24 Turbulent kinetic energy vs r/R at six downstream locations for $Re=10,000$

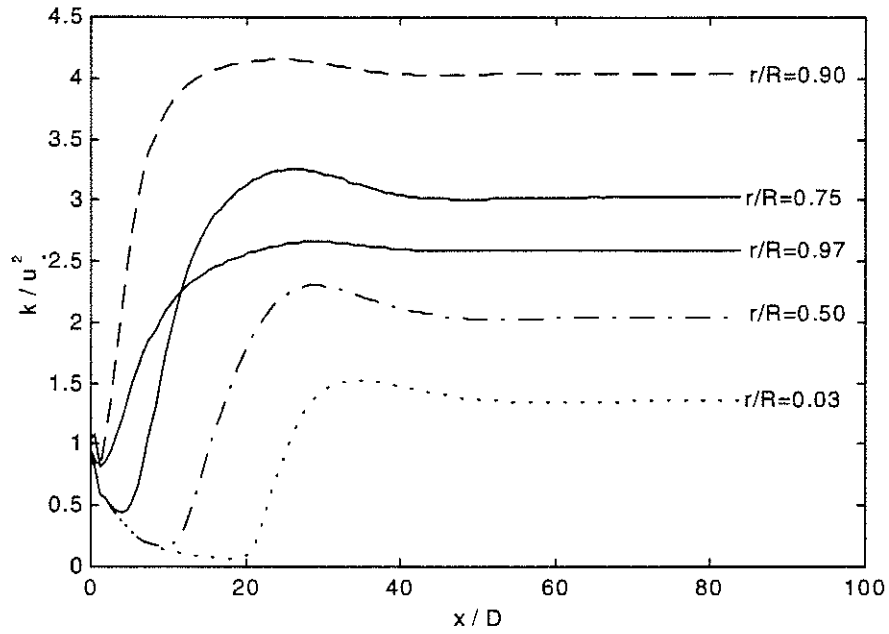


Figure 5.25 Development of turbulent kinetic energy for $Re=10,000$

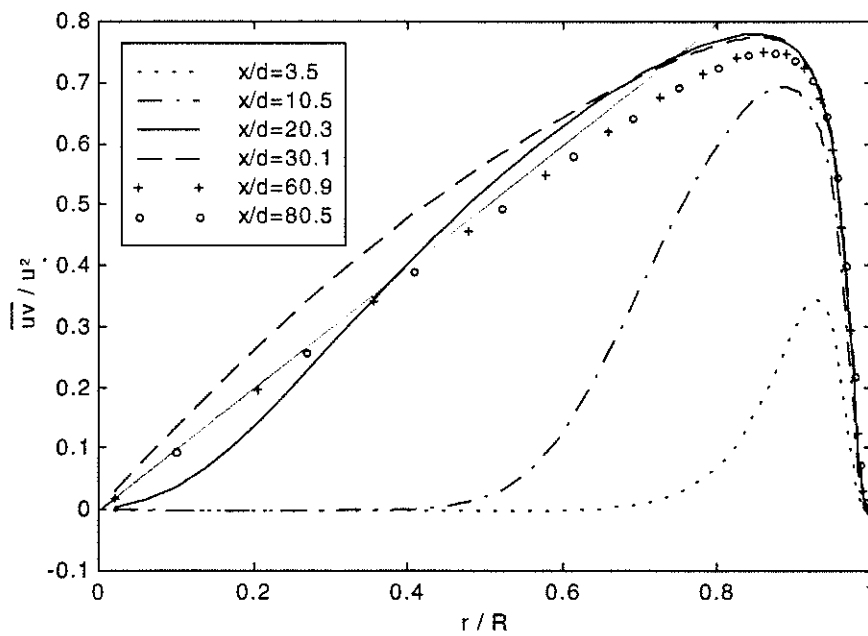


Figure 5.26 Reynolds shear stress vs r/R at six downstream locations for $Re=10,000$

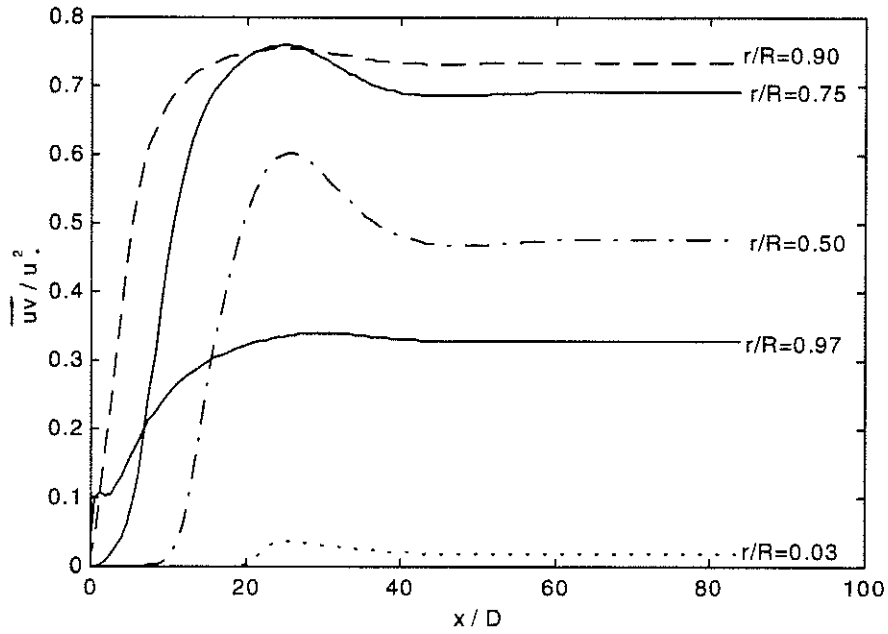


Figure 5.27 Development of Reynolds shear stress for $Re=10,000$

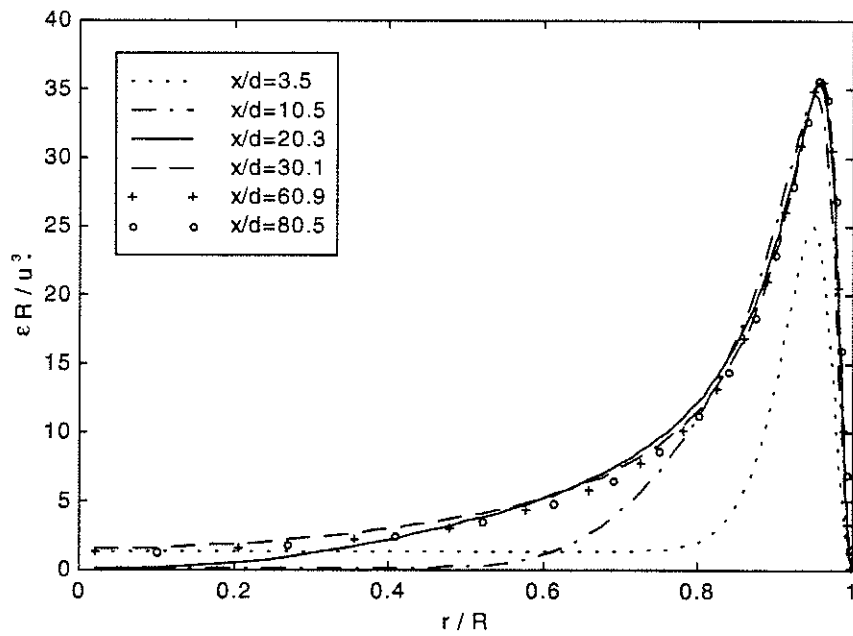


Figure 5.28 Turbulent dissipation rate vs r/R at six downstream locations for $Re=10,000$

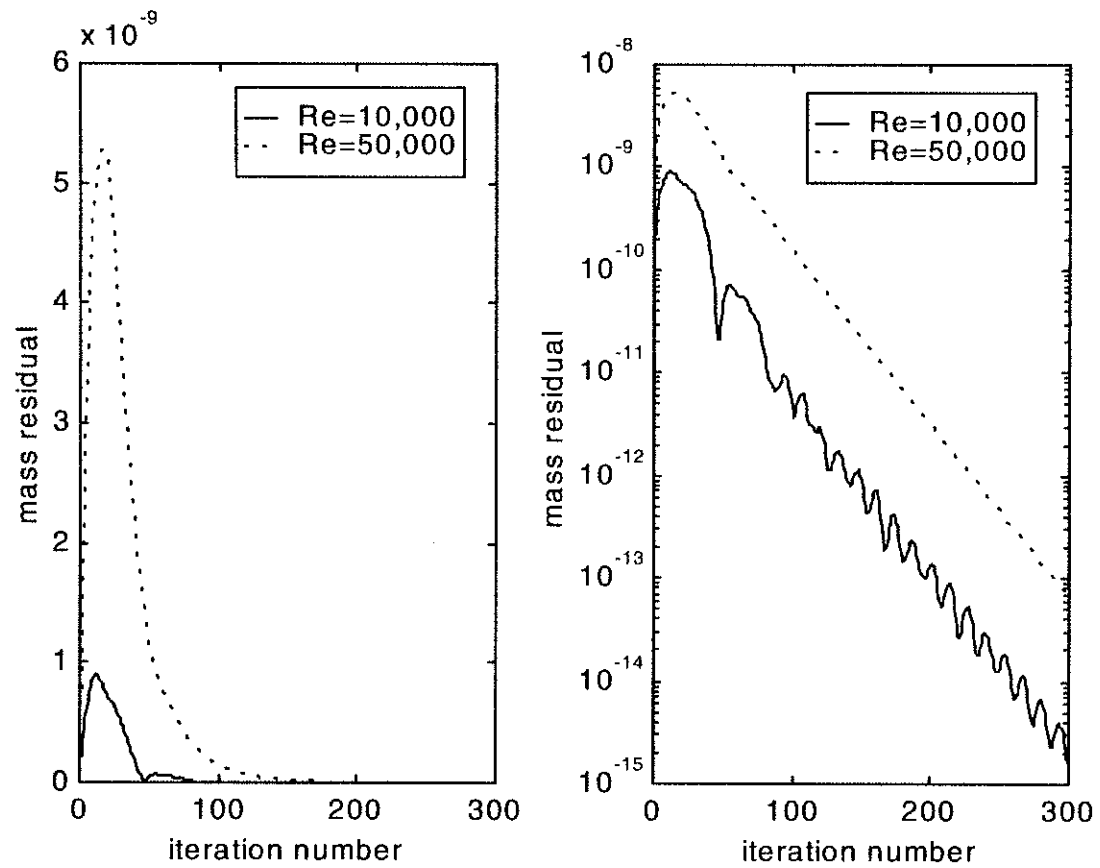


Figure 5.29 Convergence of mass residual

6. Modified k-ε-γ Model

The equations of the modified k-ε-γ model that is proposed by the author are presented in Section 6.1. This is followed by section on numerical considerations in which boundary conditions and source-term linearization are discussed. Seven model constant test results are presented in Section 6.2.3. Then a brief discussion on time evolution of solution is followed. In Section 6.2.5, accuracy analysis is given. Finally, the simulation results for Re=50,000 and Re=200,000 are presented in Section 6.3.

6.1 Model Equations

Because Cho and Chung's k-ε-γ model is based on the standard k-ε model, wall functions are required when modeling wall bounded flows. The requirement of the wall functions limits this model's applicability in complex turbulent flows. In order to eliminate the need for wall functions, a modified k-ε-γ model is proposed in this chapter. In this modified k-ε-γ model, the wall damping functions f_2 and f_μ of Chien's k-ε model are adopted. The equations of this modified k-ε-γ model are as follows.

Eddy viscosity:

$$\nu_t = C_\mu f_\mu \left\{ 1 + C_{\mu B} \frac{k^3}{\varepsilon^2} \gamma^{-m} (1-\gamma) \frac{\partial \gamma}{\partial x_k} \frac{\partial \gamma}{\partial x_k} \right\} \frac{k^2}{\varepsilon} \quad (6.1)$$

where

$$f_\mu = [1 - \exp(-C_3 y^+)]. \quad (6.2)$$

Turbulent kinetic energy:

$$\frac{Dk}{Dt} = \frac{\partial}{\partial x_i} \left(\frac{\nu_i}{\sigma_k} \frac{\partial k}{\partial x_i} \right) + P_k - \varepsilon - \frac{2\nu k}{y^2}. \quad (6.3)$$

Dissipation rate:

$$\frac{D\varepsilon}{Dt} = \frac{\partial}{\partial x_i} \left(\frac{\nu_i}{\sigma_\varepsilon} \frac{\partial \varepsilon}{\partial x_i} \right) + \frac{\varepsilon^2}{k} \left[C_{\varepsilon 1} \frac{P_k}{\varepsilon} - C_{\varepsilon 2} f_2 + C_{\varepsilon 4} \Gamma - \frac{2\nu k e^{-C_4 y^+}}{y^2 \varepsilon} \right]. \quad (6.4)$$

The equations of intermittency factor and P_k are the same as those given in the k - ε - γ model (Eq. 1.25, Eq. 1.28 and Eq. 1.29).

Model constants used in the present tests are given below:

$$\begin{aligned} C_\mu &= 0.09, \quad C_{\mu g} = 0.10, \quad m = 3.0, \quad C_{uv} = 0.33, \quad \sigma_k = 1.0, \quad \sigma_\varepsilon = 1.3, \\ \sigma_g &= 1.0, \quad C_{\varepsilon 1} = 1.35, \quad C_{\varepsilon 2} = 1.8, \quad C_{\varepsilon 4} = 0.1, \quad C_{g1} = 1.6, \quad C_{g2} = 0.15, \\ C_{g3} &= 0.16, \quad C_4 = 0.5, \quad C_3 = 0.0115. \end{aligned}$$

Further discussion on the sensitivity of the predicted values to the choice of some model constants will be given later in this Chapter.

6.2 Numerical Considerations

6.2.1 Boundary Conditions

A uniform profile was assumed for all quantities at the pipe inlet. Except for γ , all other quantities were set the same value as those in Chien's model (see 5.2.2). The entrance values for γ was specified to be very small ($\gamma=0.001$), i.e. the entrance flow was assumed to be irrotational and non-turbulent. The pipe section was chosen to be sufficiently long so that fully developed conditions could be assumed to prevail at the outlet, i.e. $\partial\phi/\partial x = 0$, where ϕ can be any of U , V , k , ε , or γ . At the pipe axis, symmetry conditions ($\partial\phi/\partial y = 0$) were

assumed for all quantities except for V ($V=0$). At the wall, the value of U , V , k and ε were set to be zero while the value of intermittency was set to be unity (because the flow at the wall was assumed to be fully turbulent). As to initial conditions, uniform profiles were assumed for all quantities, i.e., $U=U_b$, $V=0$, $k=0.005U_b^2$, $\varepsilon = C_\mu^{3/4} k^{3/2} / 0.03R$, and $\gamma=0.001$. It should be noted that the pipe inlet conditions for the turbulent quantities are not critical to the simulation results. Tests conducted by Petherick (1981) suggest the effects of the inlet conditions were negligible because they are only observed in the region where $x/D < 2$.

6.2.2 Source-Term Linearization

In the present simulations, the choice of the coefficients of S_ϕ^p and S_ϕ^c for Eq. (1.27)

is:

$$S_\phi^p = -C_{g1}\gamma v_t \left(\frac{\partial U}{\partial r} + \frac{\partial V}{\partial x} \right)^2 / k, \quad (6.5)$$

and

$$S_\phi^c = C_{g1}\gamma \frac{P}{k} + C_{g1}\gamma^2 C_{uv} k \frac{\partial U}{\partial x} + C_{g2} \frac{k^2}{\varepsilon} \left[\left(\frac{\partial \gamma}{\partial x} \right)^2 + \left(\frac{\partial \gamma}{\partial r} \right)^2 \right] - C_{g3}\gamma(1-\gamma) \frac{\varepsilon}{k} \Gamma. \quad (6.6)$$

The choice of the coefficients of S_ϕ^p and S_ϕ^c for Eq. (6.3) is:

$$S_\phi^p = - \left(\frac{\varepsilon}{k} + \frac{2\nu}{y^2} \right), \quad (6.7)$$

and

$$S_\phi^c = P. \quad (6.8)$$

The choice of the coefficients of S_ϕ^p and S_ϕ^c for Eq. (6.4) is:

$$S_\phi^p = - \left[C_{\varepsilon 2} f_2 \frac{\varepsilon}{k} + \frac{2\nu e^{-C_4 y^+}}{y^2} \right], \quad (6.9)$$

and

$$S_{\phi}^c = \frac{\varepsilon^2}{k} \left[C_{\varepsilon 1} \frac{P}{\varepsilon} + C_{\varepsilon 4} \Gamma \right]. \quad (6.10)$$

6.2.3 Model Constant Tests

Seven tests were made for $Re=200,000$ to check the sensitivity of the predicted values to the choice of six model constants. It has been noticed by many researchers that two equation k - ε models over-predict the turbulent kinetic energy near the center of the pipe in the fully developed region. One suggestion provided by Nagano and Tagawa (1988) to cover this common drawback of the k - ε models is to replace $\sigma_k=1.0$ with $\sigma_k=1.4$. The axial mean velocity and the turbulent kinetic energy based on $\sigma_k=1.4$ are shown in Figure 6.1 and Figure 6.2 respectively, compared with the predicted values based on $\sigma_k=1.0$. The analysis shows the

variation of averaged non-dimensional mean velocity $\left(\sum_{i,j}^{N,M} |U_{n1}(i,j) - U_{n2}(i,j)| / (N+M) \right)$,

where U_{n1} and U_{n2} are non-dimensional velocity values of data set one and data set two respectively, and N and M are grid numbers in axial direction and radial directions respectively) is about 1.3%. A 2.6% variation in the maximum Reynolds shear stress, and about a 10% increase in the skin friction in the pipe outlet has been reported. Finally, a 3.9% variation in the averaged peak turbulent kinetic energy values, and about a 25.5% decrease in the pipe core in the fully developed region has been reported. This amount of decrease in the pipe core is desired when we compare the predicted values with the experimental data (see Figure 7.17 and Figure 7.18). However, the increase in the skin friction in the pipe outlet is not desired (see Figure 7.22). Therefore, it is not apparent that choosing $\sigma_k=1.4$ will result in better simulations.

The second model constant test was made by increasing C_3 from 0.0115 to 0.013. The comparison of these two predicted axial mean velocity and the turbulent kinetic energy values are plotted in Figure 6.3 and Figure 6.4. Increasing of C_3 has resulted in about 0.4% variation in averaged non-dimensional mean velocity, and about 2% increase in the skin friction in the pipe outlet region, as well as 3.4% variation in the maximum Reynolds shear stress. Finally, a 0.8% variation in the averaged peak turbulent kinetic energy values, and about 3.5% increase in turbulent kinetic energy in the pipe core in the fully developed region has been reported. In his paper, Chien has reported that a decrease of C_3 from 0.0115 to 0.01 has resulted in about 4% reduction in the skin friction. It seems that our result is inconsistent with Chien's observation that an increase of C_3 will result in an increase in the skin friction. From Figure 6.3 and Figure 6.4, the difference between two predicted data sets could be noticed. However, this small variation does not help in determining which data set is best. Furthermore, at the pipe outlet, the increase in both of skin friction and turbulent kinetic energy in the pipe center is not desired, therefore C_3 should be kept as 0.0115 for further model constant tests.

The value of m employed here is taken from Ramaprian and Chandrasekhara (1985) where it was selected to be 3 by referencing the eddy-viscosity distribution in the intermittent region of a plane jet. The sensitivity of the predicted values to the choice of m has been checked by two tests: a decrease of m from 3 to 2.5 and an increase of m from 3 to 3.5. The test results are presented in Figures 6.5-6.8. A decrease of m has resulted in about 0.03% variation in averaged non-dimensional mean velocity and about 0.1% variation in the maximum Reynolds shear stress as well as a 0.06% variation in the averaged peak turbulent kinetic energy values. Only a 0.4% increase in turbulent kinetic energy in the pipe center in

the fully developed region has been reported, and the predicted skin friction has the same values as before. An increase of m again has resulted in about 0.03% variation in averaged non-dimensional mean velocity and about 0.1% variation in the maximum Reynolds shear stress, but a 0.04% variation in the averaged peak turbulent kinetic energy values. Also only a 0.6% decrease in turbulent kinetic energy in the pipe center in the fully developed region has been reported, and the predicted skin friction has the same values as before. The test results show that the prediction is insensitive to the particular value of m chosen.

The values of $C_{\mu g}$, C_{g3} and $C_{\epsilon 4}$ quoted here are taken from Cho and Chung (1992) which were selected based only on plane jet experiments. The constant $C_{\mu g}$ was determined using experimental data for plane jets (Bradbury, 1965, Gutmark and Wygnanski, 1976) near the region where $\gamma \cong 0.5$, and it turns out to be about 0.10. $C_{\epsilon 4}$ was selected to be 0.1 in order to reproduce the measured spreading rate of the plane jet in Gutmark and Wygnanski (1976), and C_{g3} was selected to be 0.16 by referring to the experimental intermittency factor profile. Due to these three model constants being based on plane jet experiments, it is worthwhile to check how sensitive the predicted results are to their choice. Increasing $C_{\mu g}$ from 0.10 to 0.15 that has resulted in about a 0.02% variation in averaged non-dimensional mean velocity and about a 0.04% variation in the maximum Reynolds shear stress as well as a 0.03% variation in the averaged peak turbulent kinetic energy values. Only a 0.4% increase in turbulent kinetic energy in the pipe center in the fully developed region has been reported, and the predicted skin friction has the same values as before. The test results are presented in Figure 6.9 and Figure 6.10, showing that the two data sets are almost identical.

Increasing C_{g3} from 0.16 to 0.20 that has resulted in about a 0.02% variation in averaged non-dimensional mean velocity and about a 0.07% variation in the maximum

Reynolds shear stress as well as a 0.06% variation in the averaged peak turbulent kinetic energy values. Only a 0.3% decrease in turbulent kinetic energy in the pipe center in the fully developed region has been reported, and the predicted skin friction has the same values as before. The test results are presented in Figure 6.11 and Figure 6.12. It is obvious that the difference between two data sets could be ignored.

Increasing $C_{\epsilon 4}$ from 0.1 to 0.2 that has resulted in about a 0.2% variation in averaged non-dimensional mean velocity and about a 0.3% variation in the maximum Reynolds shear stress as well as a 0.1% variation in the averaged peak turbulent kinetic energy values. A 9.6% increase in turbulent kinetic energy in the pipe center in the fully developed region has been reported, and the predicted skin friction has the same values as before. The test results are presented in Figure 6.13 and Figure 6.14. The difference between two data sets is not significant.

The concluding remark about the model constant test is that except for σ_k , the predicted values are insensitive to the tested model constants. It is reasonable to keep their values as listed in Section 6.1. As to model constant σ_k , using $\sigma_k = 1.4$ does improve the prediction for the turbulent kinetic energy in the pipe center region; but at the same time, because it increases the skin friction values in the outlet region, further tests are required to decide which value is best.

6.2.4 Time Evolution of Solution

As discussed in Section 3.2, the solution of a steady-state problem was obtained through the using of the discretization equations for a corresponding unsteady situation. Therefore, a “time step” was involved in the calculation. A demonstration of the time

evolution of solution towards the steady state is presented in Figure 6.15 and Figure 6.16, from time $t=0.02$ to time $t=0.4$. The “time step” Δt was selected to be 0.002. From Figure 6.15, we can see that the velocity distributions exhibited strongly damped oscillations from $t=0.1$ to somewhat less than 0.4, and it converged to its steady state distributions after $t=0.4$. From Figure 6.16, it can be seen that at $t=0.2$, the turbulent intermittency factor almost already reached its steady state distribution, so it developed fast than the axial mean velocity.

6.2.5 Accuracy Analysis

Numerical solutions are only approximate solutions that normally include three kinds of errors: modeling errors, discretization errors, and convergence errors.

Modeling Error: “Modeling errors, which are defined as the difference between the actual flow and the exact solution of the mathematical model” (Ferziger and Peric, 1996).

We will assume DNS (Direct Numerical Simulation) has no modeling error in what follows. It is very difficult to calculate the exact values of modeling error. Normally we evaluate them by comparing solutions in which the discretization and convergence errors are negligible with accurate experimental data or with data obtained by more accurate models (e.g. data from Direct Numeric Simulation). Insufficient data is available to evaluate the modeling error of the present model in detail. However, comments on the modeling error for two-equation models will be helpful, as we believe that the modeling error of present model will be similar to the two-equations’, especial to Chien model’s. For fully developed turbulent pipe flow at $Re_c \approx 7,000$ (based on centerline velocity and pipe diameter), a comparison between direct numerical simulation and experiment has been made by Eggels etc. (1994). Examining analysis results, we can get a roughly ideal about the accuracy of a

numerical solution without modeling errors. For the hot-wire anemometry measurements, the accuracy of the mean velocity measurement ranged from 1% at the pipe centerline to about 4% very close to the wall. A precision micro-manometer was used to measure the pressure drop along the test section from which the friction velocity was determined with an accuracy of 1.5%. For the laser Doppler anemometry measurements, the estimated statistical sampling errors for the measured velocities were about 0.3% for the mean and 1-2% for the r.m.s. The results of this comparison are listed in Table 6.1.

Table 6.1 Mean flow properties obtained from numerical simulations and experiments by Eggels etc.

	DNS(E)	ERROR (LDA)%	ERROR (HWA)%	DNS(U)	ERROR (LDA)%	ERROR (HWA)%	LDA	HWA
U_c/u_τ	19.31	-0.41	-0.46	19.29	-0.51	-0.56	19.39	19.40
U_b/u_τ	14.73	0.34	-0.20	14.74	0.41	-0.14	14.68	14.76
U_c/U_b	1.31	-0.76	0.00	1.31	-0.76	0.00	1.32	1.31
$C_f \times 10^3$	9.22	-0.65	0.44	9.21	-0.75	0.33	9.28	9.18

Where the DNS performed by Eggles and Nieuwstadt is referred to as DNS(E), and the DNS performed by Unger and Friedrich is referred to as DNS(U). The laser Doppler anemometry is abbreviated as LDA, and hot-wire anemometry is abbreviated as HWA. Because experimental data themselves including errors, so it is hard to estimated the DNS solution errors. But we can obtain an approximate range. For the axial mean velocity, the DNS solution error may be as large as 4.5%. In Chapter 5, we already discussed the modeling error of Chien's model. For axial mean velocity, its modeling error is estimated as 1.6%. This

value could be used as an estimation of modeling errors for axial mean velocity for present k- ϵ - γ model, and we can see that it is reasonably small comparing with other kind of numerical errors.

Discretization Errors: “Discretization Errors are defined as the difference between the exact solution of the conservation equations and the exact solution of the algebraic system of equations obtained by discretizing these equations” (Ferziger and Peric, 1996).

The discretized equations represent truncated approximations to the differential equation, and the exact solution of the differential equation does not satisfy the difference equation. The imbalance, which is due to the truncation of the Taylor series, is called truncation error. For sufficiently fine grids, the truncation error and therefore the discretization error, is proportional to the leading term in the Taylor series:

$$\varepsilon_h^d \approx \alpha h^p + H \quad (6.11)$$

where ε_h^d is discretization error on grid h , H stands for higher order terms and α depends on the derivatives at the given point but is independent of h . The discretization error can be estimated from the difference between solutions obtained on systematically refined (or coarsened) grids. First, define Φ is the exact solution of the differential equation, and ϕ_h is the exact solution of the discretized equations on grid h , then we have:

$$\Phi = \phi_h + \varepsilon_h^d = \phi_h + \alpha h^p + H = \phi_{2h} + \alpha(2h)^p + H. \quad (6.12)$$

The exponent p , which is the order of the scheme, may be estimated as follows:

$$p = \frac{\log\left(\frac{\phi_{2h} - \phi_{4h}}{\phi_h - \phi_{2h}}\right)}{\log 2}. \quad (6.13)$$

From Eq. (6.12), we also have:

$$\alpha h^p = \frac{\phi_h - \phi_{2h}}{2^p - 1}. \quad (6.14)$$

If we ignore higher order terms (H) in Eq. (6.11), we obtain the equations for estimating the discretization error as follows:

$$\varepsilon_h^p = \frac{\phi_h - \phi_{2h}}{2^p - 1}. \quad (6.15)$$

If the ratio of the grid sizes on successive grids is not two, the factor 2 in the Eq. (6.13) - Eq.(6.15) needs to be replaced by that ratio (Roache, 1994). The analysis of discretization errors for the present model for Re=200,000 is presented in Table 6.3. Calculations were carried out in three grid systems: 120 x 99, 180 x 149, and 240 x 198. Eq. (6.15) is used for discretization error estimating, with an approximate ratio factor of 1.5 instead of ratio factor of 2. Twenty points were selected from $x/D=6.286$ to 73.806 , four downstream locations, with five points at each location. For the non-dimensional axial mean velocity, the averaged discretization error, ε_h^d , is approximately -0.0010 . The data listed in Table 6.2 proves the grid independence. Also simulation results obtained by finer grids (240 x 198) and courser grids (120 x 99) for Re=200,000 are plotted in Figure 6.17.

Table 6.2 Analysis of discretization errors

x/D	r/R	$(U/U_b)_h$	$(U/U_b)_{1.5h}$	$(U/U_b)_{2h}$	p	ε_h^d	$ \varepsilon_h^d , \%$	$ \varepsilon_h^d U_b$
6.286	0.102	1.0755	1.0773	1.0852	3.6479	-0.0005	0.0531	0.0155
6.286	0.341	1.0754	1.0768	1.0840	4.0388	-0.0003	0.0338	0.0099
6.286	0.742	1.0472	1.0480	1.0472	0.0000	0.0000	0.0000	0.0000
6.286	0.932	0.8782	0.8774	0.8650	6.7597	0.0001	0.0055	0.0016
6.286	0.988	0.6665	0.6621	0.6414	3.8191	0.0012	0.1188	0.0347
22.584	0.102	1.1774	1.1777	1.1904	9.2377	0.0000	0.0007	0.0002
22.584	0.341	1.1548	1.1526	1.1579	2.1685	0.0016	0.1561	0.0456
22.584	0.742	1.0085	1.0113	1.0074	0.8172	-0.0071	0.7127	0.2081
22.584	0.932	0.8393	0.8398	0.8290	7.5782	0.0000	0.0024	0.0007
22.584	0.988	0.6488	0.6455	0.6271	4.2382	0.0007	0.0721	0.0211
45.867	0.102	1.1626	1.1618	1.1717	6.2044	0.0001	0.0070	0.0021
45.867	0.341	1.1402	1.1378	1.1437	2.2184	0.0016	0.1646	0.0481
45.867	0.742	1.0134	1.0158	1.0129	0.4667	-0.0115	1.1520	0.3364
45.867	0.932	0.8495	0.8497	0.8383	9.9714	0.0000	0.0004	0.0001
45.867	0.988	0.6574	0.6538	0.6343	4.1668	0.0008	0.0815	0.0238
73.806	0.102	1.1653	1.1644	1.1747	6.0116	0.0001	0.0086	0.0025
73.806	0.341	1.1421	1.1396	1.1455	2.1177	0.0018	0.1838	0.0537
73.806	0.742	1.0128	1.0152	1.0122	0.5503	-0.0096	0.9600	0.2803
73.806	0.932	0.8482	0.8483	0.8372	11.6151	0.0000	0.0001	0.0000
73.806	0.988	0.6562	0.6525	0.6335	4.0351	0.0009	0.0895	0.0261
					Average:	-0.0010	0.1901	0.0555

Convergence errors: “Convergence error are defined as the difference between the iterative and exact solutions of the algebraic equations systems” (Ferziger and Peric, 1994).

Errors due to iterative solution and round off are easier to control. As a detail discussion about the convergence of the iterations is given in Chapter 3, only summarized conclusions for present tests will be given here. As shown in Chapter 3 reduction of the residual is accompanied by reduction of the convergence error, so we can use the reduction of the residual as a stopping criterion for the iterations. The results of the convergence of the iteration test for $Re=50,000$ and $Re=200,000$ are presented in Figure 6.18 and Figure 6.19 respectively. Both figures show that the two data sets are almost identical. For $Re=200,000$, the standard deviation of the axial mean velocity between the two data sets at eight downstream locations were calculated, and are given in Table 6.3.

Table 6.3 The standard deviation for axial mean velocity

x/D	4.63	11.77	18.90	26.03	33.17	54.56	68.83	83.10
STD.	0.0212	0.0213	0.0201	0.0194	0.0196	0.0203	0.0201	0.0201

Finally, the convergence of the mass residual for $Re=50,000$ and $Re=200,000$ is plotted in Figure 6.20.

6.3 Results

Flow with Bulk Reynolds Number of 50,000: Figure 6.21 and Figure 6.22 are contour plots with color interpreter for the non-dimensional axial mean velocity U/U_b and radial mean velocity V/U_b respectively. The contour plot with 30 contour lines in black for the non-dimensional axial mean velocity U/U_b is plotted in Figure 6.23. The non-dimensional axial velocity profiles at six downstream locations are plotted in Figure 6.24. We can see that the

non-dimensional axial velocity profiles at $x/D = 60.9$ and $x/D = 80.5$ are almost identical. The development of the axial velocities in the downstream direction at various locations is shown in Figure 6.25. It can be seen that the flow reach its full-develop stage at about $x/D = 55$. The centerline peak overshoot position (x/D) is about 21.6, and the overshoot ratio is 1.24. The non-dimensional radial velocity profiles at six downstream locations are plotted in Figure 6.26. The contour plots of the non-dimensional turbulent kinetic energy, k/u_*^2 , and the non-dimensional Reynolds shear stress, \overline{uv}/u_*^2 , are plotted with color interpreter in Figure 6.27 and Figure 6.28 respectively. The contour plot of the non-dimensional turbulent kinetic energy, k/u_*^2 , with 25 contour lines in black is plotted in Figure 6.29. Turbulent kinetic energy vs. r/R at six downstream locations are presented in Figure 6.30, whereas the development of the turbulent kinetic energy in downstream direction is presented in Figure 6.31. Reynolds shear stress vs. r/R at six downstream locations is presented in Figure 6.32. The development of Reynolds shear stress in the downstream direction is plotted in Figure 6.33. It can be seen that after about $x/D = 10$, the maximum Reynolds stress value is not located at $r/R = 0.97$, but at $r/R = 0.90$. The turbulent dissipation rate vs. r/R at six downstream locations is presented in Figure 6.34. The contour plots for intermittency factor and pressure are plotted with color interpreter in Figure 6.35 and Figure 6.36. In the entrance region, there is an approximately triangular non-turbulent region where the intermittency factor value is less than 0.05. Then there is a narrow highly intermittent region where the intermittency factor value is larger than 0.05 and smaller then 0.95. In the wall region, the flow almost immediately reaches its approximately fully turbulent state ($\gamma > 0.95$). While at the pipe centerline, only after $x/D = 22$ does the flow reach its approximately fully turbulent

state. The contour plot for pressure (see Figure 6.36) indicates that in all the places, $\partial p / \partial y$ is almost zero. Therefore, we could say the pipe flow is a horizontal flow. In fact, the maximum radial velocity magnitude is less than 0.2% of the maximum axial velocity magnitude. It is obvious that the pressure decreases as the flow develops. All these observations are consistent with the previously findings of Richman and Azad (1973). Finally, the intermittency factor vs. r/R at eight downstream positions is plotted in Figure 6.37.

Flow with Bulk Reynolds Number of 200,000: The simulation results are presented analogously with the simulation results for flow with bulk Reynolds number of 50,000. Figure 6.38 and Figure 6.39 are contour plots with color interpreter for the non-dimensional axial mean velocity U/U_b and radial mean velocity V/U_b . The contour plot with 30 contour lines in black for the non-dimensional axial mean velocity U/U_b is plotted in Figure 6.40. The non-dimensional axial velocity profiles at six downstream locations are plotted in Figure 6.41. We can see that the non-dimensional axial velocity profiles at $x/D = 60.9$ and $x/D = 80.5$ are almost identical. The development of the axial velocities in the downstream direction at various locations is shown in Figure 6.42. The centerline peak overshoot position (x/D) is about 24, and the overshoot ratio is 1.19. It can be seen that the flow doesn't reach its full-developed state until $x/D = 70$. The non-dimensional radial velocity profiles at six downstream locations are plotted in Figure 6.43. The contour plots of non-dimensional turbulent kinetic energy, k/u_*^2 , and the non-dimensional Reynolds shear stress, \overline{uv}/u_*^2 , are plotted with color interpreter in Figure 6.44 and Figure 6.45 respectively. The contour plot of non-dimensional turbulent kinetic energy, k/u_*^2 , with 25 contour lines in black is plotted in Figure 6.46. Turbulent kinetic energy vs. r/R at six downstream locations are presented in Figure 6.47, whereas the development of turbulent kinetic energy in the downstream direction

is presented in Figure 6.48. As for Reynolds shear stress, an undershoot peak can be found at the velocity overshoot peak position again from its contour plot. Furthermore, Reynolds shear stress vs. r/R at six downstream locations is presented in Figure 6.49, whereas the development of Reynolds shear stress in the downstream direction is plotted in Figure 6.50. The turbulent dissipation rate vs r/R at six downstream locations are presented in Figure 6.51. The contour plots for intermittency factor and pressure are presented in Figure 6.52 and Figure 6.53 respectively. Comparing Figure 6.52 with Figure 6.35, it is found that the approximately non-turbulent triangle region ($\gamma < 0.05$) increased slightly, whereas the highly intermittent region increased remarkably. In the wall region, again almost immediately the flow reaches its approximately fully turbulent while on the pipe centerline the flow reached its approximately fully turbulent state after $x/D = 60$. In the pressure contour plot, it is obvious that in all the places, $\partial p / \partial y$ is almost zero again, the same as that of Figure 6.36, but the values are more than ten time of that in Figure 6.36. Finally, the intermittency factor vs. r/R at eight downstream positions is plotted in Figure 6.54.

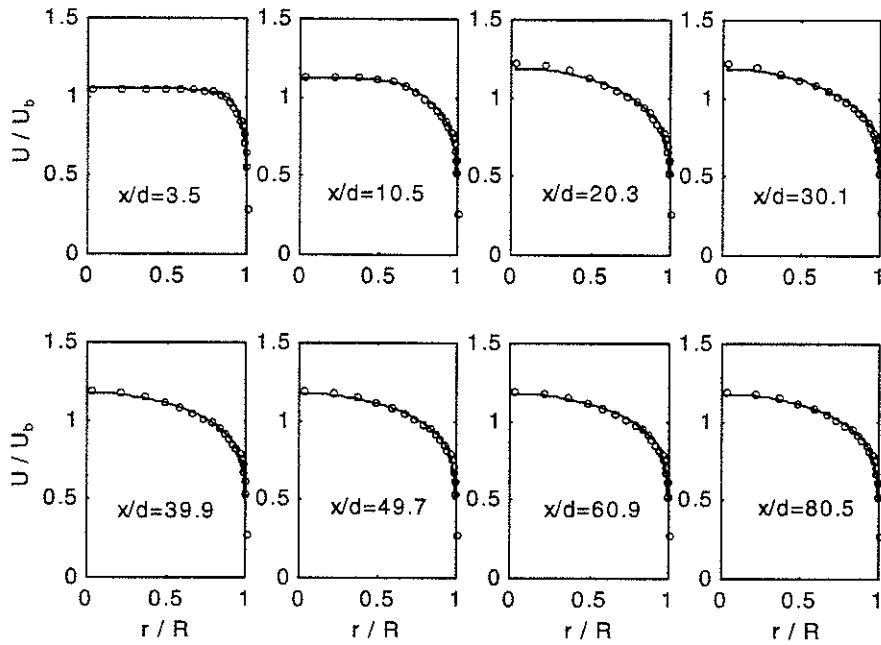


Figure 6.1 Model constant test 1 (the solid lines represent the simulation results obtained for $\sigma_k = 1.0$, and the open circles represent the simulation results obtained for $\sigma_k = 1.4$)

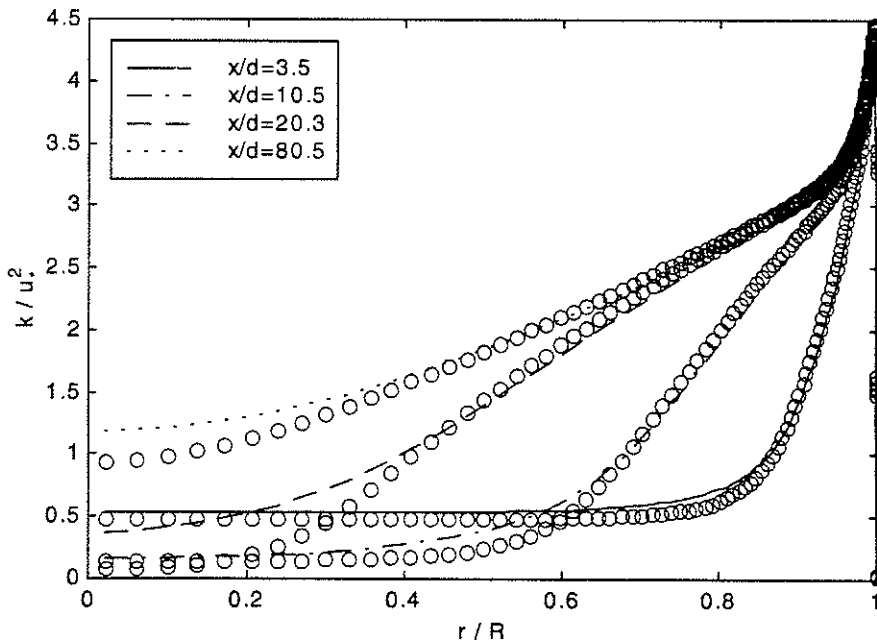


Figure 6.2 Turbulent kinetic energy distribution for model constant test 1 (the lines represent the simulation results obtained for $\sigma_k = 1.0$, and the open circles represent the simulation results obtained for $\sigma_k = 1.4$)

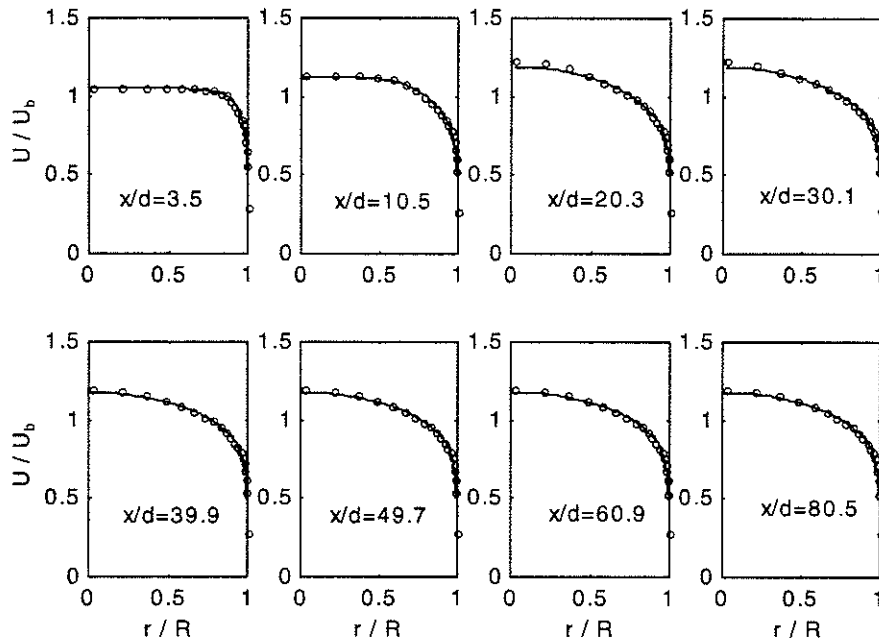


Figure 6.3 Model constant test 2 (the solid lines represent the simulation results obtained for $C_c = 0.0115$, and the open circles represent the simulation results obtained for $C_c = 0.013$)

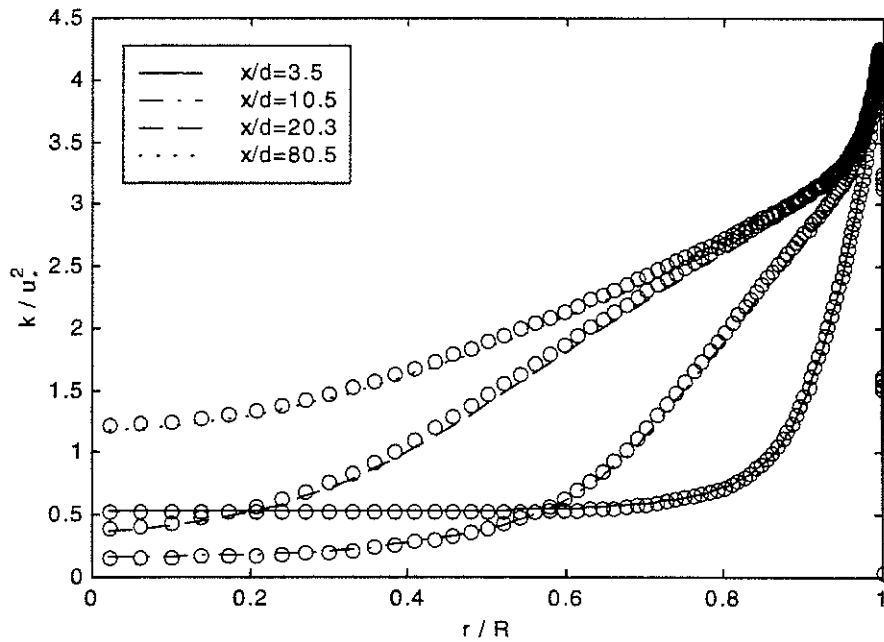


Figure 6.4 Turbulent kinetic energy distribution for model constant test 2 (the lines represent the simulation results obtained for $C_c = 0.0115$, and the open circles represent the simulation results obtained for $C_c = 0.013$)

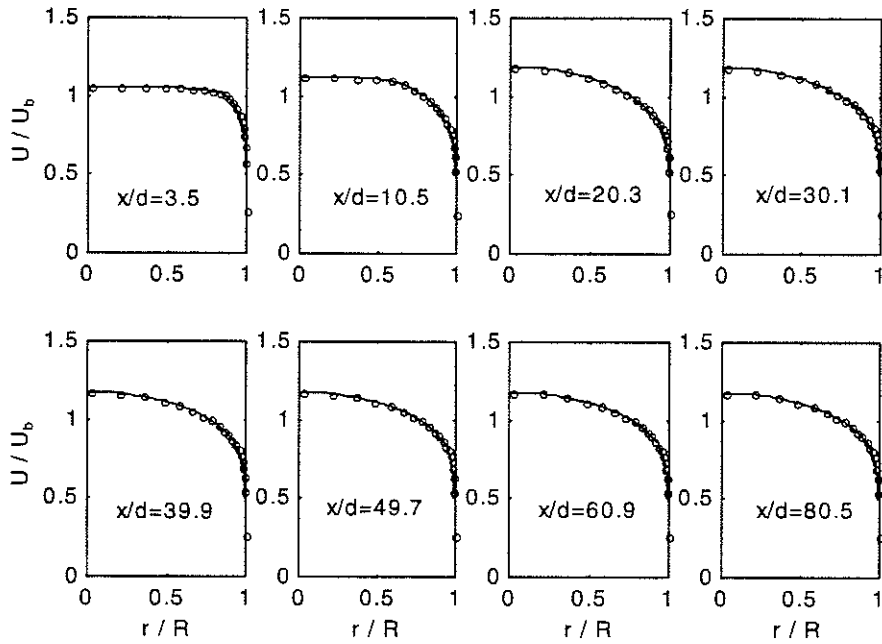


Figure 6.5 Model constant test 3 (the solid lines represent the simulation results obtained for $m = 3$, and the open circles represent the simulation results obtained for $m = 2.5$)

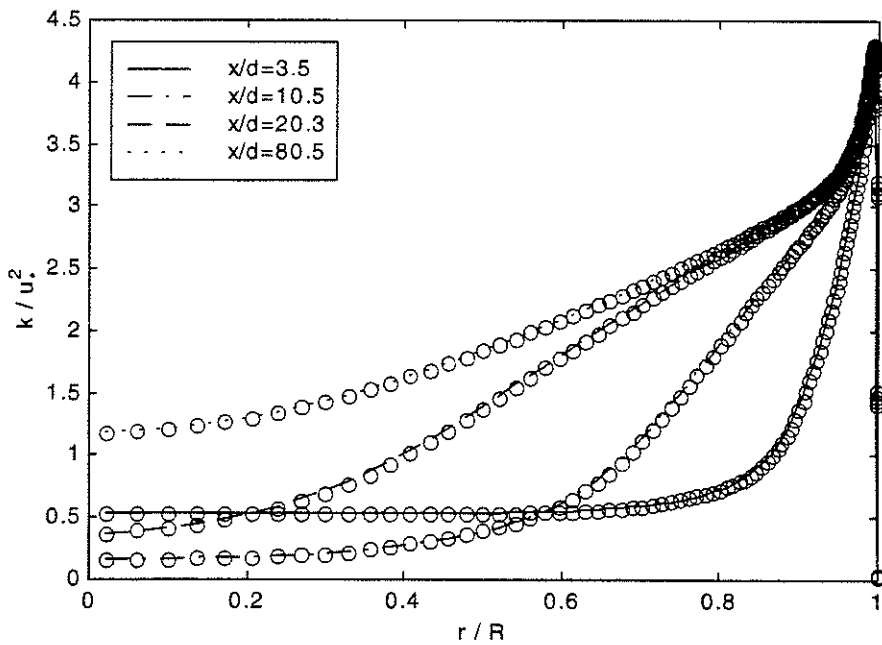


Figure 6.6 Turbulent kinetic energy distribution for model constant test 3 (the lines represent the simulation results obtained for $m = 3$, and the open circles represent the simulation results obtained for $m = 2.5$)

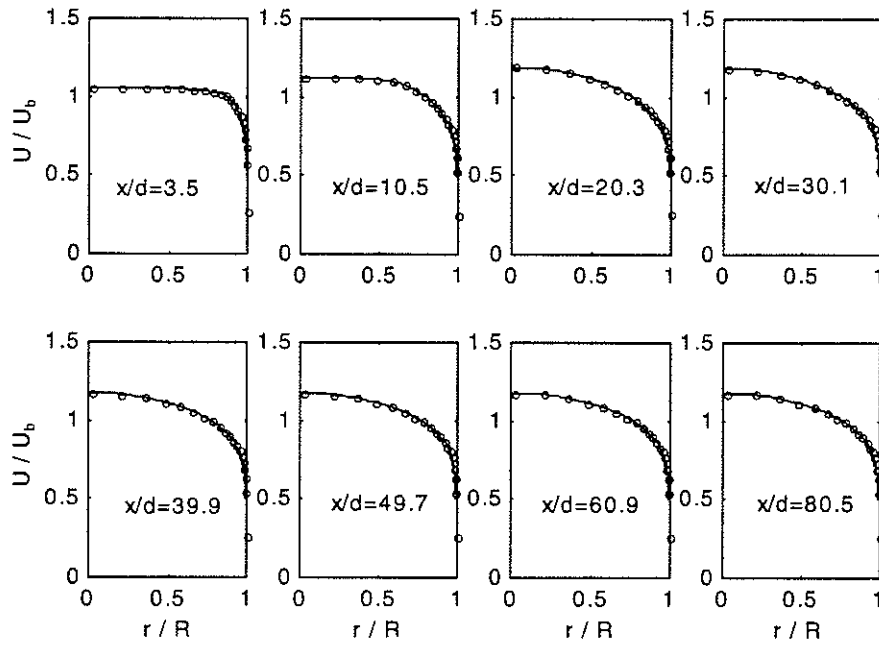


Figure 6.7 Model constant test 4 (the solid lines represent the simulation results obtained for $m=3$, and the open circles represent the simulation results obtained for $m=3.5$)

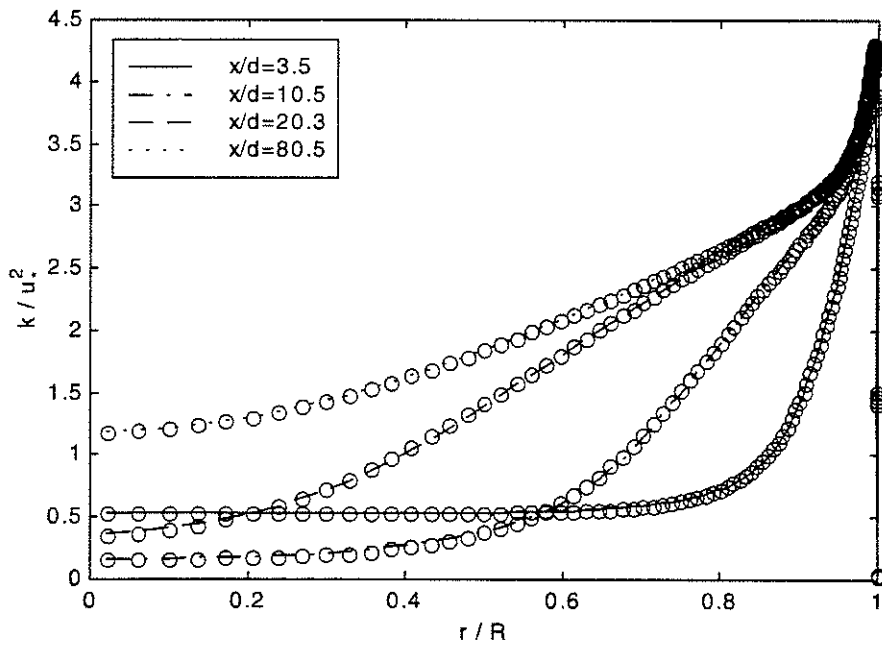


Figure 6.8 Turbulent kinetic energy distribution for model constant test 4 (the lines represent the simulation results obtained for $m=3$, and the open circles represent the simulation results obtained for $m=3.5$)

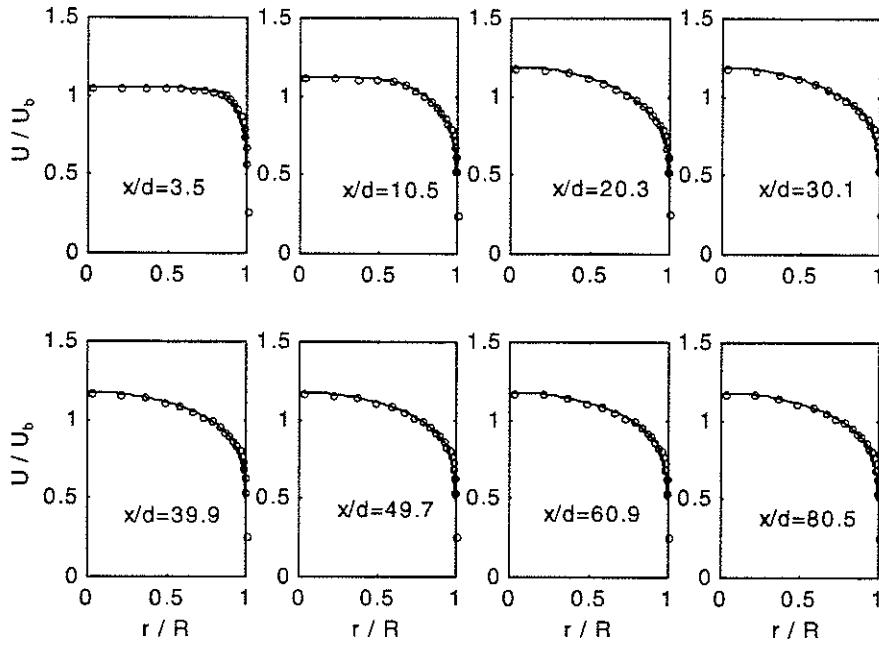


Figure 6.9 Model constant test 5 (the solid lines represent the simulation results obtained for $C_{\mu g}=0.10$, and the open circles represent the simulation results obtained for $C_{\mu g}=0.15$)

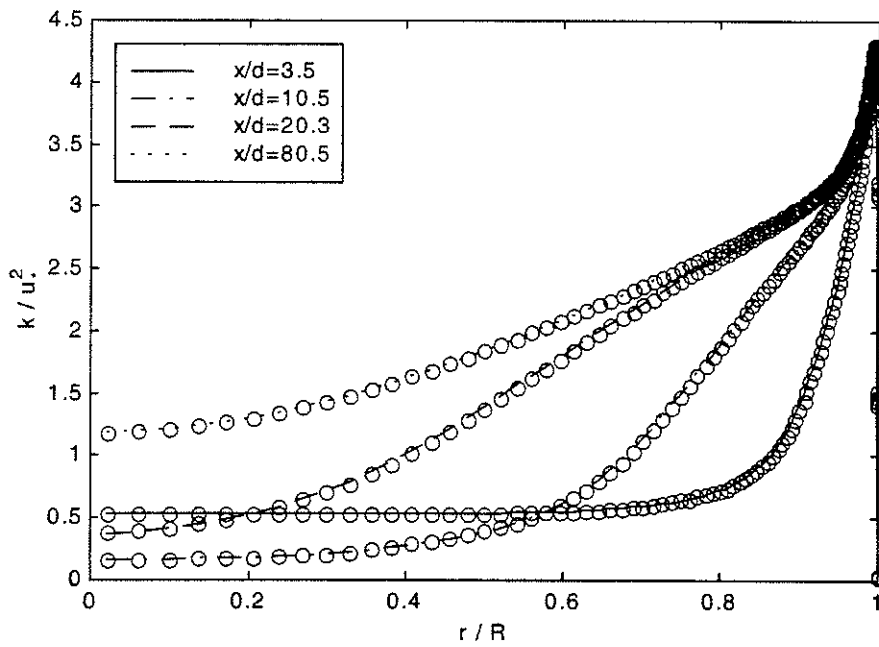


Figure 6.10 Turbulent kinetic energy distribution for model constant test 5 (the lines represent the simulation results obtained for $C_{\mu g}=0.10$, and the open circles represent the simulation results obtained for $C_{\mu g}=0.15$)

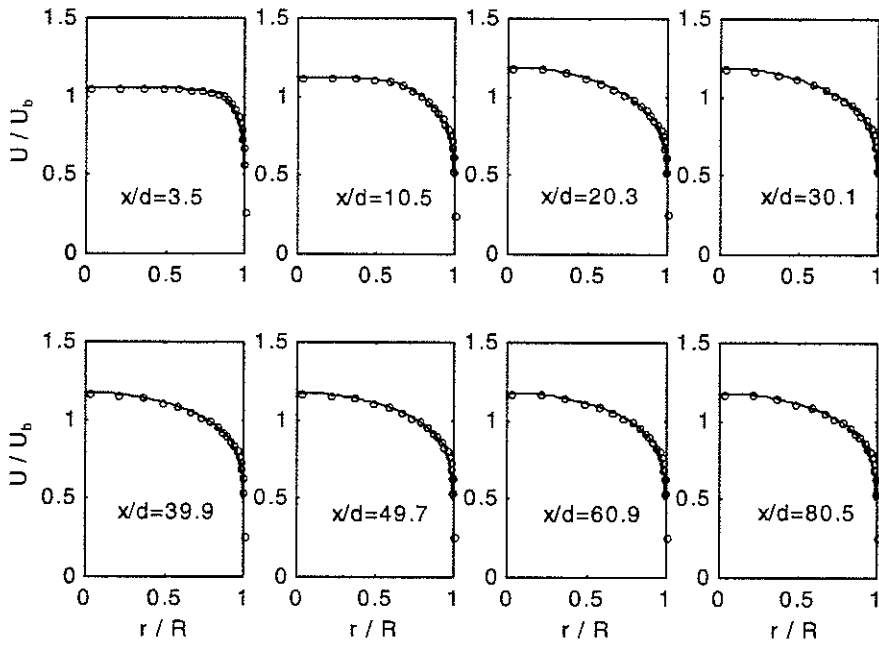


Figure 6.11 Model constant test 6 (the solid lines represent the simulation results obtained for $C_{g3} = 0.16$, and the open circles represent the simulation results obtained for $C_{g3} = 0.20$)

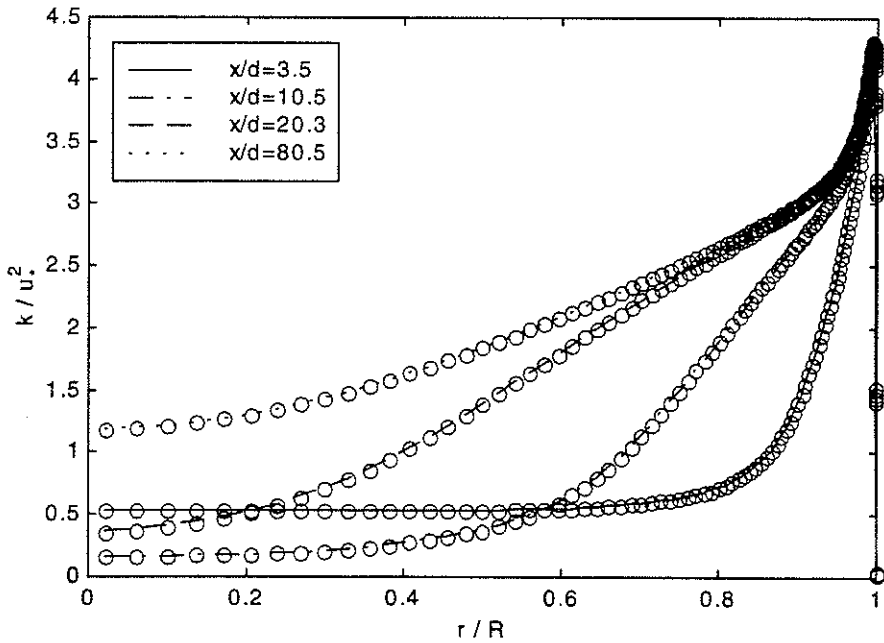


Figure 6.12 Turbulent kinetic energy distribution for model constant test 6 (the lines represent the simulation results obtained for $C_{g3} = 0.16$, and the open circles represent the simulation results obtained for $C_{g3} = 0.20$)

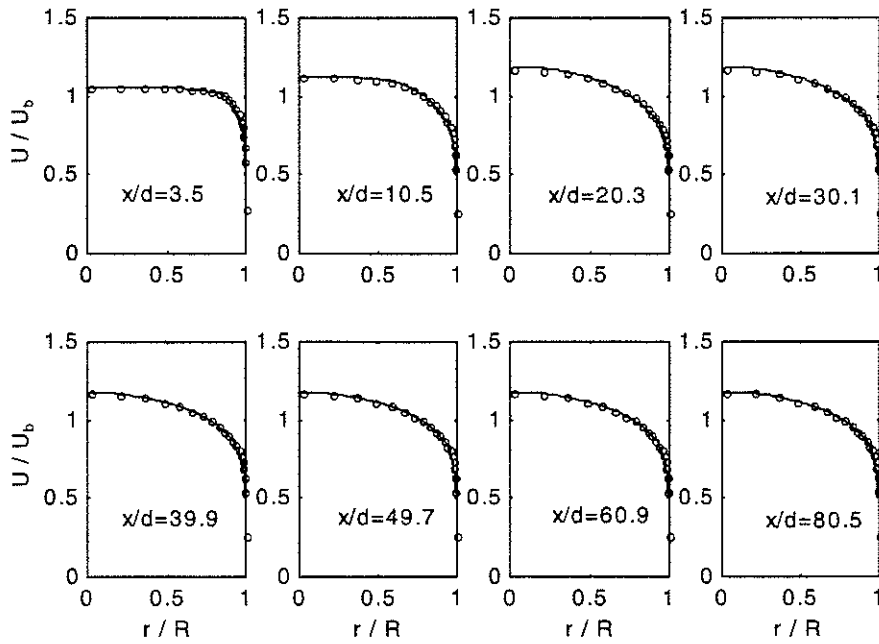


Figure 6.13 Model constant test 7 (the solid lines represent the simulation results obtained for $C_{\epsilon 4} = 0.1$, and the open circles represent the simulation results obtained for $C_{\epsilon 4} = 0.2$)

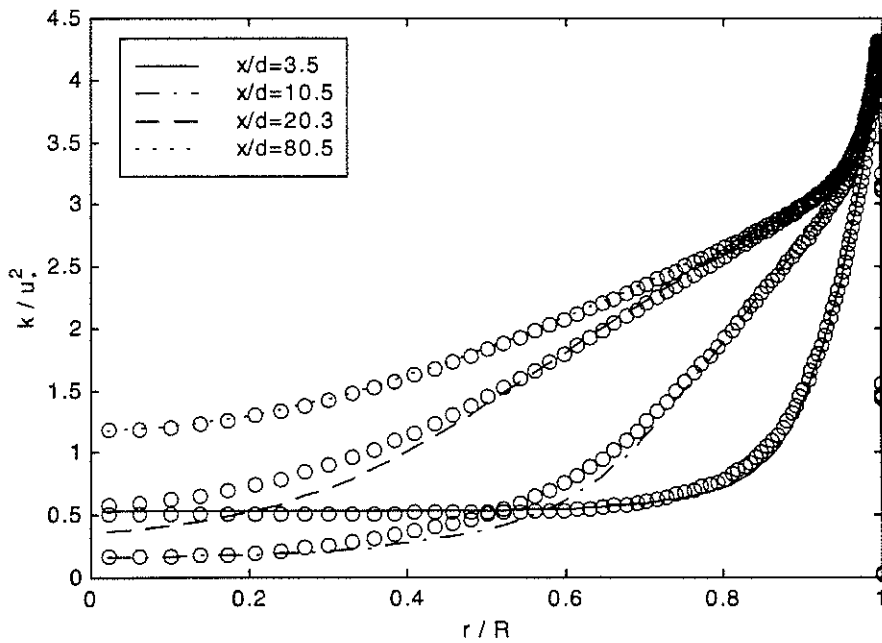


Figure 6.14 Turbulent kinetic energy distribution for model constant test 7 (the lines represent the simulation results obtained for $C_{\epsilon 4} = 0.1$, and the open circles represent the simulation results obtained for $C_{\epsilon 4} = 0.2$)

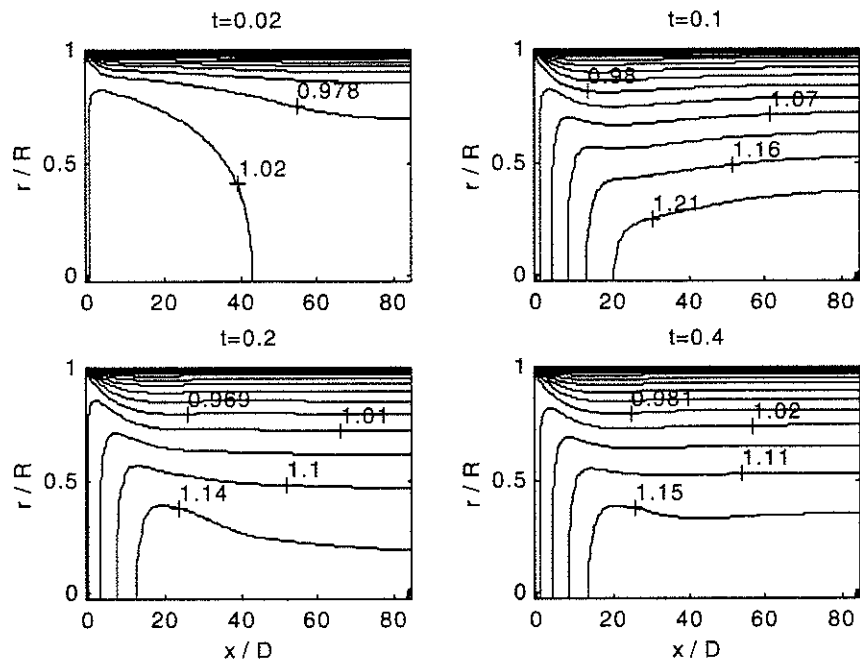


Figure 6.15 Contour plot for axial mean velocity

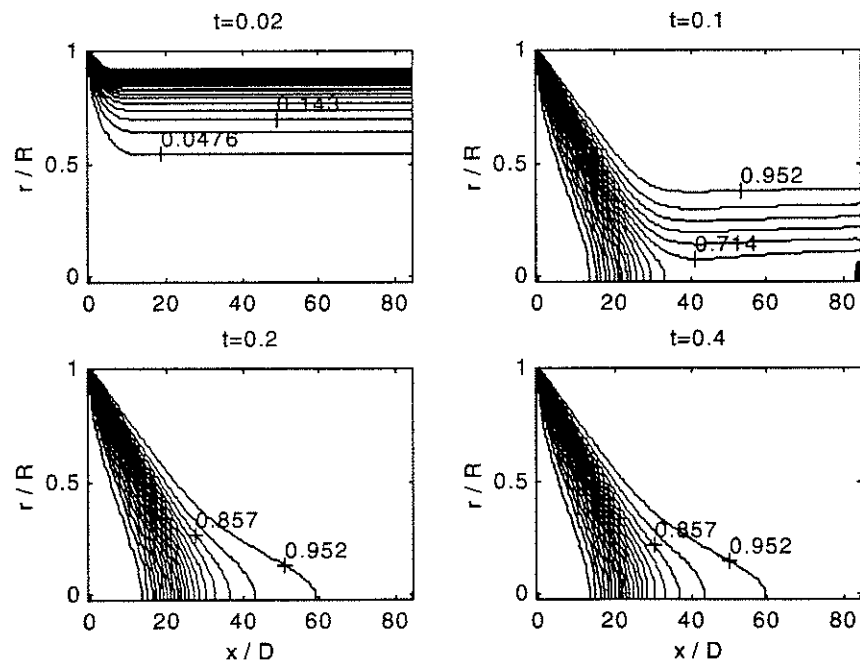


Figure 6.16 Contour plot for intermittency factor γ

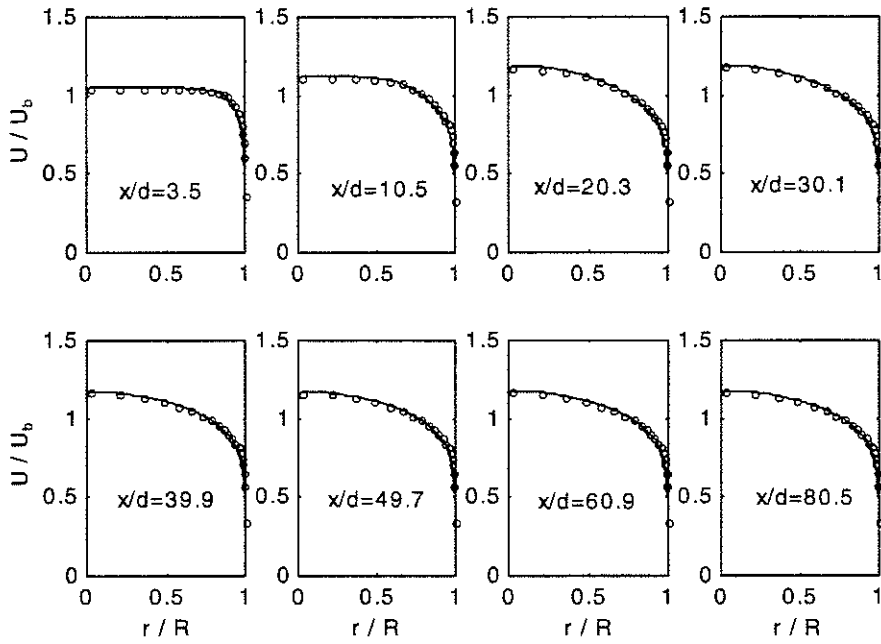


Figure 6.17 Simulation results obtained using two grid systems for $Re=200,000$ (the solid smooth lines represent the simulation results obtained using coarse grids and the open circles represent the simulation results obtained using finer grids)

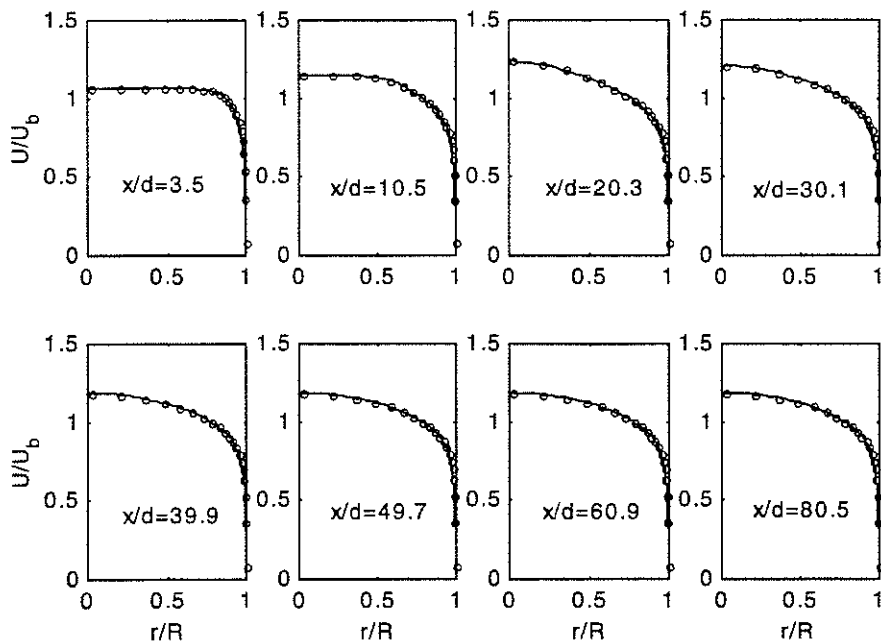


Figure 6.18 Confirmation of the convergence of the iteration for $Re=50,000$ (the solid smooth lines represent the simulation results with 1200 iterations and the open circles represent the simulation results with 600 iterations)

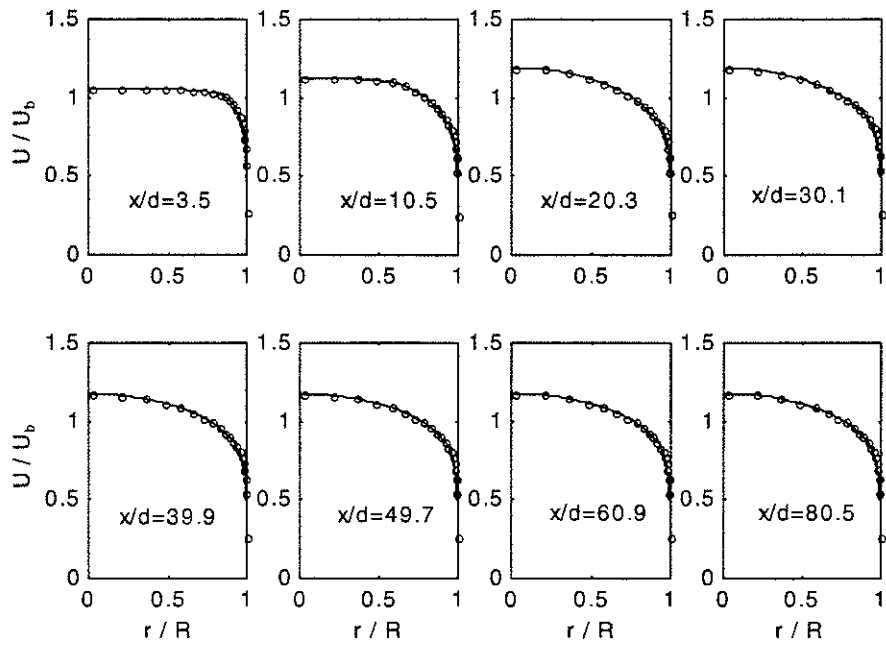


Figure 6.19 Confirmation of the convergence of the iteration for $Re=200,000$ (the solid smooth lines represent the simulation results with 600 iterations and the open circles represent the simulation results with 1200 iterations)

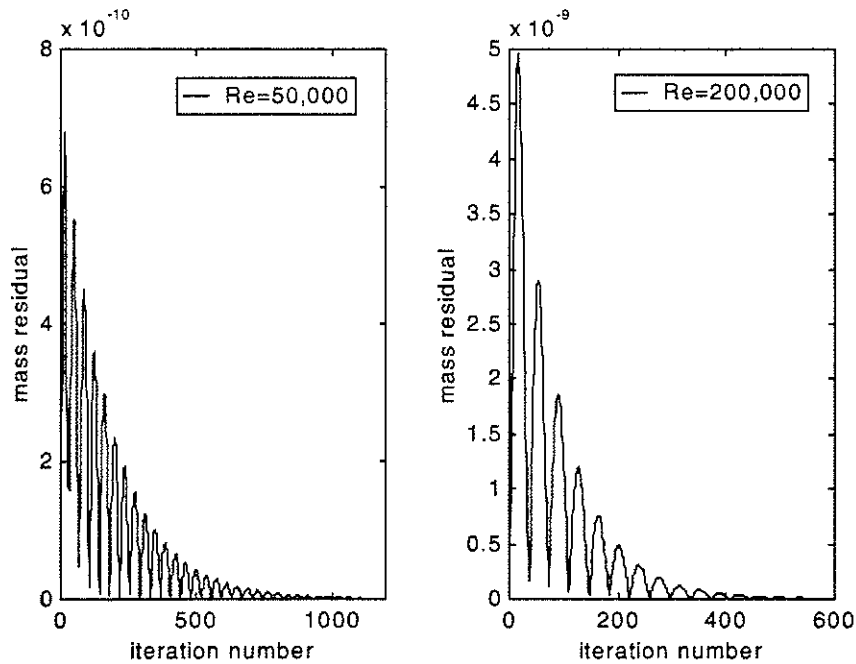


Figure 6.20 Convergence of mass residual

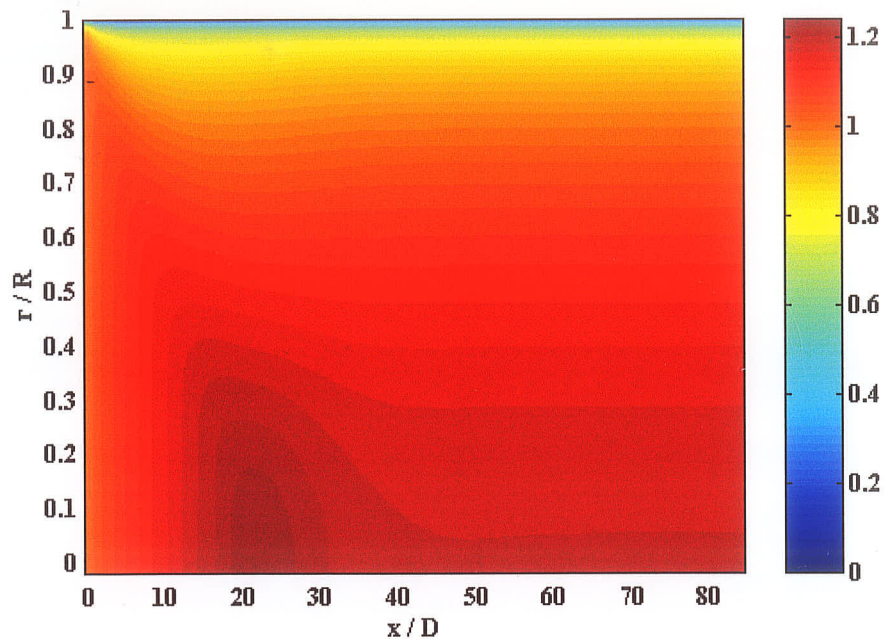


Figure 6.21 Contour plot for the non-dimensional axial velocity for $Re = 50,000$

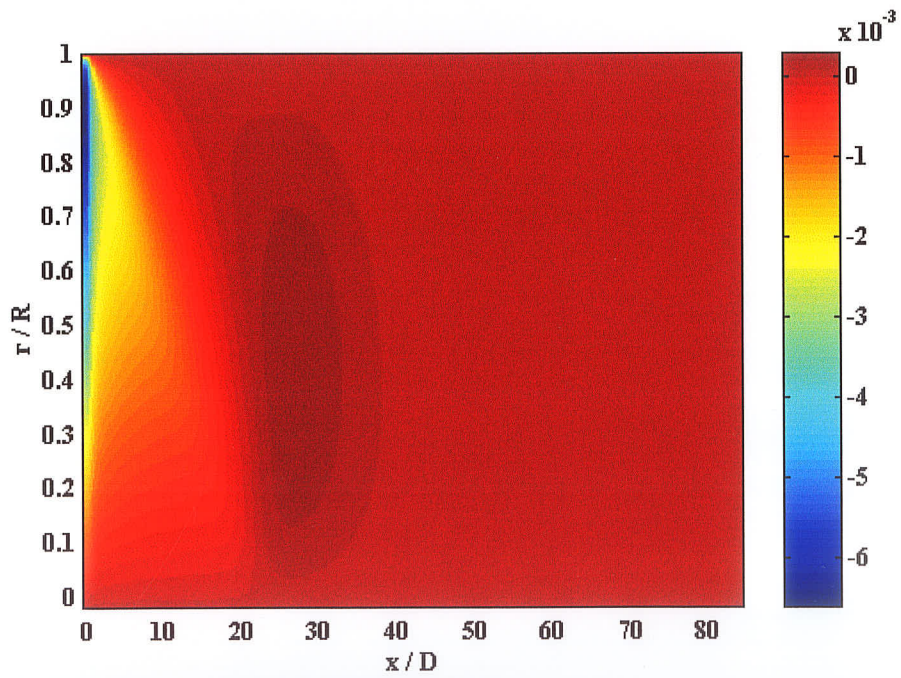


Figure 6.22 Contour plot for the non-dimensional radial velocity for $Re = 50,000$

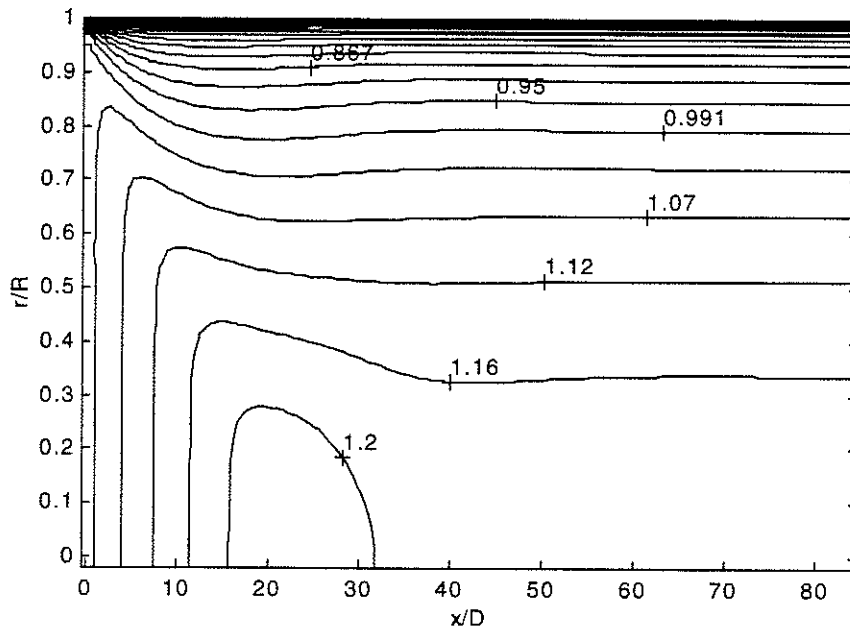


Figure 6.23 Contour plot for non-dimensional axial velocity for $Re=50,000$

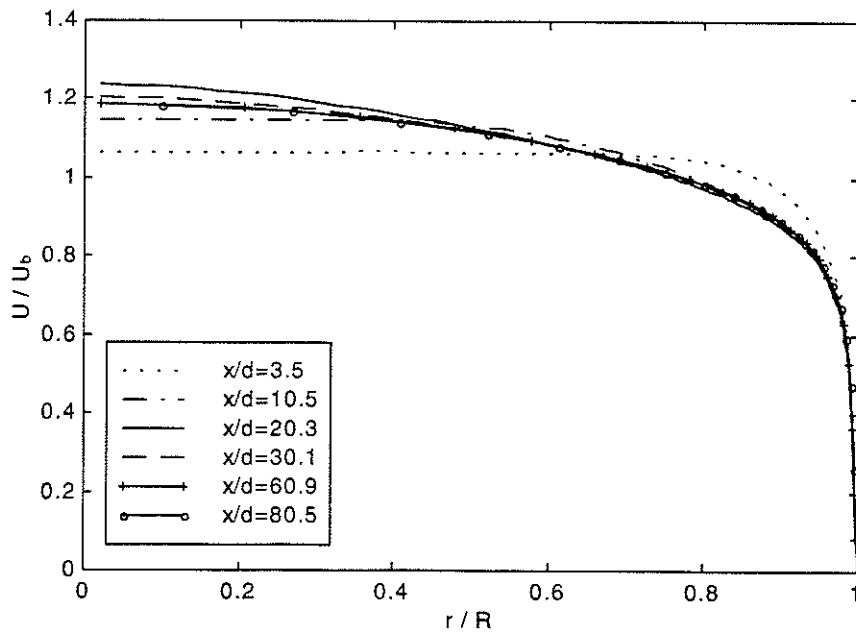


Figure 6.24 Axial velocity vs r/R at six downstream locations for $Re=50,000$

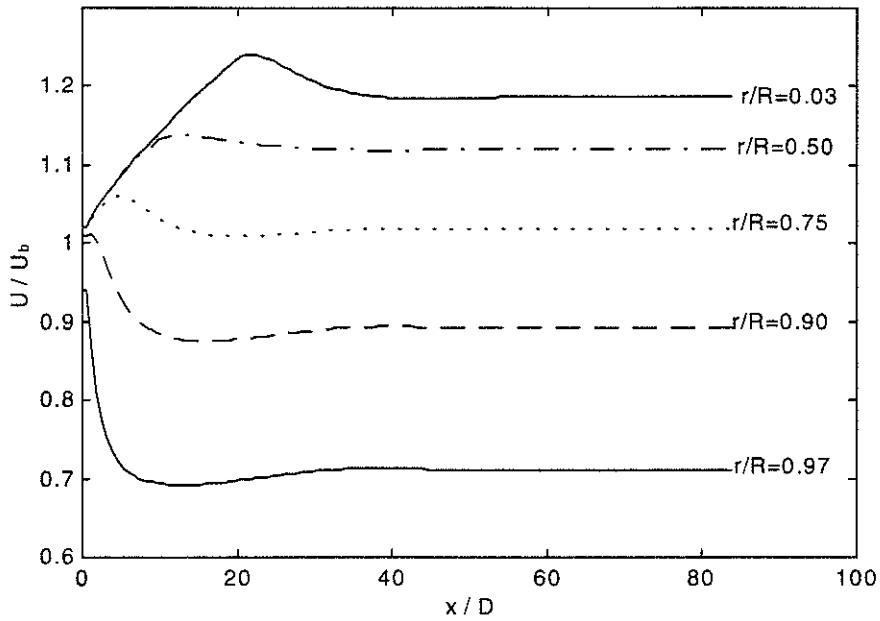


Figure 6.25 Development of axial velocity for $Re=50,000$

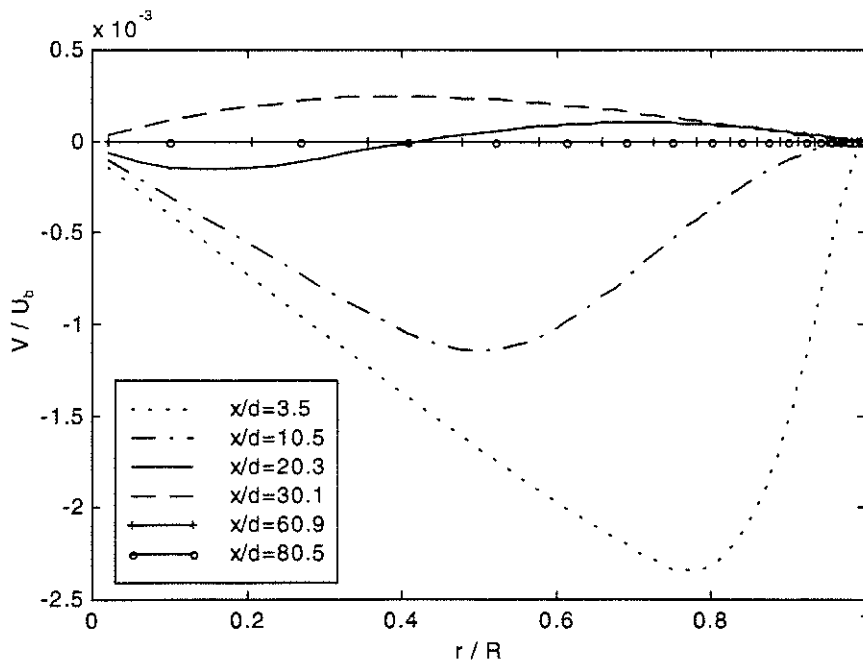


Figure 6.26 Radial velocity vs r/R at six downstream locations for $Re=50,000$

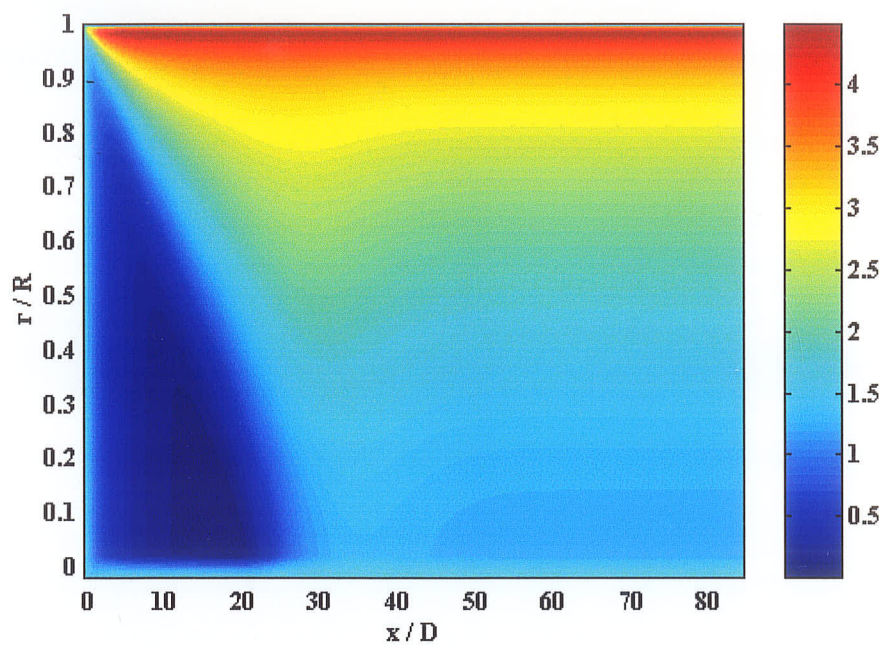


Figure 6.27 Contour plot for non-dimensional Turbulent Kinetic Energy for $Re = 50,000$

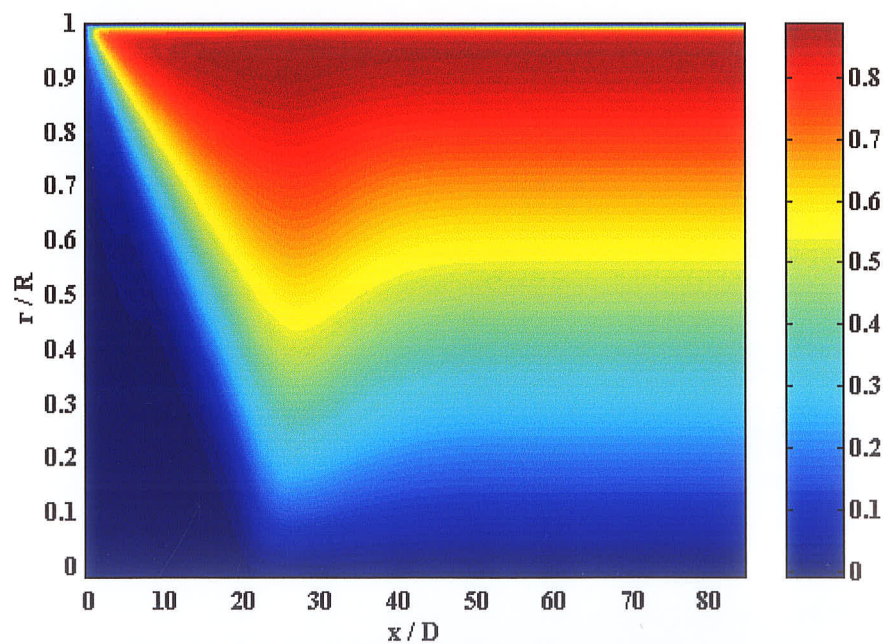


Figure 6.28 Contour plot for Reynolds shear stress for $Re = 50,000$

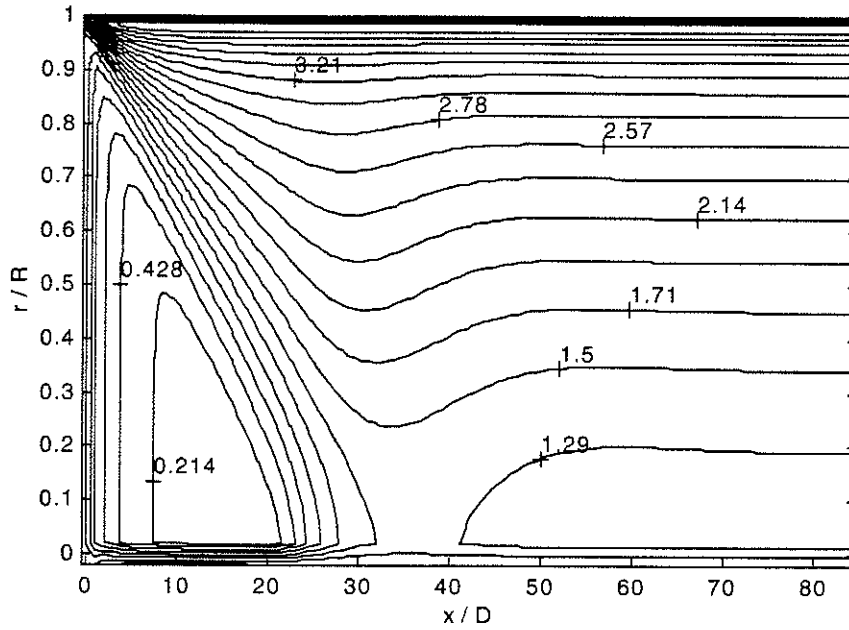


Figure 6.29 Contour plot for non-dimensional turbulent kinetic energy for $Re=50,000$

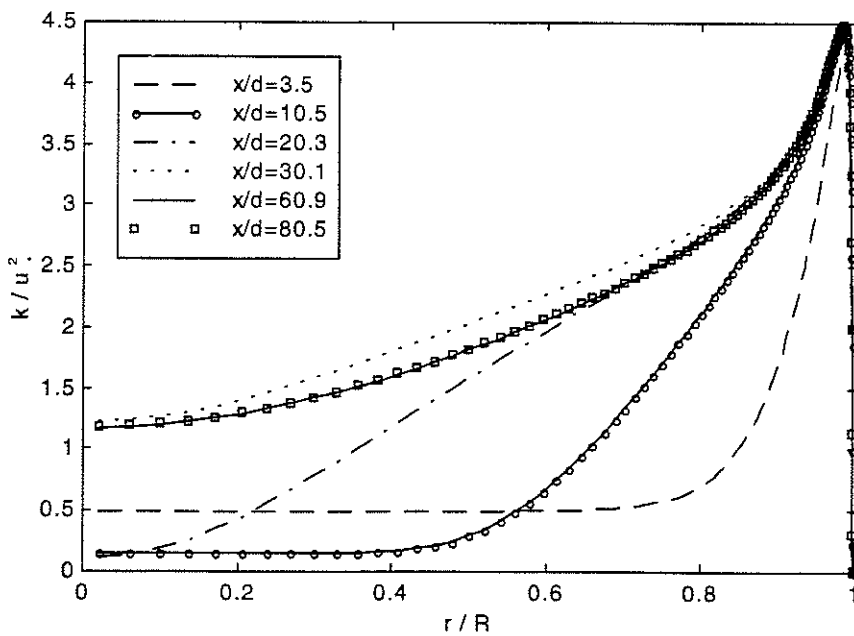


Figure 6.30 Turbulent kinetic energy vs r/R at six downstream locations for $Re=50,000$

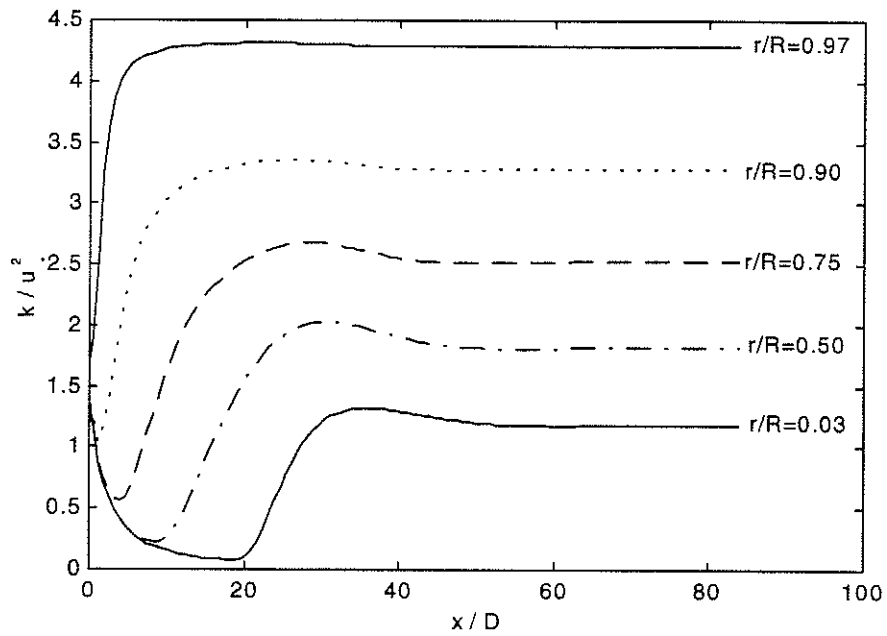


Figure 6.31 Development of turbulent kinetic energy for $Re=50,000$

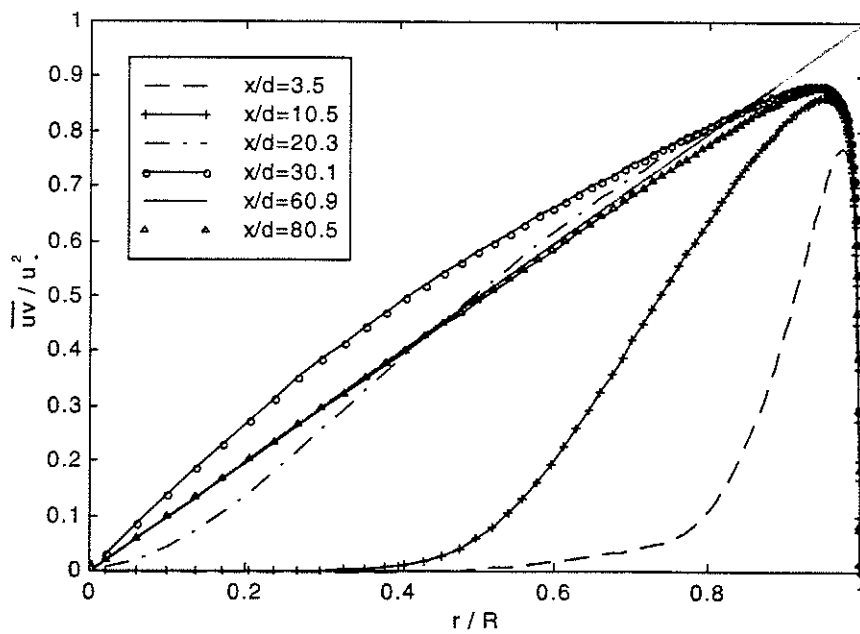


Figure 6.32 Reynolds shear stress vs r/R at six downstream locations for $Re=50,000$

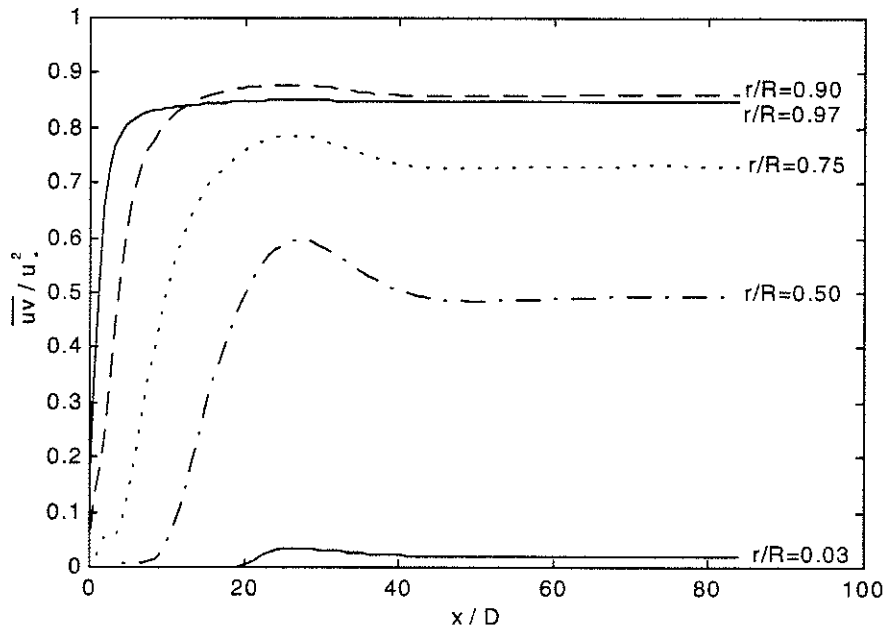


Figure 6.33 Development of Reynolds shear stress for $Re=50,000$

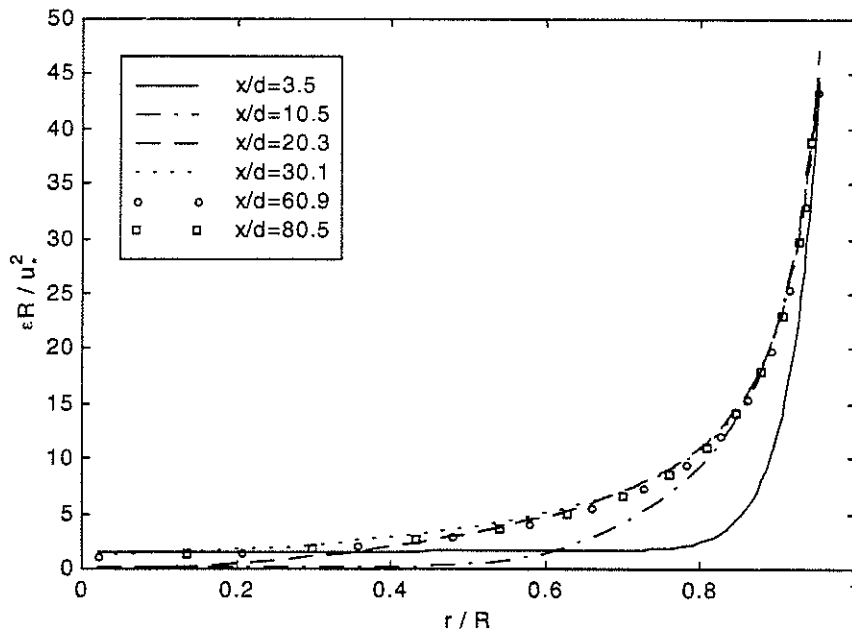


Figure 6.34 Turbulent dissipation rate vs r/R at six downstream locations for $Re=50,000$

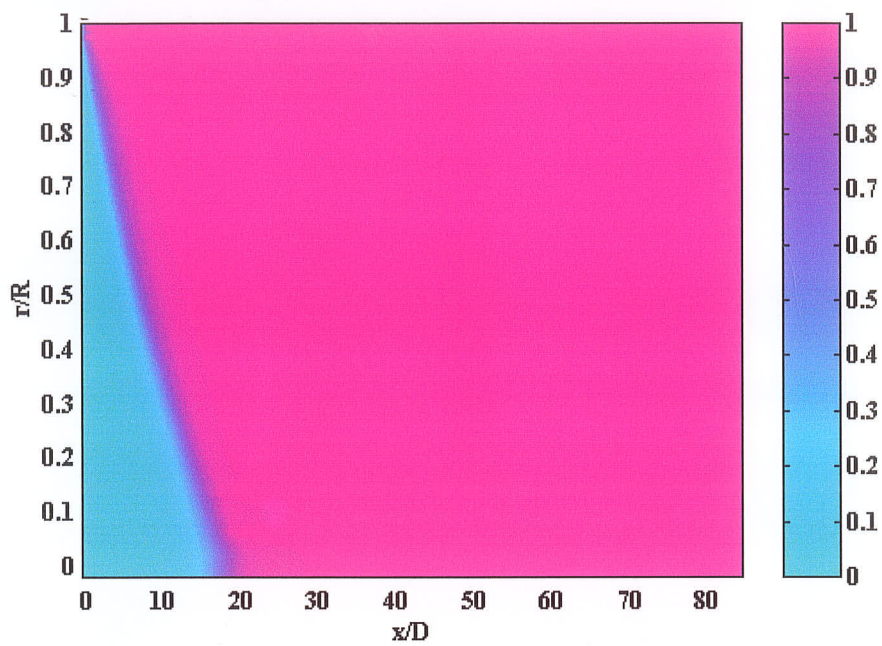


Figure 6.35 Contour plot for intermittency factor for $Re = 50,000$

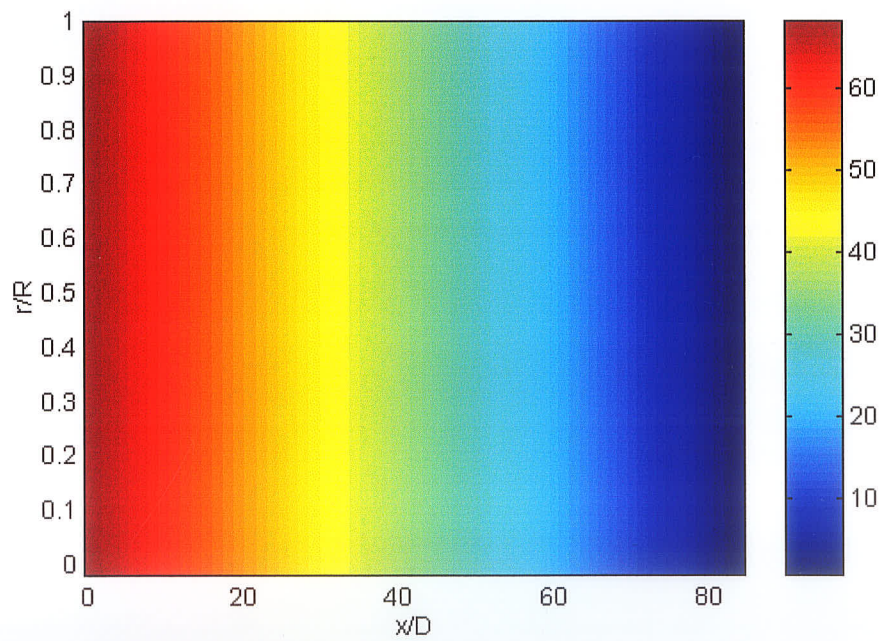


Figure 6.36 Contour plot for pressure for $Re = 50,000$

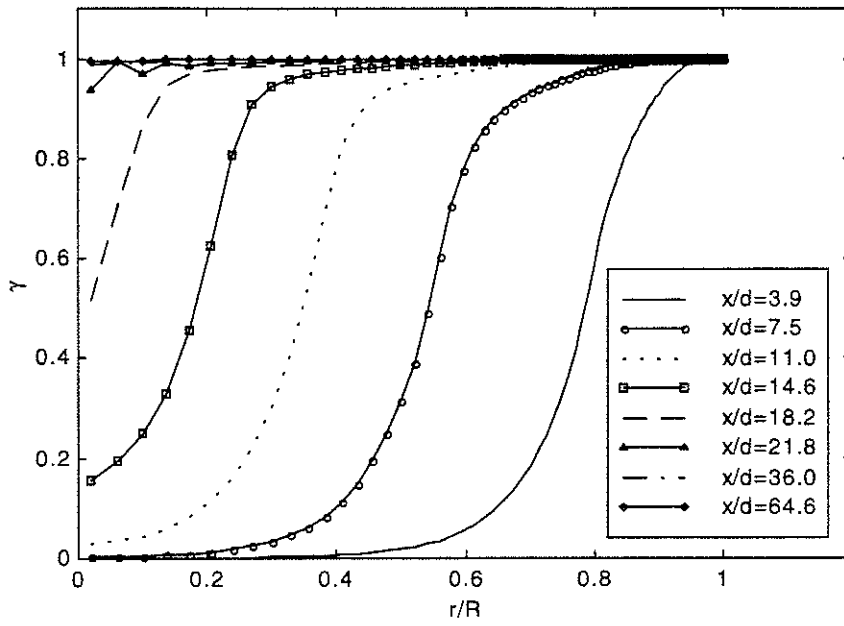


Figure 6.37 Intermittency factor vs r/R at eight different downstream positions for $Re=50,000$

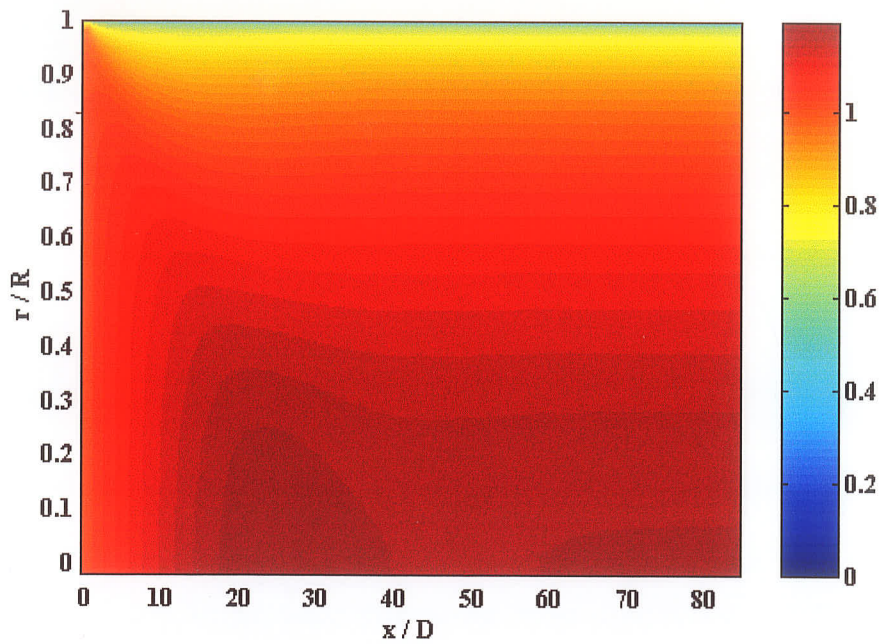


Figure 6.38 Contour plot for the non-dimensional axial velocity for $Re = 200,000$

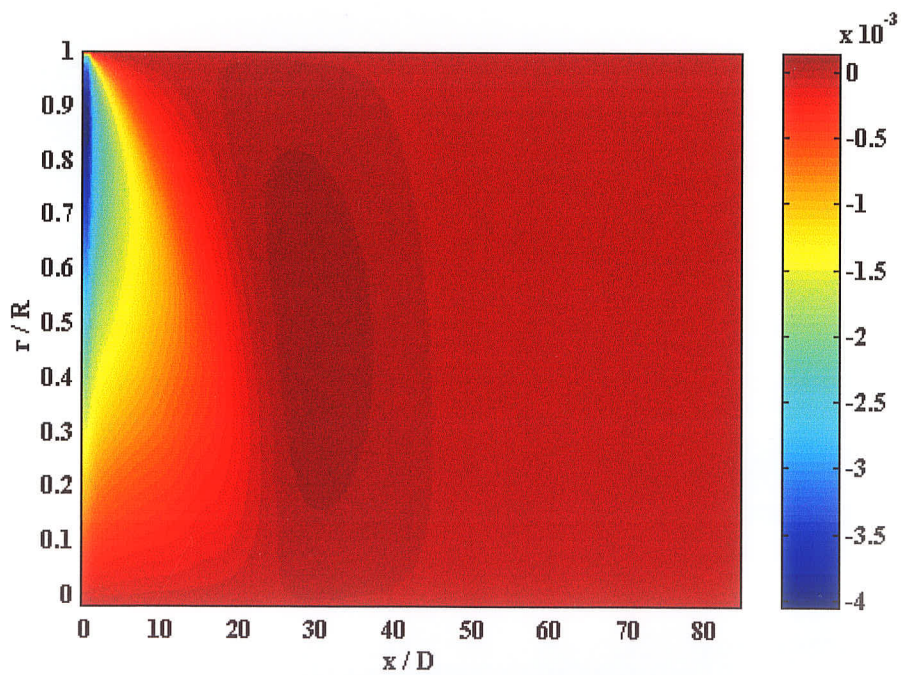


Figure 6.39 Contour plot for the non-dimensional radial velocity for $Re = 200,000$

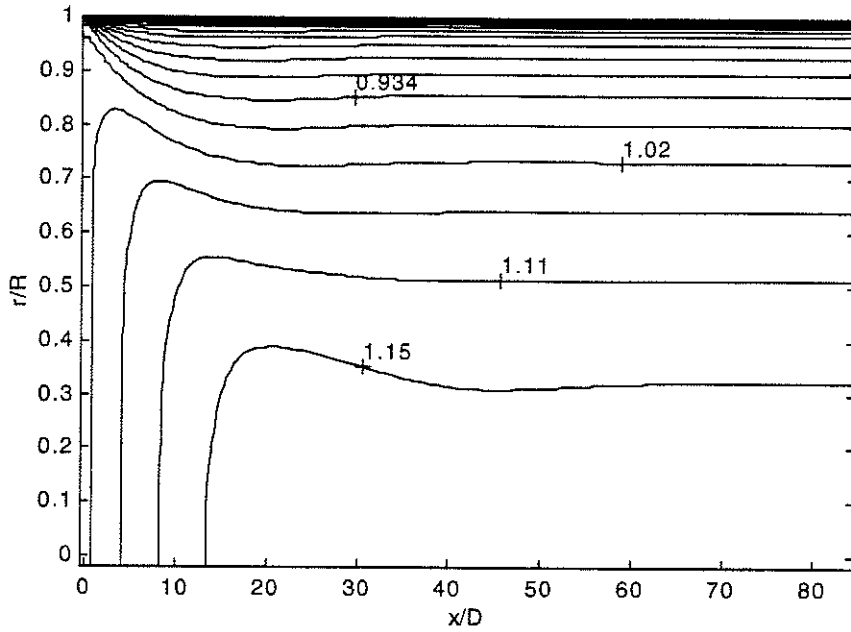


Figure 6.40 Contour plot for non-dimensional axial velocity for $Re=200,000$

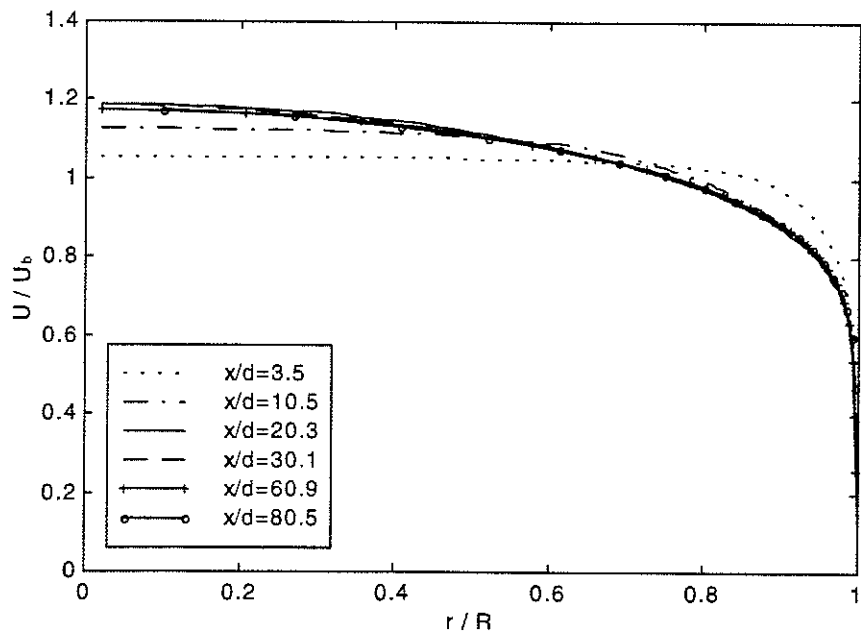


Figure 6.41 Axial velocity vs r/R at six downstream locations for $Re=200,000$

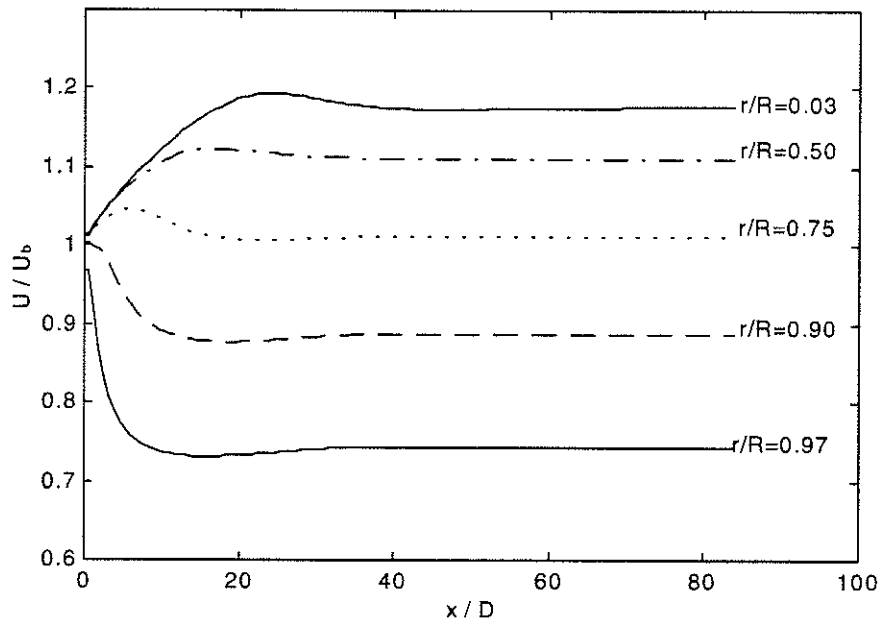


Figure 6.42 Development of axial velocity for $Re=200,000$

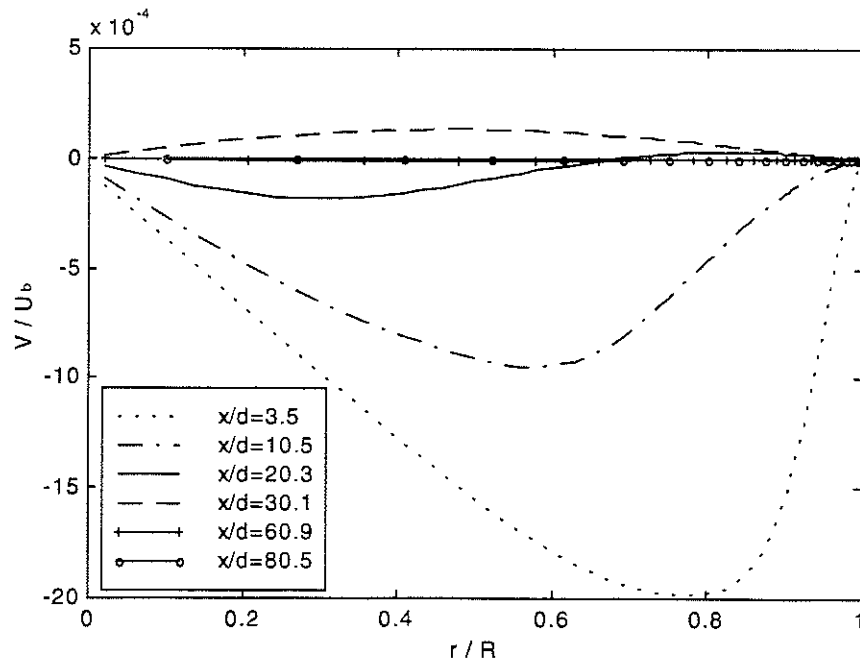


Figure 6.43 Radial velocity vs r/R at six downstream locations for $Re=200,000$

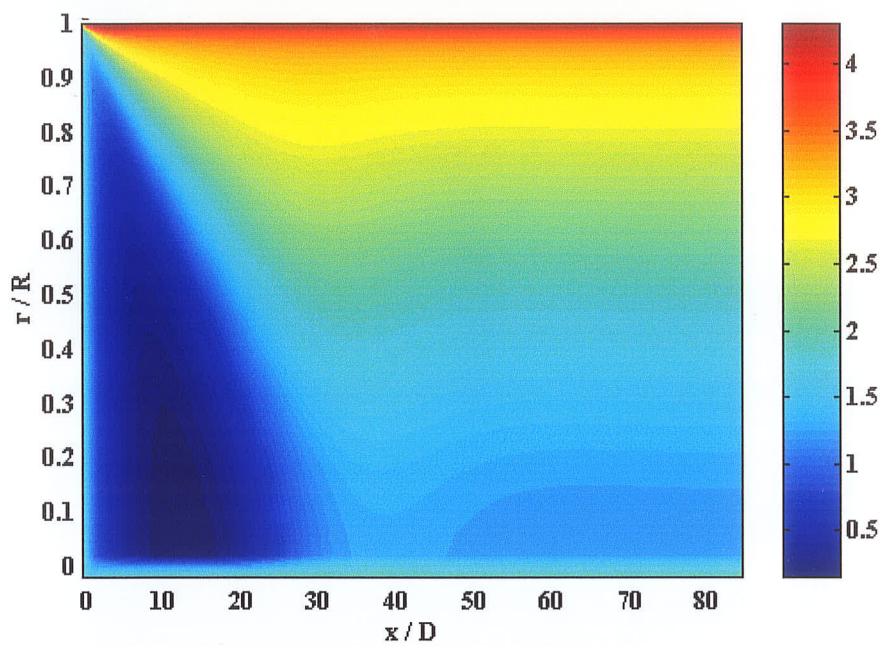


Figure 6.44 Contour plot for non-dimensional Turbulent Kinetic Energy for $Re = 200,000$

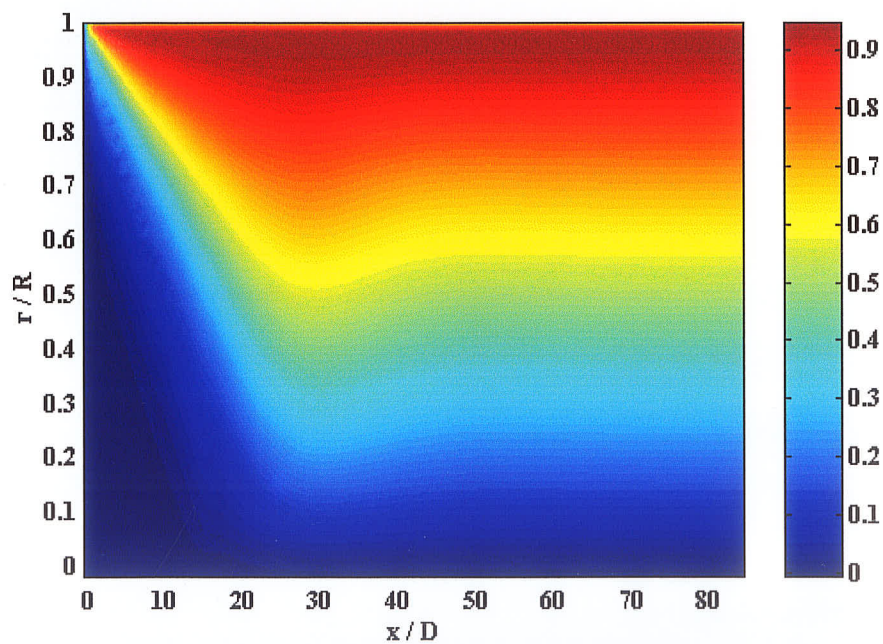


Figure 6.45 Contour plot for Reynolds shear stress for $Re = 200,000$

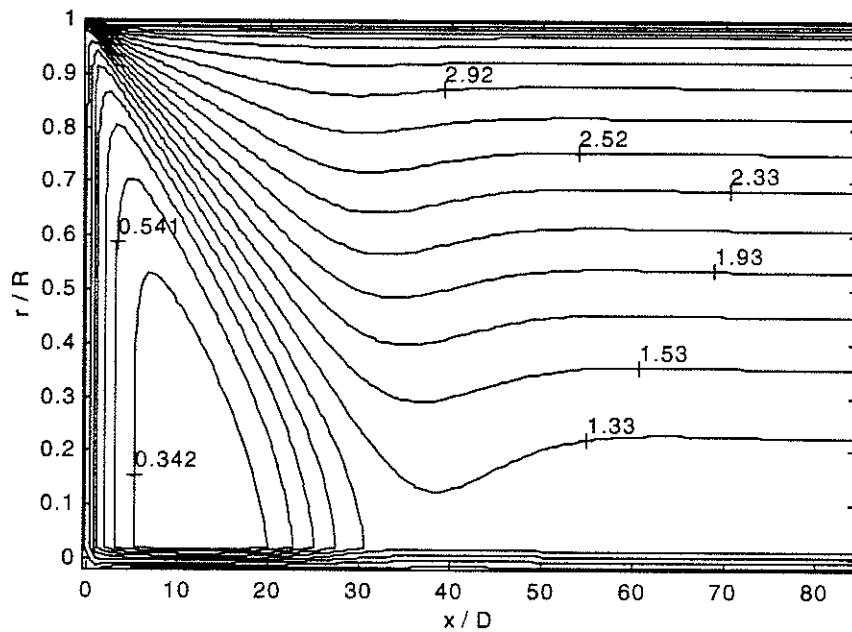


Figure 6.46 Contour plot for non-dimensional turbulent kinetic energy for $Re=200,000$

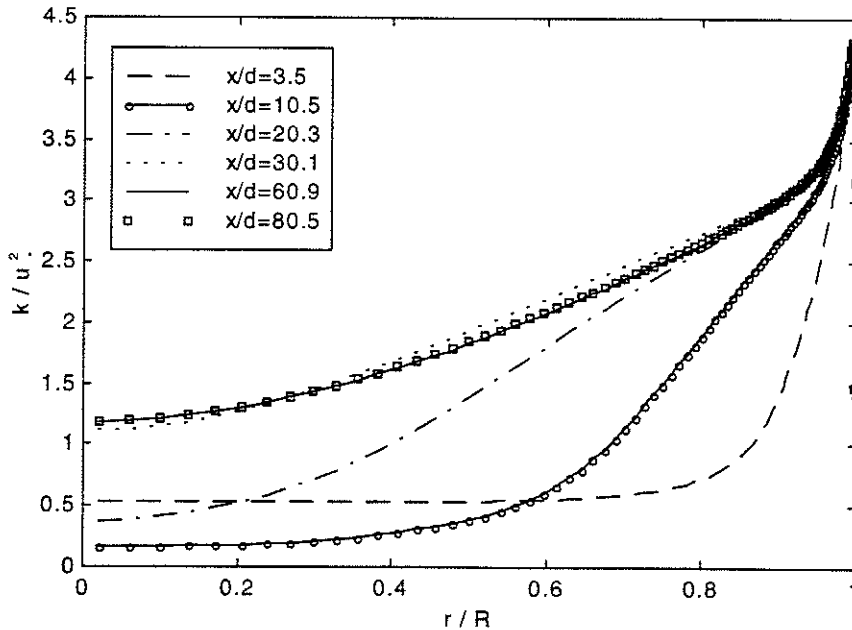


Figure 6.47 Turbulent kinetic energy vs r/R at six downstream locations for $Re=200,000$

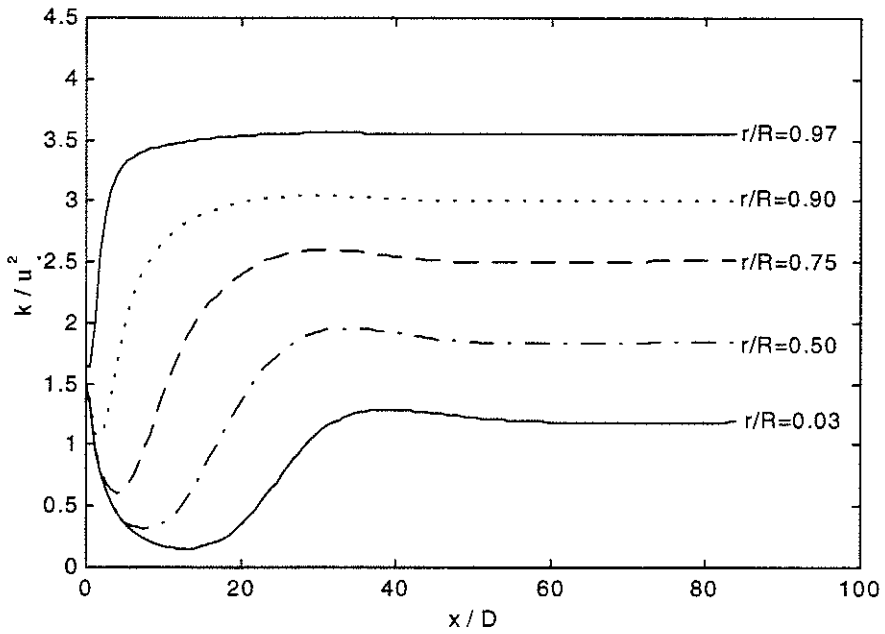


Figure 6.48 Development of turbulent kinetic energy for $Re=200,000$

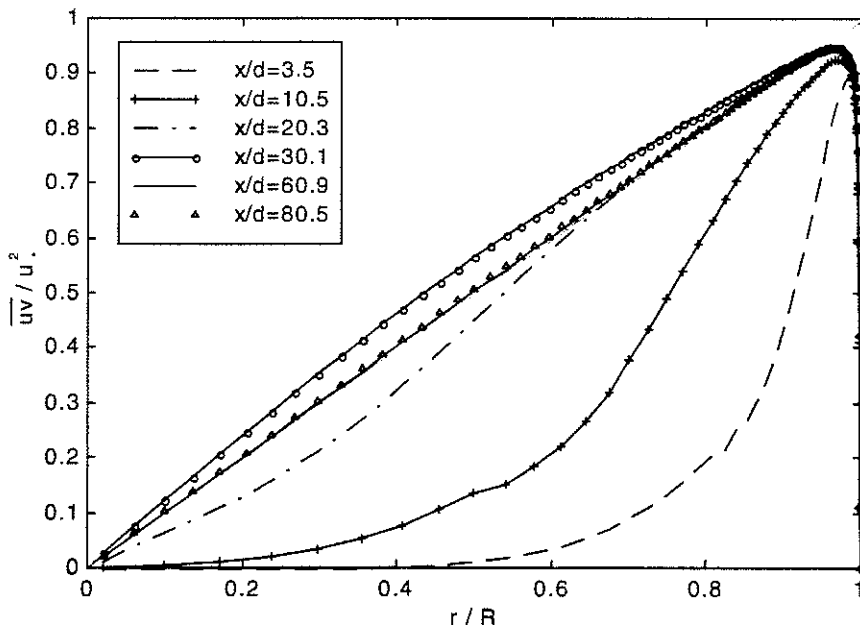


Figure 6.49 Reynolds shear stress vs r/R at six downstream locations for $Re=200,000$

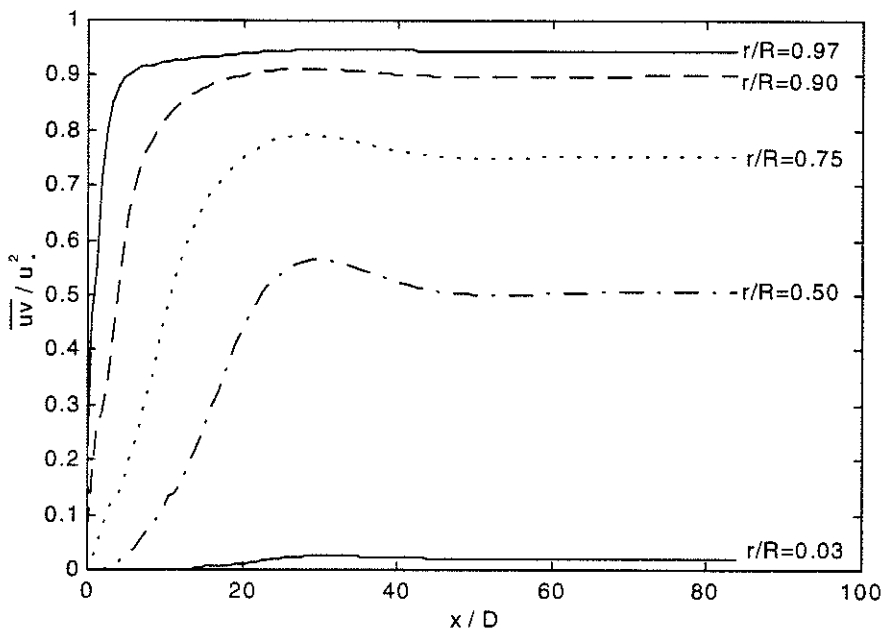


Figure 6.50 Development of Reynolds shear stress for $Re=200,000$

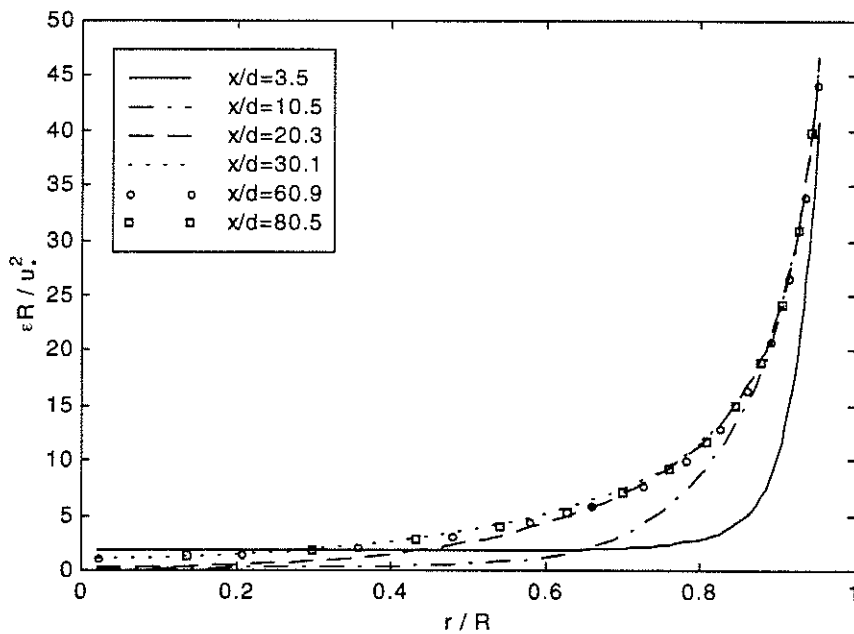


Figure 6.51 Turbulent dissipation rate vs r/R at six downstream locations for $Re=200,000$

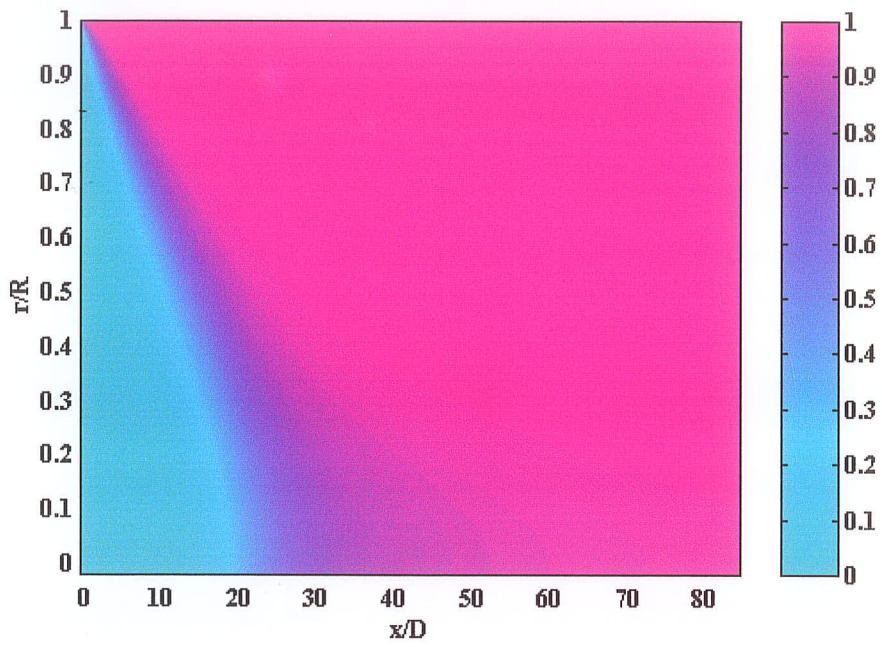


Figure 6.52 Contour plot for intermittency factor for $Re = 200,000$

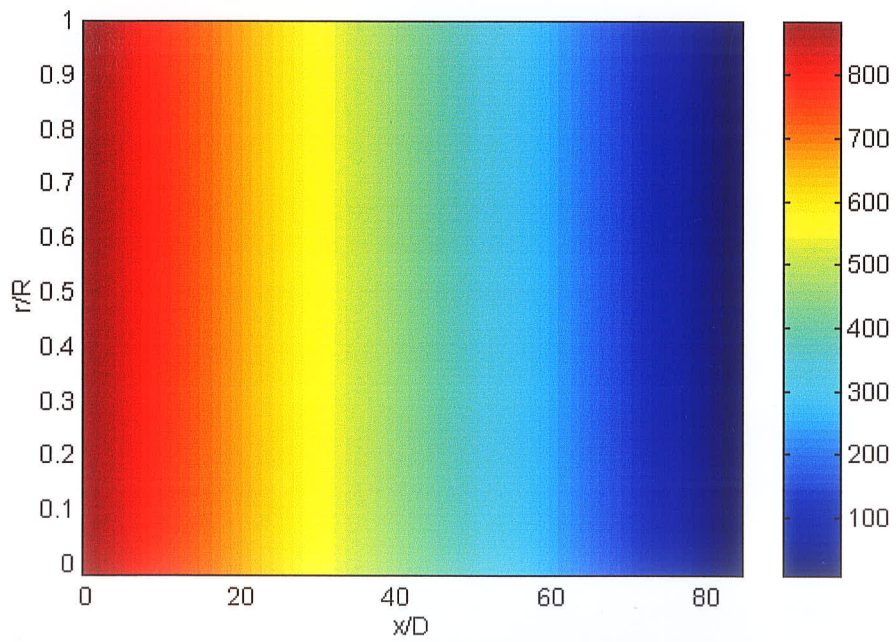


Figure 6.53 Contour plot for pressure for $Re = 200,000$

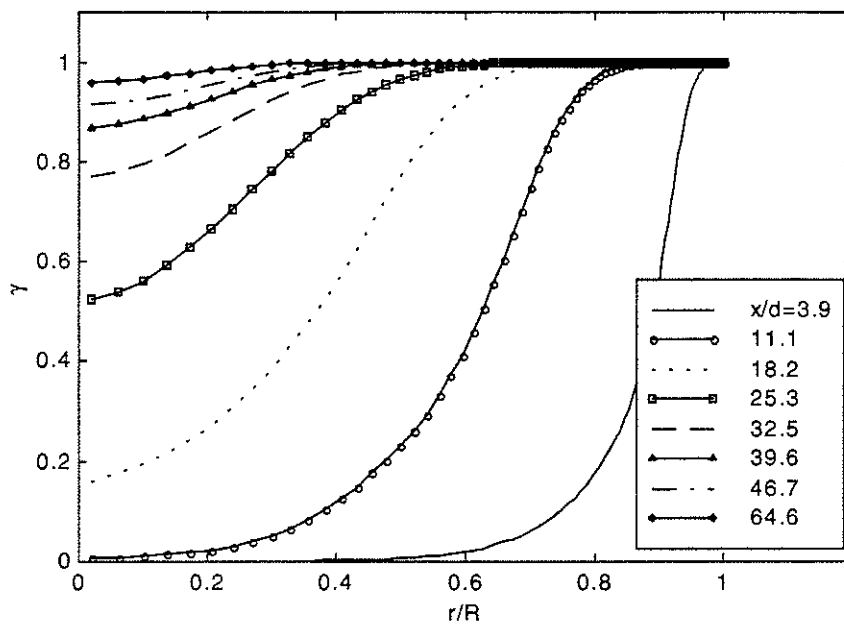


Figure 6.54 Intermittency factor vs r/R at eight different downstream positions for $Re=200,000$

7 COMPARISON OF THE FOUR MODELS

The predictions for mean velocity and turbulent quantities obtained by the four models are presented together for comparison in the first two sections respectively. Then the model performance is discussed in the next section. Finally, the physical process in the pipe flow is discussed in Section 7.4.

7.1 *Predictions for Mean Velocity*

Predictions for $Re=50,000$ with the four models have been separately discussed in Chapter 3-6. The predictions of the development of the centerline axial mean velocity with the four models are presented together in Figure 7.1, and it can be seen that the centerline mean velocity “overshoot”, which appears to be a general feature of pipe flow, has not been predicted by zero equation model. However, it has been predicted by other three models. Furthermore, the peak overshoot position that predicted by three models is quite consistent. The same conclusion is obtained from the results for $Re=300,000$ (see Figure 7.2). The centerline peak overshoot positions and peak values for various Reynolds numbers are summarized in Table 7.1.

From Table 7.1, we can see that the centerline peak overshoot position moves downstream as the flow Reynolds number increases; while the peak value decreases as the flow Reynolds number increases. It should be mentioned that a discrepancy has been found between our observation and Reichert and Azad’s (1976) experimental data about the effect of Reynolds number on the location of the centerline peak overshoot position. In their paper, they suggested that the peak position is a function of Reynolds number given by:

$$\frac{x_p}{D} = 30.80 + \frac{0.89}{10^{-5} \text{Re}} + \frac{0.79}{(10^{-5} \text{Re})^2} \quad (7.1)$$

That means the peak overshoot position decreases as Reynolds number increases. The reason that causes this discrepancy is uncertain.

Table 7.1 Centerline peak overshoot position and peak value

Re x	Standard k-ε model		Chien model		k-ε-γ model	
	x _p /D	U/U _b	x _p /D	U/U _b	x _p /D	U/U _b
10	–	–	21.74	1.3223	–	–
50	21.74	1.2412	23.18	1.2412	21.75	1.2415
150	24.61	1.2139	–	–	–	–
200	–	–	–	–	23.97	1.1944
300	26.73	1.199	27.16	1.2089	26.46	1.1802

Developing turbulent pipe flow is basically a transition from a boundary layer type flow at the entrance to a fully developed flow far downstream. The boundary thickness grows as the distance from the pipe inlet increases. In order to maintain a constant bulk flow rate, the core region accelerates as though it is being squeezed by the growing boundary layer. In the initial portion of the entrance flow the boundary layers serve to squeeze fluid into the core causing the core velocity to increase. This core acceleration is the combined result of the deceleration near the wall and conservation of mass. As the flow evolves, the boundary layers grow and eventually merge. The flow subsequently evolves to its fully developed state. The initial core acceleration is so large for a turbulent flow that the centerline velocity overshoots its fully developed value. The effect of Reynolds number is to move the peak

overshoot further downstream and reduce its magnitude, with increasing Reynolds number.

Axial velocity versus r/R for $Re=50,000$ are presented in Figure 7.3, with the experimental data of Deissler (1955) at three downstream locations for $Re=46,000$. The simulations with experimental data of Laufer (1954) for $Re=50,000$, the experimental data of Richman and Azad (1973) for $Re=100,000$, and the experimental data of Reichert and Azad (1976) for $Re=75,000$ for fully developed flow are plotted in Figure 7.4. At $Re=50,000$, the predictions obtained by the standard $k-\epsilon$ model, Chien's model and the $k-\epsilon-\gamma$ model are almost identical. It is obvious that in the developing region, the predictions obtained by the higher order models are in better agreement with experiment data of Deissler (1955) than the predictions obtained using the zero equation model. However, in the fully developed region, some experimental data (Reichert and Azad (1976), Richman and Azad (1973)) are a better fit with the predictions obtained by higher order models, and some experimental data (Deissler (1955) and Laufer (1954)) are a better fit with the prediction obtained by the zero equation model. Axial velocity versus r/R for $Re=300,000$ at six downstream locations are presented in Figure 7.5 and Figure 7.6, compared with the experimental data of Richman and Azad (1973). Variations between the predictions obtained by the three higher order models can be observed. It is encouraging to see that in the developing region, predictions obtained by $k-\epsilon-\gamma$ model match the experimental data of Richman and Azad (1973) best.

The variation of the axial velocity with downstream distance from the pipe inlet for $Re=50,000$ with the experimental data of Reichert and Azad and the experimental data of Richman and Azad are plotted in Figure 7.7 and Figure 7.8 respectively. With the exception of the pipe centerline ($r/R=0.03$) and the near wall region ($r/R=0.99$), the numerical results reproduce the experimental data well. The variation of the axial velocity with downstream

distance from the pipe inlet for $Re=300,000$ obtained by four models are plotted from Figure 7.9 and Figure 7.12 with the experimental data of Barbin and Jones (1963), and the experimental data of Richman and Azad (1973). Overall good agreement has been found between the numerical results and the experimental data. On the pipe centerline, the prediction obtained by the zero equation model fits well with the data of Barbin and Jones (1963); while predictions obtained by the $k-\varepsilon-\gamma$ model fits best with the data of Richman and Azad (1973). Fully developed profiles for $Re=50,000$ and $Re=300,000$ are presented in Figure 7.13 and Figure 7.14 respectively. It can be seen that the numerical results obtained by the higher order models are slightly higher than the experimental data, but fit Laufer's (1954) data for $Re=500,000$ well. The numerical results obtained by the zero equation model are slightly lower than the experimental data, but fit Laufer's (1954) data for $Re=50,000$ well.

Finally, the fully developed profiles are plotted as u^+ versus y^+ in Figure 7.15 and Figure 7.16 with the experimental data of Laufer (1954) and the standard law of the wall for $Re=50,000$ and $Re=300,000$ respectively. It is clear from Figure 7.15 that the agreement between the calculated results and the law of the wall is very good. The slope is especially well reproduced by the $k-\varepsilon-\gamma$ model. For higher Reynolds number flow (see Figure 7.16), the agreement between the law of the wall and simulations are poorer than at lower Reynolds numbers. However, the slope is perfectly reproduced by the $k-\varepsilon-\gamma$ model again. It should be noted that the spread in the empirical values of A and B appears to be greater in the case of the turbulent pipe flow when compared with the plane channel flow. Nikuradse (1932) found $A=2.5$, $B=5.5$ for his experimental data, and Zagarola and Smits (1998) found $A=2.29$, $B=6.15$ for their experimental data. More values for A , B can be found in the literature. It has been suspected that a departure from the assumed Reynolds number similarity might be

responsible for it. If this were the case, an effect of the Reynolds number on the constants A and B should be expected. For this reason, Hinze (1987) re-examined the old data obtained by Nikuradse (1932). He found that the general trend for the parameter A is to increase with increasing Reynolds number, and the general trend of the values of B is to decrease with increasing Reynolds number. Examining the present simulation results, it can be seen that the effect of the Reynolds number on the constant A is negligible, at least in the Reynolds number range from 50,000 and 300,000. The general trend of the values of B is similar to Hinze's (1987) observation.

7.2 Predictions for Turbulent Quantities

The distributions of the turbulent kinetic energy at four downstream locations for Reynolds numbers of 50,000 and 300,000 are presented together with the experimental data of Laufer (1954) and Lawn (1971) in Figure 7.17 and Figure 7.18, respectively. When using the standard k- ϵ model, wall functions were used to predict the flow. It is believed that the wall function should be applied to a point whose y^+ value is in the range $30 < y^+ < 100$, and is then sufficiently accurate for most situations. In our test cases, the wall function was applied at $r/R=0.957$ so that $53.0 < y^+ < 76.8$ for $Re=50,000$, and the wall function was applied at $r/R=0.990$ so that $65.0 < y^+ < 82.0$ for $Re=300,000$. The simulation results match with the experimental data of Laufer (1954) at $Re=50,000$ better than that of Lawn (1971) at $Re=252,000$ in the fully developed region. As discussed in Section 6.2.3, two equation k- ϵ models over-predict the turbulent kinetic energy near the center of the pipe in the fully developed region. The same is true for the zero equation model and the modified k- ϵ - γ model. The model constant test, which discussed in Chapter 6, has shown that replacing $\sigma_k = 1.0$ with $\sigma_k = 1.4$ will result in a decrease of turbulent kinetic energy in the pipe center in the

fully developed region. Except in the center of the pipe, the simulation results match Laufer's data well for $Re=50,000$, even in the wall region. For $Re=300,000$, the simulation results under-predicted Lawn's data in the wall region.

The profiles of \overline{uv} at $x/D=10, 30$ and 80 for $Re=50,000$ are shown in Figure 7.19. The computed results are compared with Lawn's (1971) data for $Re=38,000$ and $89,000$, measured in the fully developed region. Except in the near wall region, the agreement between the calculation results and the experimental data is fairly good. At $x/D=30$, the predicted values for the turbulence shear stresses are greater than those in the fully developed region, confirming earlier observations reported in the literature by Klein (1981) and Martinuzzi and Pollard (1989). The profiles of \overline{uv} at $x/D=10, 30$ and 80 for $Re=300,000$ are presented together with the experimental data of Richman and Azad (1973) in Figure 7.20. It can be seen that at $x/D = 10$, the predictions obtained by $k-\epsilon-\gamma$ are in better agreement with the experimental data than those obtained by the other three models. As already mentioned, the zero equation mixing-length model is a two-layer model with μ_t given by separate expressions in each layer (Eq. 3.1 and Eq. 3.2). The jagged profile of \overline{uv} close to the wall is caused by the sharp change of μ_t at the surface of the inner and outer layers. In the profile of \overline{uv} obtained by the standard $k-\epsilon$ model, a jag is also found at the location where the wall function was applied. The jag is also caused by the different expressions for μ_t . Due to the negligible effect on the quality of the prediction of the mean velocity and other turbulence quantities, no correction has been made to remove the jag in the distribution of \overline{uv} .

The variation of skin-friction coefficient with Reynolds number, based on the pipe diameter D and bulk velocity U_b is shown in Figure 7.21. The Prandtl's universal law of friction for smooth pipes (see Shlichting, 1979) is given by

$$\frac{1}{\sqrt{C_f}} = 4 \log_{10} (2 \text{Re} \sqrt{C_f}) - 1.6 \quad (7.2)$$

From Figure 7.21, we can see that Eggels' (1994) DNS data perfectly fit the universal law, while Reichert and Azad's (1976) data under predicted the skin friction coefficients compared to the universal law. As to present results, values for lower Reynolds number fit the universal law better than those for higher Reynolds number. Overall the results obtained by Chien's model and the standard k-ε model are better.

The simulation results under Re=100,000 is listed in Table 7.2, with the skin friction C_f^* , calculated by the well know Blasius friction law (Patel and Head, 1969):

$$C_f^* = 0.079 \text{Re}^{-1/4} \quad (7.3)$$

which is generally accepted as being applicable up to a Reynolds number of 100,000. It is obvious that simulations match the Blasius friction law well. The C_f calculated by the Prandtl's universal law is also listed, which is also consistent with the value obtained by the Blasius friction law. Finally, skin friction coefficients along the longitudinal distance of the pipe are compared with the data of Reichert and Azad (1976) in Figure 7.22.

Table 7.2 Skin friction coefficients for fully developed pipe flow

	Re	C_f	C_f^*	$\Delta C_f / C_f \%$
Reichert & Azad	54,000	0.0043	0.0052	-21.4
Reichert & Azad	75,000	0.0041	0.0048	-17.1
Zero equation model	50,000	0.0055	0.0053	3.6
Standard k- ϵ model	50,000	0.0056	0.0053	5.4
Chien model	10,000	0.0078	0.0079	-1.3
Chien model	50,000	0.0055	0.0053	3.6
k- ϵ - γ model	50,000	0.0058	0.0053	8.6
DNS	5,300	0.0092	0.0093	-1.1
Universal Law	3,971	0.010	0.010	0.0
Universal Law	5,715	0.0090	0.0091	-1.1
Universal Law	8,760	0.0080	0.0082	-2.5
Universal Law	14,604	0.0070	0.0072	-2.9
Universal Law	27,376	0.0060	0.0061	-1.7
Universal Law	60,956	0.0050	0.0050	0.0

7.3 Model Performance Assessment

The numerical calculations were performed using a UNIX system on an Ultra 2/2300 machine. The solution-convergence times are summarized in Table 7.3. For Chien's model and the modified k- ϵ - γ model, at Re=300,000, a 240 x 198 grid system was required in order to achieve the necessary resolution of the near wall region. This is not to say that a 240 x 198 grid is necessary, but rather the test results have shown that the grid 120 x 99 is too coarse for

Chien's model and the modified k- ϵ - γ model at Re=300,000. The convergence was declared for all the test cases in Table 7.3 if the average of magnitude of the mass residual throughout the computation domain was less than 10^{-13} .

Table 7.3 Grid selection and CPU time

Model	Re	Grid	CPU (minutes)
Zero eq.	50,000	120 x 99	37
St. k- ϵ	50,000	120 x 99	17
Chien	50,000	120 x 99	56
k- ϵ - γ	50,000	120 x 99	59
Zero eq.	300,000	120 x 99	24
St. k- ϵ	300,000	120 x 99	60
Chien	300,000	240 x 198	304
k- ϵ - γ	300,000	240 x 198	437

It is usually assumed that high order models result in high accuracy solutions but result in longer CPU time. So it is not surprise to find that the k- ϵ - γ model required longer CPU time than Chien's model, as Table 7.3 has shown. The convergence of the mass residual for Re=300,000 is plotted in Figure 7.23. Among the four models, the zero equation models convergence fastest, and the modified k- ϵ - γ model convergence slowest. The overall assessment on each model performance is summarized below.

Van Driest Mixing-Length Model: This is one of the zero equation models, the simplest of all turbulence models. It can be used without any difficult to simulate a flow at very high Reynolds number such as Re=500,000. It converges faster, and requires fewer grid points. However, the model may fail to simulate a complex flow when the process of convective or diffusive transport of turbulence is important. Actually, even for the smooth pipe flow, it fails

to predict the centerline mean velocity “overshoot”, a general feature of pipe flow.

Standard k- ϵ model: The standard k- ϵ model is one of the most widely used turbulence models. It has been successfully applied in many kinds of flow although for some cases such as weak shear layers and axisymmetric jets, satisfactory predictions can not be obtained with the standard constants. It is the ϵ equation that is to be blamed for the lack of universality. In the present tests, the simulation results obtained by this model match the experimental data quite well when the wall function was applied at a position where $30.0 < y^+ < 100.0$.

Chien’s model: Previous literature (Patel, Rodi, and Scheuerer, 1984) show that for the flat-plate boundary layer Chien’s model has the best performance among seven k- ϵ models. The best fit to the law of the wall was achieved by Chien’s model and it also predicts C_f quite accurately. However, in the present tests Chien’s model performed almost as well as the standard k- ϵ model, except it eliminated the need for wall functions.

The modified k- ϵ - γ model: The implementation of this model is quite similar to Chien’s model, except one additional equation needs to be solved. This equation for γ is solved in a manner similar to that for the k or ϵ equation. But due to its stiffness the convergence of the mass residual is oscillatory, therefore more care is required in its solution, especial in the choice of the time step. There is no doubt that this model has a large potential to represent turbulent flow features more correctly in complex flows than two-equation models. In the present tests in the inlet region, its prediction of Reynolds shear stress is in the best agreement with the experimental data among the four models. Also it predicts the mean velocity field as well as if not better than Chien’s model.

7.4 *Physical Process in Developing Turbulent Pipe Flow*

So far, the simulation results for six Reynolds numbers from 10,000 to 500,000 obtained by four models have been presented. But no many discussions on the physical process in the pipe flow have been given. As we know, the Reynolds averaged approach is regarded as an engineering approximation because it doesn't directly provide any information on turbulence structure. However, the distributions of the turbulence characteristics (mean velocity, turbulent kinetic energy, Reynolds shear stress, energy dissipation rate, intermittency factor) are also of value in understanding developing turbulent pipe flow.

For the fully developed turbulent flow in a pipe, the mean-flow conditions are independent of the axial coordinate x . From Figures 6.21-6.23, and 6.25, it can be seen that at $x/D=60$, the flow reaches its fully developed state. Comparing the radial mean velocity distributions (Figure 6.26) with the axial mean velocity distributions (6.24), we see that the magnitude of U/U_b is about 1000 times of the magnitude of V/U_b . Therefore the pipe flow is nearly a parallel flow. Furthermore, from Figure 6.26, we can see that at the inlet region, the radial mean velocity is negative (from wall to pipe center), so the radial velocity accelerates the boundary layer development. Radial mean velocity vs. r/R at more downstream locations are plotted in Figure 7.24 from which we can see that at $x/D=22.5$, the radial mean velocity becomes positive at all cross-stream locations which indicates the boundary layer has merged at this point. When the radial mean velocity in the pipe core becomes positive (from pipe center to wall), according to the mass conservation law, it will accelerate the axial mean velocity at upstream locations. That is why we find an axial mean velocity peak overshoot at $x/D=21.6$.

From Figure 7.25, we can see that in the pipe core region, in the inlet the flow is non-turbulent ($\gamma < 0.05$). Then there is a narrow intermittent region ($0.05 < \gamma < 0.95$). At $x/D=20$, the flow approximately reaches its fully turbulent state. While in the wall region, we can see that at $x/D=5$, the flow already reaches its fully turbulent state ($\gamma > 0.95$). Comparing Figure 6.28 with Figure 6.35, we can see that in both the non-turbulent and intermittent regions, the Reynolds shear stress is smaller. While in the fully turbulent region, the Reynolds shear stress increases along the radial direction from the pipe centerline toward the wall. We know that viscous shear is dominant in the viscous sublayer, so the lower values of Reynolds shear stress in the viscous sublayer makes sense. We also know that in the pipe flow, large scales exist at the near wall region, and turbulence extracts kinetic energy from the mean flow at larger scales through the Reynolds stress. This maybe can explain why both, the distributions of Reynolds shear stress vs. r/R and the distributions of the turbulent kinetic energy vs. r/R , have the peak values in the near wall region (see Figure 6.30 and Figure 6.32). We conclude that most of the turbulence production (turbulent kinetic energy) occurs in the wall region, so we say the wall region is the source of most of the turbulent energy. However, at the same time, the rate of dissipation of turbulent energy (ϵ) is also high in the wall region (see Figure 6.34). Actually, in the wall region, the turbulence production should be approximately balanced by the dissipation rate (see Hinze, Figure 7-69).

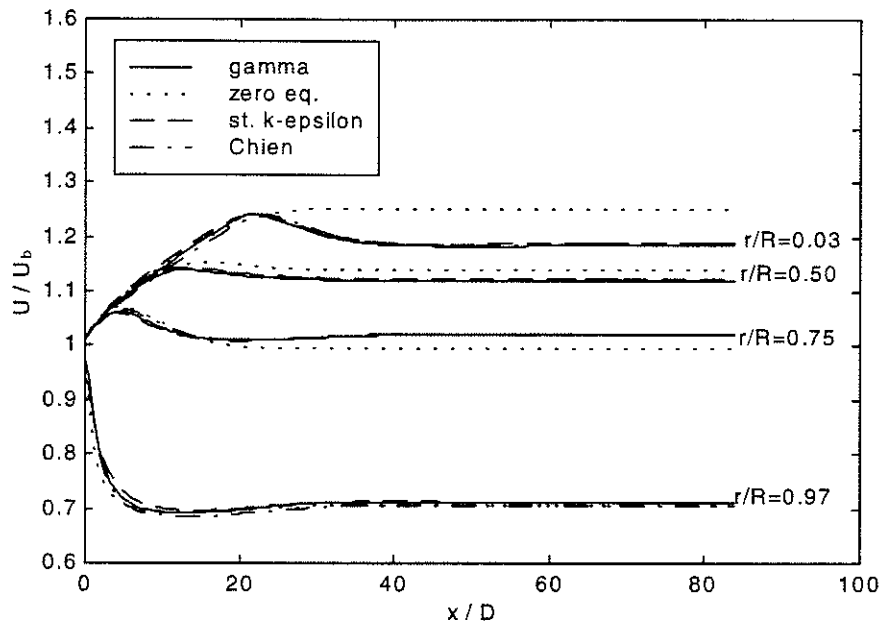


Figure 7.1 Variation of axial velocity with distance downstream of pipe inlet for $Re=50,000$ by four models.

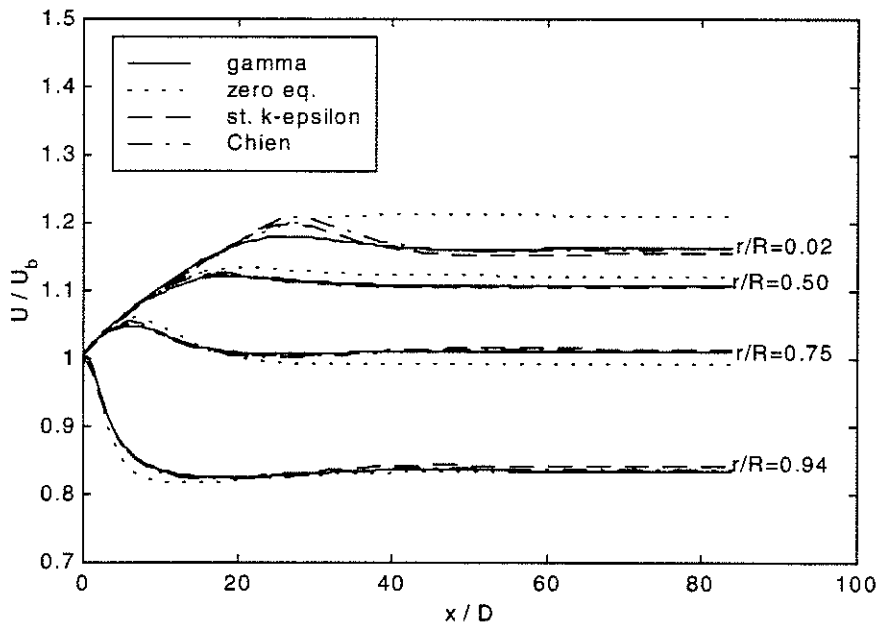


Figure 7.2 Variation of axial velocity with distance downstream of the pipe inlet for $Re=300,000$ by four models.

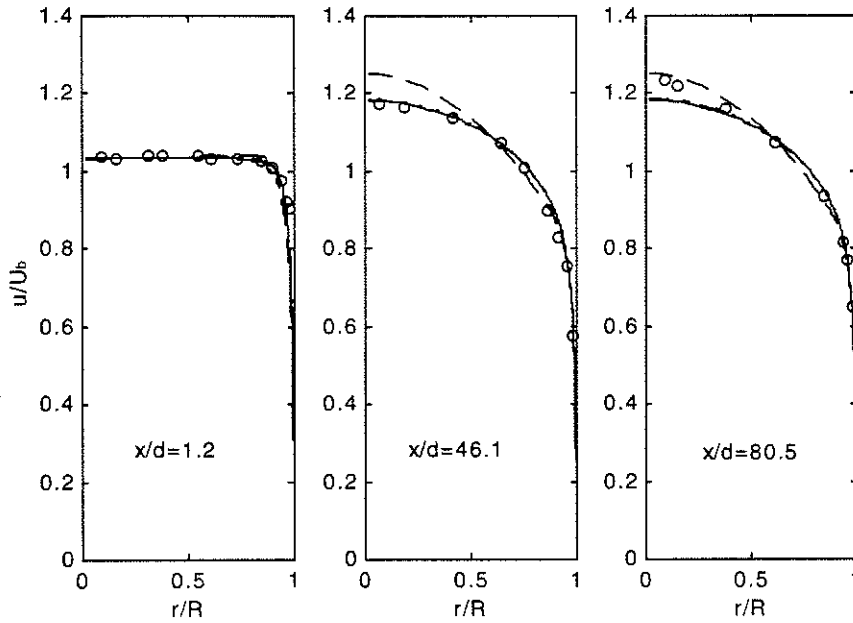


Figure 7.3 Axial velocity vs r/R for $Re=50,000$, compared with the data of Deissler. See Figure 7.4 for line style legend.

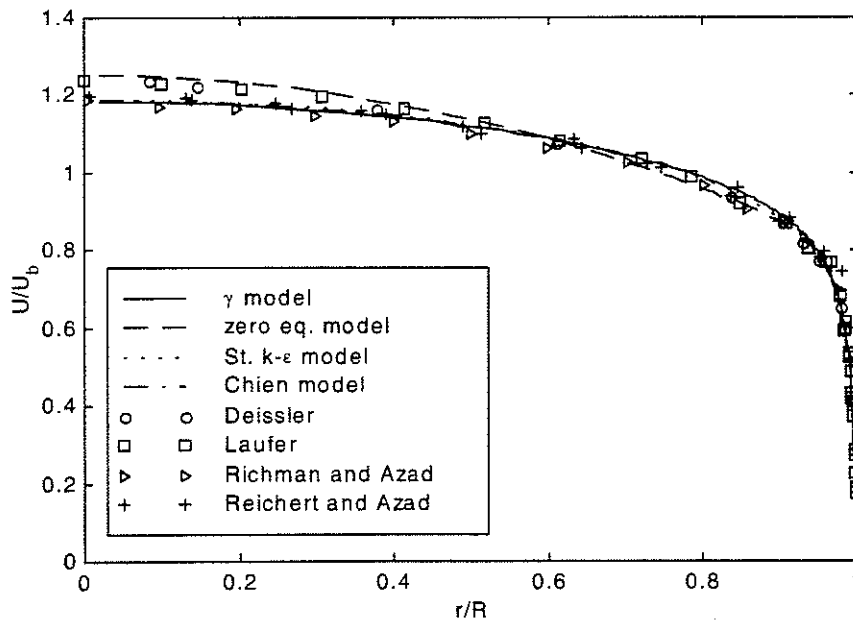


Figure 7.4 Axial velocity vs r/R at $x/D=80.5$ for $Re=50,000$.

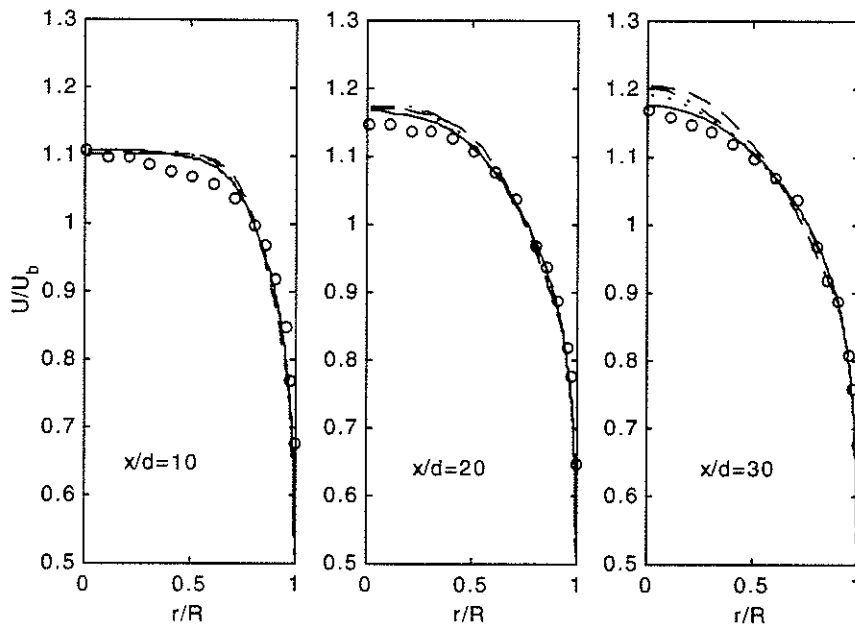


Figure 7.5 Axial velocity vs r/R at $x/D=10, 20, 30$ for $Re=300,000$, compared with the data of Richman and Azad. See Figure 7.4 for line style legend.

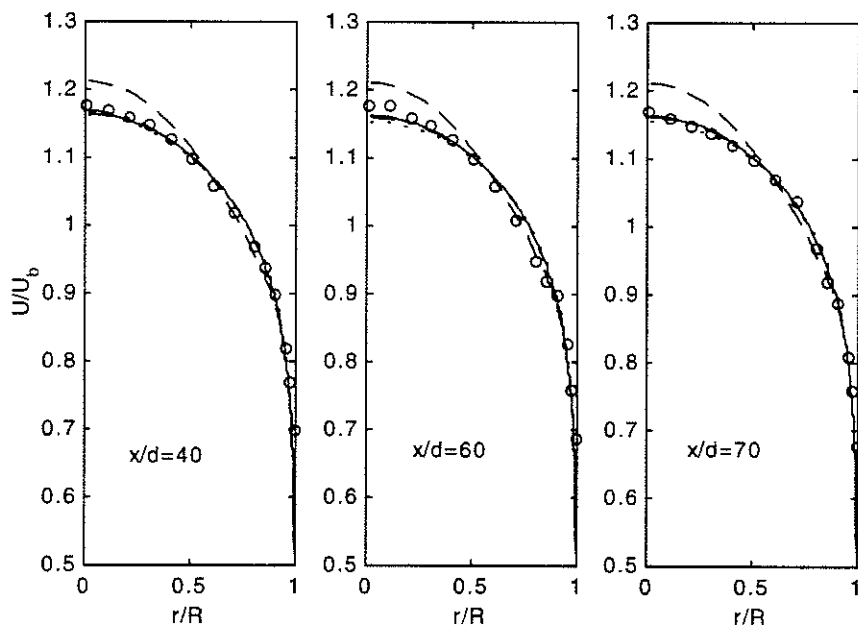


Figure 7.6 Axial velocity vs r/R at $x/D=40, 60, 70$ for $Re=300,000$, compared with the data of Richman and Azad. See Figure 7.4 for line style legend.

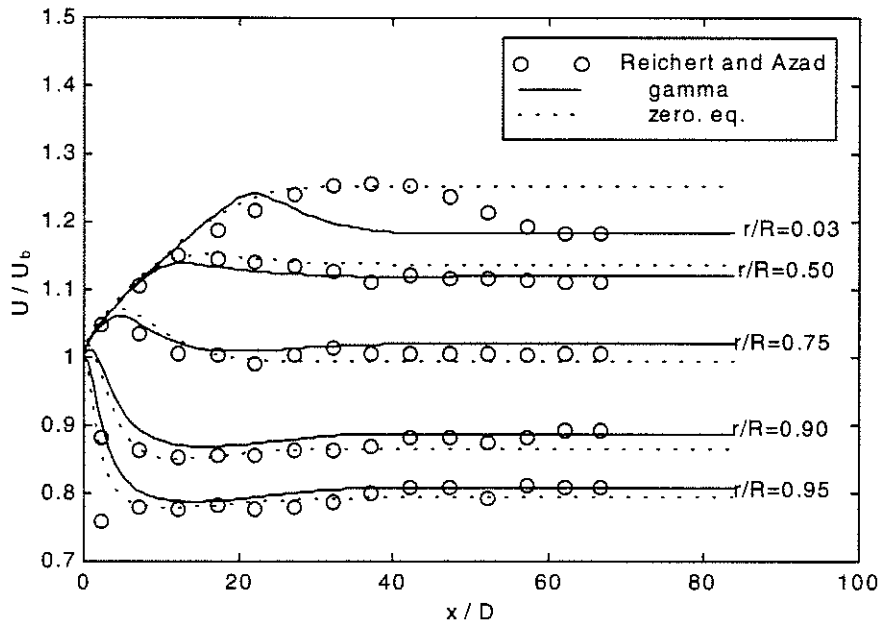


Figure 7.7 Variation of axial velocity with distance downstream of pipe inlet for $Re=50,000$, compared with the data of Reichert and Azad.

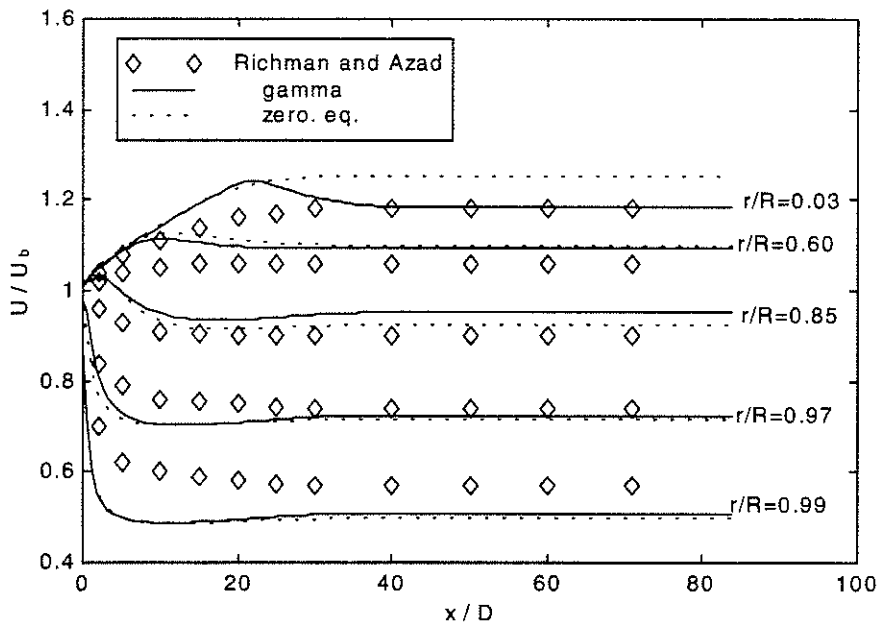


Figure 7.8 Variation of axial velocity with distance downstream of pipe inlet for $Re=50,000$, compared with the data of Richman and Azad.

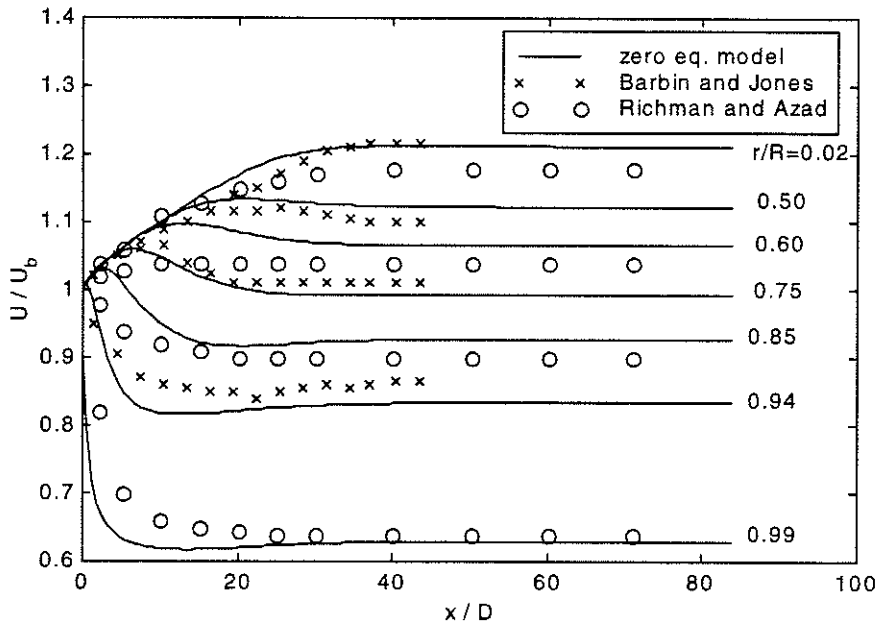


Figure 7.9 Variation of axial velocity with distance downstream of pipe inlet by zero equation model for $Re=300,000$.

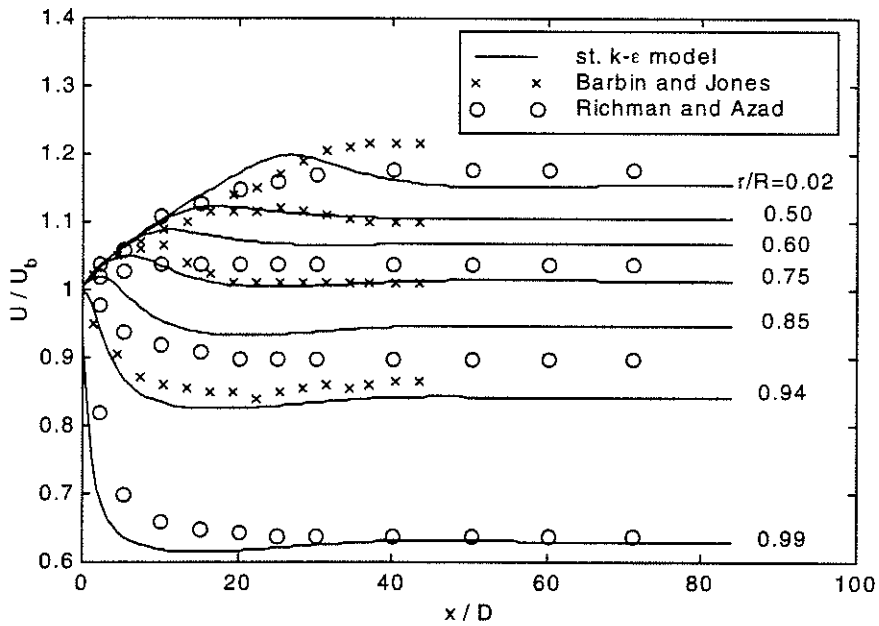


Figure 7.10 Variation of axial velocity with distance downstream of pipe inlet by standard $k-\epsilon$ model for $Re=300,000$.

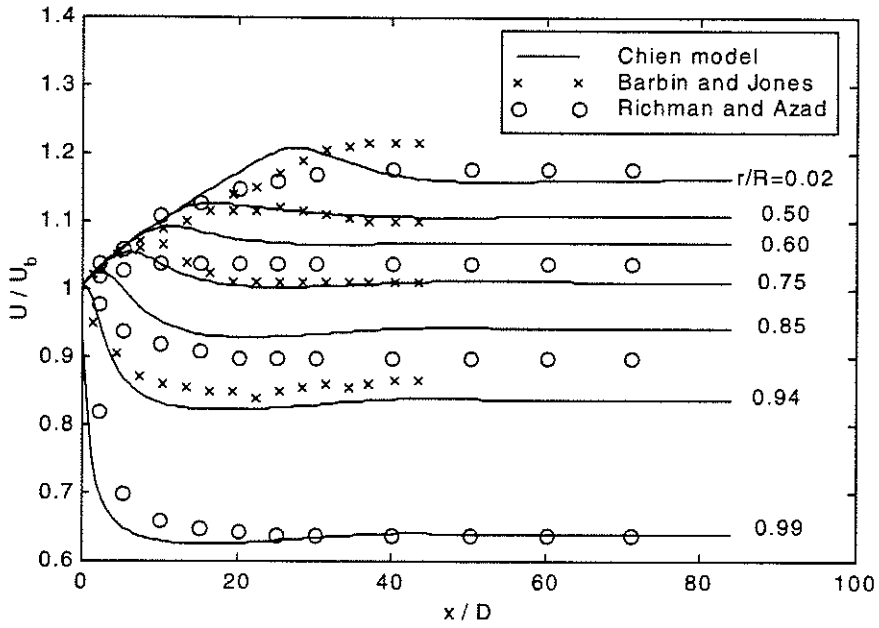


Figure 7.11 Variation of axial velocity with distance downstream of pipe inlet by Chien's model for $Re=300,000$.

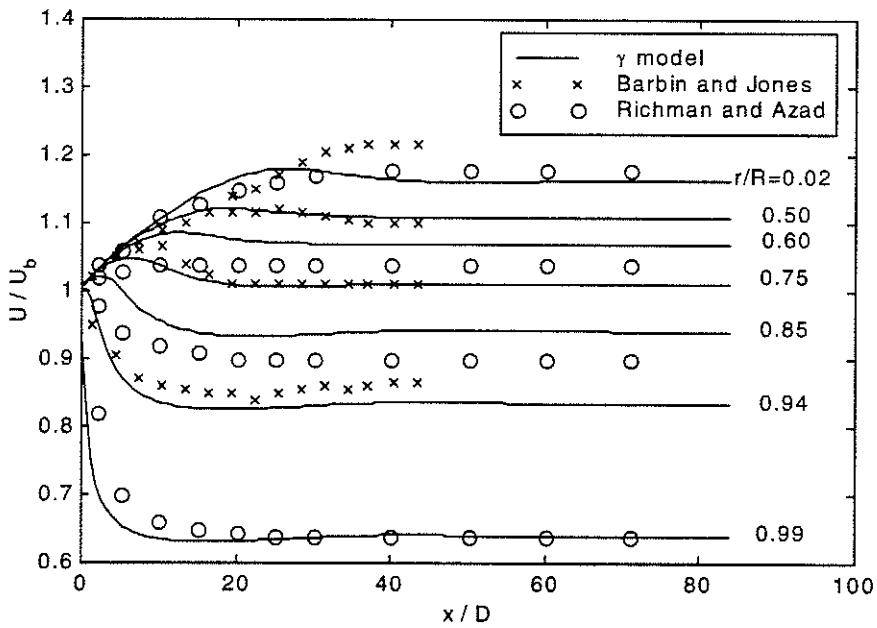


Figure 7.12 Variation of axial velocity with distance downstream of pipe inlet by $k-\epsilon-\gamma$ model for $Re=300,000$.

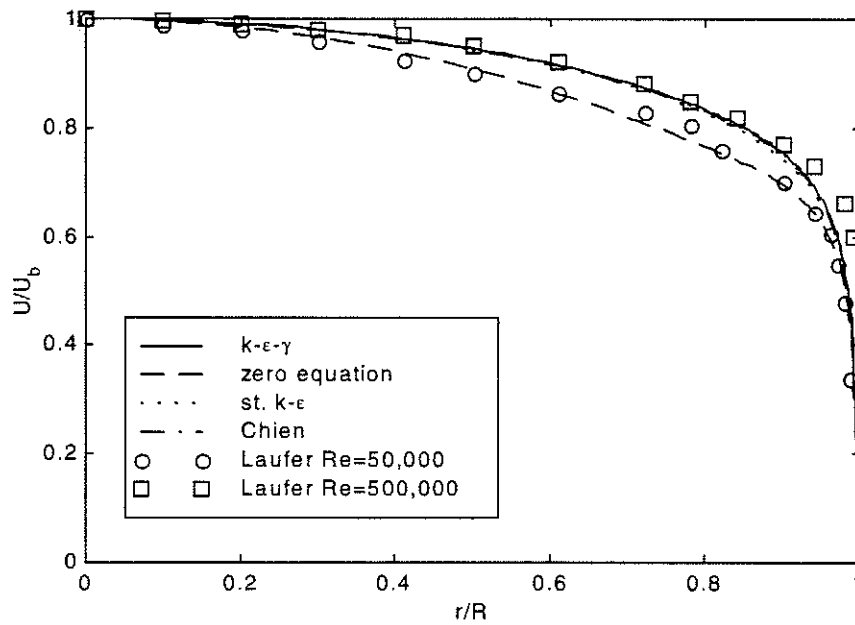


Figure 7.13 Mean velocity distribution at $x/D=83.8$ for $Re=50,000$ from the different models.

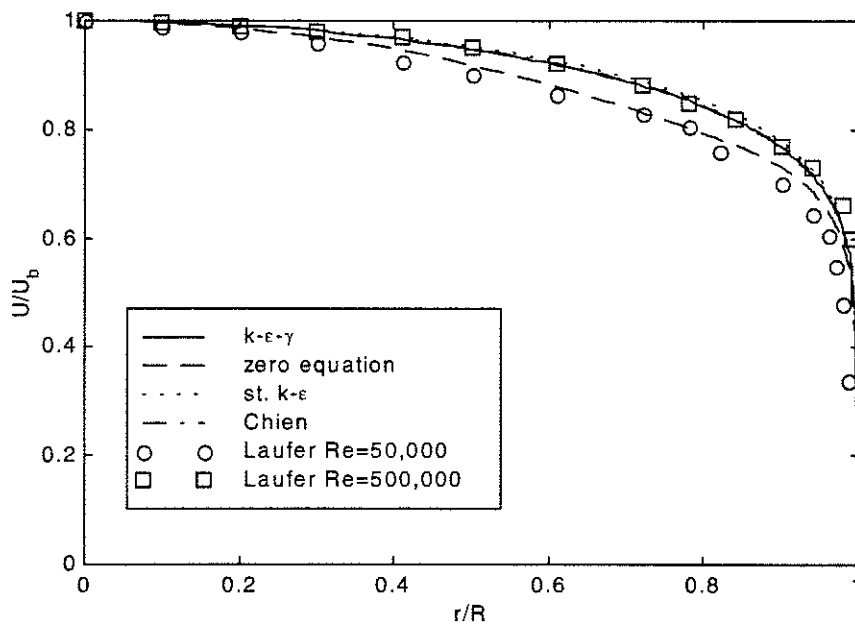


Figure 7.14 Mean velocity distribution at $x/D=83.8$ for $Re=300,000$ from the different models.

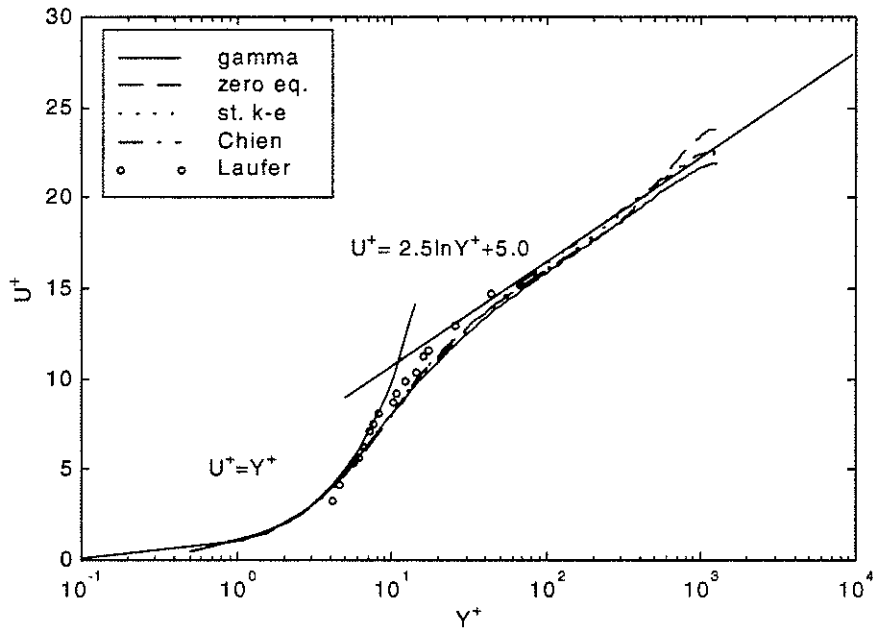


Figure 7.15 u^+ vs y^+ at $x/D=83.8$ for $Re=50,000$.

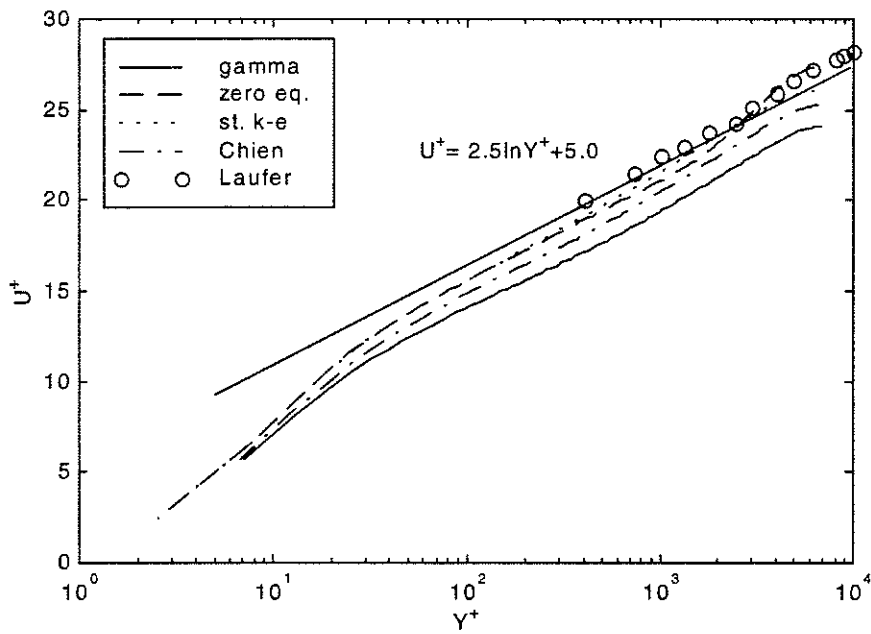


Figure 7.16 u^+ vs y^+ at $x/D=83.8$ for $Re=300,000$.

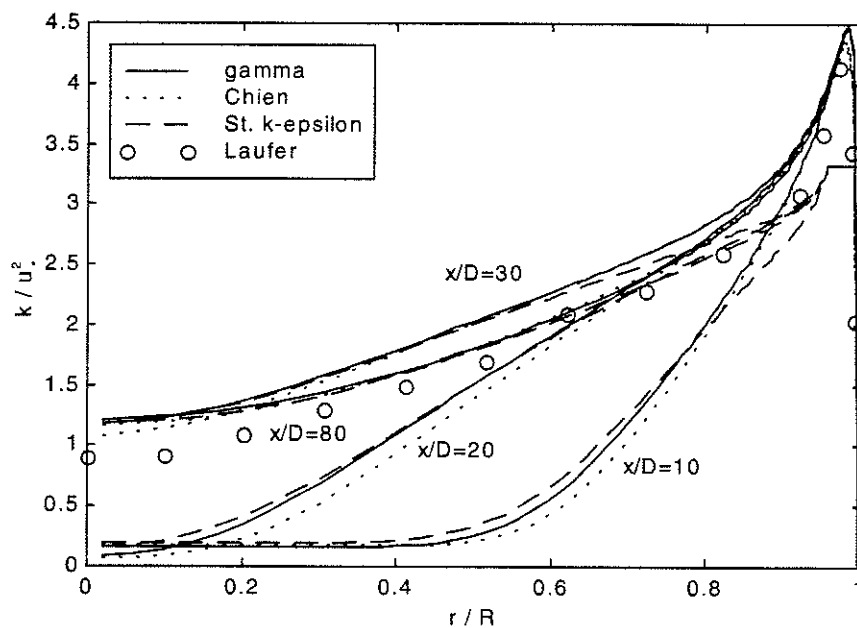


Figure 7.17 Turbulent kinetic energy vs r/R for $Re=50,000$.

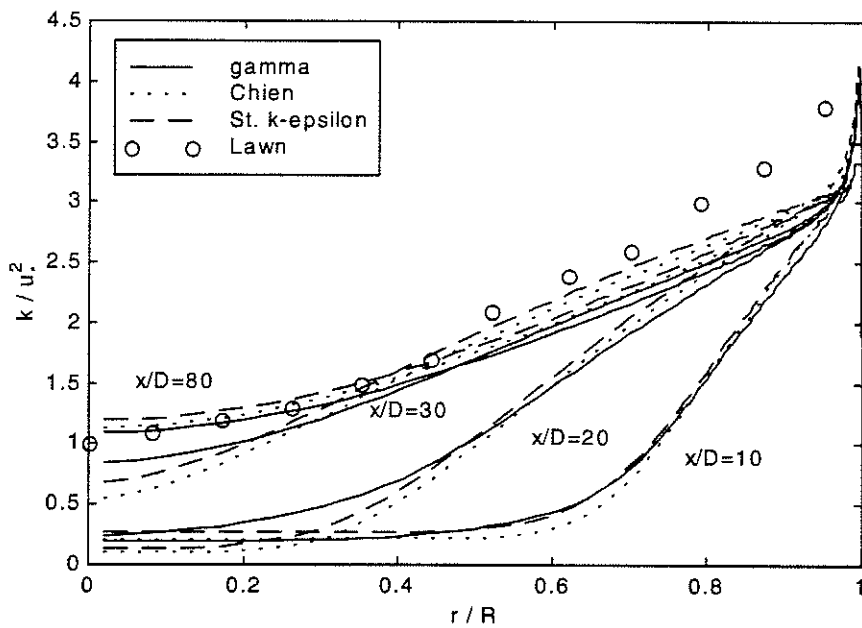


Figure 7.18 Turbulent kinetic energy vs r/R for $Re=300,000$.

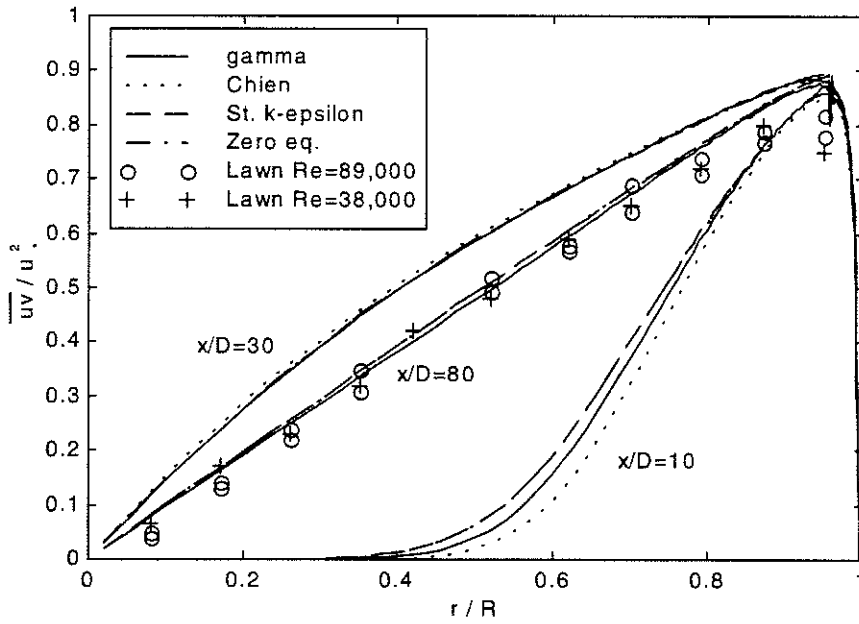


Figure 7.19 Reynolds shear stress vs r/R for $Re=50,000$.

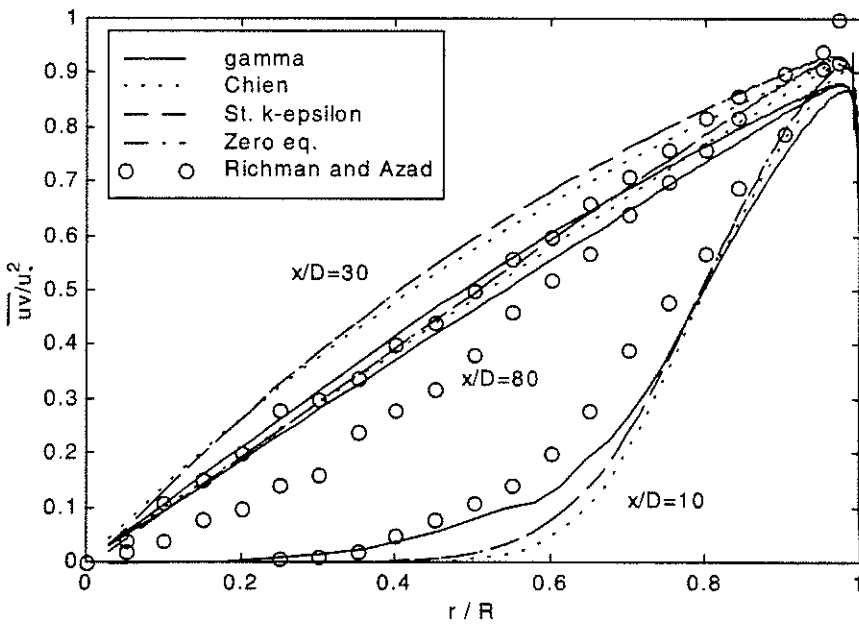


Figure 7.20 Reynolds shear stress vs r/R for $Re=300,000$.

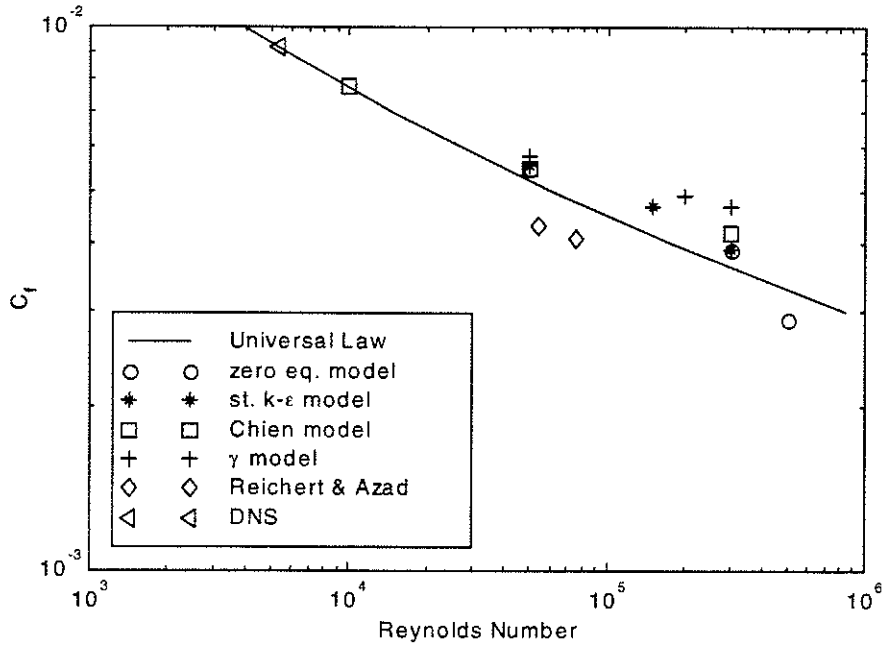


Figure 7.21 Skin friction distributions.

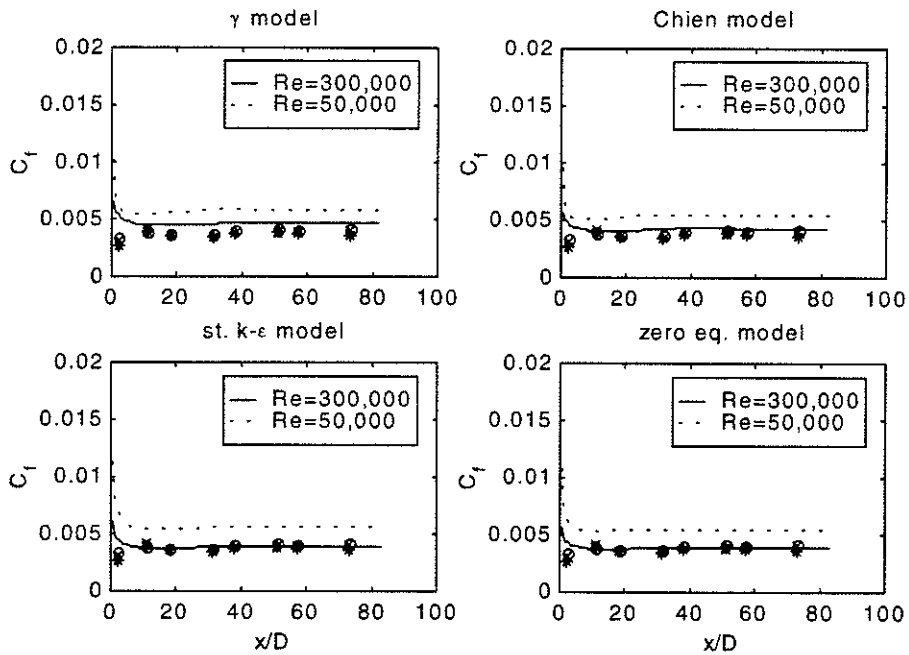


Figure 7.22 Variation of skin friction along the longitudinal distance of the pipe, compare with the data of Reichert and Azad for $Re=54,800$ (o), $Re=75,000$ (x), and $Re=133,000$ (*).

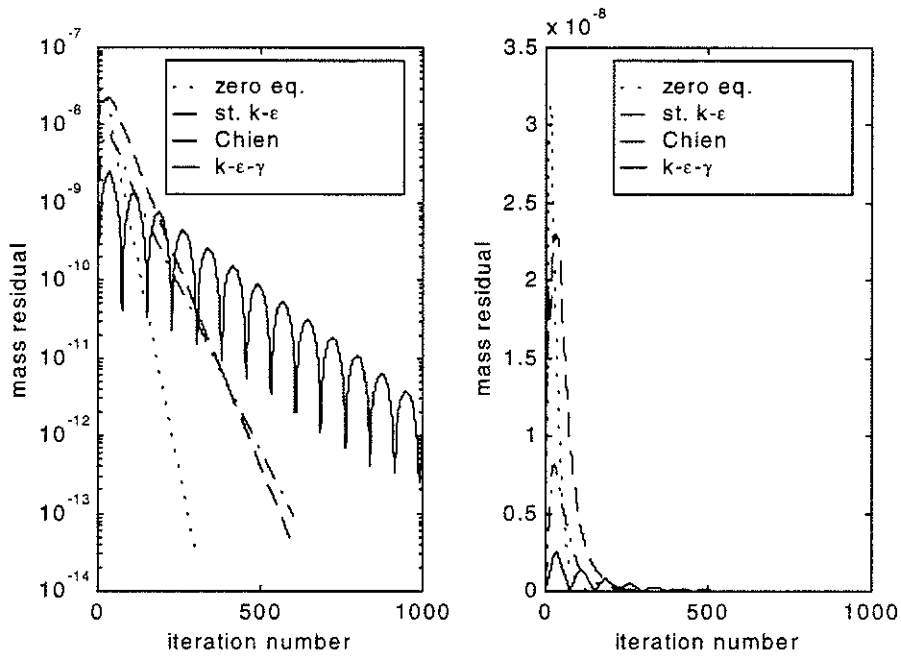


Figure 7.23 Convergence of mass residue for $Re=300,000$.

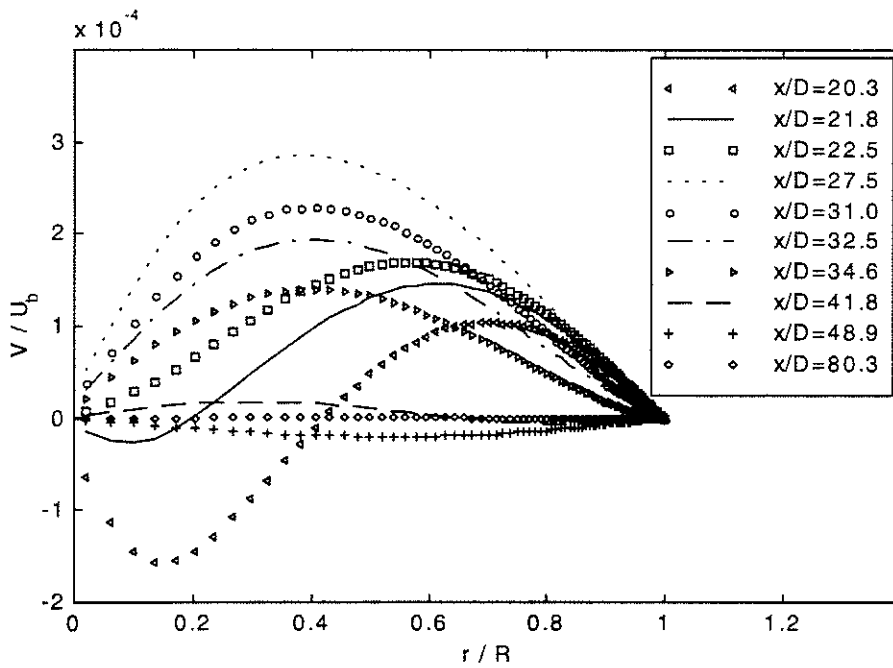


Figure 7.24 Radial velocity vs. r/R at ten downstream locations for $Re=50,000$

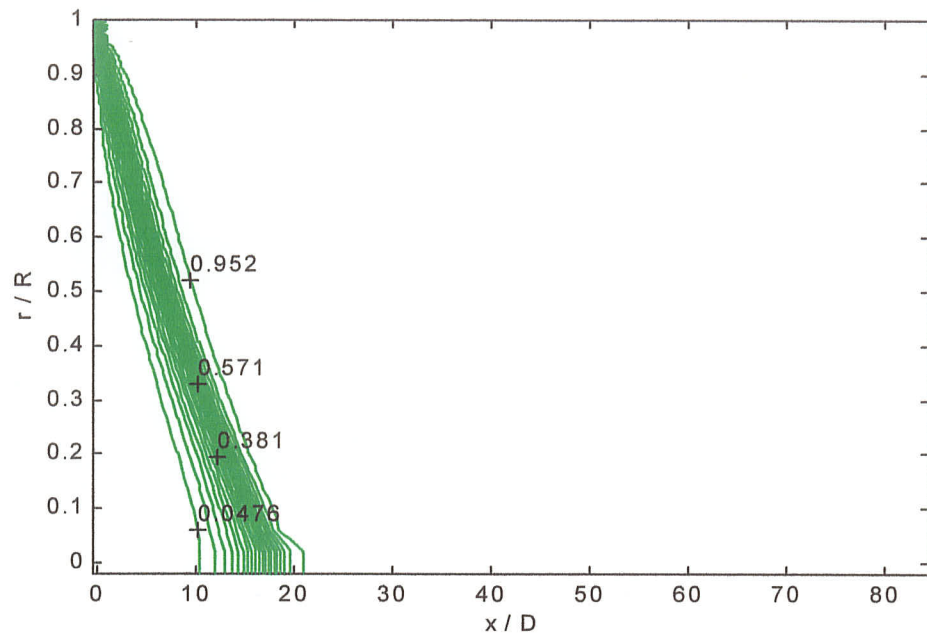


Figure 7.25 Contour plot for intermittent factor for $Re=50,000$

8. CONCLUSIONS AND RECOMMENDATIONS

A modified $k-\varepsilon-\gamma$ model that eliminates the need for wall functions has been tested for developing turbulent pipe flow. The satisfactory simulation results indicate that this intermittency model is capable of predicting internal flow. It is for the first time that the prediction of the developing turbulent pipe flow takes the intermittency into account, therefore it is for the first time that the distributions of the intermittent factor have been presented with details for the pipe flow. From an overall examination of the results of all the test cases, the following conclusions can be drawn.

- 1). Van Driest mixing-length model converges faster, and requires fewer grid points. However, it fails to predict the centerline mean velocity "overshoot", a general feature of pipe flow.
- 2). Two equation $k-\varepsilon$ models (Chien's model and the standard $k-\varepsilon$ model) have quite similar performance for predicting developing turbulent pipe flow, except Chien's model eliminates the need for wall functions. Overall, the predictions obtained by these two models are in agreement with the experimental data.
- 3). Prediction of the Reynolds shear stress at $x/D=10$ obtained by the $k-\varepsilon-\gamma$ model has the best agreement with the experimental data of Richman and Azad among the four models. Also it predicts the mean velocity field as well as if not better than Chien's model according to the comparison with various experimental data. The satisfactory simulation results indicate that this $k-\varepsilon-\gamma$ model is capable of predicting internal flows.
- 4). Contrary to Reichert and Azad's (1976) observation, the present results show that the higher the flow Reynolds number is, the further downstream the centerline mean velocity

peak overshoot position moves. The reason for this is unknown at present and further detailed study is required.

5). Both axial and radial velocity profiles show that the flow at Reynolds numbers from $Re=50,000$ to $500,000$ can be considered to be fully developed after $x/D=50$. This conclusion is consistent with Richman and Azad's (1973) finding. However, the profiles of the turbulent kinetic energy and the Reynolds shear stress indicate that turbulent quantities take longer (after $x/D=60$) to reach the fully developed state.

6). The simulation results at $Re=300,000$ confirms Eggels et al. (1994) and Patel and Head's (1969) conclusion that the mean velocity profile in the pipe fails to match the universal law of the wall, in contrast to channel flow. It also confirms Hinze's observation that the general trend of the values of B is to decrease with increasing Reynolds number.

7). The predicted skin friction coefficients in the fully developed region obtained by the four models obey the well know Blasius friction law for Reynolds number under $100,000$.

8). The present results clearly show that the static pressure is almost constant across the pipe section, and it decreases as the flow develops (as demonstrated by the $k-\varepsilon-\gamma$ model given in this thesis, the same conclusions are obtained for the other three models). This is consistent with Richman and Azad's (1973) observation.

9). The intermittency factor profiles indicate that the inlet of a smooth pipe region is a highly intermittency region, and the higher the Reynolds number is, the longer the flow takes to reach its fully turbulent state. This is consistent with the previously known characteristics of the pipe flow (White, 1986).

10). The results of the model constant test show that using $\sigma_k=1.4$ instead of $\sigma_k=1.0$ does improve the prediction for the turbulent kinetic energy in the pipe center region.

Based on conclusion 6, the author recommends that further work should be focused on obtaining a corrected law of the wall for pipe flow ($U^+ = A \ln Y^+ + B$, where A and B are not constants, but the functions of the Reynolds number). The author also recommends that more formulas should be tested for calculating $\frac{dU}{dy}$ at the near wall region in order to obtain more accurate prediction of u_* and C_f for flow with higher Reynolds number. Finally, the author recommends that more complex internal flows should be chosen as test cases in order to obtain more information about this model's performance.

REFERENCES

- Ahn, J. W., and Sung, H. J., 1995, "Prediction of Two-Dimensional Momentumless Wake by k - ϵ - γ Model," *AIAA Journal*, Vol. 33, No. 4, pp. 611-617.
- Anderson, D. A., Tannehill, J. C., and Pletcher, R. H., 1984, *Computational Fluid Mechanics and Heat Transfer*, Taylor & Francis.
- Barbin, A. J., and Jones, J. B., 1963, "Turbulent Flow in the Inlet Region of a Smooth Pipe," *ASME Journal of Basic Engineering*, Vol. 29, pp. 29-34.
- Bradbury, L. J. S., 1965, "The Structure of a Self-Preserving Turbulent Plant Jet," *Journal of Fluid Mechanics*, Vol. 23, pp. 31-64.
- Byggstoyl, S., and Kollmann, W., 1981, "Closure Model for Intermittent Turbulent Flows," *International Journal of Heat and Mass Transfer*, Vol. 24, No. 11, pp. 1811-1822.
- Byggstoyl, S., and Kollmann, W., 1986, "Stress Transport in the Rotational and Irrotational Zones of Turbulent Shear Flows," *Physics Fluids*, Vol. 29, No. 5, pp. 1423-1429.
- Byggstoyl, S., and Kollmann, W., 1986, "A Closure Model for Conditioned Stress Equations and its Application to Turbulent Shear Flows," *Physics Fluids*, Vol. 29, No. 5, pp. 1430-1440.
- Cebeci, T., Clark, R. W., Chang, K. C., Halsey, N. D., and Lee, K., 1986, "Airfoils with Separation and the Resulting Wakes," *Journal of Fluid Mechanics*, Vol. 163, pp. 323-347.
- Chevray, R., and Tutu, N. K., 1977, "Intermittency and Preferential Transport of Heat in a Round Jet," *Journal of Fluid Mechanics*, Vol. 88, pp. 136-160.
- Chien, K. Y., 1982, "Predictions of Channel and Boundary-Layer Flows with a Low-Reynolds-Number Turbulent Model," *AIAA Journal*, Vol. 20, No. 1, pp. 33-38.
- Cho, J. R., and Chung, M. K., 1992, "A k - ϵ - γ Equation Turbulence Model," *Journal of Fluid Mechanics*, Vol. 237, pp. 301-322.
- Clauser, F. H., 1956, *The Turbulent Boundary Layer*, *Advances in Applied Mechanics*, Vol. IV, Academic Press, New York.
- Cockrell, D. J., 1964, *Boundary Layer Effects in Diffusers*, PH. D. Thesis, University of Nottingham.

- Cockrell, D. J., 1967, Effect of Inlet and Outlet Conditions on Pipe and Duct Components, The Ninth Members Conference, The British Hydromechanical Research Association, SP 929.
- Cockrell, D. J., and Markland, E., 1962, "The Effect of Inlet Conditions on Incompressible Fluid Flow Through Conical Diffusers," *Journal of the Royal Aeronautical Society*, Vol. 66, pp. 51-52.
- Corrsin, S., and Kistler, A. L., 1954, The Free-Stream Boundaries of Turbulent Flows, NACA TN-3133.
- Daly, B. J., and Harlow, F. H., 1970, "Transport Equations in Turbulence," *Physics of Fluids*, Vol. 13, pp. 2634-2649.
- Deissler, R. G., 1950, Analytical and Experimental Investigation of Adiabatic Turbulent Flow in Smooth Tubes, NACA Technical Note 2138.
- Deissler, R. G., 1955, "Turbulent Heat Transfer and Friction in the Entrance Region of Smooth Passages," *Transactions of the ASME*, Vol. 77, pp. 1221-1233.
- Den Toonder, J. M. J., and Nieuwstadt, F. T. M., 1997, "Reynolds Number Effects in a Turbulent Pipe Flow for Low to Moderate Re ," *Physics of Fluids*, Vol. 9, No. 11, pp. 3398-3409.
- Derksen, R. W., and Azad, R. S., 1981, "Behavior of the Turbulent Energy Equation at a Fixed Boundary," *AIAA Journal*, Vol. 19, pp. 238-239.
- Dewan, A., Arakeri, J. H., and Srinivasan, J., 1997, "A New Turbulence Model for the Axisymmetric Plume," *Applied Mathematical Modeling*, Vol. 21, pp. 709-719.
- Donaldson, C. duP., and Rosenbaum, H., 1968, Calculation of the Turbulent Shear Flows Through Closure of the Reynolds Equations by Invariant Modeling, ARAP Report No. 127, Aeronautical Research Associates of Princeton, Princeton, NJ.
- Dopazo, C., 1977, "On Conditional Averages for Intermittent Turbulent Flows," *Journal of Fluid Mechanics*, Vol. 81, pp. 433-438.
- Dopazo, C., and O'Brien, E. E., 1979, Intermittency in Free Turbulent Shear Flows, *Turbulent Shear Flows I (Selected Papers from the First International Symposium on Turbulent Shear Flows, The Pennsylvania State University, University Park, Pennsylvania, USA, April 18-20, 1977)*, Edited by Durst, F., Launder, B. E., Schmidt, F. W., and Whitelaw, J. H., Springer-Verlag Berlin Heidelberg New York.

- Dutoya, D., and Michard, P., 1981, A Program for Calculating Boundary Layers along Compressor and Turbine Blades, Numerical Methods in Heat Transfer, edited by Lewis, R. W., Morgan, K., and Zienkiewicz, O. C., John Wiley and Sons, New York.
- Eggels, J. G. M., Unger, F., Weiss, M. H., Westweweel, J., Adrian, R. J., Friedrich, R., and Nieuwstadt, F. T. M., 1994, "Fully Developed Turbulent Pipe Flow: A Comparison between Direct Numerical Simulation and Experiment," Journal of Fluid Mechanics, Vol. 268, pp. 175-209.
- Ferziger, J. H., 1995, Large Eddy Simulation, In Hussaini, M. Y. and Gatski, T., (eds.), Simulation and Modeling of Turbulent Flows, Cambridge Univ. Press, New York.
- Ferziger, J. H., and Peric, M., 1996, Computational Methods for Fluid Dynamics, Springer-Verlag Berlin Heidelberg.
- Emmons, H. W., 1954, Shear Flow Turbulence, Proceedings of the 2nd U. S. Congress of Applied Mechanics, ASME.
- Gutmark, E., and Wygnanski, I., 1976, "The Planar Turbulent Jet," Journal of Fluid Mechanics, Vol. 73, pp. 465-495.
- Harlow, F. H., and Nakayama, P. I., 1968, Transport of Turbulence Energy Decay Rate, Los Alamos Science Lab., University of California Report LA-3854.
- Hassid, S., and Poreh, M., 1978, "A Turbulent Energy Dissipation Model for Flows with Drag Reduction," Journal of Fluids Engineering, Vol. 100, pp. 107-112.
- Haworth, D. C., and Pope, S. B., 1987, "A PDF Modeling Study of Self-Similar Turbulent Free Shear Flows," Physics of Fluids, Vol. 30, pp. 1026-1044.
- Hinze, J. O., 1987, Turbulence, Second Edition, McGraw-Hill, Inc., New York etc.
- Hoffman, G. H., 1975, "Improved form of the Low Reynolds Number k- ϵ Turbulence Model," The Physics of Fluids, Vol. 18, No. 3, pp. 309-313.
- Hwang, Y.-H., and Liou, T.-M., 1991, "Expressions for k and ϵ Near Walls," AIAA Journal, Vol. 29, No. 3, pp. 477-479.
- Janicka, J., and Kollmann, W., 1985, Reynolds-Stress Closure Model for Conditional Variables, Turbulent Shear Flows 4 (Selected Papers from the Fourth International Symposium on Turbulent Shear Flows, University of Karlsruhe, Karlsruhe, FRG, September 12-14, 1983), Edited by Bradbury, L. J. S., Durst, F., Launder, B. E., Schmidt, F. W., and Whitelaw, J. H., Springer-Verlag Berlin Heidelberg New York Tokyo.

- Jones, W. P., and Launder, B. E., 1972, "The Prediction of Laminarization with a Two-Equation Model of Turbulence," *International Journal of Heat and Mass Transfer*, Vol. 15, pp. 301-314.
- Jones, W. P., and Launder, B. E., 1973, "The Calculation of Low-Reynolds-Number Phenomena with a Two-Equation Model of Turbulence," *International Journal of Heat and Mass Transfer*, Vol. 16, pp. 1119-1130.
- Kim, K. S., and Chung, M. K., 1995, "Computation of the Turbulent Flow Field around an Aerofoil by $k-\epsilon-\gamma$ Model in a Non-Staggered, C-Type Single-Grid System," *Communications in Numerical Methods in Engineering*, Vol. 11, pp. 873-886.
- Klein, A., 1981, "Review: Turbulent Developing Pipe Flow," *Journal of Fluids Engineering*, Vol. 103, pp. 243-249.
- Kollmann, W., 1985, *Intermittent Turbulent Flow*, *Frontiers in Fluid Mechanics (A Collection of Research Papers Written in Commemoration of the 65th Birthday of Stanley Corrsin)*. Edited by Davis, S. H., and Lumley, J. L., Springer-Verlag Berlin Heidelberg New York Tokyo.
- Kolmogorov, A. N., 1942, "Equations of Turbulent Motion of an Incompressible Fluid," *Izvestia Academy of Sciences, USSR, Physics*, Vol. 6, Nos. 1 and 2, pp. 56-58.
- Kr. Sharan, V., 1974, "The Effect of Inlet Disturbances on Turbulent Boundary Layer Development in a Parallel Pipe," *Journal of Applied Mathematics and Physics (ZAMP)*, Vol. 25, pp. 659-666.
- Lam, C. K. G., and Bremhorst, K., 1981, "A Modified Form of the $k-\epsilon$ Model for Predicting Wall Turbulence," *Journal of Fluids Engineering, Transactions of the ASME*, Vol. 103, pp. 456-460.
- Laufer, J., 1954, *The Structure of Turbulence in Fully Developed Pipe Flow*, NACA Report 1174.
- Launder, B. E., Reece, G. J., and Rodi, W., 1975, "Progress in the Development of a Reynolds-Stress Turbulence Closure," *Journal of Fluid Mechanics*, Vol. 68, part 3, pp. 537-566.
- Launder, B. E., and Sharma, B. I., 1974, "Application of the Energy Dissipation Model of Turbulence to the Calculation of Flow Near a Spinning Disc," *Letters in Heat and Mass Transfer*, Vol. 1, No. 2, pp. 131-138.
- Launder, B. E., and Spalding, D. B., 1974, "The Numerical Computation of Turbulent Flows," *Computer Methods in Applied Mechanics and Engineering*, Vol. 3, pp. 269-289.

- Lawn, C. J., 1971, "The Determination of the Rate of Dissipation in Turbulent Pipe Flow," *Journal of Fluid Mechanics*, Vol. 48, pp. 477-505.
- Laws, E. M., Lim, E.-H., and Livesey, J. L., 1979, *Turbulent Pipe Flows in Development and Decay*, 2nd Symposium on Turbulent Shear Flows, Imperial College, London.
- Leonard, A. O., 1995, *Direct Numerical Simulation*, In Gatski, T., (ed.), *Turbulence and its Simulation*, Springer, New York.
- Libby, P. A., 1975, "On the Prediction of Intermittent Turbulent Flows," *Journal of Fluid Mechanics*, Vol. 68, Part 2, pp. 273-295.
- Libby, P. A., 1976, "Prediction of the Intermittent Turbulent Wake of a Heated Cylinder," *The Physics of Fluids*, Vol. 19, No. 4, pp. 494-502.
- Lumley, J. L., 1978, "Computational Modeling of Turbulent Flows," *Advanced Applied Mechanics*, Vol. 18, pp. 123-176.
- Martinuzzi, R., 1985, *Comparative Study of Turbulence Models in Predicting Turbulent Pipe Flow*, M. S. Thesis, Department of Mechanical Engineering, Queen's University, Kingston, Ontario, Canada.
- Martinuzzi, R., and Pollard, A., 1989, "Comparative Study of Turbulence Models in Predicting Turbulent Pipe Flow Part I: Algebraic Stress and k- ϵ Models," *AIAA Journal*, Vol. 27, No. 1, pp. 29-36.
- Miller, D., 1971, *Performance of Straight Diffusers, Internal Flow, A Guide to Losses in Pipe and Duct Systems, Part II*, BHRA – Fluid Engineering.
- Nagano, Y., and Tagawa, M., 1990, "An Improved k- ϵ Model for Boundary Layer Flows," *Journal of Fluids Engineering*, Vol. 112, pp. 33-39.
- Nikuradse, J., 1932, *Gesetzma β igkeit der Turbulent Stromung ig Glatten Rohren*, Verein Deutscher Ingenieure-Forschungsheft, No 356.
- Ninomiya, H., and Onishi, K., 1991, *Flow Analysis using PC*, Computational Mechanics Publication.
- Patankar, S. V., 1980, *Numerical Heat Transfer and Fluid Flow*, Hemisphere Publishing Corporation.
- Patel, V. C., and Head, M. R., 1969, "Some Observations on Skin Friction and Velocity Profiles in Fully Developed Pipe and Channel Flows," *Journal of Fluid Mechanics*, Vol. 38, Part 1, pp. 181-201.

- Patel, V. C., Rodi, W., and Scheuerer, G., 1984, "Turbulence Models for Near-Wall and Low Reynolds Number Flows: A Review," *AIAA Journal*, Vol. 23, No. 9, pp. 1308-1319.
- Patel, V. C., and Scheuerer, G., 1981, "Calculation of Two-Dimensional Near and Far Wake," *AIAA Journal*, Vol. 20, pp.900-907.
- Pozzorini, R., 1976, *Das turbulente Stromungsfeld in einem langen Kreisegel-Diffusor*, Ph. D. dissertation ETH Zurich, Eduard Truninger AG Zurich.
- Prandtl, L., 1925, "Uber die ausgebildete Turbulenz," *Z. Angew. Math. Mech.*, Vol. 5, pp. 136-139.
- Prandtl, L., 1942, "Bemerkungen Zur Theorie der freien Turbulenz," *ZAMM*, Vol. 22, pp. 241-243.
- Prandtl, L., 1945, "Uber eine neues Formelsystem fur die ausgebildete Turbulenz," *Nachr. Akad. Wiss., Goettingen, Math. Phys. Ke.*, pp. 6-19.
- Priest, A. J., 1975, *Incompressible Turbulent Flow in Pipes and Conical Diffusers*, Ph. D. Thesis, University of Salford.
- Raithby, G. D., and Torrance, K. E., 1974, "Upstream-Weighted Differencing Schemes and Their Application to Elliptic Problems Involving Fluid Flow," *Computational Fluids*, Vol. 2, pp. 191-206.
- Ramaprin, B. R., and Chandrasekhara, M. S., 1985, "LDA Measurements in Plane Turbulent Jets," *Transactions of the ASME I, Journal of Fluids Engineering*, Vol. 107, pp. 264-271.
- Reichert, J. K., and Azad, R. S., 1976, "Nonasymptotic Behavior of Developing Turbulent Pipe Flow," *Canadian Journal of Physics*, Vol. 54, pp. 268-278.
- Reichert, J. K., 1977, *A Study of Developing Turbulent Pipe Flow*, Ph. D. Thesis, University of Manitoba, Winnipeg, Canada.
- Reynolds, W. C., 1976, "Computation of Turbulent Flows," *Annual Review of Fluid Mechanics*, Vol. 8, pp. 183-208.
- Reynolds, W. C., 1987, "Fundamentals of Turbulence for Turbulence Modeling and Simulation," In *Lecture Notes for von Karman Institute, AGARD Lecture Series No. 86*, pp. 1-66, New York: NATO.
- Richman, J. W., and Azad, R. S., 1973, "Developing Turbulent Flow in Smooth Pipes," *Applied Science Research*, Vol. 28, pp. 419-441.

- Roache, P. J., 1994, "Perspective: A Method for Uniform reporting of Grid Refinement Studies," ASME Journal of Fluids Engineering, Vol. 116, pp. 405-413.
- Rodi, W., 1984, Turbulence Models and Their Application in Hydraulics: A State of the Art Review, Second Revised Edition, Institute fur Hydromechanik, University of Karlsruhe, Karlsruhe, Federal Republic of Germany.
- Saffman, P. G., 1970, "A Model for Inhomogenous Turbulent Flow," Proc. Roy. Soc., Lond., Vol. A317, pp. 417-433.
- Sale, D. E., 1967, Entrance Effects in Incompressible Diffuser Flow, M. Sc. Thesis, University of Manchester.
- Scarborough, J. B., 1958, Numerical Mathematical Analysis, 4th Edition, Johns Hopkins Press, Baltimore.
- Schetz, J. A., 1984, Foundations of Boundary Layer Theory for Momentum, Heat, and Mass Transfer, Prentice-Hall, Inc.
- Schlichting, H., 1979, Boundary Layer Theory, Seventh Edition, McGraw-Hill, New York.
- Shih, T. H., 1990, An Improved k- ϵ Model for Near-Wall Turbulence and Comparison with Direct Numerical Simulation, NASA Technical Memorandum 103221.
- Speziale, C. G., 1985, "Modeling the Pressure-Gradient-Velocity Correlation of Turbulence," Physics of Fluids, Vol. 28, pp.69-71.
- Tennekes, H., and Lumley, J. L., 1972, A First Course in Turbulence, The MIT Press.
- Uspuras, E. V., Vilemas, J. V., and Poskas, P. S., 1989, "Balance of the Energy of Turbulence of a Gas Flow in the Inlet Zone of a Pipe," Fluid Mechanics - Soviet Research, Vol. 18, No. 4, pp. 54-61.
- Van Doormal, J. P., and Raithby, G. D., 1984, "Enhancement of the SIMPLE Method for Predicting Incompressible Fluid Flows," Numerical Heat Transfer, Vol. 7, pp. 147-163.
- Van Driest, E. R., 1956, "On Turbulent Flow near a Wall," Journal of Aerospace Science, Vol. 23, pp. 1007-1012.
- Weir, J., Priest, A. J., and Sharan, V. K., 1974, "Research Note: The Effect of Inlet Disturbance on Turbulent Pipe Flow," Journal of Mechanical Engineering Science, Vol. 16, pp. 211-213.

Weighardt, K., and Tillmann, W., 1951, On the Turbulent Friction Layer for Rising Pressure, NACA TM 1314.

White, F. M., 1986, Fluid Mechanics, 2nd ed. New York: McGraw-Hill.

Wilcox, D. C., 1993, Turbulence Modeling for CFD, DCW Industries, Inc.

Yang, Z., and Shih, T. H., 1993, "New Time Scale Based k- ϵ Model for Near-wall Turbulence," AIAA Journal, Vol. 31, No. 7, pp.1191-1198.

Zagarolar, M. V., and Smits, A. J., 1998, "Mean-flow Scaling of Turbulent Pipe Flow," Journal of Fluid Mechanics, Vol. 373, pp. 33-79.

APPENDIX: LIST OF FREQUENTLY USED ABBREVIATIONS

3D	Three-dimensional
AEDS	Approximate Exponential Difference Scheme
CDS	Central Difference Scheme
CFD	Computational Fluid Dynamics
CV	Control Volume
DNS	Direct Numerical Simulation
EDS	Exponential Difference Scheme
FDM	Finite Difference Method
FEM	Finite Element Method
FV	Finite Volume
FVM	Finite Volume Method
HWA	Hot-wire Anemometry
LDA	Laser Doppler Anemometry
LES	Large Eddy Simulation
PDE	Partial Differential Equation
RANS	Reynolds Averaged Navier-Stocks equation
SIMPLE	Semi-Implicit Method for Pressure-Linked Equations
SIMPLEC	SIMPLE-Consistent
SOR	Successive Over-Relaxation
TDMA	Tridiagonal Matrix Algorithm